# Experimental Investigation of Ciliary Flow with C. reinhardtii
## Hydrodynamics, Ultrastructure, and Ciliary difference

Wei, D.

**DOI**
10.4233/uuid:b803bf1d-cf2d-4049-baab-c5de098bdeb9

**Publication date**
2020

**Document Version**
Final published version

**Citation (APA)**
Wei, D. (2020). *Experimental Investigation of Ciliary Flow with C. reinhardtii: Hydrodynamics, Ultrastructure, and Ciliary difference.* [Dissertation (TU Delft), Delft University of Technology].
https://doi.org/10.4233/uuid:b803bf1d-cf2d-4049-baab-c5de098bdeb9

# EXPERIMENTAL INVESTIGATION OF CILIARY FLOW WITH *C. reinhardtii*

## HYDRODYNAMICS, ULTRASTRUCTURE, AND CILIARY DIFFERENCE

# EXPERIMENTAL INVESTIGATION OF CILIARY FLOW WITH *C. reinhardtii*

HYDRODYNAMICS, ULTRASTRUCTURE, AND CILIARY DIFFERENCE

## Proefschrift

ter verkrijging van de graad van doctor
aan de Technische Universiteit Delft,
op gezag van de Rector Magnificus prof. dr. ir. T.H.J.J. van der Hagen, voorzitter van het College voor Promoties,
in het openbaar te verdedigen op donderdag 1 oktober 2020 om 10:00 uur

door

**Da WEI**

Master of Science in Physics,
University of Science and Technology of China, Hefei, China.
Born in Hefei, China.

Dit proefschrift is goedgekeurd door de

promotor: Dr. M. -E. Aubin-Tam
copromotor: Dr. D. S. W. Tam

Samenstelling promotiecommissie:

| | |
|---|---|
| Rector Magnificus, | voorzitter |
| Dr. M. -E. Aubin-Tam, | Technische Universiteit Delft, promotor |
| Dr. D. S. W. Tam, | Technische Universiteit Delft, copromotor |
| | |
| *Onafhankelijke leden:* | |
| Dr. G. Amador, | Wageningen University & Research |
| Prof. dr. G. H. Koenderink, | Technische Universiteit Delft |
| Dr. ir. L. Laan, | Technische Universiteit Delft |
| Prof. dr. ir. J. M. J. den Toonder, | Technische Universiteit Eindhoven |
| Prof. dr. ir. J. Westerweel, | Technische Universiteit Delft |

*Keywords:* *C. reinhardtii*, flagella, optical tweezers, hydrodynamics, flagellar hair, synchronization
*Printed by:* IPSKAMP printing
*Front & Back:* Graphics design by Da Wei and Qiao Yu.



ISBN 978-90-8593-450-9
Casimir PhD-series 2020-23

An electronic version of this dissertation is available at
http://repository.tudelft.nl/.

This thesis is dedicated to my grandfather
Wang Mei-Xue (1931-2018);
I was not there, I'm so sorry

# CONTENTS

# SUMMARY

The microscopic world is surprisingly busy with swimming micro-organisms. In a droplet of pond water, there can be tens of thousands of microbes. They are predators and preys, producers and consumers, and they form the bottom levels of the ecology of our world.

The swimming micro-organisms can be in general classified into prokaryotes and eukaryotes. Eukaryotes come later in evolution. They are higher organisms than the prokaryotes as they possess more complex cellular structures such as the nucleus and mitochondria. Motile eukaryotic micro-organisms all use an active hair-like structure for swimming, known as flagella or cilia. Although nuanced difference exists between flagella (cilia) of different species, their general internal structure and driving mechanisms are mostly the same. In some sense, they are one of the bestselling machines for locomotion on the micron scale.

Although flagella are the first-ever documented organelles in cell biology, our understanding of them is still limited. For example, we have only begun to appreciate how the conformational change of single protein motors results in the waveform on the scale of a flagellum. Our understanding of the flow generated by even a single flagellum is rudimentary: resolving the temporal features of such flow field remains experimentally challenging. On a larger scale, how thousands of cilia interact with each other to facilitate fluid transport is still elusive: theoretical models and simulations are waiting for experimental verification.

In this thesis, I explore different topics centering around flagellar/ciliary motility by employing novel experimental and numerical techniques, and hence advance our understanding.

My experimental investigation starts by resolving the flow generated by the beating cilia of single cells. Due to the high beating frequency, high temporal resolution is required to map the time-varying flow field, which conventional tracer particle-based flow velocimetry techniques cannot provide. To tackle this challenge, I implemented an optical tweezers-based flow velocimetry (OTV) technique.

In this technique, a bead is trapped and placed at a particular location by a focused laser beam. The local flow displaces the bead from the trapping center. This displacement, although small, can be accurately monitored by laser interferometry and converted into an electrical signal by photoelectric detectors. Essentially, we gain the desired accuracy and temporal resolution by exploiting the high resolution and large bandwidth of interferometric and electrical measurements.

With this technique, I revealed that the ciliary flow deviates fundamentally from how it is often modeled by Stokes equations. More specifically, the flow's amplitude decays faster spatially, and its phase shifts over distance. These discrepancies are resolved by adding a linear unsteady term to Stokes equations. Furthermore, I systematically characterized the ciliary flow field created by captured *C. reinhardtii* cells. The flow field in different directions and over the ciliary beating plane are measured experimentally,

modelled numerically, and analyzed theoretically. Results displayed excellent agreement with each other, and altogether increased our knowledge in the ciliary flow.

With the OTV measurements, I not only studied the basic hydrodynamics of ciliary flow but also addressed a long-standing hypothesis regarding the function of a ciliary appendage. Many cilia have fibrous ultrastructures called mastigoneme. These fibrous appendages are believed to help cells swim faster by increasing the ciliary surface area. Our experiments, together with numerical studies, completely refute this hypothesis: such fibrous hairs do not show any hydrodynamic significance in *C. reinhardtii*. Instead, its absence in genetically modified mutants appeared to result in some behavioral changes, causing the cells to turn abruptly more often than usual. Therefore, I have re-opened the question about the function of the fibrous mastigonemes. Future investigation towards this direction is needed and is likely to lead to more exciting findings.

Lastly, I attempted to bridge the physics of ciliary flow with the biology of ciliary beating. I focused on the ciliary difference and investigated it by selectively loading each cilium of *C. reinhardtii* with external flows. The ciliary difference is critical for the steering of biflagellates (micro-organisms swimming with two flagella/cilia). I observed an unreported functional difference between the two cilia, as I found that the coupling between the two cilia is unilateral. One cilium serves as the coordinator of beating, and a cell is coupled to external hydrodynamic forces mostly through this coordinating cilium.

Altogether, by introducing the OTV technique and incorporating different numerical methods, I was able to elucidate the ciliary flow in a time-resolved way, updating the current understanding in these unsteady flows. The effectiveness of this methodology was demonstrated again by its application in studying the function of the fibrous ultrastructures. By further moving on to the biological aspect of ciliary beating, we found a new type of difference between the two cilia, which enriches our knowledge in inter-ciliary coupling.

# SAMENVATTING

De microscopische wereld is verrassend druk met allerlei zwemmende microorganismen. In één druppel vijverwater kunnen maar liefst tienduizenden microben voorkomen. Ze zijn predator en prooi, producenten en consumenten, en samen vormen ze de basis van de ecologie van onze wereld.

De zwemmende microorganismen kunnen in het algemeen geclassificeerd worden als prokaryoten of eukaryoten. Eukaryoten ontstonden later in de evolutie. Ze zijn hogere organismen dan de prokaryoten, omdat zij in bezit zijn van complexere cellulaire onderdelen zoals de celkern en mitochondria. Motiele eukaryotische microorganismen zwemmen met behulp van actief bewegende haarachtige aanhangsels. Dit worden flagellen of ciliën genoemd. Hoewel er genuanceerde verschillen bestaan tussen de flagellen (ciliën) van verschillende soorten microorganismen, is hun interne structuur en aandrijfmechanismen nagenoeg hetzelfde. Bij wijze van spreken, zijn ze één van de best verkochte machines voor voortbeweging op de micronschaal.

Hoewel flagellen de eerste-ooit gedocumenteerde organellen in cellenbiologie zijn, blijft onze kennis over ze beperkt. Bijvoorbeeld, we beginnen pas net te begrijpen hoe de conformationele verandering van individuele eiwitmotoren resulteert in een golfvorm op flagellumschaal. Onze kennis over de stroom die gegenereerd wordt door de actie van één enkel flagellum is nog rudimentair: van de tijdelijke kenmerken van zo'n stromingsveld blijft experimenteel uitdagend. Op een groter schaal is de manier hoe duizenden ciliën met elkaar werken om vloeistofvervoer voort te brengen nog steeds ongrijpbaar: theoretische modellen en simulaties wachten nog op experimentele verificatie.

In dit proefschrift onderzoek ik verscheidene onderwerpen rondom flagellaire/ciliaire motiliteit door middel van unieke experimentele en computationele technieken, om hiermee onze kennis te verdiepen.

Mijn experimentele onderzoek begint met het opnemen van de stroom gegenereerd door de slaande ciliën van individuele cellen. Vanwege de hoge slagfrequentie is een hoge temporale resolutie vereist om het tijdsafhankelijk stromingsveld in kaart te brengen. Gebruikelijke velocimetrie methoden, gebaseerd op het volgen van traceer-deeltjes, kunnen zo'n hoge opnamefrequentie niet aan. Om deze uitdaging aan te gaan heb ik een velocimetrietechniek geïmplementeerd op basis van een optische-pincet.

Bij deze techniek wordt een klein balletje op een bepaalde locatie vastgehouden door een geconcentreerde laserstraal. De lokale stroom verplaatst het balletje uit het centrum van de locatie waar het balletje met laserstraal wordt vastgehouden. Deze verplaatsing, hoewel erg klein, kan door laser interferometrie nauwkeurig gemeten worden en omgezet in een elektrisch signaal door foto-elektrische detectoren. Effectief bereiken we de gewenste nauwkeurigheid en temporale resolutie door gebruik te maken van de hoge resolutie en ruime bandbreedte van de interferometrische en electrische metingen.

Met gebruik van deze techniek heb ik ontdekt dat de stroom die door de ciliën ontstaat fundamenteel verschilt met hoe het vaak doormiddel van de Stokes vergelijking ge-

modelleerd wordt. Specifieker, de amplitude van de stroomsnelheid daalt met een korter lengteschaal af, en zijn fase verschuift met afstand. Deze verschillen kunnen worden opgelost door het toevoegen van een lineaire tijdsafhankelijke term aan de Stokes momentumvergelijking. Daarnaast karakteriseerde ik systematisch het ciliaire stroomveld wat ontstaan is door op hun plek vastgehouden *C. reinhardtii* cellen. Het stroomveld in verschillende richtingen en binnen het ciliaire slagvlak is experimenteel gemeten, computationeel gemodelleerd, en op basis van bestaande theorien geanalyseerd. De resultaten uit het experiment, het model, en theorie kwamen uitstekend met elkaar overeen en laten samen zien dat onze kennis en begrip over ciliaire stroom is toegenomen.

Met de OTV metingen heb ik niet alleen de fundamentele hydrodynamica van ciliaire stroom bestudeerd, maar ook een lang-staande hypothese over de functie van de ciliaire aanhangsels behandeld. Vaak hebben ciliën haarachtig structuren, die mastigonemen worden genoemd. Deze vezelachtig aanhangsels worden verondersteld cellen sneller te laten zwemmen door een vergroting van het effectieve ciliaire oppervlakte. Mijn experimenten, samen met computationele studies, weerleggen deze hypothese: de vezelachtige haren hadden geen hydrodynamische invloed in *C. reinhardtii*. In genetisch gemodificeerde mutanten leek de afwezigheid van de mastigonemen te leiden tot veranderingen in hun gedrag, waarbij cellen vaker dan normaal plotseling draaien. Vanwege deze resultaten heb ik de vraag over de functie van deze vezelachtige mastigonemen heropend. Verder onderzoek in deze richting is nodig en zal waarschijnlijk tot meer boeiende vindingen leiden.

Tenslotte probeerde ik een verbinding te maken tussen de fysica van ciliaire stroom en de biologie van ciliaire beweging. Mijn focus lag op de verschillen tussen de twee ciliën van één *C. reinhardtii* individu. Ik onderzocht dit door elke cilium selectief te belasten met behulp van een externe stroom. Verschil tussen de ciliën is essentieel in de besturing van biflagellaten (microorganismen die zwemmen met twee flagellen/ciliën). Ik observeerde een niet eerder gerapporteerd functioneel verschil tussen de twee ciliën in dit onderzoek, namelijk dat de koppeling tussen de twee ciliën eenzijdig blijkt te zijn. Één cilium dient als coördinator van de gekoppeld ciliaire beweging, en de cel is gekoppeld aan externe hydrodynamische krachten vooral via dit coördinerende cilium.

In het geheel, door de OTV techniek te introduceren en door incorporatie van verschillende computationele methoden, was ik in staat om de ciliaire stroom in een tijdvariërend wijze te doorgronden. Hiermee heb ik de huidige kennis over deze stromen geactualiseerd. De effectiviteit van deze methodologie was nogmaals bewezen door toepassing in het onderzoek naar de vezelachtige mastigoneme structuren. Door mijn verdere verdieping in het biologische aspect van ciliaire beweging, vond ik een tot nu toe onbekend verschil tussen de twee ciliën, waardoor onze kennis over interciliaire koppeling verrijkt is.

# 1

# INTRODUCTION

*There's plenty of room at the bottom*

Richard Feynman

1

## 1.1. MICROBIAL MOTILITY

### 1.1.1. "PLENTY OF ROOM AT THE BOTTOM"

"There's plenty of room at the bottom" is a famous quote from Richard Feynman, the Nobel laureate in Physics 1965, and it is often used as the quote that unfolds our current era of nano-technology. Interestingly, this could have also made a perfect quote for Antoni Van Leeuwenhoek. He observed the teeming microbial world in a droplet of pond water for the first time and essentially initiated the investigation of the microscopic world.

It happened about 300 years before Feynman received his Nobel prize. In the 1660s, from a lake near Delft where our university is located, Antoni van Leeuwenhoek sampled the water and found the micro-organism moving in it. He wrote [1, 2]:

> *... dit was voor mijn onder alle de wonderheden, die ik inde natuer heb ontdekt, het alderverwonderendste, en ik moet seggen, datter voor mij, tot nog toe geen grooter vermaek in mijn oog is geweest, als dese gesigten, van soo veel duisenden, van levende schepsels, in een kleijn droppeltje water te sien, door malcanderen bewegen, ijder bijsonder schepsels, sijn bijsonder beweging hebbende.*

and it translated to:

> *... this was for me among all the marvels, that I have discovered in nature, the most marvellous, and I must say, that for me, up to now has been no greater pleasure in my eye, as these sights, of so many thousands, of living creatures, to see in a small drop of water, moving through each other, each special creature, having its special motion.*

For those thousands of "very small animals" ("zere kleine dierkens" as van Leeuwenhoek later put it) that were "moving through each other, ...each having its special motion", even just a droplet of water seemed to be indeed plenty of room.

Three hundred years later, now we know that the micro-organisms are the most pervasive life form on earth, they share with us our habitat but take advantage of the "plenty of room at the bottom" of the scale. They also explore the environment that is extreme in salinity [3], acidity[4], radiation[5], or temperature [5, 6] - where no other life form can bear to live.

Like van Leeuwenhoek, when looking into the microscope and seeing the busy inhabitants of the microscopic world for the first time, most of us are swept away. We cannot help starting to ask a series of questions, for example, why are they moving, and how do they do it?

### 1.1.2. WHY AND HOW THEY MOVE

The primary reason for the micro-organisms is to survive. This includes to find food, to avoid becoming other's food, and to reproduce. For example, autotrophic micro-organisms, which produce their own food from inorganic energy sources such as light, search for the best conditions to produce [7, 8]. In the mean time, heterotrophic micro--organisms move to search for organic carbon sources - which include other micro-organisms [9–11]. Lastly, gametes such as sperms move to search for egg cells to fuse.

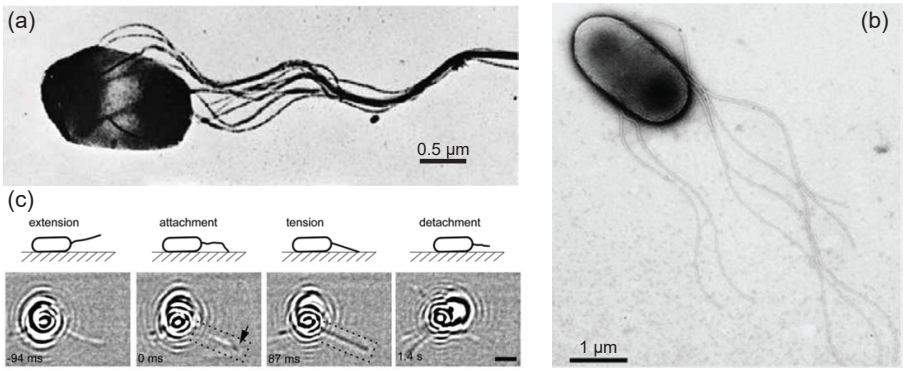


Figure 1.1: **Prokaryotic motility** (a) A bacteria, *Salmonella*, swimming with its flagella rotating and forming a bundle. Adapted from [13] with permission, copyright by IOP Publishing, all rights reserved. (b) An archaeon, *Halobacterium piscisalsi*, swimming with rotating archaella, but without forming a bundle. Adapted from [3] with permission. (c) A bacterium *P. aeruginosa* crawling (twitching) on the surface with type-IV pilus. Schematics show the corresponding action of the bacterium. Pilus in focus (black) means attachment with the surface. Scale bar: 2 μm. Adapted from [14] with permission.

While their purpose is mostly uniform, their moving strategies and apparatuses of locomotion vary a lot from one species to another. To better understand the variety, it is convenient to first categorize the micro-organisms into prokaryotes and eukaryotes, as each category employs different organelles for locomotion.

The term *prokaryote* is from Greek, with "pro" meaning "before" and "karyon" meaning "nut" or "kernel". Literally, the term refers to the micro-organisms that do not have the cell membrane-bounded nucleus to encapsulate their genetic material[12]. Prokaryotes include bacteria and archaea. While being relatively simple, they are capable of swimming [13] and crawling (twitching) [14]. **Fig. 1.1** demonstrates the typical ways of prokaryotic motility.

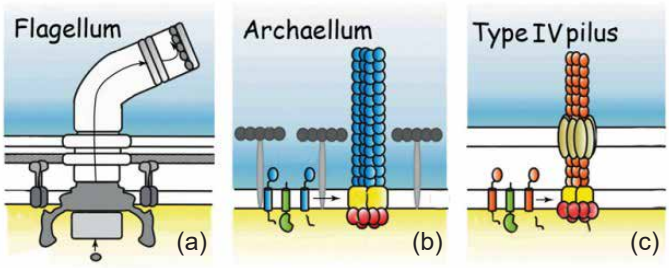


Figure 1.2: **Passive filaments in prokaryotes that facilitate locomotion.** (a) Bacterial flagellum, driven by the rotor on the anchor site. (b) Archaeal flagellum, also called archaellum, is structurally similar to the type-IV pilus, but rotates to facilitate swimming. (c) Bacterial type-IV pilus. Motility is achieved by the elongation and disassembly of the filament. Credit: Sonja-Verena Albers of the MaxPlanck Institute of Terrestrial Microbiology.

1

Their motility apparatuses include bacterial [13] and archaeal flagellum (archaellum) [15, 16], and type-IV pilus [14], shown in **Fig. 1.1**a-c, respectively. These apparatuses appear as protruding passive filaments from the cell bodies, and are driven by embedded molecular motors in the cells, **Fig. 1.2**.

Eukaryotes came later in evolution than prokaryotes. They are more complex in the sense that their genetic material is encapsulated in the cell nucleus, and they possess membrane-bounded cellular organelles. In general, eukaryotes are larger than prokaryotes. They move by swimming and crawling. Most motile eukaryotic micro-organisms exploit a single type of organelle called flagella or cilia (see **Sec. 1.3** for detail). Depending on how many flagella or cilia one organism possesses, eukaryotes can be further categorized. **Fig. 1.3** shows micro-organisms with one, two, four, and hundreds of cilia, respectively.

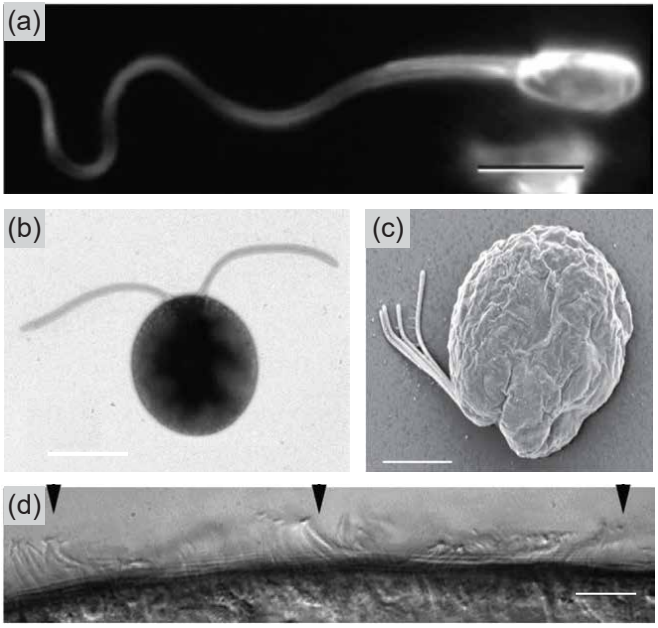


Figure 1.3: **Eukaryotic motility** (a) Bovine sperm cell swims with one flagellum. Adapted from [17] with permission. (b) A single cellular green alga, *Chlamydomonas reinhardtii*, swims with two flagella/cilia. (c) Another single cellular green alga, *Tetraselmis indica*, swims with four flagella/cilia. Adapted from [18] with permission, copyright © 2013 Taylor & Francis Group. (d) Ciliated epithelium of a flatworm, *Schmidtea mediterranea*. Large number of cilia beat in sync to propel fluid, forming a pattern known as the metachronal wave, which is akin to the "Mexican wave" seen in a packed stadium. This is also how ciliates swim. Black arrows mark the wavelength of the metachronal wave. Adapted from [19] with permission. Scale bars: 5 µm for (b), 10 µm for the rest.

Although the cilia of different eukaryotic organisms differ in length, number, and possibly ultrastructures, the cores of these cilia are strikingly similar. In fact, through evolution, it is structurally so conserved that it is sometimes called one of the bestsellers of nature [20]. Cilia also differ dramatically from the passive filaments that prokaryotes

use to swim. A cilium has its motors distributively arrayed along its scaffold such that the structure itself is active: it can bend and twist in isolation from the cell - if chemical energy is supplied.

In this thesis, eukaryotic flagella and cilia will be our focus. Interestingly, this fascinating cellular organelle is also first documented by Antoni van Leeuwenhoek [21].

### 1.1.3. FIRST EVER IDENTIFIED CELLULAR ORGANELLE

After being marvelled by various micro-organisms each swimming in its own way, van Leeuwenhoek started describing the different swimming gaits of the micro-organisms. In two cases out of many, he noticed that swimming was achieved by some tiny feet, legs or fins. He wrote [1]:

> *I also discovered a second sort of animalcules, whose figure was an oval; and I imagined that their head was placed at the pointed end. These were a little bit bigger than the animalcules first mentioned. Their belly is flat,* ***provided with divers incredibly thin little feet, or little legs, which were moved very nimbly****, and which I was able to discover only after sundry great efforts, and wherewith they brought off incredibly quick motions.*
>
> *Furthermore, I discovered a third sort of little animals, ..., and to my eye quite eight times smaller than the animalcules first mentioned; and I imagined, although they were so small,* ***that I could yet make out their little legs, or little fins****. Their motion was very quick, both roundabout and in a straight line.*

Now with the development of microscopy and fast cinematography, we have been able to observe the beating of these "nimble legs" for decades [22]. Time-resolved patterns of the beating have been recorded and studied in detail. Before going into details of how cilia beat and what is its structural basis, let us first revisit the general rules for evolution to come up with such patterns. For that, we return to the basics - the hydrodynamic interaction between the micro-organism and their ambient fluid.

## 1.2. LIFE AT LOW REYNOLDS NUMBER

### 1.2.1. GOVERNING EQUATIONS AND THE SCALING

To describe the microscopic fluid, there is actually no new physics other than Newton's second law of motion and the law of conservation of mass. According to the law of motion, the net force $F$ exerted on an object of mass $m$ will result in an acceleration $a$ that satisfies $F = ma$. According to the law of conservation of mass, the fluid mass must remain constant over time. Based on these laws, one may break down different sources of forces and then write the governing equation for describing the fluid motion around micro-organisms. The equations are famously known as the Navier-Stokes equations:

$$\begin{aligned} -\nabla p + \mu\nabla^2\mathbf{u} + \mathbf{f} &= \rho\left(\frac{\partial \mathbf{u}}{\partial t} + (\mathbf{u}\cdot\nabla)\mathbf{u}\right), \\ \nabla\cdot\mathbf{u} &= 0 \end{aligned} \tag{1.1}$$

1

The two equations represents the law of motion and the law of conservation of mass respectively. The left-hand side of the first equation in Eq. (1.1) describes forces exerted on the fluid. $\mathbf{u}(\mathbf{r},t)$ and $p(\mathbf{r},t)$ are the velocity and the pressure field respectively, and $\mu$ is the dynamic viscosity of the fluid. Together, the term $-\nabla p + \mu\nabla^2\mathbf{u}$ describes the stress force inside the fluid. $\mathbf{f}(\mathbf{r},t)$ represents the distribution of the body force such as gravity within the fluid. The right-hand side terms describe the fluid acceleration, where $\rho$ is the fluid density, and the terms are equivalent to the right-hand side of $F = ma$. Meanwhile, $\nabla\cdot\mathbf{u} = 0$ represents the conservation of fluidic mass when we assume the fluid to be incompressible. With these equations, theoretically, one is able to compute the fluid's state of motion (velocity, acceleration) at any point $\mathbf{r}$ at any given time $t$.

With the progress of computers, it is technically possible to calculate the fluid field by these equations by brute force. However, it is computationally costly and inefficient, because not all terms in the equation play an equally important role in the problem of interest, but every term consumes computational power. Moreover, brute-force computation provides less physical insights, as it does not help clarify which force dictates the fluid motion. Therefore, in studying different problems in hydrodynamics, before diving into the complete version of Navier-Stokes equations, one usually needs to weight the different terms to capture the dominating one. This weighting process is done by scaling.

The goal of scaling is to select the appropriate time ($\tau$), length ($L$), and velocity scales ($U$), so that every term itself is represented by a kernel of the order of magnitude 1, times a coefficient comprised of the chosen scales. The coefficients thus indicate the terms' relative significance compared to each other.

For example, if we are studying the dynamics of the fluid around a swimming microorganism, whose length is about $L$ and whose velocity is approximately $U$; and we are interested in what happens to the fluid on a time scale $\tau$, we can then scale Eq. (1.1) by $\tilde{\mathbf{r}} = \mathbf{r}/L$, $\tilde{\mathbf{u}} = \mathbf{u}/U$, $\tilde{t} = t/\tau$, and $\tilde{p} = p/\frac{\mu U}{L}$. We neglect the body force $\mathbf{f}$ in this scenario, as it consists mostly of gravity which is orders of magnitude smaller than the other terms. Then Eq. (1.1) reads[1]:

$$\begin{aligned} -\nabla\tilde{p} + \nabla^2\,\tilde{\mathbf{u}} &= \frac{\rho L^2}{\mu\tau}\frac{\partial\tilde{\mathbf{u}}}{\partial\tilde{t}} + \frac{\rho UL}{\mu}(\tilde{\mathbf{u}}\cdot\nabla)\tilde{\mathbf{u}} \\ \nabla\cdot\tilde{\mathbf{u}} &= 0 \end{aligned} \tag{1.2}$$

There are now two coefficients, $\frac{\rho L^2}{\mu\tau}$ and $\frac{\rho UL}{\mu}$. They tell whether the two corresponding terms are negligible, and we will discuss them in more detail in the last part of this section. For now, to give a flavour of the insightfulness of scaling a problem, we further simplify the equations by assuming that the time scale of interest is the advective time scale, which is the time the organism needs to move by a body length, $\tau_{\text{adv}} = L/U$. Then Eq. (1.2) reads:

$$-\nabla\tilde{p} + \nabla^2\,\tilde{\mathbf{u}} = Re\left(\frac{\partial\tilde{\mathbf{u}}}{\partial\tilde{t}} + (\tilde{\mathbf{u}}\cdot\nabla)\tilde{\mathbf{u}}\right) \tag{1.3}$$

[1] As the incompressibility condition, $\nabla\cdot\tilde{\mathbf{u}} = 0$, does not change form anymore, we drop it in the following equations.

There is now only one coefficient, $Re = \rho UL/\mu$. This dimensionless number is famously known as the "Reynolds number"[2]. Oftentimes, the Reynolds number is said to describe the competition between the inertia of the object (the organism in this case) and the viscosity of the fluid. However, what does this "competition" mean, and what does it entail? As it is critical for understanding flagellar and ciliary beating (and it is fun), let us now examine the Reynolds number more closely.

### 1.2.2. REYNOLDS NUMBER

By writing the Reynolds number $Re$ in different forms, one can interpret the "competition between inertia and viscosity" in different ways. Depending on the problem of interest, one way to interpret $Re$ can be more straightforward than the other and gives more physical insights.

Classically, $Re = \rho UL/\mu$ can be obtained by the ratio of the typical inertial terms in the Navier–Stokes equation, $\sim \rho \mathbf{u} \cdot \nabla \mathbf{u}$, to the viscous forces per unit volume, $\sim \mu \nabla^2 \mathbf{u}$, when a steady flow with typical velocity $U$ flows around an object of size $L$ [23]. A transparent way of getting this is as follows [24]:

$$Re = \frac{\text{inertial forces}}{\text{viscous forces}} = \frac{ma}{\sigma A} = \frac{\rho V \cdot \frac{du}{dt}}{\mu \frac{du}{dx} \cdot A} \tag{1.4}$$

$V$ and $A$ are the typical volume and cross-section area of the object, $\sigma = \mu \frac{du}{dx}$ is the shear stress. As $V \propto L^3$ and $A \propto L^2$, $V/A \propto L$, Eq. (1.4) becomes:

$$Re \propto \frac{\rho L \cdot \frac{dx}{dt}}{\mu} = \frac{\rho UL}{\mu} \tag{1.5}$$

Another way to write $Re$ is as the competition between time scales, $Re = \rho UL/\mu = \tau_{\text{diff}}/\tau_{\text{adv}}$, where $\tau_{\text{adv}} = L/U$ is the advective time scale and $\tau_{\text{diff}} = \rho L^2/\mu$ the diffusive time scale. For example, consider an object of size $L$ accelerating from stationary to a velocity $U$ almost instantaneously. For this perturbation to be transported convectively over one body size of the object $L$, the time scale is the advective time scale $\tau_{\text{adv}} = L/U$. On the other hand, for such perturbation to be transported diffusively over $L$, the time scale is $\tau_{\text{diff}} = \rho L^2/\mu$. $\tau_{\text{diff}}$ can be obtained from the diffusion equation $L^2 = D\tau_{\text{diff}}$, where $D$ is the diffusion coefficient. For momentum diffusion in fluid, $D = \mu/\rho$, and hence $\tau_{\text{diff}} = \rho L^2/\mu$. In this way, the "competition" between inertia and viscosity means: in which way does the momentum transport more quickly through the fluid, convectively or diffusively [23].

Although there are many more ways of writing and interpreting $Re$, in the context of studying the swimming of micro-organisms, arguably, the most straightforward way to illustrate $Re$ is as **Ref.** [23, 25] put it. It goes as follows.

If a swimmer of length $L$ and density $\rho_s$ suddenly stops moving its body parts in the medium of density $\rho$, the distance $d$ to which it can coast will follow the relation $d/L \sim Re \cdot \rho_s/\rho$. Therefore, given the density of the organism and the fluid are similar,

[2] The "Reynolds" behind this name is Osborne Reynolds, a British physicist who popularized this concept. However, the concept itself had been introduced earlier by George Stokes (the "Stokes" in the Navier-Stokes equations).

$\rho_s/\rho \sim 1$, in the regime where $Re \ll 1$ (*e.g.*, $Re = 10^{-2}$ or $10^{-3}$), once the micro-organism stops propelling fluid, it coasts only a hundredth or a thousandth of its body length $L$, which is at nm level. In other words, the locomotion will also stopped immediately.

This negligible coasting length compared to the length scale of interest tells clearly that a swimmer at $Re \ll 1$ cannot count on its momentum (inertia) to move through the fluid. Mathematically, this means that the terms on the right-hand side of Eq. (1.3) can all be neglected:

$$-\nabla \tilde{p} + \nabla^2 \tilde{\mathbf{u}} = 0 \tag{1.6}$$

Eq. (1.6) is famously known as the Stokes equation. It is both linear and time-independent. Its form is simple but has far-reaching implications, as we will see in the next section.

### 1.2.3. SCALLOP THEOREM

The implication of Eq. (1.6) for swimmers at low Reynolds number was first brought into light publicly by Purcell [25]. He noted that, with the negligible coasting length at low Reynolds number, no matter how fast a swimmer was moving before it stopped deforming its body, it would be stationary almost immediately and remained at the same spot where it stopped. In this light, for those micro-swimmers that want to move through the fluid by changing their body shape, as Purcell wrote, "*...inertia is totally irrelevant. We know that $F = ma$, but they could scarcely care less.*"

Then from the fact that Eq. (1.6) is (explicitly) time-independent, he noted that the rates of change in either the pressure field $p$ or the velocity $\mathbf{u}$, also do not matter. He wrote: *"... Time, in fact, makes no difference—only configuration. If I change quickly or slowly, the pattern of motion is exactly the same."* As the configuration is the only thing that matters, locomotion for swimmers at low Reynolds number derives from a purely geometrical approach [26].

Thereafter, Purcell concluded his finding as that there exists a class of shape changes that can never be used for locomotion in this regime [26]. This class of shape changes was termed "reciprocal" by him, and in his own words, it means *"... I change my body into a certain shape and then I go back to the original shape by going through the sequence in reverse."* For example, if a swimmer deforms its body slowly from $A$ to $B$ configuration, and quickly goes back to $A$ reciprocally, it will first go along a trajectory slowly, and then come back along the same trajectory quickly. However, there is no net motion. In this light, the rate of shape change only affects how fast the swimmer moves along the trajectory, not the shape of the trajectory and nor the ending point.

Purcell used a scallop to exemplify what he meant. In nature, scallop opens its shell slowly and closes it fast, squirting out water so as to move. We can see this from **Fig. 1.4**a. Opening up from half to fully took the scallop $\sim 0.4$ s (2 to 3), but closing from fully to half takes $\sim 0.01$ s (3 to 4). Moreover, after the shell had closed fully, the scallop moved by the inertia it accumulated during closing quickly (5 to 6). This cyclic pattern of moving is demonstrated in **Fig. 1.4**b. As a scallop has only one hinge, it has only one degree of freedom in its bodily configuration, which is the angle between the upper and the lower shell. As Purcell pointed out, a swimmer with only one degree of freedom is bound to move reciprocally. Therefore, unfortunately for a hypothetical microscopic scallop in

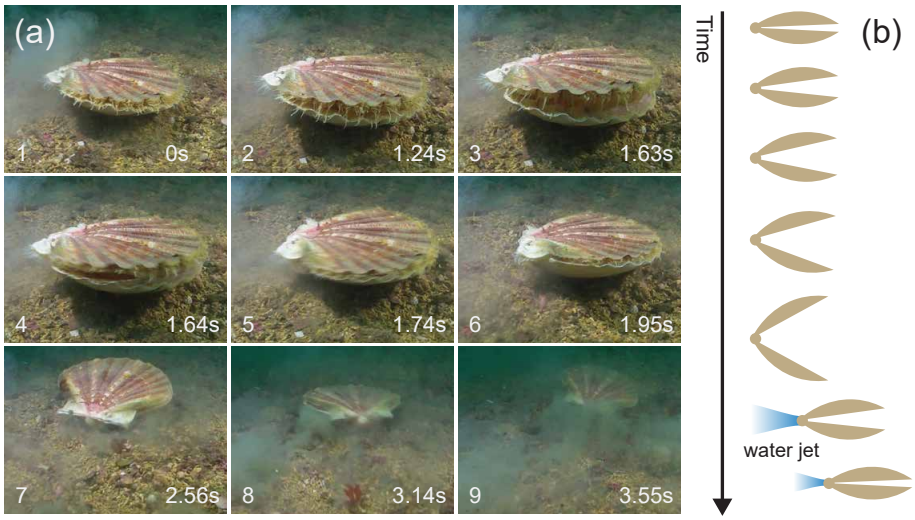


Figure 1.4: **Motion of a king scallop in water** (a) A scallop slowly opens its shell (1-3), and closes it quickly (4-6). After a cycle (1-6), the net effect is locomotion. (7-9) Location of the scallop after N = 1, 2, and 3 more cycles, respectively. Snapshots adapted from [27]. (b) Schematic drawing of a typical propulsion cycle of the scallop. Please note that the water jet comes out from the hinge side of the scallop, unlike many have assumed.

water or a normal scallop in honey, it could go nowhere but oscillate around the same spot. This vivid example has been henceforth used to term Purcell's finding regarding the implications of Eq. (1.6) - "the scallop theorem".

### 1.2.4. REAL-WORLD REALIZATION OF NON-RECIPROCAL WAVEFORM

Now we know that reciprocal shape changes cannot be used for swimming at low Reynolds number, a question follows immediately: what are the typical non-reciprocal shape changes that are adopted by the micro-swimmers?

**Fig. 1.5** displays some examples. A sperm cell swims by beating its flagellum, and such shape changes (waveform) can be regarded as a sinusoidal wave travelling from the proximal to the distal end of the flagellum (**Fig. 1.5**a). Such a nearly 2D waveform is widely adopted by uniflagellates [13] and biflagellates with one dominant flagellum such as *Ochromonas* [29]. Another typical non-reciprocal waveform is similar to the rotation of a corkscrew. Inspired by bacteria flagella and archealla shown in **Fig. 1.1**a-b, researchers have fabricated artificial micro-swimmers swimming with the same waveform, which are driven and guided by external magnetic fields [28] (**Fig. 1.5**b-c). Lastly, another class of typical non-reciprocal pattern is that of the eukaryotic cilia. **Fig. 1.5**d shows how a single-cellular green alga (*Chlamydomonas reinhardtii*) swims forward by beatings its two cilia. The ciliary shapes through a cycle are summarized in sub-panel 8. Similar to the picture of propagating wave on a sperm flagellum, the ciliary pattern can also be broken down to a travelling wave, but this time the wave travels on a curved track [30].

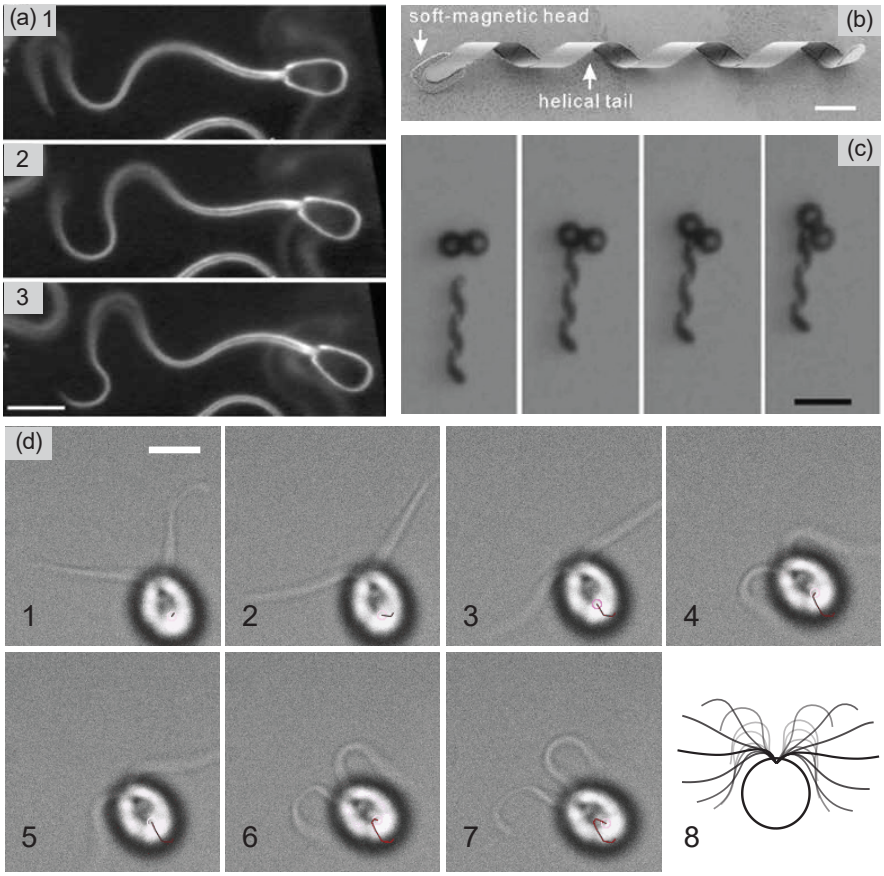


Figure 1.5: **Typical non-reciprocal shape changes adopted by micro-swimmers** (a) Non-reciprocal shape changes of a bovine sperm. A wave propagates towards the distal end of the flagellum. Panel 1-3 are taken with 200 ms interval. Adapted from [17] with permission. (b-c) An artificial micro-swimmer adopting the corkscrew waveform to swim. (b) SEM image of the micro-swimmer; (c) the artificial micro-swimmer moves towards two micro-beads within 2 s. Adapted from [28], with the permission of AIP Publishing. (d) *C. reinhardtii* employs a typical ciliary waveform to swim forward. Panel 1-7 are taken with 3 ms interval. The solid red line drawn on the cell body tracks the motion. Panel 8 displays the ciliary shapes during a cycle. Scale bars: (a) 10 µm, (b) 4 µm, (c) 15 µm, (d) 5 µm.

Now we have come back to the eukaryotic cilia with more understanding in its beating pattern. In **Sec. 1.3**, we will go into more details of this organelle. I will introduce the architecture of cilia, and their structural and molecular basis for beating.

### 1.2.5. A FURTHER NOTE ON THE STOKES EQUATION

One needs to notice that in simplifying Eq. (1.2) into Eq. (1.3), we are assumed to be interested in the fluid dynamics on the advective time scale $\tau_{adv} = L/U$. However, when it is not the case, even when $Re \ll 1$, the first term on the right-hand side of Eq. (1.2) can be non-negligible:

$$-\nabla \tilde{p} + \nabla^2 \tilde{\mathbf{u}} = \frac{\rho L^2}{\mu \tau} \frac{\partial \tilde{\mathbf{u}}}{\partial \tilde{t}} \tag{1.7}$$

This dimensionless number $\frac{\rho L^2}{\mu \tau}$ may be rewritten as $\frac{\rho L^2}{\mu \tau} = Re \cdot L/(U\tau) = Re \cdot \tau_{adv}/\tau$. In this way, we see that this number includes both the competition between inertia and viscosity, and the competition between the time scale of interest and the advective time scale. For this reason, we denote it as $Re_\tau$. The difference between $Re_\tau$ and $Re$ means that, even at small Reynolds numbers ($Re \ll 1$), on a time scale $\tau$ much smaller than $\tau_{adv}$, inertia will still play a significant role in the fluid dynamics.

$Re_\tau$ can also be written differently as $Re_\tau = (L/\delta)^2$, with $\delta = \sqrt{\mu\tau/\rho}$. In this way, the competition between inertia and viscosity and between different time scales, are combined into a competition between length scales - the length scale of the problem, $L$, and the characteristic length scale of vorticity diffusion $\delta = \sqrt{\mu\tau/\rho}$. The latter length scale, $\delta$, means how much the momentum (vorticity) propagates within the time scale $\tau$ of the problem.

## 1.3. EUKARYOTIC FLAGELLA AND CILIA

### 1.3.1. DISAMBIGUATION

When referring to the active structure responsible for locomotion and fluid transport, eukaryotic flagella and cilia mean virtually the same, with flagella referring to structures that are longer (>10 μm) and appear in small numbers on a single organism. However, these two terms can both refer to multiple different structures. For instance, *flagella* is also used for the motility apparatuses in prokaryotes (**Sec. 1.1**), and *cilia* for structures on insects wings. Therefore, it is advisable to clarify their usage before we proceed.

The word *flagellum* and *cilium* both come from Latin, and mean "whip" and "eyelash" respectively. As discussed in **Sec. 1.1**, flagella are organelles defined by function rather than structure [31]. Both passive filaments driven by different single motors in bacteria and archaea, and active[3] organelles driven by thousands of dyneins in eukaryotes, are termed flagella. On the other hand, cilia are defined by structure rather than function. When used for micro-organisms, the term *cilia* is limited to eukaryotes [32]. They have a highly conserved internal structure across species from nematodes to ancient protozoa [33].

In the following part of the thesis, the terms *flagellum(a)* and *cilium(a)* refer only to eukaryotic flagella and cilia whose major function is propelling fluid. For the model organism we use, *C. reinhardtii*, the two terms are used interchangeably in literature. In this thesis, to be consistent with each research's implication, the term *cilium(a)* will be used for **Chap. 2** and **Chap. 3**, and the term *flagellum(a)* for **Chap. 4** and **Chap. 5**.

[3] Whether a structure is passive or active depends on whether it can undergo shape changes in isolation from the cell - given external supply of chemical energy. Cilia were first proved to be active by [34, 35]

1

### 1.3.2. UNIVERSALITY OF THE CILIARY STRUCTURE

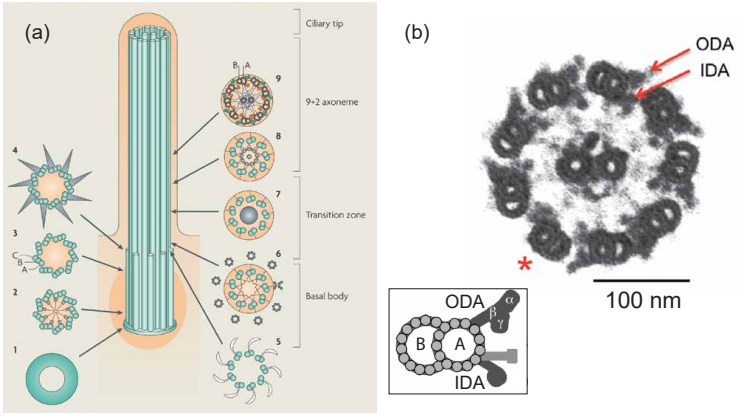


Figure 1.6: **General structure of a cilium.** (a) Cross-sectional cytoskeletal structure of different ciliary region, length not to scale. Reprinted from [36] with permission. (b) Cross-section of an *C. reinhardtii* cilium in its typical "9+2" region. ODA (IDA): outer (inner) dynein arm. *: It it long known that the cylindrical symmetry breaks in the ciliary cross section, as one doublet does not possess ODA [37]. Adapted from [38] under the terms of the Creative Commons Attribution License. Inset: dynein arms on a microtubule doublet (A,B). Adapted from [39] under the terms of the Creative Commons Attribution License (CC BY 4.0).

A cilium is comprised of more than 300 different polypeptides [40]. It is a cytoskeletal scaffold equipped by dynein motors distributively and further wrapped up by a lipid membrane with embedded channels. Its core, the axoneme, which includes the scaffold and the motor proteins, is essentially a macro-molecular machine [41] with stunning sophistication. By somehow having the thousands of different types of motors work in a well-orchestrated fashion, this machine converts chemical energy from the cell to mechanical work, and hence enables cells to swim [42].

The ciliary core, the axoneme, is highly organized [41, 43] and highly conserved through evolution [33, 44]. As shown in **Fig. 1.6**a, a cilium extends from its basal body (BB). The basal body is ~0.4 µm in length [45], and its core consists of 9 microtubule triplets. After a region of ~0.2 µm long, the 9 triplets in the basal body transition to 9 microtubule doublets (MTDs) in the axoneme. Approximately after the transition zone ends, 2 microtubule singlets appear in the centre of the 9 MTDs [46]. The two singlets are called the central pair (CP), and they are linked to the MTDs with radial spokes (RSs). This forms the well-known "9+2" structure of a cilium (**Fig. 1.6**b), and this structure persists until the ciliary tip [46].

Each of the 9 MTD has a distinctive structure with a complete ring of 13 protofilaments (the A tubule) and an incomplete ring of 10 protofilaments[4] (the B tubule), see the inset of **Fig. 1.6**b. Each protofilament is formed from tubulin dimers stacked head-to-tail, which gives rise to an intrinsic polarity. The microtubule plus end lies at the ciliary tip and the minus end is anchored to the basal body [7]. A detailed description of the relevant proteins and a state-of-the-art visualization of the microtubule structure can be found in **Ref.** [41].

[4] Literature reported the number of protofilaments comprising B tubule inconsistently (10 or 11) [47]. However, in a recent study, the 11$^{th}$ one was found to be not a protofilament [41].

What drive the cytoskeletal structure is the dyneins arrayed along the MTDs. Dyneins are ATPases that undergo cyclic conformational changes, and thereby convert chemical energy to mechanical work [48]. The dyneins are located in the two arm-like structures on the A-tubule of the MTDs. Such structures are called the inner- and outer dynein arm (IDA and ODA)[5]as they point inward and outward respectively, see **Fig. 1.6**b. In addition to the "9+2" cross-sectional regularity, an axoneme also displays regularity in its longitudinal direction as it appears in a 96 nm repeating unit [41, 49], see **Fig. 1.7**. In general, in each 96 nm repeat on each MTD, there are 4 ODAs and 1 IDA, together with some radial spokes connecting to the central singlets, plus some regulatory complexes.

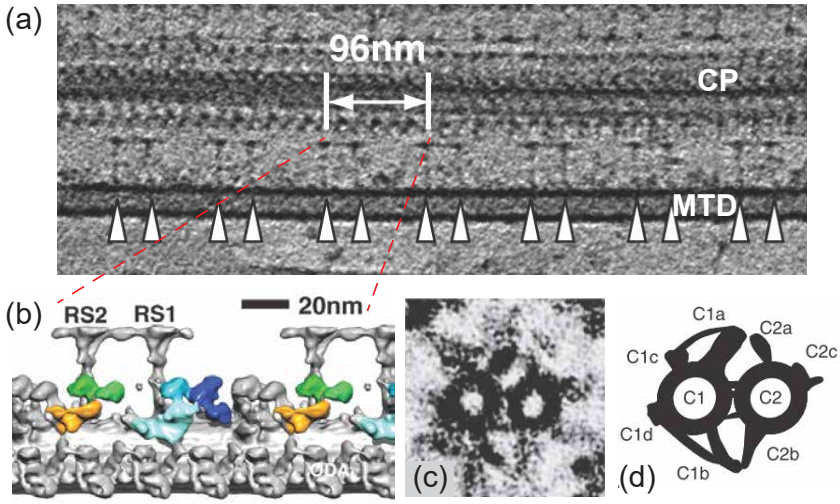


Figure 1.7: **Structure of the central pair (CP) and the radial spokes (RS).** (a) TEM image of the longitudinal section of a cilium of wildtype *C. reinhardtii.* MTD: microtubule doublet. Arrows: radial spokes (RSs). (b) 3D reconstruction of the 96 nm repeat shown in (a). (a-b) Adapted from [49] with permission from AAAS. (c) Cross-sectional TEM image of the central pair (CP). (d) Schematic of the CP connection. (c-d) Adapted from [7] Vol.3, Chap.15 with permission.

In an oversimplified picture, to bend the axoneme, the dyneins cling to the B-tubule of their neighbouring MTD and attempt to slide along it [50]. However, as the MTDs are fixed on their bases and are interlinked, bending takes place instead of sliding. In this process, the inner-arm dyneins are most relevant to the ciliary bending amplitude, while the outer-arm dyneins are responsible for the beating frequency [38]. In other words, the inner-arms are akin to motors of high torque but low speed (frequency), while the outer-arms akin to motors of high speed but low torque [44].

[5] In literature, two sets of abbreviations are commonly used in this context and can be easily confusing, namely, IDA/ODA and IAD/OAD. To clarify, IDA and ODA are used to describe the arm-like structures, which contain not only dyneins but also other polypeptides serving either sensory or structural purposes. On the other hand, IAD and OAD are short for inner- and outer-arm dyneins, which specifically refer to the multiple species of dyneins in the inner-arm, and the single species of 3- (or 2-) headed outer-arm dynein, respectively.

### 1.3.3. DIVERSITY OF THE CILIARY STRUCTURE

With such a highly conserved ciliary structure, an intriguing question follows: where does the diversity of the ciliary beating frequency and gait come from? For example, the flagellum of bovine sperm and sea urchin (*Tripneustes gratilla*) sperm are both ~ 100 µm long and undergo similar waveform. However, they beat at drastically different frequencies: the former at ~ 2 Hz [17], and the latter at ~ 50 Hz [51]. As another example, *C. reinhardtii* cilia and mammalian epithelial cilia are also of similar length and beat with similar waveform, but the former is at ~ 50 Hz while the latter at ~ 10 Hz [52]. Additionally, the *C. reinhardtii* cilia can also readily perform the typical waveform of a sperm cell at ~80 Hz, while it is not reported whether mammalian cilia can behave the same.

In fact, among cilia across species, there exists diversity in the structure, motor proteins, and chemical sensors [39]. For instance, the 96 nm repeat in sea urchin (*Strongylocentrotus*) sperm cell [53] has 3 radial spokes, while in *C. reinhardtii*, it has only 2. Moreover, an inter-MTD linker that breaks the rotational symmetry of the 9 MTDs in these two organisms is likely not homologous [53]. On a molecular level, while *Ciona* [39] and *Strongylocentrotus* sperm flagellum [48], and mammalian cilium [52] have outer-arm dyneins of only 2 heads (with which they cling to the neighboring MTD), in *C. reinhardtii* the number of heads per ODA is 3.

Meanwhile, in addition to the ciliary diversity across species, the structural properties of a given cilium vary at different lengths [43]. In the longitudinal direction, not only the "9+2" structure may vary as shown in **Fig. 1.6**a, but also the dynein composition varies [54]. More specifically, at different lengths of the cilia, the power of bending differs.

Finally, the rotational symmetry between the 9 MTDs of a cilium must also be broken. Otherwise, it is hard to imagine how a cylindrically symmetric axoneme could generate a mostly planar beating waveform [37, 44]. In *C. reinhardtii*, the rotational symmetry was firstly found to be broken as 1 MTD does not possess ODAs, and 2 other MTDs are connected by a special linker [37]. In the recent decade, thanks to the advancement of cryo-EM, the 9 MTDs are revealed to be different in both composition and longitudinal profile. For an excellent report on this topic, the readers are invited to **Ref.** [43]; and for a thorough and up-to-date review on this topic of ciliary asymmetry, readers are invited to **Ref.** [55].

### 1.3.4. THE MANY UNKNOWNS

After decades of research in the kinematic bending pattern, structural properties, and the molecular basis of cilia, our understanding of this fundamental swimming motor for eukaryotes has dramatically deepened and is still progressing rapidly [55, 56]. However, with all these being said, there are still many unknowns about it.

For example, currently, there are many simplified models to describe how the collective motion of the dyneins results in ciliary bending, and how the frequency of oscillation is derived from buckling instability [57–61]. Nevertheless, there is still no definite answer to which model is the most accurate [62]. Although modelling parameters can be tweaked to bring about different ciliary waveforms [61], what do the parameters mean for the ciliary molecular structures is elusive [63]. Also, a very recent study [42] has confirmed on the single dynein scale, that bending happens due to inhibition of the dynein

motors on the inner side of bending, and this inhibitory signal propagates from the base to the tip, giving rise to the propagating wave along cilia and flagella [42, 64]. How do the dyneins couple to each other to cooperate? Moreover, how to account for these new findings in the models? These are all just a few of the many open challenges at the moment.

Now that we have a general idea about why and how the cilia beat in such a way, in the next section, I will proceed with introducing the model organism, *Chlamydomonas reinhardtii*, which we use to investigate the ciliary flow, ciliary ultrastructure, and the ciliary difference in this thesis.

## 1.4. THE MODEL ORGANISM C. REINHARDTII

### 1.4.1. WHY *C. reinhardtii*

In the investigation of ciliary structure, assembly, function, as mentioned frequently in the previous section of dynein functions, the single-cellular green algae *Chlamydomonas reinhardtii* has been employed as a model organism [65, 66]. A model organism is a non-human species that is extensively studied to understand particular biological phenomena, with the expectation that discoveries made in the model organism will provide insight into the workings of other organisms [67]. *Chlamydomonas reinhardtii* serves well as a model organism for at least the following reasons [65, 66, 68].

First, it has a well-studied genetics [65]; and hundreds of readily available mutants [69, 70] - either by identification and isolation or by genetic mutagenesis. Such an advantage allows researchers to map the function of different proteins and obtain a mechanistic understanding of ciliary functions.

Second, the cell can be cultured with relative ease - compared to mammalian cells. *C. reinhardtii* can grow in several different media, including minimal ones (see [7] Vol.1, Chap.8). In principle, several autoclaved Ellen-Meyer flasks, some silicone tubes, an aquarium pump, a filter, and a light bulb are all the instruments needed for preparing a liquid culture of *C. reinhardtii*. Moreover, after the liquid culture is inoculated, barely any maintenance is needed.

Third, the cell has several features that benefit different types of research. The features include at least the ones listed below:

- Its cell cycle can be easily entrained by the laboratory day/night cycle. This allows us to have macroscopic suspensions of cells whose progression through the cell cycle is (essentially) perfectly synchronised, facilitating, *e.g.*, proteomic and metabolomic research (see [7] Vol.1, Chap.8 and [68]).
- The whole suspension of cells can synchronously shed their cilia upon mild pH-shock (pH $\approx$ 4.5), allowing purification and preparation of a suspension of cilia [71].
- The cell's geometry and ciliary beating pattern are advantageous for experimentation. The cells are ellipsoidal and hence tracking them is relatively simple; and their two cilia beat mostly in the same plane, allowing simultaneous observation for both of them, and hence investigation into their kinematics and dynamics [72–74].

The species *C. reinhardtii* was named in honour of the Ukrainian botanist Ludwig Reinhardt. Currently, there are three principal strains used for research globally: namely, the Sager line, the Cambridge line, and the Ebersold/Levine 137c line[6]; which are all considered as wildtype (see [7] Vol.1, Chap.1). Although all three lines are supposedly derived from the same zygospore (akin to a fertilized egg), they somehow turn out to be different as the 137c line carries a mutation in nitrate utilization. In any case, the three lines have been separate since at least the early 1950s.

In this thesis, all our experimental results are obtained from the plus mating type (plus and minus are mating types akin to male and female in sexual reproduction), *cc-125 mt+*, from Ebersold/Levine 137c line.

### 1.4.2. CELL ARCHITECTURE

*C. reinhardtii* is a single cellular green alga. At first glance, it has an ellipsoidal cell body that is ~8 µm in length; and it possesses two cilia, a cell wall, and an orange eyespot which breaks the rotational symmetry of the cell body, **Fig. 1.8**a. As a plant cell, *C. reinhardtii* has both chloroplast and mitochondria, and its photosynthesis is similar to land plants (see [7] Vol.2, Chap.8). It can be autotrophic - living on photosynthesis, heterotrophic - living on external carbon sources such as acetate, or mixotrophic, which combines the former both. Here only the cellular structures that are relevant to this thesis will be introduced; for a complete review into this topic, the readers are referred to **Ref.** [7].

#### CILIA

*C. reinhardtii* has two cilia that are ~12 µm long and ~400 nm thick, **Fig. 1.8**b. The two cilia are termed the *cis* cilium and the *trans* cilium respectively, by their distance to the eyespot, with the *cis* being the closest one. The two cilia usually beat synchronously at ~50 Hz, with an almost mirrored waveform that together is akin to the breaststroke of a human swimmer. They also beat almost within the same plane. In this light, the two cilia seem to be identical; however, in **Sec. 1.4.3**, we shall discuss their inherent differences and the significance of these differences to the cell.

Each cilium is covered by two arrays of glycoprotein fibres called mastigoneme, as shown in **Fig. 1.8**b. Mastigonemes are found only on the distal two third of each cilium. These fibres are ~1 µm long and ~15 nm thick. Their function has been proposed to be enhancing cell swimming speed; however, as we shall refute this in **Chap. 4**, it remains enigmatic.

As *C. reinhardtii* has a cell wall, the cilia need to go through the wall structure. The site for passing through is called the "collar", **Fig. 1.8**c. The collar is featured by a bar-like protein structure distinct from the matrix-like surrounding. During the beating, the collars are possibly in direct contact with the cilia, resulting in a slightly reduced beating frequency (**Chap. 4**).

Another distinct feature on the anchor site of the cilia are structures formed by intramembranous particles [45]. The particles form two different rings around the cilium

[6] The annotation "137c" means: the third ("c") zygote colony, recovered from the **soil sample** numbered "137", designated by G. M. Smith. As *C. reinhardtii* is actually a soil alga, it is so far unclear how do they live in the wild, namely, if swimming is their most common state [75].

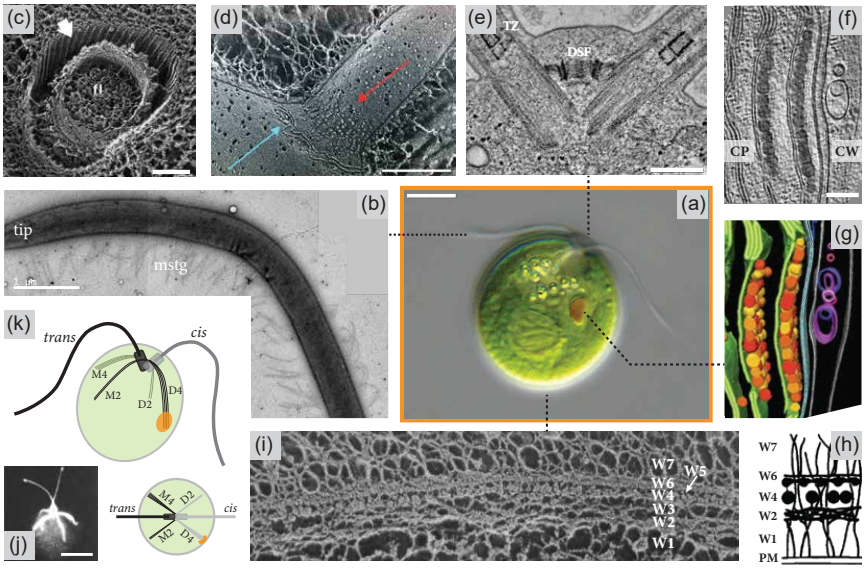


Figure 1.8: **Cell architecture of *C. reinhardtii*.** Panel index starts from the centre (a) and rotates clock-wise around the centre (b-k). (a) Optical microscopy of a *C. reinhardtii* cell. Courtesy of Wolfgang Bettighofer, Kiel (www.protisten.de). (b) TEM microscopy of a *C. reinhardtii* cilium. Mastigonemes (mstg) are observed on the cilium and display certain flexibility (*e.g.*, near the base). (c) The site where a cilium (marked "fl") grows out from the cell and is in contact with the cell wall. The structure is termed the "collar", and is featured by the bar-shaped proteins which are distinct from the surrounding cell wall matrix. Adapted from [7] Vol.1, Chap.2 with permission. (d) The site where the cytoplasmic membrane and the ciliary membrane meet, featured by two types of intramembranous particles, namely, the ciliary necklace (red arrow) and the ciliary bracelet (blue arrow), (e) Anchor sites of the two *C. reinhardtii* cilia. The basal bodies of the two cilia are connected by different fibres. Shown in this figure is the distal striated fibre (DSF). TZ: ciliary transition zone. (d-e) Adapted from [45] under the terms of the Creative Commons Attribution License (CC BY 4.0). (f-g) Cross sectional TEM microscopy (f) and 3D reconstruction (g) of the *C. reinhardtii* eyespot. CP: cytoplasmic side, CW: cell wall side. The dark granules in (f) are the carotenoid-rich granules, and are colored red and orange in (g). Adapted from [76] under the terms of the Creative Commons Attribution License (CC BY 4.0). (h-i) Schematic and EM microscopy of the layered *C. reinhardtii* cell wall structure. W1-7: cell wall layer 1-7, PM: cytoplasmic membrane. Adapted from [77] with permission from Rockefeller University Press . (j) Fluorescent microscopy of the rootlet structure inside a *C. reinhardtii* cell. There are 4 rootlets extending from the basal bodies into the cell body. Adapted from [78] with permission. (k) Schematic of the rootlets structure. Upper: side view, similar to the view point in (a); lower: top view, from outside of the cell's anterior pole. M and D stand for *mother* and *daughter* rootlets; 2 and 4 indicate the number of microtubules comprising the rootlet. Scale bars: (a) 5 µm, (b) 1 µm, (c) 100 nm, (d-e) 200 nm, (f-g) 200 nm, and (j) 5 µm.

and are termed by their appearances as ciliary/flagellar necklace and bracelet, respectively, **Fig. 1.8**d. The region between the necklace and the bracelet is possibly a domain for targeting and fusion of transport vesicles coming from the Golgi apparatus ([7] Vol.3, Chap.11). Also, as the domain of ciliary membrane and the cell body membrane are different in composition, and there is evidence for the existence of a barrier to inter-domain free diffusion of the membrane proteins, it is tempting to hypothesize that the necklace

or the bracelet may act as the barrier.

#### BASAL BODY AND PROBASAL BODY

As discussed in **Sec. 1.3**, cilia anchor on the basal bodies (BBs). The two basal bodies orient approximately 90° from each other and are connected by two fibrous structures at both ends [45]. The better-understood one is the distal striated fibre (DSF), which connects the distal ends of the two BBs and displays a striated pattern, **Fig. 1.8**e. DSF is rich in centrin, a calcium-binding contractile protein [79]. As a result, upon elevation of ambient calcium concentration, the DSF contacts and brings the basal bodies to a more parallel configuration [80]. Together with an altered ciliary waveform, the cell thus swims temporally backwards. The contraction does not consume energy, while the re-extension does [81]. The mechanical coupling provided by DSF has been proved to be critical for the ciliary synchrony in captured cells [82, 83]. On the contrary to the well-studied DSF, the proximal striated fibre (PSF), which binds the BBs at the proximal ends, is of unknown composition and dynamic function (see [7] Vol.3, Chap.2).

Each basal body is also accompanied by a probasal body (an immature basal body), which will develop into the new basal body in the daughter cell [78, 84]. This process may be related to the ciliary difference, which will be introduced in detail in **Sec. 1.4.3**.

#### ROOTLETS

The BBs are also known to be linked to the cell nucleus [85], and are further anchored into the cell body by four microtubule bundles. These bundles are called rootlets. **Fig. 1.8**j and k show a fluorescent microscopy of the rootlets [78] and their schematic drawing, respectively.

Depending on which BB the microtubule rootlet attaches to, they are denoted as M (mother) and D (daughter) rootlets. The mother rootlet attaches to the older BB inherited from the mother cell, and the daughter rootlets to the BB developed from the corresponding probasal body, **Fig. 1.8**k. Furthermore, depending on how many microtubules a rootlet has, they are denoted as M/D2 and M/D4. These rootlets also contain centrin and contract upon elevation in calcium concentration [79, 86], therefore, together with the fibrous structure (DSF), they form a rather sophisticated mechanical network that anchors the cilia pair in the cell body. After the formation of the rootlets, the daughter cell forms the new eyespot around the D4 rootlet [78].

#### EYESPOT

In appearance, the eyespot is an orange disk near the cell's equator. It is ~1 μm in size, and slightly bulges out from the cell, **Fig. 1.8**a. The organelle is light-sensitive and facilitates phototactic behaviours (swimming towards or away from the light) [87, 88]. It also breaks the geometric symmetry of the ellipsoidal cell body and is thus used to term the two cilia [55].

The eyespot consists of a specialized cytoplasmic membrane region, two layers of regularly arrayed granules, and several other membrane structures [89], as shown in **Fig. 1.8**f-g. The structure is light-sensitive because the cytoplasmic membrane contains many copies of a light-gated ion channel protein, channelrhodopsin [68]. The protein is sensitive in the 450–700nm spectral range, and upon opening up, it creates photo-

current by calcium influx [90].

Meanwhile, the eyespot's orange appearance derives from the two layers of regularly arranged granules, which are rich in carotenoid pigment [89]. The granules are 70-100 nm in diameter [76], and they help increase the sensitivity of light detection as much as ~100 folds [91]. Altogether, the two layers serve functionally as a mirror. They shield the channelrhodopsins from the light coming through and focused by the cell body [88], and reflect the light from the other side, making them pass through the channelrhodopsins twice [91]. It is worth noticing that, determining the direction of light with one's isotropically sensitive eye (channelrhodopsins) embedded in an almost transparent body is a challenging task. However, it is also a task that micro-algae have to tackle [92]. In this light, the devising of the layered granules, which is analogous to putting a mirror on one side of a flat eye, so it only sees one direction, often strikes me as an ingenious way to break the spatial symmetry.

After cell division, the two daughter cells both form their new eyespot around the D4 rootlet [89]. It is located near the equator and is 45° from the ciliary beating plane [22, 91], **Fig. 1.8**k. In this way, the cell will be able to maintain a prolonged swim towards or away from the light. For an excellent illustration of how this is achieved, the readers are invited to **Ref.** [87].

#### CELL WALL

The cell wall of *C. reinhardtii* is ~300 nm thick (from the negatively stained TEM samples in our lab). Unlike the cell wall of land plants, it contains no cellulose but is instead rich in glycoprotein. In total, 20-25 proteins are found to form the cell wall [93]. ~20 proteins out of these form a crystalline structure [94, 95], and the several other proteins form a noncrystalline structure that is responsible for the integrity and the overall shape of the wall [94].

A cross-section of the cell wall is displayed in **Fig. 1.8**h-i. Instead of being a homogeneous and randomly cross-linked matrix, the cell wall possesses remarkably organized features. It was first thought to consist of 7 layers, denoted as W1-W7 by [96]; however, the W3 and W5 layers were later found to be probably spaces [77]. Here we use the same notation of W1-W7 as in [96] and [7] Vol.1, Chap.2 for consistency.

The *C. reinhardtii* cell wall is not only organized in the stacking but also can be highly organized within layers. For example, the layer that separates the outer domain (W7) from the inner layers (W1,2,4), has two sub-layers, which both display a stunning hexagonal lattice structure [95].

More than ten different cell wall-deficient mutants are isolated and characterized ([7] Vol.1, Chap.2). A commonly used one, *cw15*, will be employed in **Chap. 4** together with its genetically modified derivative *mstg*. The *cw15* cells possess neither a multi-layered cell wall nor the ciliary collars [97]; instead, a single layer of fibres wrap the cell around, which is similar to the outer layer (W7) of the cell wall of wildtype *C. reinhardtii*. As we shall see in **Chap. 4**, the loss of such structures probably results in a 10% increase in the ciliary beating frequency, showing that the cell wall is not only relevant to studying cell structure but also to studying swimming dynamics.

What makes this wall structure more intriguing is that there also exists evidence showing that it makes a difference in calcium signalling [98]: *cw15* responds to hyper-

and hypo-osmotic stress differently from the wildtype.

### 1.4.3. *cis-trans* CILIARY DIFFERENCE

In Latin, *cis* and *trans* are prefixes meaning "this side of" and "the other side of" respectively. Therefore, the complete terms that describe the two cilia more accurately should be the *cis*-eyespot cilium and the *trans*-eyespot cilium.

To the best of my knowledge, they were indeed termed so in the first place in 1982 [99]. Later, in 1984, in studying the cells and cell models[7] circling on the bottom of the observation chamber, the two cilia were termed as the *cis*- and the *trans* flagellum (cilium) for the first time - based on whether the eyespot is inward or outward the circling path. In the same spirit, when fast-cinematography was first applied to study the swimming kinematics of *C. reinhardtii* in 1985, *fi* and *fo*, which mean the flagellum (cilium) inward and outward the cell's helical swimming path respectively, were also used to term them [22]. The terms became unanimous as *cis*- and *trans* flagellum (cilium) in 1987 at latest [100, 101], dropping the "eyespot" part.

Investigations in the *cis-trans* ciliary difference in *C. reinhardtii* were initiated to understand phototactic behaviours in this organism [102]. To swim towards or away from the light, a cell must be able to steer. For a biflagellate such as *C. reinhardtii*, steering hinges on the difference between the two cilia. So far, the two cilia are known to differ in two general aspects, namely, beating frequency and activity modulation. In this section, the experiments that advanced our understanding of the *cis-trans* difference will be reviewed.

#### FREQUENCY

The two cilia were found to be able to beat at different frequencies in as early as 1967. Ringo [46] reported that "the synchrony may be disturbed for brief periods". Later in 1985, by introducing fast-cinematography, Rüffer and Nultsch [22] were able to observe ciliary kinematics at a time resolution of 2 ms (500 fps) and reported for the first time how much the frequency differs.

In 1987, Rüffer and Nultsch [101] started using micro-pipettes to fix *C. reinhardtii* cells by aspiration. Although this may seem trivial, it was a crucial measure that advanced our understanding of ciliary beating. Previously, a cell could only be studied briefly during the several beats that it stayed in focus, and its cilia were visible for only a small fraction of time during this observation. By fixing the cell body, one is finally able to track the ciliary kinematics of a single cell for a long time. Thereby, Rüffer and Nultsch [101] reported that the *trans* cilium could beat at a higher frequency, which was a conclusion often revisited and found highly reproducible [22, 73, 100, 101, 103].

Rüffer and Nultsch [101] also observed the two asynchronous beating modes of *C. reinhardtii* that are now termed "slip" (or "phase slip") [73], and "drift" [66]. A slip lasts a couple of beats, while the drift last tens or hundreds of beats. In both modes, the *trans* cilium beats faster than the *cis*[8]. In the same year, Kamiya and Hasegawa [100] also reported such frequency difference, based on uniflagellated live *C. reinhardtii* cells and

[7] Cell models are cells treated with detergent so that both their cytoplasmic and ciliary membranes are permeablized, and hence the axonemes are subjected directly to the environmental concentration of chemicals. Given energy supply (ATP), cell models can mimic the beating and even the swimming of intact cells.

reactivated cell models.

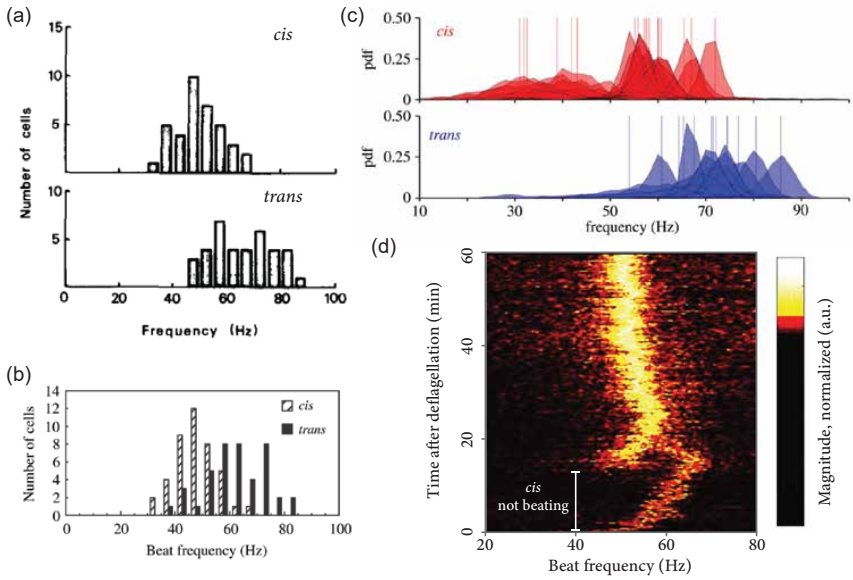


Figure 1.9: **Frequency difference between the *cis* and the *trans* cilium** (a) Observed in live uniflagellated *C. reinhardtii* cells produced by shear flow, N = 37 cells for each panel. Adapted from [100], with permission from Elsevier. (b) *cis*- and *trans* frequency observed in detergent-treated and reactivated wildtype cell models, N = 42. Final ATP concentration 1 mM. Adapted from [104] with permission. (c) *cis*- and *trans* frequency observed in uniflagellated *C. reinhardtii* cells produced by pipette suction. Shaded profile: normalized frequency distribution; vertical line: the average frequency over time. Adapted from [103] under the terms of the Creative Commons Attribution License (CC BY 3.0). (d) Long time observation (60 min) after deflagellating the *cis* cilium of a wildtype *C. reinhardtii* cell. The *cis* cilium was not beating until ~15 min, while the *trans* cilium gradually increases its frequency to ~70 Hz during that time.

How much do the frequencies differ? While it is quite unanimous that the *trans* beats 30-40% faster than the *cis* [20, 82, 100, 103, 104], there is still a point to pay attention to. For both partially deflagellated live cells and the reactivated cell models beating with one cilium, their beating cilium has a quite variable frequency. Over a population of cells or cell models, the spans of the *cis* and the *trans* frequency are as large as ~40 Hz [100, 103, 104, 107], and the spans overlap greatly, **Fig. 1.9**a-b. Furthermore, for every single live cell that is partially deflagellated, the frequency of its remaining cilium undergoes significant temporal, which can be as large as 30 Hz [103], **Fig. 1.10**c. Additionally, our preliminary results showed that the temporal frequency variation in partially deflag-

[8] In [73, 105], the slip and drift were reported to be of either sign, meaning that the *cis* cilium could also beat faster than the *trans*. However, this was probably due to either the use of another line of *C. reinhardtii* wildtype (UTEX89, from the "Cambridge line"), or the use of the medium SVM. After the authors switching into *cc-124* and *cc-125* (wildtypes from the Ebersold/Levine 137c line) and the TAP medium, the *cis* cilium was never reported to beat faster [103, 106].

ellated cells displayed intriguing patterns, **Fig. 1.10**d. Therefore, one should avoid oversimplifying the two cilia as two pendulums, whose intrinsic frequencies are well-defined and will immediately manifest after being decoupled from each other.

In resolving the origin of this frequency difference, the outer dynein arm mutants *oda* have played a crucial role [107–110]. In 1988, by screening slow-swimming phenotypes, Kamiya [108] isolated mutants that lost the ODAs. These mutants swim slower than the wildtype because their beating was at a much lower frequency (~ 20 Hz) [108].

Later, based on cell models of the mutant *oda1*, Sakakibara and Kamiya [109] first noted that the *cis-trans* frequency difference might derive from the ODA. After supplementing extracts of wildtype cilia to the *oda1* cell models, they found that the models' beating frequencies were recovered to the level of the wildtype cell models, and they confirmed with TEM observation that the models' ODAs were also structurally restored. Nevertheless, intriguingly, the recovered *oda1* models did not display the *cis-trans* frequency difference. Therefore, they hypothesized that the *cis* and *trans* cilium originally had different molecular subunits in their ODAs that were responsible for the frequency difference. However, because the ODAs were restored with mixed components from the two cilia, the frequency difference was therefore lost.

Years later, Takada and Kamiya [110] revisited this dynein arm recombination experiments with other *oda* mutants (*oda1-6*). Among these mutants, *oda2,4,5,6* still possess the ODA docking complex, while *oda1,3* do not [111]. ODA-recombination experiments with these two groups revealed a crucial difference: the former group regained the *cis-trans* frequency difference whereas the latter group did not, while both of them could recover to higher beating frequencies [110]. Therefore, the docking complex (ODA-DC) has been hypothesized to be a key subunit responsible for the *cis-trans* frequency difference since then.

Nevertheless, the ODA-DC is probably not the only subunit that is responsible for the frequency difference. In studying another *oda* mutant, *oda11*, which lacks one of the three outer-arm dynein heads, Sakakibara *et al.* [107] found that its *cis-trans* frequency difference was much reduced, if not completely lost. Therefore, the missing dynein head, $\alpha$-heavy chain (together with a light polypeptide chain [112]), probably also plays a role in the frequency difference.

How do these subunits differ in the *cis* and the *trans* cilium? It is still unknown. But one possibility points to phosphorylation ([7] Vol.3, Chap.6). The $\alpha$-heavy chain is found to phosphorylate *in vivo*, which may control the outer-arm dynein activity. Also, one docking complex subunit, ODA-DC2, is found to phosphorylate at two sites at least, giving rise to different isoforms that may have different regulatory properties. However, direct experimental evidence is still lacking.

#### ACTIVITY MODULATION

The two cilia of *C. reinhardtii* are also known to respond differently to second chemical messengers such as calcium and cAMP. While the former has been especially well-studied for decades [102, 104, 113–115], the latter is demonstrated in experiments only recently [116].

The seminal work in the cilium-specific $Ca^{2+}$-response in *C. reinhardtii* dated back to 1984. Kamiya and Witman [102] studied the ciliary activity of wildtype cell models

under various free calcium concentrations ($[Ca^{2+}]_{free}$), **Fig. 1.10**a. They found that 10 min after the reactivation, most (> 95%) cell models were circling on the bottom, and such circling motion would last for another 10 min. As circling means that one cilium is effectively turning the cell, Kamiya and Witman [102] referred to this driving cilium as the "dominant" one. Interestingly, during the time of circling, the *cis* cilium was found to be dominant in most cells (~80%) at low free calcium concentration ($[Ca^{2+}]_{free} < 10^{-8}$ M); and the *trans* cilium was found to be dominant in most cells (~80%) at high concentration ($[Ca^{2+}]_{free} > 10^{-7}$ M)[9].

Kamiya and Witman [102] also performed similar assays with live cells. By adding EGTA, a calcium chelator that captures free calcium and makes it unusable for cells, they depleted the cells' intracellular free calcium. They found that ~70% of the cells fell onto the bottom after 1 hour, and virtually all of them were circling with their *cis* cilium beating and their *trans* cilium stopped. This finding is in line with the finding in reactivated cell models that the *trans* cilium is less active at low calcium concentrations. However, unlike cell models, those circling cells could readily recover helical swimming upon addition of free calcium.

As this difference in $Ca^{2+}$-response is believed to be key for phototaxis in *C. reinhardtii* [72, 102], it has been often revisited and further investigated with phototactic mutants [104, 113, 114]. The relevant results are collected and displayed in **Fig. 1.10**b-e.

In these results, the mutant *ptx1*, which is inefficient in phototaxis, played a critical role. Horst and Witman [113] investigated both live cells and reactivated cell models of *ptx1* and they reported calcium-dependent behaviours that drastically differed from the wildtype cells.

In live cells subjected to calcium depletion after 1 hour, more than 80% *ptx1* cells kept swimming straight and smoothly [40, 113], as opposed to ~ 80% wildtype cells circling [40, 102, 113], **Fig. 1.10**b. In cell models, during the circling stage, the fraction of cell models turning by the *trans* cilium was ~50%, regardless of the calcium concentration [104, 113], **Fig. 1.10**c-d.

Based on these findings, Horst and Witman [113] proposed a model regarding the differential response to calcium in wildtype cells, and this model was further elaborated by Okita *et al.* [104].

First, the *cis* and the *trans* cilium are biochemically different; and the difference is in a transducer (or a binary switch) in the calcium signalling pathway. The *cis*- and *trans* transducer adjust the activity (*e.g.*, beating amplitude) of the two cilia with opposite signs upon binding to calcium.

Second, in live cells, some key mechanisms keep the intra-ciliary calcium level at

[9] It needs to be noted that the reactivation of cell models will only last for ~20 min so that both cilia will stop after a certain time, and the reactivation rates (fraction of reactivated cell models) are not the same under different $[Ca^{2+}]_{free}$. The latter is likely to pose a challenge for testing the *trans*-dominance. For example, at $[Ca^{2+}]_{free} = 10^{-6}$ M, Wakabayashi *et al.* [115] found the cell models to display poor or no movement, and so did we in our reactivation assay. Meanwhile, in [102], the reactivation rate was also reported to be lower at this calcium concentration, but there were enough circling cells to determine the *trans* cilium-dominance.

Such discrepancy possibly results from the very details of the reactivation protocols. In a very recent book chapter [117] co-authored by the researchers mentioned above, several specific tricks are mentioned. To name a few: one should use the minimum possible volume of demembranation solution, **must not** autoclave the plasticware, and use 0.5 mL Eppendorf tube instead of 1.5 mL ones, to achieve a higher reactivation rate.

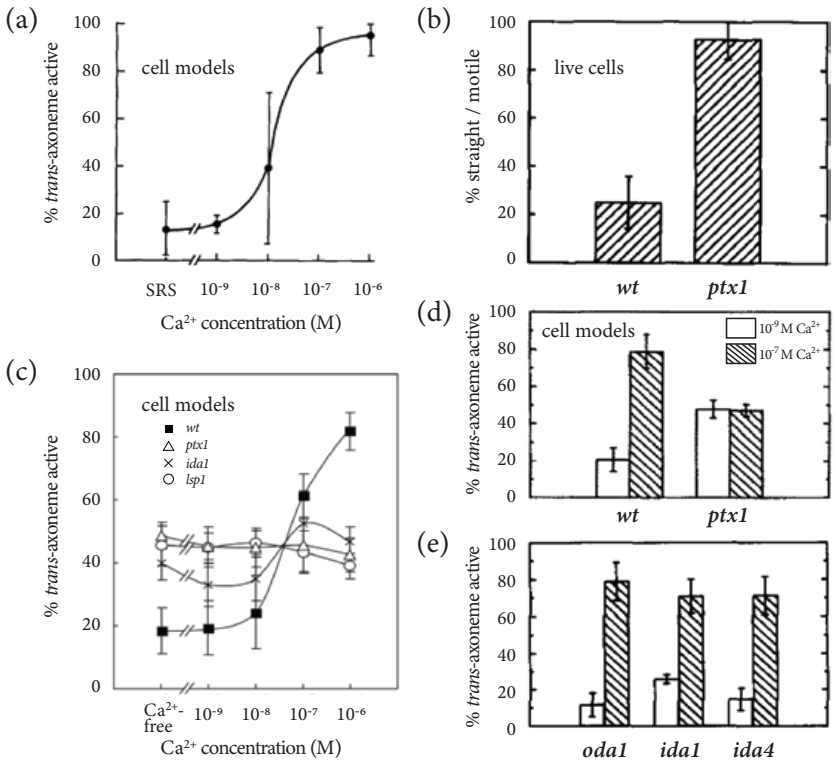


Figure 1.10: **Cilium-specific $Ca^{2+}$-response in live cells and cell models** (a) Fraction of wildtype cell models that are turning with their *trans* axonemes. SRS: standard reactivation solution, where $[Ca^{2+}]_{free} < 10^{-9}$ M. Points and error bars: mean±std from 10 experiments. Adapted from [102] with permission from Rockefeller University Press . (b) Live wildtype (*wt*) and *ptx1* cells subjected to EGTA-induced calcium depletion. Y axis: ratio of the straight swimming cells to the total motile ones; the rest of the motile cells have one of their cilia inactivated. Bar and error bar: mean±std. from 6 trials, ~200 cells for each strain. Adapted from [113] with permission from Rockefeller University Press . (c) Similar to (a), cilium-specific $Ca^{2+}$-response of wildtype (*wt*) cell models reexamined together with 3 mutants: *ptx1* and *lsp1* which are ineffective in phototaxis, and *ida1* which lacks the inner-arm dynein species f. Points and error bars: mean±std. from 6 experiments for each strain. Adapted from [104] with permission. (d-e) cilium-specific $Ca^{2+}$-response of cell models from 5 strains including *wt*, examined at two calcium concentrations as denoted. Bar and error bar: mean±std. from > 16 trials that account for > 1600 cells (d), or > 4 trials that account for > 300 cells (e). (d-e) Adapted from [113] with permission from Rockefeller University Press . All $Ca^{2+}$ concentration denotes the free calcium concentration.

an equilibrium, where both cilia are similarly active. Upon photo-stimulation, the internal calcium concentrations in both cilia increase or decrease together. This change momentarily shifts the equilibrium in the two cilia towards the opposite directions. For example, when the calcium concentrations in both cilia increase, the *cis* will tend to be inactivated while the *trans* further activated. As a result, the *trans* cilium will beat with

larger amplitude and turn the cell to the opposite side.

This model can also explain the calcium-dependent ciliary dominance in cell models. In wildtype cells models, although both cilia (axonemes) tend to be inactive, the different transducers in each cilium will accelerate this process in one cilium while slow it down in the other. This is why one cilium stays active for a longer time than the other, which causes the cells to circle before they become eventually quiescent. However, in *ptx1* cell models, as both cilia possess the same type of transducer, it is only a matter of chance which cilium stops beating first. Therefore, regardless of the calcium concentration, the *trans*-dominance will always be observed in ~50% of the cell models.

There have also been many efforts in trying to locate such a calcium-sensitive transducer. Okita *et al.* [104], Horst and Witman [113] tested the calcium-dependent ciliary dominance with several other mutants that lack certain subunits of the inner- or the outer-arm dynein, **Fig. 1.10**e. As a result, the calcium-dependent ciliary dominance is unaffected in *ida1*[10], *ida4*, and *oda1*. In total, these strains lack the inner-arm dynein species a, c, d, f, and the complete ODA together with the ODA-DC ([7] Vol.3, Chap.6). Therefore, we know that these components are not responsible for the cilium-specific $Ca^{2+}$-response. So far, we still do not know which axonemal subunit is different in the two cilia.

Another intriguing question is, are the *cis-trans* differences in frequency and calcium-response related or are they independent? Two lines of evidence support the idea that they are independent: (1) regardless of the calcium concentration, the *trans* frequency is constantly ~ 30% higher than the *cis* frequency in wildtype cell models [100]; (2) the mutant *oda1* that does not have the frequency difference, still displays cilium-specific $Ca^{2+}$-response (**Fig. 1.10**e) [113]. However, as the mutant *ptx1* is known to have a mutation [113] and it has lost both ciliary differences, the possibility that the two ciliary differences have shared mechanisms cannot be ruled out.

Very recently, cAMP was experimentally tested for its modulation of ciliary activity in *C. reinhardtii*. Saegusa and Yoshimura [116] employed caged-cAMP, which is not a chemical messenger for *C. reinhardtii* but can generate cAMP by UV light-stimulation, to study the effect of cAMP on single cell models swimming in helices. They found the geometry of the helices to change significantly by cAMP, and they evidenced that it was because cAMP modulates mostly the beating amplitude of the *cis* cilium.

## 1.5. THESIS OUTLINE

### 1.5.1. FLOW CREATED BY A SINGLE BEATING CILIUM

Our experimental investigation in ciliary flow begins with resolving its spatiotemporal dynamics.

Ciliary flow is critical for eukaryotic micro-organisms (**Sec. 1.1**) and humans alike [33, 36]. To better understand these flows, observing them with high spatial and temporal resolution is the foundation.

Experimentally resolving the collective flow created by thousands of beating cilia is

[9] Such key mechanisms are most likely to be lost during demembranation [113]. Meanwhile, as pointed out in [100], they are also likely to be prerequisites for ciliary synchronization in *C. reinhardtii*.

[10] Data differs slightly between [113] and [104], but are qualitatively the same.

possible but rather challenging. The samples (*e.g.*, mammalian epithelial cells) are delicate, and it is challenging to track the thousands of cilia simultaneously. Additional, it is also difficult to correlate the flow's collective property to that of a single cilium. Therefore, it is ideal to: isolate the flow's building block, which is the flow created by a single typical cilium; and to experimentally investigate the properties of such flow with a readily accessible sample in a controlled environment. *C.reinhardtii* meets all the needs for the study of the ciliary flow. The cell has only two cilia, whose beating pattern is representative. The two cilia beat in the same plane and can be tracked simultaneously, and this facilitates studies of the ciliary interaction. Last but not least, the cell culture is easy to maintain, and single captured cells survive various experimental conditions.

Previously, the time-averaged component of the ciliary flow, which is responsible for the net propulsion of the organism, has been studied [118, 119]. Nevertheless, the rich temporal dynamics of the flow, while being theoretically analyzed [120], has remained mostly unstudied experimentally. A lack of appropriate velocimetry techniques is the main reason. The established tracer particle-based techniques depend on measuring the displacement of particles to reveal the flow field. The larger the displacement between two observations is, the more accurately one can measure the flow velocity field. However, given the frequency of the ciliary flow is often ~50 Hz, to resolve the flow every 1/10 of a cycle means measuring particle displacement every 2 ms. Even at low required accuracy of the flow velocity, for example, 10 μm/s, this would equal to resolving particle displacement of 20 nm, which is 1/5-1/10 of a pixel size in general, and 1/20-1/50 of the tracer particle size. Additionally, another difficulty arises when the interval between observations is too short: the Brownian motion of the particle becomes comparable to or larger than the flow-induced displacement and renders the measurement inherently inaccurate.

To tackle these challenges and achieve the desired temporal resolution, we develop a velocimetry technique based on optical tweezers. Essentially, we gain the desired resolution by incorporating laser interferometry and measuring flow velocity as an electrical signal. With the technique, we studied the time-resolved behaviour of the flow around single beating cilia in detail.

In **Chap. 2** and **Chap. 3**, we will show how this technique helps to advance our understanding of the ciliary flows. The two chapters have different focuses. **Chap. 2** focuses on asking whether the quasi-steady approximation still holds for the dynamic part of the ciliary flow (**Sec. 1.2.5**); and **Chap. 3** focuses on characterizing the ciliary flow field created by single *C. reinhardtii* cells. As a result, the quasi-steady approximation is found to breakdown for the oscillatory component of ciliary flow. Furthermore, the flows around single beating cilia are systematically characterized, with measurements over many cells, numerical simulations, and idealized theoretical models.

### 1.5.2. FUNCTION OF CILIARY ULTRA-STRUCTURE

After having resolved the spatiotemporal features of ciliary flow, we further implement the technique in studying the structure-fluid interaction of a single cilium. As shown in **Sec. 1.4**, a cilium is more than a smooth and slender rod as it possesses ultrastructures such as two rows of mastigonemes. Although this structure has been observed for decades, its function has eluded direct hydrodynamic examination.

The mastigonemes were actively maintained by *C. reinhardtii* cells. In **Ref.** [121], cells whose mastigonemes were lost due to the application of an antibody regrew them after several hours. As synthesizing the mastigoneme-related proteins and transporting them through the cilia costs energy, the mastigonemes must be providing some advantages for the cells' survival; otherwise, they would have been lost during evolution. Till now, such an advantage is commonly believed to be an enhancement in the swimming speed of *C. reinhardtii*. However, experimental observation which supports this idea has been limited to a brief description that the *C. reinhardtii* cells without mastigonemes swim ~30% slower [121]. There is no information about how such decrease happens: for example, whether the loss of mastigonemes affects the ciliary beating pattern, or whether the efficiency of propulsion per beat decreases.

Aiming to resolve this structure-fluid interaction, we measure the flow in the vicinity of two groups of *C. reinhardtii* cells, one group has hairless cilia due to genetic mutagenesis, and the other group has normal mastigonemes as control. We systematically studied the cells' free-swimming kinematics, the ciliary beating patterns, and the ciliary flow field close to the cell and from afar. We conclude that the mastigonemes have no hydrodynamic effect in propelling the cells. The only intriguing difference we observed between the two groups of cells was that the ones without mastigonemes were more prone to drastic turnings when they swam.

With this study, we demonstrate the effectiveness of the velocimetry technique again, and we reopen the question to the function of this ciliary ultrastructure. Further research is needed to resolve if the mastigonemes are directly responsible for helping the cells maintain a straighter swimming path and how this is achieved. Such knowledge is not only of interest for phytologists and zoologists, but can also help design novel microswimmers [122].

### 1.5.3. CILIARY DIFFERENCE DURING SYNCHRONIZED BEATING

After having studied in detail the flow that one beating cilium creates, we further employ *C. reinhardtii* to study another cornerstone of the collective ciliary flow: synchronization.

When thousands of cilia beat together, instead of each beating independently, an emergent "collaboration" emerges among them, as shown in **Fig. 1.3**d. This phenomenon is termed the metachronal wave and is akin to the "Mexican wave" seen in a packed stadium. The key characteristic of metachronal wave is twofold. One is that the frequencies of cilia become identical; the other is that each cilium differs slightly from its neighbours in the phase in a cycle. On the bottom of this metachronal pattern is the one-to-one interaction between two cilia. In this regard, *C. reinhardtii* again serves as an ideal platform for it has the minimal number of cilia to study the ciliary synchronization. Its two cilia beat in sync with each other [101], and their collective beating can be further synchronized to an external source [82], which is known as external flow entrainment.

Recently, consensus about the mechanism responsible for synchronization between cilia is finally reached. Quaranta *et al.* [82], Wan and Goldstein [83] employed *C. reinhardtii* cells and somatic cells of *Volvox*, and proved that coupling through the intracellular fibre and hydrodynamics interaction could both establish synchronization for captured cells, while the primary mechanism differs from organisms. For freely swim-

ming *C. reinhardtii* cells, Geyer *et al.* [20] proved that the dominant mechanism is the cell body rocking.

In the last part of the thesis, we study synchronization in *C. reinhardtii* from a different angle from the previous research. Instead of asking what helps overcome the difference between the two cilia of *C. reinhardtii*, we ask, after such synchronization has been established, what remains different between the two cilia. To the current knowledge, one of the two cilia slightly lags in their synchrony [103], and they respond differently to light stimuli [72]. However, in general, a lack of technique to actively stimulate the two cilia differently has limited us from further answering this question.

To meet this challenge, we employ the technique developed by **Ref.** [82], where an external periodic flow is applied to load the cilia and to entrain their beating. In this study, instead of along the cell's central axis around which the two cilia are symmetric, flows are applied from different angles. In this way, the flows exert different loads on the two flagella.

By comparing the cells' responses to flows that selectively load the *cis* cilium and the *trans* cilium, we found the flows selectively loading the *cis* always entrain the cell more effectively. We further performed numerical simulations to compute the hydrodynamic loads on the cilia, and we resolved that the load on the *cis* cilium determines the cell's coupling to external flows, and the *trans* cilium disregards its own loads and follows the beating of the *cis* strictly. Such a coordinating role of the *cis* cilium tells us that the two cilia are mechanically connected in a delicate way such that the coupling between them is unilateral.

## REFERENCES

[1] A. van Leeuwenhoek, *Concerning little animals by him observed in rain-well-sea- and snow water; as also in water wherein pepper had lain infused,* Philosophical Transactions , 821 (1677).

[2] D. Anderson, *Counting the little animals,* https://lensonleeuwenhoek.net/content/counting-little-animals (2018), [Online; accessed 10-November-2019].

[3] M. Yachai, S. Tanasupawat, T. Itoh, S. Benjakul, W. Visessanguan, and R. Valyasevi, *Idiomarina piscisalsi sp. nov., from fermented fish (pla-ra) in thailand,* International journal of systematic and evolutionary microbiology **58**, 2136 (2008).

[4] C. Baker-Austin and M. Dopson, *Life in acid: ph homeostasis in acidophiles,* Trends in Microbiology **15**, 165 (2007).

[5] T. Hashimoto, D. D. Horikawa, Y. Saito, H. Kuwahara, H. Kozuka-Hata, T. Shin-I, Y. Minakuchi, K. Ohishi, A. Motoyama, T. Aizu, A. Enomoto, K. Kondo, S. Tanaka, Y. Hara, S. Koshikawa, H. Sagara, T. Miura, S.-i. Yokobori, K. Miyagawa, Y. Suzuki, T. Kubo, M. Oyama, Y. Kohara, A. Fujiyama, K. Arakawa, T. Katayama, A. Toyoda, and T. Kunieda, *Extremotolerant tardigrade genome and improved radiotolerance of human cultured cells by tardigrade-unique protein,* Nature Communications **7**, 12808 (2016).

[6] R. Wirth, M. Luckner, and G. Wanner, *Validation of a hypothesis: Colonization of black smokers by hyperthermophilic microorganisms,* Frontiers in Microbiology **9**, 524 (2018).

[7] E. H. Harris, *The Chlamydomonas Sourcebook, 2nd Edition* (Elsevier, Oxford, UK, 2009).

[8] N. Ueki, S. Matsunaga, I. Inouye, and A. Hallmann, *How 5000 independent rowers coordinate their strokes in order to row into the sunlight: Phototaxis in the multicellular green alga volvox,* BMC Biology **8**, 103 (2010).

[9] P. J. Hansen, P. K. Bjørnsen, and B. W. Hansen, *Zooplankton grazing and growth: Scaling within the 2-2000 µm body size range,* Limnology and Oceanography **42**, 687.

[10] T. Kiørboe, *How zooplankton feed: mechanisms, traits and trade-offs,* Biological Reviews **86**, 311.

[11] T. Kiørboe and H. Jiang, *To eat and not be eaten: optimal foraging behaviour in suspension feeding copepods,* Journal of The Royal Society Interface **10**, 20120693 (2013).

[12] Wikipedia contributors, *Prokaryote — Wikipedia, the free encyclopedia,* https://en.wikipedia.org/w/index.php?title=Prokaryote&oldid=945601799 (2020), [Online; accessed 17-March-2020].

[13] J. Elgeti, R. G. Winkler, and G. Gompper, *Physics of microswimmers—single particle motion and collective behavior: a review,* Reports on Progress in Physics **78**, 056601 (2015).

[14] L. Talà, A. Fineberg, P. Kukura, and A. Persat, *Pseudomonas aeruginosa orchestrates twitching motility by sequential control of type iv pili movements,* Nature Microbiology **4**, 774 (2019).

[15] S. Reindl, A. Ghosh, G. Williams, K. Lassak, T. Neiner, A.-L. Henche, S.-V. Albers, and J. Tainer, *Insights into flai functions in archaeal motor assembly and motility from structures, conformations, and genetics,* Molecular Cell **49**, 1069 (2013).

[16] S.-V. Albers and K. F. Jarrell, *The archaellum: how archaea swim,* Frontiers in Microbiology **6**, 23 (2015).

[17] D. M. Woolley, R. F. Crockett, W. D. I. Groom, and S. G. Revell, *A study of synchronisation between the flagella of bull spermatozoa, with related observations,* **212**, 2215 (2009).

[18] M. Arora, A. C. Anil, F. Leliaert, J. Delany, and E. Mesbahi, *Tetraselmis indica (chlorodendrophyceae, chlorophyta), a new species isolated from salt pans in goa, india,* European Journal of Phycology **48**, 61 (2013).

[19] P. Rompolas, R. S. Patel-King, and S. M. King, *An outer arm dynein conformational switch is required for metachronal synchrony of motile cilia in planaria,* Molecular Biology of the Cell **21**, 3669 (2010).

[20] V. F. Geyer, F. Jülicher, J. Howard, and B. M. Friedrich, 10.1073/pnas.1300895110.

[21] P. Satir, *Landmarks in cilia research from leeuwenhoek to us,* Cell Motility **32**, 90.

[22] U. Rüffer and W. Nultsch, *High-speed cinematographic analysis of the movement of Chlamydomonas,* Cell Motility **5**, 251 (1985).

[23] E. Lauga and T. R. Powers, *The hydrodynamics of swimming microorganisms,* Reports on Progress in Physics **72**, 096601 (2009).

[24] Wikipedia contributors, *Reynolds number — Wikipedia, the free encyclopedia,* https://en.wikipedia.org/w/index.php?title=Reynolds_number&oldid=935251133 (2020), [Online; accessed 14-January-2020].

[25] E. M. Purcell, *Life at low reynolds number,* American Journal of Physics **45**, 3 (1977).

[26] E. Lauga, *Life around the scallop theorem,* Soft Matter **7**, 3060 (2011).

[27] Atlantic Scuba, *King scallop escape swimming,* https://www.youtube.com/watch?v=TNNh8qWTF2Y (2017), [Online; accessed 12-January-2020].

[28] L. Zhang, J. J. Abbott, L. Dong, B. E. Kratochvil, D. Bell, and B. J. Nelson, *Artificial bacterial flagella: Fabrication and magnetic control,* Applied Physics Letters **94**, 064107 (2009).

[29] G. B. Bouck, *The structure, origin, isolation, and composition of the tubular mastigonemes of the Ochromonas flagellum,* The Journal of Cell Biology **50**, 362 (1971).

[30] V. F. Geyer, P. Sartori, B. M. Friedrich, F. Jülicher, and J. Howard, *Independent control of the static and dynamic components of the Chlamydomonas flagellar beat,* Current Biology **26**, 1098 (2016).

[31] Wikipedia contributors, *Flagellum — Wikipedia, the free encyclopedia,* https://en.wikipedia.org/w/index.php?title=Flagellum&oldid=931150883 (2019), [Online; accessed 9-January-2020].

[32] Wikipedia contributors, *Cilium — Wikipedia, the free encyclopedia,* https://en.wikipedia.org/w/index.php?title=Cilium&oldid=926753248 (2019), [Online; accessed 9-January-2020].

[33] H. M. Mitchison and E. M. Valente, *Motile and non-motile cilia in human pathology: from function to phenotypes,* The Journal of Pathology **241**, 294 (2017).

[34] H. Hoffmann-Berling, *Geisselmodelle und adenosintriphosphat (atp),* Biochimica et Biophysica Acta **16**, 146 (1955).

[35] C. Brokaw, *Movement and nucleoside polyphosphatase activity of isolated flagella from polytoma uvella,* Experimental Cell Research **22**, 151 (1961).

[36] M. Fliegauf, T. Benzing, and H. Omran, *When cilia go bad: cilia defects and ciliopathies,* Nature Reviews Molecular Cell Biology **8**, 880 EP (2007).

[37] H. J. Hoops and G. B. Witman, *Outer doublet heterogeneity reveals structural polarity related to beat direction in Chlamydomonas flagella.* The Journal of Cell Biology **97**, 902 (1983).

[38] R. Kamiya and T. Yagi, *Functional diversity of axonemal dyneins as assessed by in vitro and in vivo motility assays of Chlamydomonas mutants,* Zoological Science **31**, 633 (2014).

[39] K. Inaba, *Calcium sensors of ciliary outer arm dynein: functions and phylogenetic considerations for eukaryotic evolution,* Cilia **4**, 6 (2015).

[40] G. J. Pazour, N. Agrin, J. Leszyk, and G. B. Witman, *Proteomic analysis of a eukaryotic cilium,* The Journal of Cell Biology **170**, 103 (2005).

[41] M. Ma, M. Stoyanova, G. Rademacher, S. K. Dutcher, A. Brown, and R. Zhang, *Structure of the decorated ciliary doublet microtubule,* Cell **179**, 909 (2019).

[42] J. Lin and D. Nicastro, *Asymmetric distribution and spatial switching of dynein activity generates ciliary motility,* **360** (2018), 10.1126/science.aar1968.

[43] K. H. Bui, T. Yagi, R. Yamamoto, R. Kamiya, and T. Ishikawa, *Polarity and asymmetry in the arrangement of dynein and related structures in the Chlamydomonas axoneme,* The Journal of Cell Biology **198**, 913 (2012).

[44] R. Kamiya, *International review of cytology,* (Academic Press, 2002) Chap. Functional diversity of axonemal dyneins as studied in Chlamydomonas mutants, pp. 115–155.

[45] S. K. Dutcher and E. T. O'Toole, *The basal bodies of Chlamydomonas reinhardtii,* Cilia **5**, 1 (2016).

[46] D. L. Ringo, *Flagellar motion and fine structure of the flagellar apparatus in Chlamydomonas,* The Journal of Cell Biology **33**, 543 (1967).

[47] R. W. Linck and R. E. Stephens, *Functional protofilament numbering of ciliary, flagellar, and centriolar microtubules,* Cell Motility **64**, 489.

[48] J. Lin, K. Okada, M. Raytchev, M. C. Smith, and D. Nicastro, *Structural mechanism of the dynein power stroke,* Nature Cell Biology **16**, 479 (2014).

[49] T. Oda, H. Yanagisawa, R. Kamiya, and M. Kikkawa, *A molecular ruler determines the repeat length in eukaryotic cilia and flagella,* **346**, 857 (2014).

[50] K. E. Summers and I. R. Gibbons, *Adenosine triphosphate-induced sliding of tubules in trypsin-treated flagella of sea-urchin sperm,* Proceedings of the National Academy of Sciences of the United States of America **68**, 3092 (1971), 5289252[pmid].

[51] C. Shingyoji, K. Yoshimura, D. Eshel, K. Takahashi, and I. R. Gibbons, *Effect of beat frequency on the velocity of microtubule sliding in reactivated sea urchin sperm flagella under imposed head vibration.* **198**, 645 (1995).

[52] P. Satir and S. T. Christensen, *Overview of structure and function of mammalian cilia,* Annual Review of Physiology **69**, 377 (2007).

[53] J. Lin, T. Heuser, K. Song, X. Fu, and D. Nicastro, *One of the nine doublet microtubules of eukaryotic flagella exhibits unique and partially conserved structures,* PloS one **7**, e46494 (2012).

[54] T. Yagi, K. Uematsu, Z. Liu, and R. Kamiya, *Identification of dyneins that localize exclusively to the proximal portion of chlamydomonas flagella,* **122**, 1306 (2009).

[55] S. K. Dutcher, *Asymmetries in the cilia of Chlamydomonas,* Philosophical Transactions of the Royal Society B: Biological Sciences **375**, 20190153 (2020).

[56] W. Gilpin, M. S. Bull, and M. Prakash, *The multiscale physics of cilia and flagella,* Nature Reviews Physics (2020), 10.1038/s42254-019-0129-0.

[57] C. J. Brokaw, *Bend propagation by a sliding filament model for flagella,* **55**, 289 (1971).

[58] C. B. Lindemann, *A "geometric clutch" hypothesis to explain oscillations of the axoneme of cilia and flagella,* Journal of Theoretical Biology **168**, 175 (1994).

[59] P. V. Bayly and K. S. Wilson, *Analysis of unstable modes distinguishes mathematical models of flagellar motion,* Journal of The Royal Society Interface **12**, 20150124 (2015).

[60] P. Sartori, V. F. Geyer, A. Scholich, F. Jülicher, and J. Howard, *Dynamic curvature regulation accounts for the symmetric and asymmetric beats of Chlamydomonas flagella,* eLife **5**, e13258 (2016).

[61] B. Chakrabarti and D. Saintillan, *Spontaneous oscillations, beating patterns, and hydrodynamics of active microfilaments,* Phys. Rev. Fluids **4**, 043102 (2019).

[62] P. Cicuta, *The use of biophysical approaches to understand ciliary beating,* Biochemical Society Transactions (2020), 10.1042/BST20190571, bST20190571.

[63] C. Shingyoji, *11 - regulation of dynein-driven ciliary and flagellar movement,* in *Dyneins (Second Edition)*, edited by S. M. King (Academic Press, 2018) second edition ed., pp. 336 – 367.

[64] S. M. King, *Turning dyneins off bends cilia,* Cytoskeleton **75**, 372.

[65] S. S. Merchant, S. E. Prochnik, O. Vallon, E. H. Harris, S. J. Karpowicz, G. B. Witman, A. Terry, A. Salamov, L. K. Fritz-Laylin, L. Maréchal-Drouard, W. F. Marshall, L.-H. Qu, D. R. Nelson, A. A. Sanderfoot, M. H. Spalding, V. V. Kapitonov, Q. Ren, P. Ferris, E. Lindquist, ..., and A. R. Grossman, *The Chlamydomonas genome reveals the evolution of key animal and plant functions,* Science **318**, 245 (2007).

[66] R. E. Goldstein, *Green Algae as Model Organisms for Biological Fluid Dynamics,* Annual Review of Fluid Mechanics **47**, 343 (2015).

[67] Wikipedia contributors, *Model organism — Wikipedia, the free encyclopedia,* https://en.wikipedia.org/w/index.php?title=Model_organism&oldid=931074962 (2019), [Online; accessed 12-January-2020].

[68] R. Jeanneret, M. Contino, and M. Polin, *A brief introduction to the model microswimmer Chlamydomonas reinhardtii,* The European Physical Journal Special Topics **225**, 2141 (2016).

[69] X. Li, R. Zhang, W. Patena, S. S. Gang, S. R. Blum, N. Ivanova, R. Yue, J. M. Robertson, P. A. Lefebvre, S. T. Fitz-Gibbon, *et al.*, *An indexed, mapped mutant library enables reverse genetics studies of biological processes in Chlamydomonas reinhardtii,* The Plant Cell **28**, 367 (2016).

[70] X. Li, W. Patena, F. Fauser, R. E. Jinkerson, S. Saroussi, M. T. Meyer, N. Ivanova, J. M. Robertson, R. Yue, R. Zhang, J. Vilarrasa-Blasi, T. M. Wittkopp, S. Ramundo, S. R. Blum, A. Goh, M. Laudon, T. Srikumar, P. A. Lefebvre, A. R. Grossman, and M. C. Jonikas, *A genome-wide algal mutant library and functional screen identifies genes required for eukaryotic photosynthesis,* Nature Genetics **51**, 627 (2019).

[71] B. Craige, J. M. Brown, and G. B. Witman, *Isolation of Chlamydomonas flagella,* Current Protocols in Cell Biology **59**, 3.41.1 (2013).

[72] U. Rüffer and W. Nultsch, *Flagellar photoresponses of Chlamydomonas cells held on micropipettes: II. Change in Flagellar Beat Pattern,* Cell Motility and the Cytoskeleton **18**, 269 (1991).

[73] R. E. Goldstein, M. Polin, and I. Tuval, *Noise and synchronization in pairs of beating eukaryotic flagella,* Phys. Rev. Lett. **103**, 168103 (2009).

[74] R. Ma, G. S. Klindt, I. H. Riedel-Kruse, F. Jülicher, and B. M. Friedrich, 10.1103/PhysRevLett.113.048101.

[75] S. Sasso, H. Stibor, M. Mittag, and A. R. Grossman, *The natural history of model organisms: From molecular manipulation of domesticated Chlamydomonas reinhardtii to survival in nature,* eLife **7**, e39233 (2018).

[76] B. D. Engel, M. Schaffer, L. Kuhn Cuellar, E. Villa, J. M. Plitzko, and W. Baumeister, *Native architecture of the Chlamydomonas chloroplast revealed by in situ cryo-electron tomography,* eLife **4**, e04889 (2015).

[77] U. W. Goodenough and J. E. Heuser, *The Chlamydomonas cell wall and its constituent glycoproteins analyzed by the quick-freeze, deep-etch technique.* The Journal of Cell Biology **101**, 1550 (1985).

[78] J. Holmes and S. Dutcher, *Cellular asymmetry in chlamydomonas reinhardtii,* **94**, 273 (1989).

[79] B. E. Taillon, S. A. Adler, J. P. Suhan, and J. W. Jarvik, *Mutational analysis of centrin: an EF-hand protein associated with three distinct contractile fibers in the basal body apparatus of Chlamydomonas.* The Journal of Cell Biology **119**, 1613 (1992).

[80] M. Hayashi, T. Yagi, K. Yoshimura, and R. Kamiya, *Real-time observation of $Ca^{2+}$-induced basal body reorientation in Chlamydomonas,* Cell Motility and the Cytoskeleton **41**, 49 (1998).

[81] J. L. Salisbury, *Roots,* Journal of Eukaryotic Microbiology **45**, 28.

[82] G. Quaranta, M.-E. Aubin-Tam, and D. Tam, *Hydrodynamics versus intracellular coupling in the synchronization of eukaryotic flagella,* Physical Review Letters **115**, 238101 (2015).

[83] K. Y. Wan and R. E. Goldstein, *Coordinated beating of algal flagella is mediated by basal coupling,* Proceedings of the National Academy of Sciences **113**, E2784 (2016).

[84] E. T. O'Toole and S. K. Dutcher, *Site-specific basal body duplication in Chlamydomonas,* Cytoskeleton **71**, 108.

[85] J. L. Salisbury, M. A. Sanders, and L. Harpst, *Flagellar root contraction and nuclear movement during flagellar regeneration in Chlamydomonas reinhardtii.* Journal of Cell Biology **105**, 1799 (1987).

[86] K. F. Lechtreck and M. Melkonian, *An update on fibrous flagellar roots in green algae,* Protoplasma **164**, 38 (1991).

[87] K. Schaller, R. David, and R. Uhl, *How Chlamydomonas keeps track of the light once it has reached the right phototactic orientation,* Biophysical Journal **73**, 1562 (1997).

[88] N. Ueki, T. Ide, S. Mochiji, Y. Kobayashi, R. Tokutsu, N. Ohnishi, K. Yamaguchi, S. Shigenobu, K. Tanaka, J. Minagawa, T. Hisabori, M. Hirono, and K.-i. Wakabayashi, *Eyespot-dependent determination of the phototactic sign in Chlamydomonas reinhardtii,* Proceedings of the National Academy of Sciences **113**, 5299 (2016).

[89] C. L. Dieckmann, *Eyespot placement and assembly in the green alga Chlamydomonas,* BioEssays **25**, 410.

[90] H. Harz and P. Hegemann, *Rhodopsin-regulated calcium currents in Chlamydomonas, Nature,* Nature **351**, 489 (1991).

[91] D. G. W. Roberts, M. R. Lamb, and C. L. Dieckmann, *Characterization of the eye2 gene required for eyespot assembly in chlamydomonas reinhardtii,* **158**, 1037 (2001).

[92] K. Yoshimura and R. Kamiya, *The Sensitivity of Chlamydomonas Photoreceptor is Optimized for the Frequency of Cell Body Rotation,* Plant and Cell Physiology **42**, 665 (2001).

[93] S. Imam, M. Buchanan, H. Shin, and W. Snell, *The Chlamydomonas cell wall: Characterization of the wall framework,* The Journal of cell biology **101**, 1599 (1985).

[94] S. H. Imam and W. J. Snell, *The Chlamydomonas cell wall degrading enzyme, lysin, acts on two substrates within the framework of the wall.* The Journal of Cell Biology **106**, 2211 (1988).

[95] U. W. Goodenough and J. E. Heuser, *Molecular organization of cell-wall crystals from Chlamydomonas reinhardtii and Volvox carteri,* **90**, 717 (1988).

[96] K. Roberts, M. Gurney-Smith, and G. J. Hills, *Structure, composition and morphogenesis of the cell wall of chlamydomonas reinhardi: I. ultrastructure and preliminary chemical analysis,* Journal of Ultrastructure Research **40**, 599 (1972).

[97] B. C. Monk, W. S. Adair, R. A. Cohen, and U. W. Goodenough, *Topography of chlamydomonas: fine structure and polypeptide components of the gametic flagellar membrane surface and the cell wall,* Planta **158**, 517 (1983).

[98] P. Bickerton, S. Sello, C. Brownlee, J. K. Pittman, and G. L. Wheeler, *Spatial and temporal specificity of $Ca^{2+}$ signalling in Chlamydomonas reinhardtii in response to osmotic stress,* New Phytologist **212**, 920 (2016).

[99] B. Huang, Z. Ramanis, S. K. Dutcher, and D. J. L. Luck, *Uniflagellar mutants of Chlamydomonas: Evidence for the role of basal bodies in transmission of positional information,* Cell **29**, 745 (1982).

[100] R. Kamiya and E. Hasegawa, *Intrinsic difference in beat frequency between the two flagella of Chlamydomonas reinhardtii,* Experimental Cell Research **173**, 299 (1987).

[101] U. Rüffer and W. Nultsch, *Comparison of the beating of cis- and trans-flagella of Chlamydomonas cells held on micropipettes,* Cell Motility and the Cytoskeleton **7**, 87 (1987).

[102] R. Kamiya and G. B. Witman, *Submicromolar levels of calcium control the balance of beating between the two flagella in demembranated models of Chlamydomonas,* Journal of Cell Biology **98**, 97 (1984).

[103] K. Y. Wan, K. C. Leptos, and R. E. Goldstein, *Lag, lock, sync, slip: the many phases of coupled flagella,* Journal of The Royal Society Interface **11**, 20131160 (2014).

[104] N. Okita, N. Isogai, M. Hirono, R. Kamiya, and K. Yoshimura, *Phototactic activity in Chlamydomonas 'non-phototactic' mutants deficient in $Ca^{2+}$-dependent control of flagellar dominance or in inner-arm dynein,* Journal of Cell Science **118**, 529 (2005).

[105] M. Polin, I. Tuval, K. Drescher, J. P. Gollub, and R. E. Goldstein, *Chlamydomonas swims with two "gears" in a eukaryotic version of run-and-tumble locomotion,* Science **325**, 487 (2009).

[106] K. Y. Wan and R. E. Goldstein, *Rhythmicity, recurrence, and recovery of flagellar beating,* Phys. Rev. Lett. **113**, 238103 (2014).

[107] H. Sakakibara, D. R. Mitchell, and R. Kamiya, *A Chlamydomonas outer arm dynein mutant missing the alpha heavy chain,* The Journal of cell biology **113**, 615 (1991).

[108] R. Kamiya, *Mutations at twelve independent loci result in absence of outer dynein arms in Chylamydomonas reinhardtii.* The Journal of Cell Biology **107**, 2253 (1988).

[109] H. Sakakibara and R. Kamiya, *Functional recombination of outer dynein arms with outer arm-missing flagellar axonemes of a Chlamydomonas mutant,* Journal of Cell Science **92**, 77 (1989).

[110] S. Takada and R. Kamiya, *Beat frequency difference between the two flagella of Chlamydomonas depends on the attachment site of outer dynein arms on the outer-doublet microtubules,* Cell Motility and the Cytoskeleton **36**, 68 (1997).

[111] S. Takada and R. Kamiya, *Functional reconstitution of Chlamydomonas outer dynein arms from alpha-beta and gamma subunits: requirement of a third factor.* The Journal of Cell Biology **126**, 737 (1994).

[112] K.-i. Wakabayashi and S. M. King, *Modulation of Chlamydomonas reinhardtii flagellar motility by redox poise ,* The Journal of Cell Biology **173**, 743 (2006).

[113] J. Horst and G. B. Witman, *Ptx1, a nonphototactic mutant of Chlamydomonas, lacks control of flagellar dominance,* The Journal of Cell Biology **120**, 733 (1993).

[114] G. J. Pazour, O. A. Sineshchekov, and G. B. Witman, *Mutational analysis of the phototransduction pathway of Chlamydomonas reinhardtii.* The Journal of Cell Biology **131**, 427 (1995).

[115] K.-i. Wakabayashi, T. Ide, and R. Kamiya, *Calcium-dependent flagellar motility activation in Chlamydomonas reinhardtii in response to mechanical agitation,* Cell Motility and the Cytoskeleton **66**, 736 (2009).

[116] Y. Saegusa and K. Yoshimura, *cAMP controls the balance of the propulsive forces generated by the two flagella of Chlamydomonas,* Cytoskeleton **72**, 412 (2015).

[117] K.-i. Wakabayashi and R. Kamiya, *Biophysical Methods in Cell Biology*, Vol. 127 (Elsevier Ltd, 2015) pp. 387–402.

[118] J. S. Guasto, K. A. Johnson, and J. P. Gollub, *Oscillatory flows induced by microorganisms swimming in two dimensions,* Physical Review Letters **105**, 168102 (2010).

[119] K. Drescher, R. E. Goldstein, N. Michel, M. Polin, and I. Tuval, *Direct measurement of the flow field around swimming microorganisms,* Physical Review Letters **105**, 168101 (2010).

[120] S. Wang and A. M. Ardekani, *Unsteady swimming of small organisms,* Journal of Fluid Mechanics **702**, 286–297 (2012).

[121] S. Nakamura, G. Tanaka, T. Maeda, R. Kamiya, T. Matsunaga, and O. Nikaido, *Assembly and function of Chlamydomonas flagellar mastigonemes as probed with a monoclonal antibody,* Journal of Cell Science **109**, 57 (1996).

[122] S. Tottori and B. J. Nelson, *Artificial helical microswimmers with mastigoneme-inspired appendages,* Biomicrofluidics **7**, 061101 (2013).

# 2

# Is the Zero Reynolds Number Approximation Valid for Ciliary Flows?

**D. Wei, P. G. Dehnavi, M. -E. Aubin-Tam, D. S. W. Tam**

*Stokes equations are commonly used to model the hydrodynamic flow around cilia on the micron scale. The validity of this assumption is investigated experimentally with a flow velocimetry approach based on optical tweezers, which allows the measurement of periodic flows with high spatial and temporal resolution. We find that beating cilia generate a flow, which fundamentally differs from the stokeslet field predicted by Stokes equation. In particular, the flow velocity spatially decays at a faster rate and is gradually phase delayed at increasing distances from the cilia. This indicates that the quasi-steady approximation and use of Stokes equations for unsteady ciliary flows is often not justified and the finite timescale for vorticity diffusion cannot be neglected. Our results have significant implications in studies of synchronization and collective dynamics of micro-swimmers.*

Parts of this chapter have been published in [1]. **Fig. 2.2** to **Fig. 2.5** and parts of the text are adapted from [1], copyright (2019) by the American Physical Society

## 2.1. INTRODUCTION

Cilia and flagella are organelles essential for motility that extend from eukaryotic cells. For eukaryotic organisms, these organelles are the generic solution to the physical challenges posed by pumping fluids and generating propulsion, on the viscosity-dominated micron scale [2]. To generate flow fields, cilia actively bend in periodic power-recovery strokes, and interact with the surrounding fluid [3, 4]. Modelling the hydrodynamics around cilia is of high interest, and is central to studies of single cell locomotion [5–8], synchronization of cilia in metachronal waves [9–15] and interactions and collective motion between micro-swimmers [16, 17].

On the micron scales, flow is dominated by viscosity, and the Reynolds number $Re = \rho U l/\mu$ is small. Here, $\rho$ denotes the density of the fluid, $\mu$ the kinematic viscosity, $l$ and $U$ the characteristic length and velocity scale. In this regime, the equations governing the hydrodynamics are commonly approximated by the Stokes equations, corresponding to the limit of zero $Re$:

$$\nabla \cdot \mathbf{u} = 0\,, \quad -\nabla p + \mu \nabla^2 \mathbf{u} = \mathbf{0}\,, \tag{2.1}$$

where $\mathbf{u}$ and $p$ are the velocity and pressure fields [18]. Eq. (2.1) is a simplification of the Navier-Stokes equations, in the limit when vorticity instantly diffuses to infinity and the viscous boundary layer extends to the entire fluid domain. One fundamental solution to Eq. (2.1) is the stokeslet, which represents the flow induced by a point-force and whose velocity field decays in $1/r$. The stokeslet is the cornerstone of theoretical models in micro-hydrodynamics, and is relevant to established numerical methods, *e.g.* the Boundary Element Method (BEM) [19] or the method of regularized stokeslet [20], as well as reduced models representing the flow around cilia and micro-swimmers [8, 21]. Time varying stokeslets have been used to represent the periodic motion of hydrodynamically coupled oscillators and elucidate the emergence of synchronization and metachronal waves in cilia [9–11, 22]. However, unsteady flows induced by cilia are characterized by Reynolds numbers, which, though small, are not zero. This has implications for the motility of microorganisms and synchronization [7, 23]. This study investigates the validity of the stokeslet approximation with experimental velocimetry measurements. Such direct experimental measurements of time varying flows are challenging owing to the high frequency of the ciliary motion $f = 10 - 100$ Hz. Previous quantitative measurements around cilia have been limited to average flow velocities [21, 24].

Here, we use an optical tweezers-based velocimetry (OTV) [25, 26] to measure unsteady flows around a cilium. We find the flow around a cilium to differ fundamentally from the flow predicted in the zero $Re$ regime. First, the rate of spatial decay of the velocity is much higher, thereby limiting the range of hydrodynamic interactions. In addition, we evidence an important phase delay of the oscillatory velocity component, which gradually leads to flow inversion away from the cilium. Our experimental results highlight the limitations of using stokeslets to represent unsteady flows and in particular for studies of synchronization in cilia and micro-swimmers.

In our OTV method, we directly measure the hydrodynamic force exerted on a microbead to determine the flow velocity. The optical trap is built around an inverted bright field microscope (Nikon Eclipse T*i*-U) and is similar to the setup used in **Ref.** [27]. The schematic of the setup is shown in **Fig. 2.1**a. The laser beam (Nd:YAG, $\lambda$=1064 nm) for trapping goes through an isolator, a half-wave plate, and an acousto-optic deflector

(AOD) consecutively, and is finally focused through a water immersion objective of numerical aperture NA=1.20. Back-focal-plane interferometry (BFPI) is employed for bead position detection. A separate laser ($\lambda$=880 nm) is designated for this purpose and is aligned to the trapping laser in the focal plane of the microscope. After going through the trapped bead, the detection laser is converged by a condenser and received by a position sensitive detector (PSD, First Sensor DL100-7) at the back focal plane of the condenser (block (iv) in **Fig. 2.1**a). In BFPI, the fraction of the laser going through the trapped bead interferes with the rest of itself, creating an interferometric pattern, which is sensitive to the bead position and can be used for detection [28, 29].

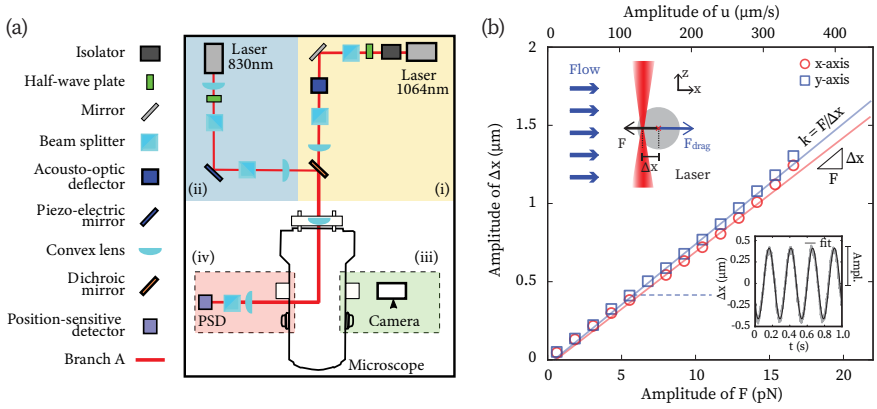


Figure 2.1: (a) Schematic of the setup. The setup consists of four main blocks: the trapping laser (i), the detection laser (ii), bright-field microscopy and videography (iii), and laser interferometric detection (iv). Courtesy of Victor Marin. (b) Calibration of trap stiffness $k$ in both $x$- and $y$-direction is performed by applying a series of low-frequency (2-4 Hz) sinusoidal flows of known amplitudes/drags. By measuring the amplitude of the bead displacement from the centre ($\Delta\mathbf{x}$), $k$ can be extracted from the slope. Upper inset: demonstration of principle of velocity measurements. The focused trapping laser captures a micro-bead. The trapping force on the bead $\mathbf{F} = -k\Delta\mathbf{x}$ always balances the flow drag $\mathbf{F}_{\text{drag}} = \gamma\mathbf{u}$, where $\gamma$ and $\mathbf{u}$ are the Stokes drag coefficient of the bead and the local flow velocity, respectively. Lower inset: a calibration flow recording. The amplitude of $\Delta\mathbf{x}$ is extracted from the sinusoidal fit (solid line).

The basis of the OTV technique is to deduce the flow velocity $\mathbf{u}(t)$ at the trap location by the intra-trap displacement of a bead $\Delta\mathbf{x}$. Beads within the trap are subject to a trapping force $\mathbf{F} = -k\Delta\mathbf{x}$. Here the spring constant $k$ is called the trap stiffness. For steady flows, as the trapping force always equals the flow drag $\mathbf{F} = \mathbf{F}_{\text{drag}} = \gamma\mathbf{u}$, the local flow velocity can be measured as $\mathbf{u} = -k\Delta\mathbf{x}/\gamma$, with $\gamma$ the Stokes drag coefficient for the trapped bead, see the upper inset in **Fig. 2.1**b. For unsteady flows, the dynamics of the trapped bead is governed by the Boussinesq-Basset-Oseen (BBO) equation. The particle Reynolds number $Re_a = \rho|\mathbf{u}|a/\mu$ is small $Re_a \approx 10^{-5} - 10^{-4}$ and the inertia, added mass and Basset forces are negligible [18]. The BBO equation then reduces to a first order equation balancing the trapping force and the hydrodynamic drag:

$$\frac{\mathrm{d}\Delta\mathbf{x}}{\mathrm{dt}} + \frac{k}{\gamma}\Delta\mathbf{x} = \mathbf{u}(t)\,, \tag{2.2}$$

which allows us to deduce the flow velocity $\mathbf{u}(t)$ from the displacement $\Delta\mathbf{x}$ [30].

Calibration of the trap stiffness $k$ is performed by applying flows of known velocities to the trapped bead, shown in **Fig. 2.1**b. A series of low-frequency (*e.g.*,2 Hz) sinusoidal flows with known amplitudes are applied to the bead, and the corresponding bead displacements are recorded. For oscillatory flows whose frequency $f \ll k/2\pi\gamma$, Eq. (2.2) further reduces to $\frac{k}{\gamma}\Delta\mathbf{x} = \mathbf{u}(t)$, which is the same equation for steady flows[1]. Therefore, for known flow amplitude $u_{\text{calib}}$, the trap stiffness can be obtained as $k = \gamma u_{\text{calib}}/\Delta x$, which is the slope in **Fig. 2.1**b. In our experiments, we use beads of radii $a = 1-2.5$ µm and trap stiffnesses $k = 12-50$ pN/µm. With BFPI, $\Delta\mathbf{x}$ in our experiments is monitored with a temporal resolution <0.1 ms.

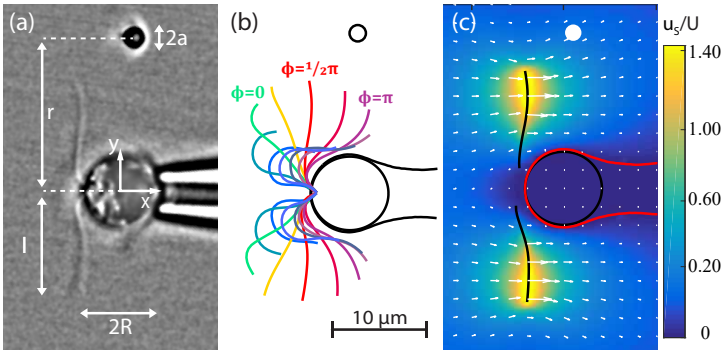


Figure 2.2: (a) An optically trapped bead measures the local flow around the cilia of a *Chlamydomonas reinhardtii* cell held by a micropipette. (b) Tracked flagellar shapes from image analysis of a video-recorded beating cycle. (c) Flow velocity field corresponding to the cell in (a). The velocity field is computed by solving Stokes equations with the Boundary Element Method (BEM) from the ciliary shapes, cell and pipette surfaces extracted from video recordings. $U = lf \approx 600$ µm/s, with $l$ and $f$ the ciliary length and frequency respectively.

The OTV measurements are synchronized with high-speed video recordings. We use an sCMOS camera (PCO.edge 5.5) at a frame rate of 400-850 fps to record the shapes of the beating cilia, **Fig. 2.2**a. We track the ciliary shape in each frame and reconstruct the periodic deformations, see **Fig. 2.2**b. A ciliary phase $\phi(t)$ is then used to denote the shapes, with $\phi = 0$ denoting the cilia shapes at the transition from the recovery to the power stroke, which extend the furthest from the cell, see **Fig. 2.2**b. The tracked ciliary deformations are employed to compute the flow velocity fields predicted by Eq. (2.1). Stokes equations (Eq. (2.1)) are solved numerically using a hybrid BEM/slender-body approach, similar to [18]. The cell body and the glass pipette are represented with a completed double layer boundary integral equation, with the singularities of completion

[1] There are two important advantages in using low-frequency sinusoidal flows. First, measuring bead displacement under steady flows is less accurate. Such measurement is prone uncertainties in determining the trap centre location, which drifts over time. Under low-frequency sinusoidal flows, one measures the peak-to-peak amplitude of bead displacement instead, and the uncertainty in determining trap centre is avoided. Second, applying flows of constant speed is practically challenging. Flows are generated by driving a piezoelectric stage, which can only move within a limited range *e.g.* 100 µm. Near the extremes of such range, as the stage needs to decelerate and accelerate, the actual waveform of motion deviates drastically from the desired form, resulting in varied speeds. In contrast, for sinusoidal flows, such waveform deformation is negligible.

flow distributed along the centreline of the pipette [31]. The cilia are represented using slender-body theory [32]. We use this computational approach to compare OTV velocity measurements $\mathbf{u}(t)$ with the flow velocity field predicted by the Stokes equations $\mathbf{u}_S$, see **Fig. 2.2**c .



## 2.2. RESULTS AND DISCUSSION

The flow velocity $\mathbf{u} = (u, v)$ is measured around the beating cilia of single *C. reinhardtii* cells, held by suction with a glass pipette, at a height of 120 µm from the bottom of the flow chamber, following **Ref.** [33]. Cells varied in cell body radius $R = 4.4 \pm 0.8$ µm, cilia length $l = 11.5 \pm 2.0$ µm and ciliary beating frequency $f = 53.0 \pm 5.0$ Hz. We measured the flow velocity using the OTV method at different positions from the cell centre, in the $xy$-plane of the cilia, where the $x$ direction is aligned with cell-pipette axis, **Fig. 2.2**a. The flow induced by the cilia is notably larger in the $x$ direction, an we report the velocity component $u$. We first focus on the velocity along the $y$ axis for positions $(x = 0, y = r)$ at increasing lateral distances from the cell centre $r \approx 20 - 120$ µm.

**Fig. 2.3** presents flow measurements for $r/l = 1.7$ and $r/l = 4.9$. Results are non-dimensionalized with $l$, the length of the cilia, $f$ the beating frequency and $U = lf$ the typical cilia velocity. OTV measurements of $u$ as a function of time are compared with the flow velocities predicted from solving the Stokes equations $u_S$ for the tracked ciliary deformations. Close to the cilia, for $r/l = 1.7$, the velocity measurements are in quantitative agreement with the solution to the Stokes equations, **Fig. 2.3**a. In particular, the measurements capture the high frequency periodicity of the ciliary flow, with positive flow velocities $u(y, t)$ caused by the power stroke and negative flow velocities by the recovery stroke. A few cilia length away from the cell, the flow measurements show significant discrepancies with Stokes flow. **Fig. 2.3**b represents our flow measurements at $y/l = 4.9$. At these distances, the periodicity of the ciliary flow can still be clearly seen from the raw data and the amplitude of the flow oscillations is reduced as expected for Stokes flow. However, the OTV measurements reveal a phase shift in the flow velocity $u$, which the solution $u_S$ to the Stokes equations does not predict, see **Fig. 2.3**b and inset. This phase shift $\theta$ is deduced from computing the cross-correlation between $u(t)$ and $u_S(t)$. The time shift in **Fig. 2.3**b is $\approx 3.7$ms corresponding to a phase shift of $\theta \approx 3\pi/8$ at $r/l \approx 4.9$.

OTV measurements for one beating cycle are deduced from averaging $sim50$ beating cycles. **Fig. 2.3**c and d represent $u$ and $u_S$ as a function of the ciliary phase $\phi$. The velocity oscillations generated by the power-recovery strokes become gradually phase-delayed as the distance to the cell increases, **Fig. 2.3**c. Close to the cell, $u$ reaches a maximum in the middle of the power stroke, for $\phi \approx \pi/2$, as predicted by Stokes equations, whereas 4.9 ciliary length away, $u$ reaches its maximum later in the stroke, towards the beginning of the recovery stroke, when $\phi \approx \pi$, see the dashed line in **Fig. 2.3**c. Hence, the velocity magnitude at $r/l \approx 4.9$ reaches a maximum when the velocity magnitude close to the cell (at $r/l \approx 1.7$) reaches a minimum. The flow is therefore fundamentally different than the flow $u_S$, expected in the zero Reynolds number limit, where the flow is in-phase at all distances, see **Fig. 2.3**d.

We further investigate the spatial decay in flow velocity at increasing distances $r$ from the cell, **Fig. 2.4**. We first consider $u_S$ predicted from solving Stokes equations. At a given

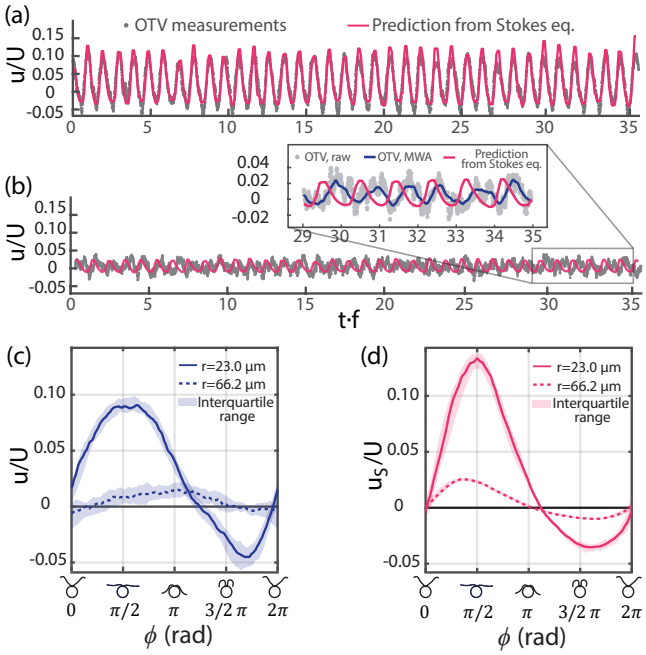


Figure 2.3: Comparison between the flow velocity experimentally measured with OTV (grey) and the flow computed with BEM (magenta). (a) Close to the cell, $r = 23.0\,\mu$m, the measurements appear in phase. (b) At larger distances from the cell centre, $r = 66.2\,\mu$m, the OTV measurements of the velocity is phase-delayed compared to what is predicted from solving Stokes equations. (inset) OTV raw data (grey), moving-window-averaged data (blue), and the flow computed with BEM (magenta). (c-d) Flow velocity $u$ over one period, averaged for $\sim 40$ periods, for the OTV measurements (c) compared to $u_S$ calculated with BEM from the tracked shapes (d). Solid and dashed lines correspond to the velocity at $r = 23.0\,\mu$m and $r = 66.2\,\mu$m respectively. A beat cycle begins when the cilia reach the most forward position, at the start of the power stroke. The flow velocity predicted by Stokes equations are in phase at different distances from the cell (d), whereas they are phase delayed in our OTV measurements (d).

phase $\phi$ during the stroke, $u_S$ has the same sign at all locations along the $y$-axis and oscillates between being positive at all $r$ during the power stroke and being negative everywhere during the recovery stroke, see **Fig. 2.4**a. This is because Stokes equations assume the instantaneous diffusion of vorticity and momentum to infinity. The direction of Stokes flow always follows the direction of the forcing in the entire fluid domain. In contrast, our measurements of $u$ reveal flow inversion, where the flow direction changes at increasing distances from the cell. The sign of $u$ only agrees with the numerical solution to Stokes equation, in the vicinity of the cell and is the opposite far away, see **Fig. 2.4**a and b. For example, when $\phi \approx \pi/10$ (green line in **Fig. 2.4**b), the cilia is at the beginning of the power stroke, $u$ is positive close to the cell, but negative beyond an inversion point when $r/l \geq 2.7$. The inversion point, for which $u = 0$, moves away from the cell as the phase increases, and reaches $r/l = 5.6$, in the middle of the power stroke, when

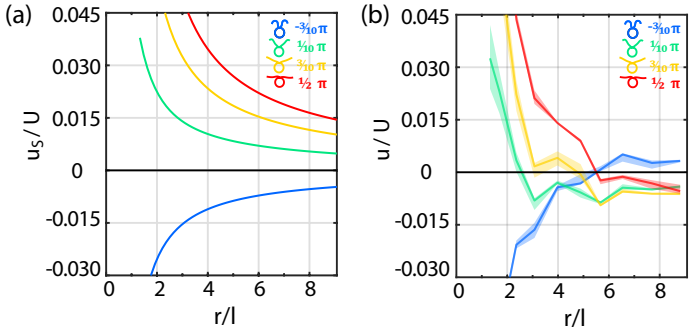


Figure 2.4: Flow velocity as a function of the distance to the cell centre at separate ciliary phases. (a) corresponds to the flow computed with the BEM from the tracked shapes, (b) to the OTV measurements. (a-b) Velocity profiles are represented at the same stages during the power-recovery strokes. Each color represents different ciliary phases, $\phi$, as indicated in the legend. OTV measurements (b) reveal the existence of an inversion point, where the direction of the flow reverses, which is not predicted by the BEM computation.

$\phi \approx \pi/2$ (red line in **Fig. 2.4**b) and $u$ is maximum close to the cell. At the beginning of the recovery stroke, when the cilia reverts the direction of its motion, another inversion point is created near the cell and later propagates away from the cell, see the blue line in **Fig. 2.4**b. The instantaneous velocity distribution is markedly different from Stokes predictions throughout the beating cycle and differences appear as close as $r/l \sim 2-3$. For the flow field over the entire beat compared with Stokes flow, please see the online supplementary material of [1].

The experimental results in **Fig. 2.3** and 2.4 are reminiscent of Stokes' second problem and point towards the breakdown of the quasi-steady approximation of Stokes flows. The OTV allows us to resolve the finite time required for the vorticity created at the surface of the organism to diffuse to the bulk. Although commonly neglected, the effect of the unsteady term of Navier-Stokes equations in micro-hydrodynamics is well known [7, 18, 34]. Theoretically, the solution to the unsteady Stokes equation for an oscillating point force prototypically shows how small $Re$ alters the zero $Re$ solution [18]. In this case, the relevant length scale is $\delta = \sqrt{\mu/\rho f}$, the characteristic length scale of vorticity diffusion $\delta \approx 130$ µm. At short distances from the point force $r \ll \delta$, the transient associated with the diffusion of vorticity is very short and the solution tends to the stokeslet. For large distances $r$, the spatial decay of the flow velocity becomes significantly stronger than for the stokeslet and scales with $1/r^3$ [18]. In addition, flow oscillations are predicted to be phase delayed with the forcing. It is interesting to then decompose the velocity measurements as $u(y,t) = \bar{u}(y) + u'(y,t)$, where $\bar{u}(y)$ is the average flow and $u'(y,t)$ are the zero-averaged oscillations. We further denote $\delta u'(y)$ the amplitudes of the flow oscillations $u'$. In the limit of zero $Re$, $\bar{u}$ and $\delta u'$ are expected to both follow the same $1/r$ rate of decay as the stokeslet. However, from linearity, one would expect very different rates of spatial decay for the average flow $\bar{u}$ and the oscillations $\delta u'$, if transient effects are important.

**Fig. 2.5** represents the velocity field measured for several different cells. In total, N

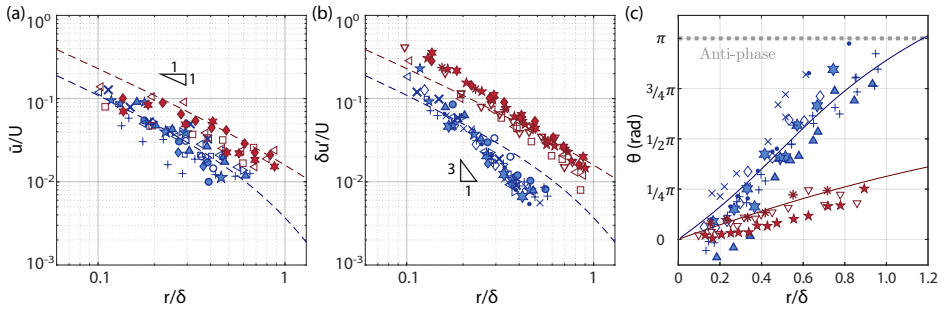


Figure 2.5: Characteristics of the flow measured with the OTV as a function of $r/\delta$. Different symbols represent datasets for different cells, with beads of 1 µm (open symbols) or 2.5 µm (other symbols) radii. In total, N = 14, 21, and 9 cells are presented in (a), (b), and (c), respectively. Measurements are taken along the $y$-axis (blue) at positions ($x = 0$, $r$) and along the $x$-axis (red) at positions ($r$, $y = 0$). We report the average flow velocity $\bar{u}$ (a) and the amplitude of the zero-averaged oscillatory component $\delta u'$ (b). Dashed lines show predictions from Stokes equations for a point force located 120 µm above a solid surface (Blake tensor). The decay rate of the oscillatory flow $\delta u'$ ($\sim 1/r^3$) is faster compared to the decay rate of the average flow $\bar{u}$ ($\sim 1/r$). (c) Phase shift $\theta$ between the experimental and the computed results. Solid lines show predictions from the unsteady Stokes equations for an oscillating point force.

= 14, 21, and 9 cells are presented in **Fig. 2.5**a, b, and c, respectively. Data along $x$ and $y$-axis are represented by red and blue symbols respectively. $\bar{u}$ is obtained directly by computing the average velocity over the entire duration of the experiment and $\delta u'$ is the average amplitude of $u'$. The rate of spatial decay of $\bar{u}$ and $\delta u'$ is different and can be compared to the rate of velocity decay expected from the solution to Stokes equations for a point force located 120 µm from a solid wall (Blake tensor, see **Chap. A** for detail), **Fig. 2.5**a and b. By solving the Blake tensor with the realistic wall distance, the decay of $\bar{u}$ along $y$ axis is reproduced, which is of a rate of $\sim 1/r$, **Fig. 2.5**a. On the other hand, the rate of decay of $\delta u'$ is different and we find $\delta u'$ to decay faster than $1/r$, expected from Eq. (2.1), and closer to $1/r^3$ predicted by the unsteady Stokes equation, **Fig. 2.5**b.

We now consider the phase delay $\theta$, between the cilium and the oscillatory flow $u'$. We find the phase delay $\theta$ to increase with distance from $\theta = 0$ (in-phase) to $\theta \approx \pi$ (anti-phase), see **Fig. 2.5**c (blue symbols). At a distance $r \approx \delta$, which can be regarded as the boundary layer thickness, the flow is in anti-phase with the cilium, which quantitatively agrees with the flow predicted from the unsteady Stokes equations for an oscillating point force [18], **Fig. 2.5**c. The slope in **Fig. 2.5**c (blue symbols) corresponds to a phase increase of $\sim 0.032 \pm 0.003$ rad/µm and hence to a $\sim \pi/2$ phase shift over a distance of ~50 µm.

To further elaborate the spatial profile of the flow field, we investigate the rates of flow velocity decay and phase delay along the $x$ axis (**Fig. 2.5**, red symbols). Similar to the stokeslet field around a point force in the $x$ direction, $u$ is larger along the $x$ axis compared to the $y$ axis; see **Fig. 2.5**a and b. Along the $y$ axis, we find similar trends as along the $x$ axis: the rate of decay of the average flow agrees with predictions from Stokes equations, **Fig. 2.5**a, while the oscillatory component decays faster. Furthermore, we find the phase increase of the $x$ component of the velocity to be lower along the $x$ axis than along

the $y$ axis. This agrees with the solution to the unsteady Stokes equations for an oscillating point force along the $x$ axis (**Fig. 2.5**c, solid lines). This solution is axisymmetric about the $x$ axis and the phase increase depends on the direction: it is minimum in the direction of the oscillating force, the $x$ axis, in agreement with our measurements, and is maximum in any direction perpendicular to the $x$ axis, in agreement with our measurements along the $y$ axis. Though not shown here, the phase increase along the $z$ axis is expected from the axisymmetry of the solution, and confirmed with later experiments, to be similar to the reported $y$ axis measurements, see **Chap. 3**.



## 2.3. CONCLUSION

In this chapter, we present direct experimental evidence of the shortcomings of using Stokes equations to represent micron scale flows generated by beating cilia and flagella. We find the amplitude of the oscillatory flow velocity to decay much faster than for the stokeslet, and the oscillations of the flow velocity to be gradually phase shifted at increasing $r$. While the zero Reynolds number limit is justified to model hydrodynamic forces on cilia for motility studies, it does not accurately predict the range and nature of hydrodynamic interactions, for oscillatory flows relevant to synchronization. The discrepancies in amplitude and phase are not limited to the far field, for $r \gg \delta$ beyond the diffusive length scale. Instead, significant differences between our measurements and Stokes predictions already appear at surprisingly short distances from the cell of $r \approx 2-3l$. The inaccuracy of the zero Reynolds number approximation originates in the quasi-steady approximation, which fails to take into account the diffusive timescale of vorticity. Our experimental observations are general and characteristic of how the unsteady term in the Navier-Stokes equations affects the flow, and will be present in other flow configurations, *e.g.*, for a cilia close to a no-slip wall. For such a point force close to a wall, the decay of the velocity field will increase from $1/r^3$, for the quasi-steady approximation given by the Blake tensor, to $1/r^5$. Our results have implications in studies of hydrodynamic synchronization between cilia and flagellated micro-swimmers.

## 2.4. AUTHOR CONTRIBUTIONS

D. W. conducted the experiments, analyzed the data, and wrote the draft. P. G. D. analyzed the data. D. T. and M.-E. A.-T. supervised the work and prepared the manuscript.

## 2.5. ACKNOWLEDGEMENT

The authors thank R. Kieffer for technical support and acknowledge a conversation with B. Eckhardt. D. W. thanks Shuyue Wang for her help in performing some early OTV measurements.

## REFERENCES

[1] D. Wei, P. G. Dehnavi, M.-E. Aubin-Tam, and D. Tam, *Is the zero reynolds number approximation valid for ciliary flows?* Physical Review Letters **122**, 124502 (2019).

[2] E. Lauga and T. R. Powers, *The hydrodynamics of swimming microorganisms,* Reports on Progress in Physics **72**, 096601 (2009).

[3] R. Golestanian, J. M. Yeomans, and N. Uchida, *Hydrodynamic synchronization at low reynolds number,* Soft Matter **7**, 3074 (2011).

[4] J. Elgeti, R. G. Winkler, and G. Gompper, *Physics of microswimmers—single particle motion and collective behavior: a review,* Reports on Progress in Physics **78**, 056601 (2015).

[5] V. F. Geyer, F. Jülicher, J. Howard, and B. M. Friedrich, 10.1073/pnas.1300895110.

[6] R. R. Bennett and R. Golestanian, *Emergent run-and-tumble behavior in a simple model of chlamydomonas with intrinsic noise,* Phys. Rev. Lett. **110**, 148102 (2013).

[7] G. S. Klindt and B. M. Friedrich, *Flagellar swimmers oscillate between pusher- and puller-type swimming,* Phys. Rev. E **92**, 063019 (2015).

[8] K. Ishimoto, H. Gadêlha, E. A. Gaffney, D. J. Smith, and J. Kirkman-Brown, *Coarse-graining the fluid flow around a human sperm,* Phys. Rev. Lett. **118**, 124501 (2017).

[9] B. Guirao and J.-F. Joanny, *Spontaneous creation of macroscopic flow and metachronal waves in an array of cilia,* Biophysical Journal **92**, 1900 (2007).

[10] A. Vilfan and F. Jülicher, *Hydrodynamic flow patterns and synchronization of beating cilia,* Phys. Rev. Lett. **96**, 058102 (2006).

[11] T. Niedermayer, B. Eckhardt, and P. Lenz, *Synchronization, phase locking, and metachronal wave formation in ciliary chains,* Chaos: An Interdisciplinary Journal of Nonlinear Science **18**, 037128 (2008).

[12] N. Uchida and R. Golestanian, *Synchronization and collective dynamics in a carpet of microfluidic rotors,* Phys. Rev. Lett. **104**, 178103 (2010).

[13] J. Elgeti and G. Gompper, *Emergence of metachronal waves in cilia arrays,* Proceedings of the National Academy of Sciences **110**, 4470 (2013).

[14] D. R. Brumley, M. Polin, T. J. Pedley, and R. E. Goldstein, *Hydrodynamic synchronization and metachronal waves on the surface of the colonial alga volvox carteri,* Phys. Rev. Lett. **109**, 268102 (2012).

[15] D. R. Brumley, K. Y. Wan, M. Polin, and R. E. Goldstein, *Flagellar synchronization through direct hydrodynamic interactions,* eLife **3**, e02750 (2014).

[16] C. M. Pooley, G. P. Alexander, and J. M. Yeomans, *Hydrodynamic interaction between two swimmers at low reynolds number,* Phys. Rev. Lett. **99**, 228103 (2007).

[17] G. J. Elfring and E. Lauga, *Synchronization of flexible sheets,* Journal of Fluid Mechanics **674**, 163–173 (2011).

[18] S. Kim and S. J. Karrila, *Microhydrodynamics: Principles and Selected Applications* (Dover Publications, Mineola, NY, USA, 2013).

[19] C. Pozrikidis, *A Practical guide to Boundary Element Methods with the Software Library BEMLIB* (CRC Press, Boca Raton, FL, USA, 2002).

[20] R. Cortez, *The method of regularized stokeslets,* SIAM Journal on Scientific Computing **23**, 1204 (2001).

[21] K. Drescher, R. E. Goldstein, N. Michel, M. Polin, and I. Tuval, *Direct measurement of the flow field around swimming microorganisms,* Physical Review Letters **105**, 168101 (2010).

[22] A. Maestro, N. Bruot, J. Kotar, N. Uchida, R. Golestanian, and P. Cicuta, *Control of synchronization in models of hydrodynamically coupled motile cilia,* Communications Physics **1**, 28 (2018).

[23] M. Theers and R. G. Winkler, *Synchronization of rigid microrotors by time-dependent hydrodynamic interactions,* Phys. Rev. E **88**, 023012 (2013).

[24] J. S. Guasto, K. A. Johnson, and J. P. Gollub, *Oscillatory flows induced by microorganisms swimming in two dimensions,* Physical Review Letters **105**, 168102 (2010).

[25] P. Almendarez-Rangel, B. Morales-Cruzado, E. Sarmiento-Gómez, R. Romero-Méndez, and F. G. Pérez-Gutiérrez, *A microflow velocity measurement system based on optical tweezers: A comparison using particle tracking velocimetry,* European Journal of Mechanics - B/Fluids **72**, 561 (2018).

[26] G. Knöner, S. Parkin, N. R. Heckenberg, and H. Rubinsztein-Dunlop, *Characterization of optically driven fluid stress fields with optical tweezers,* Phys. Rev. E **72**, 031507 (2005).

[27] M. J. Lang, C. L. Asbury, J. W. Shaevitz, and S. M. Block, *An automated two-dimensional optical force clamp for single molecule studies,* Biophysical Journal **83**, 491 (2002).

[28] F. Gittes and C. F. Schmidt, *Interference model for back-focal-plane displacement detection in optical tweezers,* Optics Letters **23**, 7 (1998).

[29] A. Farré, F. Marsà, and M. Montes-Usategui, *Optimized back-focal-plane interferometry directly measures forces of optically trapped particles,* Opt. Express **20**, 12270 (2012).

[30] M.-T. Wei, O. Latinovic, L. A. Hough, Y.-Q. Chen, H. D. Ou-Yang, and A. Chiou, *Optical-tweezers-based microrheology of soft materials and living cells,* in *Handbook of Photonics for Biomedical Engineering*, edited by A. H.-P. Ho, D. Kim, and M. G. Somekh (Springer Netherlands, Dordrecht, 2017) pp. 731–753.

[31] E. E. Keaveny and M. J. Shelley, *Applying a second-kind boundary integral equation for surface tractions in stokes flow,* Journal of Computational Physics **230**, 2141 (2011).

[32] J. B. Keller and S. I. Rubinow, *Slender-body theory for slow viscous flow,* Journal of Fluid Mechanics **75**, 705 (1976).

[33] G. Quaranta, M.-E. Aubin-Tam, and D. Tam, *Hydrodynamics versus intracellular coupling in the synchronization of eukaryotic flagella,* Physical Review Letters **115**, 238101 (2015).

[34] S. Wang and A. M. Ardekani, *Unsteady swimming of small organisms,* Journal of Fluid Mechanics **702**, 286–297 (2012).

# 3

# MEASUREMENTS OF THE UNSTEADY FLOW FIELD AROUND BEATING CILIA

**D. Wei*, P. G. Dehnavi*, M. -E. Aubin-Tam and D. S. W. Tam**

*The swift deformations of flagella and cilia are crucial for locomotion and fluid transport on the micron scale. Most hydrodynamic models of flagellar and ciliary flows assume the zero Reynolds number limit and model the flow using Stokes equations. Recent work has demonstrated that this quasisteady approximation breaks down at increasing distances from the cilia. Here, we use Optical Tweezers-based Velocimetry to measure the flow velocity with high temporal accuracy, and to reconstruct the entire unsteady flow field around beating cilia. We report both the steady and the unsteady component of the ciliary flow and compare them with the solutions to both the Stokes and the Navier-Stokes equations. Our experimental measurements of the velocity and vorticity fields are in agreement with the numerical solution to the Navier-Stokes equations and show significant differences with the solution to Stokes equations. We characterize the phase difference between the flow oscillations and the oscillations of the ciliary motion and evidence a significant anisotropic phase lag. We show that this phase lag presents the spatiotemporal characteristics of the unsteady Stokes equations and that the flow field around beating cilia is well represented by the fundamental solution to the unsteady Stokes equations: the oscillet.*

* Equal contribution

## 3.1. INTRODUCTION

Cilia and flagella are ubiquitous hair-like structures that are highly-conserved among eukaryotic organisms. These organelles are functionally diverse, and their proper functioning is critical for the survival of many living organisms, from small scale microorganisms [1, 2] to humans [3, 4]. Flagellar and ciliary functions include: microbial motility [5, 6], cleansing [7], reproduction [8], and sensing [4]. A fine control of flagellar and ciliary motility supports the precise navigation of spermatozoa following chemical gradients during fertilization [9], the taxis of micro-algae towards desirable environments [10, 11], feeding of *Paramecium* [12], and the transport of mucus to clear airways [7]. Most of these functions depend on the generation of flows on the micron scale. This has led to extensive work to develop theoretical models and design experiments to characterize the flow around cilia.

The flows generated by cilia and flagella have been modelled for studies of a single beating cilium or flagellum of microswimmers, for studies of hydrodynamic interactions between multiple flagella/cilia, and for studies of multiple microswimmers in a suspension [6]. Previous work on a single beating flagellum or on an isolated microswimmer have included studies of single free-swimming bacteria [13], of single sperm cells swimming away [14] and close to surfaces [15, 16], and of micro-algae swimming freely [17, 18] and captured by pipette suction [19–21]. In these studies, flow fields are often described with reduced hydrodynamic models such as single or multiple stokeslet singularities [14, 17, 22, 23]; force dipoles [13] or multipole expansions [24]. Studies of hydrodynamic interactions between two or more beating flagella/cilia have often focused on synchronization. Such studies require simple and accurate models to represent the flow fields around cilia. Beating cilia have been represented as rotating spheres (or stokeslets) with prescribed trajectories [19, 25–30]. A more detailed representation describes a cilium as undulating filaments with prescribed waveforms discretized into stokelets or spheres [31–33]. Studies of internal dynamics and kinematics of flagella/cilia [34–37] have made use of non local slender-body theory to model the hydrodynamics [38]. Finally, studies of suspensions of microswimmers have focused on the onset of collective motion and the effect on the rheology of the active suspension [39]. These efforts also require efficient hydrodynamic models for active particles [40–43].

In most of the aforementioned studies, Stokes equations are used to represent the dynamics of the fluid [44]. Stokes equations imply a quasi-steady approximation, which assumes that the vorticity, created by the no-slip condition at the surface of a deformable microswimmer, propagates to infinity instantaneously. Thus, Stokes equations neglect the unsteady effects associated with the small, but finite, time scale for vorticity diffusion. These unsteady effects have been suggested theoretically to be critical for hydrodynamic synchronization [30], to be used by microswimmers for locomotion [45, 46], sensing [47], and to interact with each other in a way that is different from what predicted by Stokes equations [48].

Flow velocity fields around beating cilia have been measured experimentally [17–19]. However, characterizing the significance of the unsteady component of ciliary flow is challenging. One major reason is that the ciliary beating frequency is high (~10-100Hz) and hence the time scale for the unsteadiness is short. Established velocimetry techniques based on measuring the displacements of passive tracer particles are inaccurate

over short time scales, because of the thermal diffusivity of the tracer particles. Recently, Wei *et al.* [49] directly measured the unsteady flow around beating cilia and measured the asymptotic decay in the velocity field along two principal directions. These measurements were performed using Optical Tweezers Velocimetry (OTV) [50]. The asymptotic behaviour of the flow was shown to deviate fundamentally from the stokeslet in terms of rate of spatial decay, and more importantly, the unsteady flow is spatially phase shifted, at distances smaller than the characteristic length of vorticity diffusion $\delta = \sqrt{\mu/\rho f}$ where $\mu$ is the dynamic viscosity of water, $\rho$ the density and $f$ the ciliary beating frequency.



In this study, we use Optical Tweezers Velocimetry to fully characterize the time resolved flow velocity fields around beating cilia. Our measurements illustrate the rich spatiotemporal dynamics of the flow around cilia. We report the asymptotic behaviour of both the steady and the unsteady flow components along the different principal directions. The spatial and time resolution allow us to compare our velocity measurements in the entire flow field with the fundamental solution of the unsteady Stokes equations. We further perform numerical simulations and compare our experimental velocimetry measurements with the computed velocity fields. We solve both Stokes equations using the Boundary Element Method and the unsteady Stokes equations using direct numerical simulations. This comparison shows that the measured flow fields display key features, which are direct results of the unsteady term in the equation, and are not accounted for in Stokes equations.

This paper is organized as follows. **Sec. 3.2** introduces the theoretical framework, with **Sec. 3.2.1** introducing the governing equations, and **Sec. 3.2.2** the numerical results showing the behaviour of an oscillet. **Sec. 3.3** introduces the experimental and computational methodology. **Sec. 3.4** focuses on characterizing the asymptotic behaviours of the ciliary flow field along different axes. **Sec. 3.4.1**, **Sec. 3.4.2**, and **Sec. 3.4.3** present results of the spatial decay of the steady flow, the spatial decay of the unsteady flow, and the phase shift of the unsteady flow, respectively. Lastly, in **Sec. 3.5**, we present the time-resolved ciliary flow field over the entire $xy$-plane. In **Sec. 3.5.1**, we display the flow field consisting of both the steady and the unsteady components. Then we focus on characterizing the unsteady velocity field over the plane in **Sec. 3.5.2**, **Sec. 3.5.3**, and **Sec. 3.5.4**, where we introduce the direct numerical simulation method, map the phase shift over the plane, and visualize the vorticity diffusion, respectively.

## 3.2. THEORETICAL BACKGROUND

### 3.2.1. GOVERNING EQUATIONS

The fluid dynamics of the incompressible fluid around beating cilia are governed by the Navier-Stokes equations:

$$\begin{aligned} -\nabla p + \mu \nabla^2 \mathbf{u} + \mathbf{f} &= \rho \left( \frac{\partial \mathbf{u}}{\partial t} + (\mathbf{u} \cdot \nabla)\mathbf{u} \right), \\ \nabla \cdot \mathbf{u} &= 0 \end{aligned} \tag{3.1}$$

where $\rho$ and $\mu$ are the density and the dynamic viscosity of the fluid, $\mathbf{u}(\mathbf{r}, t) = (u, v, w)$ and $p(\mathbf{r}, t)$ the velocity and the pressure fields, and $\mathbf{f}(\mathbf{r}, t)$ represents the distribution of

body force. We consider a flow with a characteristic time scale of $\tau = 1/f$, characteristic velocity $U$ and length scale $L$. With these scales, we non-dimensionalize equations Eq. (3.1)

$$\begin{aligned} -\nabla\tilde{p} + \nabla^2\tilde{\mathbf{u}} + \tilde{\mathbf{f}} &= Re_\tau \frac{\partial\tilde{\mathbf{u}}}{\partial\tilde{t}} + Re(\tilde{\mathbf{u}}\cdot\nabla)\tilde{\mathbf{u}}), \\ \nabla\cdot\tilde{\mathbf{u}} &= 0. \end{aligned} \tag{3.2}$$



Equations Eq. (3.2) depends on two non-dimensional parameters, namely the classical Reynolds number $Re = \rho UL/\mu$ and the unsteady Reynolds number $Re_\tau = \rho L^2/(\mu\tau)$. The Reynolds number $Re$ describes the relative magnitude between the non-linear inertial term and the viscous term in equations Eq. (3.1). The unsteady Reynolds number $Re_\tau$ characterizes the relative magnitude of the transient inertial term and the viscous term. In studies of micro-motility and flagellar hydrodynamics, both the transient and the non-linear inertial terms are often neglected, such that equations Eq. (3.1) simplify to the Stokes equations, which are used to compute the flow field:

$$-\nabla p + \mu\nabla^2\mathbf{u} + \mathbf{f} = \mathbf{0}. \tag{3.3}$$

For ciliary flows, the Reynolds number $Re$ is very small. For example, for a micro-algae 10 µm long swimming at 100 µm/s the Reynolds number is $Re \sim 10^{-3}$ and the non-linear inertial term is negligible. Next, we consider the unsteady Reynolds number. $Re_\tau$ can be interpreted as the ratio of two time scales, $Re_\tau = \tau_{\text{diff}}/\tau$, where $\tau_{\text{diff}} = \rho L^2/\mu$ is the time scale for the diffusion of vorticity over a length scale $L$ and $\tau$ is the relevant characteristic time scale. Considering the flow field at very short distances $L$ from the beating flagella/cilia, $\tau_{\text{diff}}$ is small such that $\tau_{\text{diff}} \ll \tau$. In this case, the viscous boundary layer can be considered to have diffused over a length scale much larger than $L$ and it is therefore justified to assume a quasi-steady approximation within this boundary layer and to represent the flow field with Stokes equations (Eq. (3.3)). On the other hand, if we consider the flow field at distances $L$ such that $\tau_{\text{diff}} \geq \tau$, the quasi-steady approximation does not hold and the flow should be represented with the unsteady Stokes equation, which retains the transient term:

$$-\nabla p + \mu\nabla^2\mathbf{u} + \mathbf{f} = \rho\frac{\partial\mathbf{u}}{\partial t}. \tag{3.4}$$

In this study, we characterize experimentally the unsteady flow around beating cilia. For this, it is instructive to decompose the flow velocity into a steady and an unsteady component: $\mathbf{u} = \overline{\mathbf{u}} + \mathbf{u}'$. The steady component $\overline{\mathbf{u}}$ of the velocity field corresponds to the time-average of the ciliary flow, $\overline{\mathbf{u}} = \int_0^T \mathbf{u}(\mathbf{r}, t)dt/T$, with $T$ the period of beating. By definition, this term is time-independent, and therefore it is expected to satisfy the Stokes equations Eq. (3.3). The unsteady component $\mathbf{u}' = \mathbf{u} - \overline{\mathbf{u}}$ corresponds to the zero-average fluctuations and satisfies the unsteady Stokes equations (Eq. (3.4)). Solutions to the unsteady Stokes equations (Eq. (3.4)) and to Stokes equations (Eq. (3.3)) are fundamentally different and one therefore expects the steady and the unsteady flow components to present different characteristics. We illustrate these key differences by looking at the fundamental solutions to both these equations.

### 3.2.2. FUNDAMENTAL SOLUTIONS: THE STOKESLET AND THE OSCILLET

Both Stokes and the unsteady Stokes equations are linear partial differential equations, for which general solutions can be constructed by the linear superposition of fundamental solutions. One of such fundamental solutions to Stokes equations is the stokeslet, which corresponds to the Stokes flow created by a point force $\mathbf{f} = \mathbf{F}\delta(\mathbf{r})$. Here $\delta(\mathbf{r})$ is the Kronecker delta function. The flow field of a stokeslet is [51]:

$$\begin{aligned} \mathbf{u}_S(\mathbf{r}) &= \mathbf{F} \cdot \frac{\mathbf{G}(\mathbf{r})}{8\pi\mu}, \\ \mathbf{G}_{ij}(\mathbf{r}) &= \frac{\boldsymbol{\delta}_{ij}}{r} + \frac{\mathbf{x}_i \mathbf{x}_j}{r^3} \end{aligned} \tag{3.5}$$



Similarly, the fundamental solution to the unsteady Stokes equations with an oscillating point force $\mathbf{f} = \mathbf{F}\delta(\mathbf{r})e^{\mathrm{i}\cdot 2\pi \mathrm{f} t}$ can be derived [51, 52] and can be written:

$$\begin{aligned} \mathbf{u}_O(\mathbf{r}) &= \mathbf{F} e^{\mathrm{i}\cdot 2\pi \mathrm{f} t} \cdot \frac{\mathbf{S}(\mathbf{r})}{8\pi\mu}, \\ \mathbf{S}_{ij}(\mathbf{r}) &= \frac{\boldsymbol{\delta}_{ij}}{r}\mathscr{A}(R) + \frac{\mathbf{x}_i \mathbf{x}_j}{r^3}\mathscr{C}(R), \\ \mathscr{A}(R) &= 2\left(1 + \frac{1}{R} + \frac{1}{R^2}\right)e^{-R} - \frac{2}{R^2}, \\ \mathscr{C}(R) &= -2\left(1 + \frac{3}{R} + \frac{3}{R^2}\right)e^{-R} + \frac{6}{R^2} \\ R &\equiv \sqrt{2\pi} \cdot \frac{r}{\delta} e^{-\mathrm{i}\cdot\pi/4}, \delta \equiv \sqrt{\frac{\mu}{\rho f}} \end{aligned} \tag{3.6}$$

Following [53], we refer to this fundamental solution as an *oscillet*. In the near field, where $R \to 0$, one can easily verify that $\mathscr{A}(R \to 0) = 1$ and $\mathscr{C}(R \to 0) = 1$, such that $\mathbf{S}(\mathbf{r}) \approx \mathbf{G}(\mathbf{r})$. Therefore, in the vicinity of the point force, the oscillet is simply an oscillating stokeslet. In the far field, there are two major differences between the behaviour of an oscillating stokeslet Eq. (3.5) and that of an oscillet Eq. (3.6). First, in the far field, the magnitude of the stokeslet flow $\mathbf{u}_S$ decays as $1/r$, while the amplitude of the flow oscillations of the oscillet decays as $1/r^3$. Second, the flow field around an oscillating stokeslet always oscillates in phase with the point force at the origin of the flow. This is because of the quasi-steady approximation of Eq. (3.3), which assumes that the flow has instantaneously reached the steady state stokeslet field. For an oscillet, on the other hand, the oscillations of the flow velocity will be phase delayed with respect to the oscillations of the forcing. This phase delay is a direct consequence of the finite diffusion time of vorticity, and the oscillet is analogous to Stokes' second problem, corresponding to the flow created by an oscillating flat surface.

We illustrate the important differences between the stokeslet and the oscillet by representing the velocity fields associated with both singularities. **Fig. 3.1** illustrates the velocity field and streamline pattern for a point force located at the origin and oscillating along the $x$-axis. **Fig. 3.1**a corresponds to an oscillating stokeslet, while **Fig. 3.1**b corresponds to an oscillet. For the stokeslet, it is noteworthy that the $x$-component of the velocity field $\mathbf{u}$ has the same sign in the entire domain and remains always the same as the sign of the point force $\mathbf{F}$. The oscillet flow, **Fig. 3.1**b, resembles the stokeslet flow

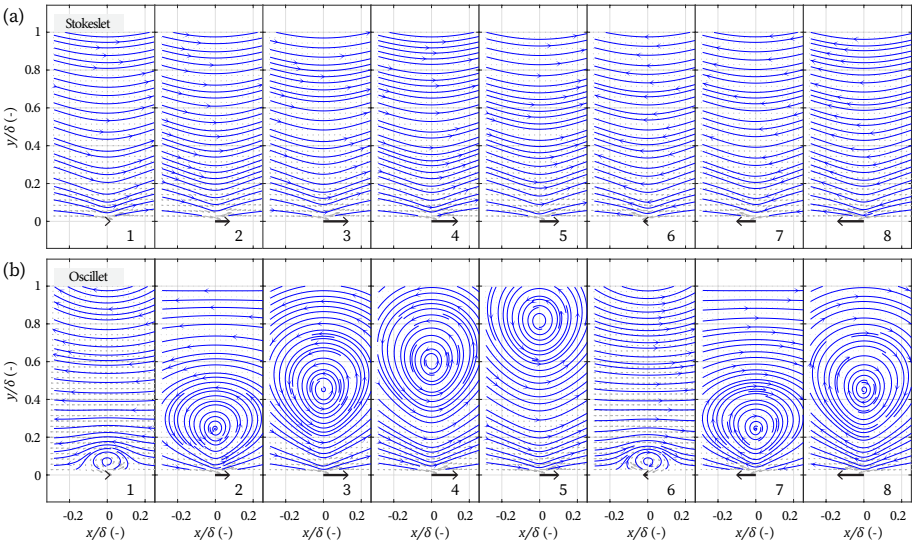


Figure 3.1: Streamlines deduced from the velocity field of a stokeslet with oscillating force (a) and that of an oscillet (b). The oscillating force $F\sin(2\pi t/T)$ is represented by the black arrow at the origin. From panel 1 to 8, $t/T = 0.03, 0.10, 0.20, 0.28, 0.39, 0.52, 0.60, 0.70$. Grey arrows represent the velocity vector field.

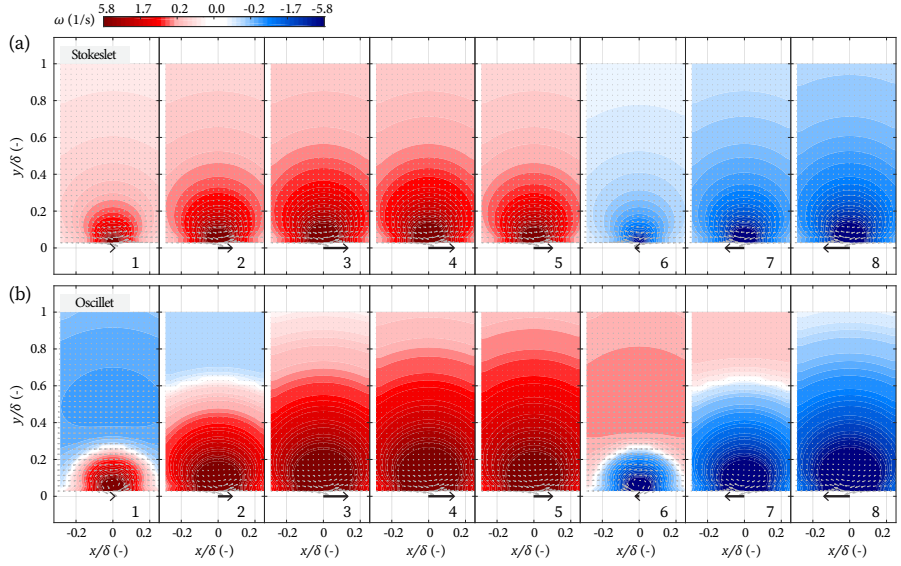


Figure 3.2: Vorticity field, $\boldsymbol{\omega} = \nabla \times \mathbf{u}$, of a stokeslet with oscillating force (a) and that of an oscillet (b). Panels are taken at the same instants as in **Fig.** 3.1 respectively.

only in the immediate vicinity of the origin, where the point force is located. The flow field is characterized by the presence of a stagnation point and that of closed streamlines around the stagnation point. The flow direction is therefore not uniform in the entire field. Along the $y$-axis, the sign of the velocity component $u$ changes beyond the stagnation point, which correspond to a flow inversion point. This stagnation point moves away from the origin, **Fig. 3.1**b panel 1 to 5. A new stagnation point is generated at the origin, every time the point force changes direction, **Fig. 3.1**b panel 6. This new stagnation point, then, moves away from the origin, **Fig. 3.1**b panel 6-8. The propagation of the stagnation point is related to the diffusion of vorticity, which we consider next.

**Fig. 3.2** represents the $z$-component of the vorticity field in the $xy$-plane at different instants during a cycle. For a stokeslet, the vorticity field has a uniform sign in the entire field and is positive (respectively negative) for a positive (respectively negative) point force **F**, **Fig. 3.2**a. The vorticity field of the oscillet does not have a uniform sign. Vorticity is generated at the origin, **Fig. 3.2**a panel 1, and diffuses into the field, see panels 1-5. When the force direction reverses and becomes negative, negative vorticity is then generated at the point force, **Fig. 3.2**a panel 6, but the vorticity remains positive in the rest of the field.

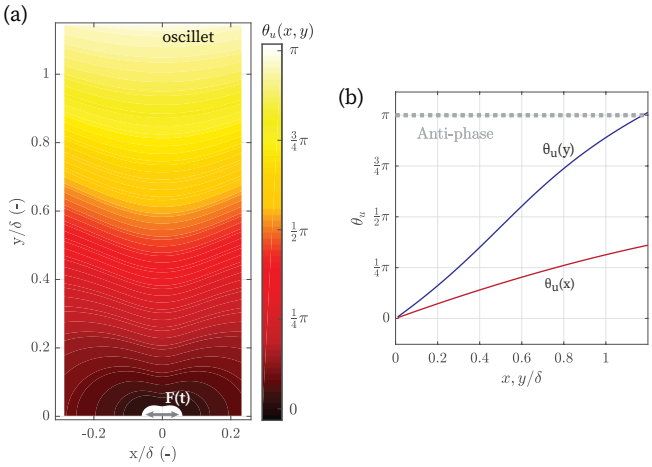


Figure 3.3: Phase shift between the $x$ velocity component, $u$, and the forcing, or $\theta_u$, computed with Eq. (3.6). The point force is at the origin and oscillates along the $x$-axis. (a) Phase shift in $xy$-plane. (b) Phase shift $\theta_u$ along the $x$- (red) and the $y$-axis (blue). Axes are scaled by $\delta = \sqrt{\mu\tau/\rho}$.

Finally, in the oscillet flow, there is phase delay between the oscillation of the flow velocity and the oscillation of the point force. This is not the case for the stokeslet flow. **Fig. 3.3** represents $\theta_u$, the phase delay between $u$ and the point force. A distinct feature is that the phase increase is not isotropic. The phase increases slowly along the direction of the forcing, the $x$-axis, and significantly faster along directions perpendicular to the forcing, the $y$- and $z$-axis, see **Fig. 3.3**b. It bears emphasis, that the increase in phase delay occurs already at short distances from the point force, and is not limited to the far field. In fact, the phase increases the fastest at distances smaller than the diffusive length scale $\delta$.

## 3.3. METHODOLOGY

### 3.3.1. OPTICAL TWEEZERS VELOCIMETRY (OTV)



We measure the flow field around beating biological cilia. In nature, cilia beat at frequencies ranging from 10 to 100 Hz and generate flows with rich temporal dynamics. Resolving such dynamics requires high temporal and spatial accuracy. On these scales, velocimetry techniques based on passive tracers, such as particle image velocimetry (PIV) and particle tracking velocimetry (PTV) become inappropriate because the advection of passive tracers cannot be distinguished from Brownian motion [50]. While the displacements due to the advection of the particle by the flow scale with $\sim U\tau$, the displacements due to diffusion scale with $\sim \sqrt{D\tau}$, where $D$ is the diffusion coefficient of the tracer particle. The ratio of these length scales defines the Péclet number $Pe \sim U\sqrt{\tau/D}$, which represents a signal to noise ratio for passive tracer-based velocimetry. For unsteady ciliary flows, $Pe$ can be of order one or smaller, and thus both PIV and PTV cannot accurately capture the such flow. To tackle these challenges, we employ the Optical Tweezers Velocimetry (OTV) technique [49, 50]. Previously, optical tweezers have been employed to measure velocity of steady flows [54], however, here we leverage the high spatial-temporal resolution of the optical tweezers-based measurement in resolving both the steady and the unsteady component of the ciliary flow. In this technique, a bead is trapped by a focused laser beam. The local flow velocity directly relates to the displacement of the bead from the laser focal point. The desired temporal resolution in measuring the flow ($\lesssim 0.1$ ms) is achieved by using back focal plane interferometry [55, 56] in monitoring the bead position $\Delta\mathbf{x}(t)$.

The OTV experimental setup is presented in **Fig. 3.4**a-b and is briefly summarized hereafter. Two laser beams are aligned and focused by a water immersion objective (NA=1.20, 60×). A Nd:YAG ($\lambda$=1064 nm) laser is used to trap spherical polystyrene beads of radii $a$ = 0.5 µm-2.5 µm at the focal point. Back focal plane interferometry is performed with a second detection laser ($\lambda$=880 nm), which is used to detect the position of the bead with a position sensitive detector (PSD, First Sensor DL100-7) ( **Fig. 3.4**a). The experimentally acquired electrical signal from the PSD is converted into bead position following the same methodology as Lang *et al.* [57]. The bead position $\Delta\mathbf{x}$ can be directly related to the local flow velocity $\mathbf{u}$, by considering the force balance between the force due to the optical tweezers $\mathbf{F}_\mathrm{t} = -k\Delta x$, and the hydrodynamic force $\mathbf{F}_\mathrm{h}(t)$ due to the external flow $\mathbf{u}$, where $k$ is the stiffness of the optical tweezers. The Reynolds number of the bead, $Re_a = \rho|\mathbf{u}|a/\mu$, is small $Re_a \approx 10^{-5} - 10^{-4}$, such that the hydrodynamic force on the bead reduces to the viscous drag only, and the flow velocity can hence be deduced from equation:

$$\dot{\Delta\mathbf{x}} + \frac{k}{\gamma}\Delta\mathbf{x} = \mathbf{u}(t), \tag{3.7}$$

where $\gamma = 6\pi\mu a$ is the Stokes drag coefficient. Using Eq. (3.7), we deduce the local flow velocity $\mathbf{u}(\mathbf{t})$ from the bead displacements $\Delta\mathbf{x}(t)$ using a Kalman filter, see Dehnavi *et al.* [50] for detail.

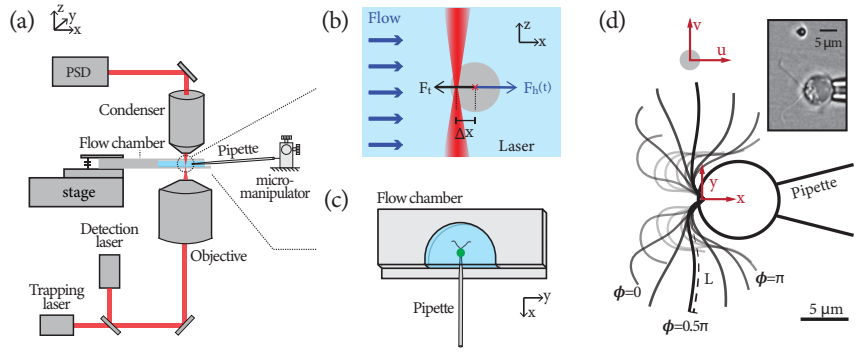


Figure 3.4: Optical Tweezers Velocimetry (OTV) (a) Scheme of OTV. Lasers are used for trapping beads and detecting the bead's displacement. Information on the bead's displacement is obtained by back focal plane interferometry, which is facilitated by a condenser and a position sensitive detector (PSD). (b) Zoom-in of the dashed circle in (a). The recovery force $\mathbf{F}_t$ exerted by the optical tweezers equals the hydrodynamic force $\mathbf{F}_h(t)$. (c) Schematics showing how the biological sample is loaded. A customized flow chamber in a semi-circle shape of 15 mm diameter with a 2 mm thickness is used for experiments. Cells with beating cilia are captured by suction force applied through a glass micro-pipette. The cell and the pipette are mounted on a micro-manipulator which controls their relative position with respect to the laser trap. (d) Experimental configuration. A bead is optically trapped nearby to resolve the local flow velocities $u$ and $v$. The ciliary shapes during a typical beat are displayed. The ciliary phase $\phi \in [0, 2\pi)$ is used to describe the shapes, with the most forward-reaching shape defined as $\phi = 0$. Inset shows a light microscope image of the corresponding experiment, in which the ciliary shapes correspond to approximately $\phi = 0$.

### 3.3.2. EXPERIMENTAL SETUP AND MEASUREMENT SETTINGS

Wildtype *C. reinhardtii* cells (cc-125 mt+) cultured in TRIS-minimal medium (pH = 7.0) are used as biological samples to generate ciliary flows. In the OTV experiments, cell suspensions ($\sim 2 \times 10^4$ cells/mL) with uncoated polystyrene beads ($\sim 1 \times 10^5$ /mL) are filled into the custom-made flow chambers, see **Fig. 3.4**c. The flow chamber is a semi-circle of 7.5 mm radius in the $xy$-plane and is 2.0 mm in height in $z$. Single cells are captured by suction force applied through custom-made micro-pipettes **Fig. 3.4**c-d. The opening of the pipettes are of $2-5$ µm diameter. As shown in **Fig. 3.4**a, the pipette is held by a micro-manipulator (SYS-HS6, WPI) and can be moved in $x$, $y$, and $z$ directions with ~1 µm precision. With this, the cells are placed at different measurement locations with respect to the trapped bead. Unless otherwise mentioned, the ciliary beating plane is always aligned with the $xy$-plane. To record the ciliary beating of the captured cell, we use bright-field microscopy and high speed videography using an sCMOS camera (LaVision PCO.edge) at frame rates of 400-1400 fps. At each location, OTV measurement was carried out at a sampling frequency of 10 kHz and lasted $5-10$ s.

A typical experimental configuration is displayed in **Fig. 3.4**d, with a light microscope image from our experiments in the inset at the top right. The captured cells are held at 120 µm above the bottom of the flow chamber. To prevent background flows due to evaporation during experiments, we seal the flow chamber with a layer of silicone oil. We record the flow velocity $\mathbf{u}(\mathbf{r}, t)$ sequentially at a series of locations with respect to the cell $\mathbf{r}_i$ ($i = 1, 2, 3, \ldots$). The point where the cilia are anchored to the cell body is taken

as the origin of the Cartesian coordinate system. The asymptotic behaviour of the flow along different axes, and the flow field over the $xy$-plane, are studied with different sets of sampled flow velocity $\mathbf{u}(\mathbf{r}_i, t)$ ($i = 1, 2, 3, ...$).

In addition to the OTV measurement, we simultaneously track the shapes of the beating cilia from the video recordings, **Fig. 3.4**d. We define the ciliary phase $\phi \in [0, 2\pi)$ to describe the shapes, with the most forward-reaching shape defined as $\phi = 0$ (inset of **Fig. 3.4**d). For each frame, we determine the phase associated with the ciliary shape. To do this, we first time stamp the beginnings of each ciliary beat by identifying the most forward-reaching ciliary shapes ($\phi = 0$) for consecutive beats, based on the video taken synchronously with the measurement. Second, the ciliary phase between two marked instants are linearly interpolated between 0 and $2\pi$. **Fig. 3.5**d displays the ciliary shapes that are marked by the user as $\phi = 0$, and are considered as $\phi = 0.5\pi$ and $\pi$ by interpolation, from left to right, respectively. The point clouds represent the corresponding shapes from different cycles, and the solid lines represent the median shapes. The narrow spans of the point clouds confirm the accuracy of the time-stamping.

### 3.3.3. BOUNDARY ELEMENT METHOD AND SLENDER-BODY THEORY

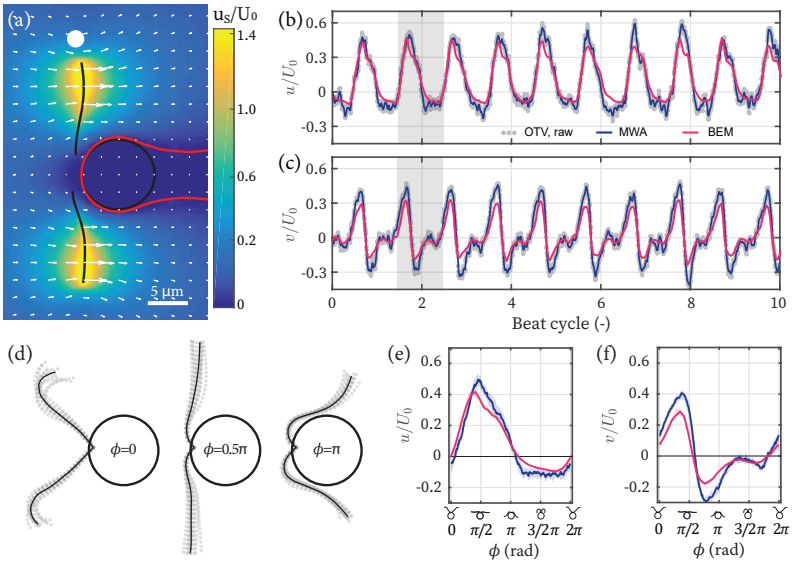


Figure 3.5: Numerical method and signal post treatment. (a) Flow field is computed numerically with boundary element methods (BEM) using tracked ciliary shapes shown in **Fig. 3.4**d. (b-c) The axial ($x$) and the lateral ($y$) velocity component, $u$ and $v$, measured by OTV and computed by BEM. Raw OTV data are presented as grey dots in the background, while blue lines show the signal after moving window average (MWA). BEM computations are overlaid in red. A typical beat is shaded, which begins with the most forward-reaching ciliary shapes ($\phi$=0). (d) Accuracy of the time-stamping method. Grey dots represent the shapes stamped as $\phi = 0$, $0.5\pi$, and $\pi$, respectively. Black lines represent the median shapes. (e-f) The average cycle of $u$ and $v$. Solid lines and the shadings represent the median and the interquartile range for flows sample over ~40 cycles. All flow velocities are scaled by $U_0 = Lf \approx 600$ μm/s.

To compute the flow velocity predicted by Stokes equations (Eq. (3.3)), a hybrid method combining boundary element method (BEM) and slender-body theory (SBT) [38] is employed. For simplicity, in the following parts, we refer to this method as the BEM, and it will be later further integrated with direct numerical simulations (DNS) to compute the flow field (**Sec. 3.5.2**).

In this BEM approach, the cell body and the pipette are represented as one entity, with a completed double layer boundary integral equation. Stresslet singularities are distributed on the surface of the cell-pipette; while stokeslet and rotlet singularities are distributed along the centreline of the cell-pipette. Altogether, no-slip boundary condition on the cell-pipette surface is satisfied [58]. The cilia are represented using slender-body theory with 26 discrete points along each of the cilium's centreline. The time-dependent motion of each of the 26 discrete points on a beating cilium are tracked from video; and stokeslets are placed at the points so that no-slip boundary condition is satisfied on the ciliary surface [38].



For each computation, we adjust the size of the pipette opening and the cell body shape according to the corresponding experiment. Realistic ciliary shapes are tracked from the video frames (**Fig. 3.4**d) and represented using SBT. Flow field corresponding to each frame is then computed. **Fig. 3.5**a shows the computed flow field in the middle of the power stroke. Computed velocity $\mathbf{u}_S(t)$ at the bead's position (the white circle) is displayed in **Fig. 3.5**b-c. The computed signals (red) are overlaid with the OTV results (grey and blue), showing great accuracy of the numerical method. Flow velocities are scaled by $U_0 = Lf$, with $L$ and $f$ the ciliary length and frequency.

Because $\mathbf{u}_S(t)$ is computed by solving Stokes equations (Eq. (3.3)), where the entire fluid domain is in phase with the forcing, in the following sections, $\mathbf{u}_S(t)$ is regarded as the reference signal and its phase represents the phase of the forcing (ciliary beating).

## 3.4. ASYMPTOTIC BEHAVIOUR OF THE FLOW FIELD AROUND BEATING CILIA

We start with investigating the asymptotic behaviours of the flow field around beating cilia, which include the rates of spatial decay in the near field and far field, of both the steady and the unsteady component of the ciliary flow, and the rate of spatial phase shift of the unsteady component. We measure the ciliary flow along the $x$-, $y$-, and $z$-axis, by sampling flow velocities along ($x$, 0±5μm, 0), (0±5μm, $y$, 0), and (0±5μm, 0±5μm, $z$), respectively. The uncertainties of ±5 μm result from aligning the measurement locations to the origin (the anchor point of cilia, **Fig. 3.4**d). Each dataset presented consists of 8-30 sampled points along a specific axis for a given cell. In total, the present study includes N=30 cells and N=38 datasets. Note that some cells were used to study the flow behaviour along more than one axis. Most measurements are performed within a maximum distance of ~ 160 μm and a minimum distance of ~ $L$+5 μm from the origin, where $L$ is the cilium length of each cell. $L$ varies from 8 to 18 μm over cells used in this study, and the average is $\overline{L}$ = 12 μm. This minimum distance of ~ $L$+5 μm is chosen to avoid interference of the trapping laser and the trapped bead with the ciliary beating. We present a systematic study of the behaviours of both the axial and the lateral flow components along different axes. We compare the experimentally observed asymptotic behaviours to

those of the reduced theoretical models of stokeslets and oscillets, which shed light on the nature of the ciliary flow. Practically, this knowledge can help build more accurate models in simulation, and hence potentially help us better understand ciliary synchronization.

### 3.4.1. AMPLITUDE OF THE STEADY COMPONENT



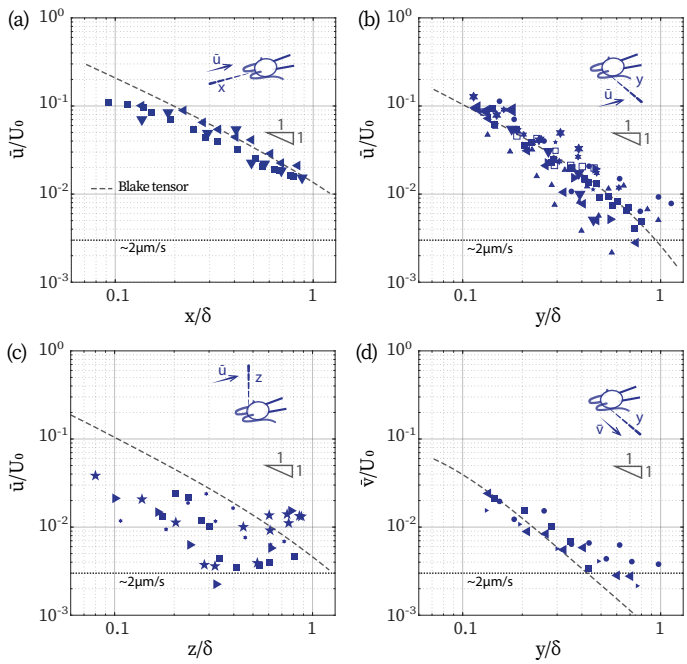


Figure 3.6: (a-c) Axial average flow ($\overline{u}$) measured along the $x$-, $y$-, and $z$-axis. (d) Lateral average flow ($\overline{v}$) measured along the $y$-axis. Measurement configurations are shown by the schematics respectively. Flow velocities are scaled by $U_0 = Lf \approx 600$ μm/s. Distances are scale by $\delta \approx 140$ μm. Different markers represent different cells. Dashed lines: flow amplitudes of a Blake tensor of forcing strength $F = 23.3$ pN.

We first discuss the measurements of the steady component, i.e., the average flow. **Fig. 3.6** displays the axial average flow $\overline{u}$ along the $x$-, $y$-, and $z$-axis, and the lateral average flow $\overline{v}$ along the $y$-axis, respectively. Due to the symmetry of the breaststroke, $\overline{v}$ along the $x$- and $z$-axis are approximately zero and therefore are not presented. The measurement settings are displayed by the schematics in each panel. Different markers represent different cells. Flow velocities are scaled by $U_0 = Lf$, with $L$ and $f$ the ciliary length and frequency, as $U_0$ accounts for the different sizes and frequencies over different cells. Distances are scaled by the characteristic length of vorticity diffusion $\delta = \sqrt{\mu/\rho f} \approx 140\,\mu$m.

We find that both $\overline{u}$ and $\overline{v}$ follow a $1/r$ decay along the $x$-, $y$- and $z$-axis, **Fig. 3.6** in agreement with Drescher *et al.* [17] and Guasto *et al.* [18]. The experimental velocity

measurements can be compared with the solution to Stokes equations for a point force in the $x$-direction and located $h = 120\,\mu\text{m} \approx 0.8\delta$ above a no-slip wall, obtained from the Blake tensor [59]. The dashed lines in **Fig. 3.6** represent the amplitudes of the average flow along the different axes, computed with the Blake tensor, for a forcing strength of $F = 23.3$ pN. We see that the rates of the spatial decay $(1/r)$ are captured quantitatively for $r < h \approx 0.8\delta$. Also, it is worth noticing that the flow amplitudes within the $xy$-plane are predicted accurately and simultaneously with the same point force (**Fig. 3.6**a-b and d). This indicates that the average flow created by captured *C. reinhardtii* cells within the ciliary beating plane can be accurately represented by a single stokeslet [19]. Lastly, we find the velocity magnitude to be smaller in the $z$-direction normal to the beating $xy$-plane, compared to the $y$-direction. This highlights the limitations of representing a cilium beating in a plane with an axisymmetric stokeslet.



### 3.4.2. AMPLITUDE OF THE UNSTEADY COMPONENT

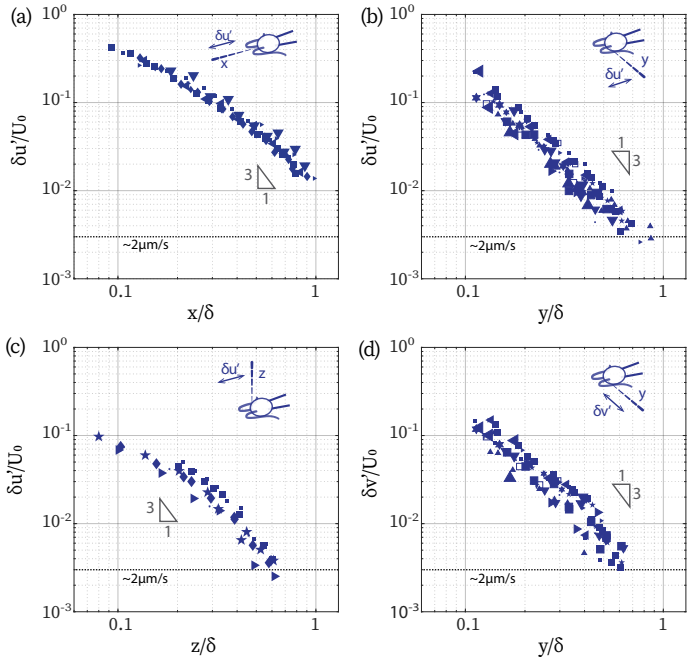


Figure 3.7: (a-c) Amplitude of the axial oscillatory flow ($\delta u'$) measured along the $x$-, $y$-, and $z$-axis. (d) Amplitude of the lateral oscillatory flow ($\delta v'$) measured along the $y$-axis.

We now discuss the unsteady component of ciliary flow, or the oscillatory flow, $\mathbf{u}' = \mathbf{u} - \overline{\mathbf{u}}$. By definition, it generates zero net flow per cycle, and we thus report the decay of the amplitude of the oscillations, $\delta\mathbf{u}'$ computed as half of the peak-to-peak amplitude of $\mathbf{u}'$. **Fig. 3.7** represents the axial ($\delta u'$) and the lateral ($\delta v'$) amplitude of the oscilla-

tory flow, along the $x$-, $y$-, and $z$-axis. The important observation is that the asymptotic behaviour of the unsteady component differs markedly from that of the corresponding average component. The rates of spatial decay of the unsteady component are higher, see **Fig. 3.7**. While the amplitude of the average flow decays in $1/r$, the amplitude of the flow oscillations decays at a rate close to $1/r^3$. This difference in the asymptotic behaviours between the average $(\overline{u}, \overline{v})$ and the oscillatory $(u', v')$ flow suggests that they are not governed by the same equations. A $1/r$ rate of decay is consistent with the stokeslet solution to the Stokes equation, while a higher rate of decay observed is consistent with the oscillet solution to the unsteady Stokes equation. Further features are reminiscent of the oscillet solution. The rate of decay of $\delta\mathbf{u}'$ becomes stronger than $1/r$ at shorter distances along the $y$- and $z$-axis, which are normal to the point force, compared to the $x$-axis, see **Fig. 3.7**a-c. This is also the case for the oscillet Eq. (3.6). The decrease of $\delta\mathbf{v}'$ along the $y$-axis, **Fig. 3.7**d, is stronger than that of $\delta\mathbf{u}'$ along the $x$-axis, **Fig. 3.7**a, at short distances from the cilia. This is due to the fact that we measure the flow generated by two cilia, beating in an anti-symmetric breaststroke. In the $x$-direction, the cilia beat in the same direction and the flow generated by each cilium in the $x$-direction contributes to the velocity $u$. In the $y$-direction on the other hand, the cilia beat in anti-symmetric fashion, and the flow generated by each cilium tend to cancel each other, leading to the observed faster rate of decay.

### 3.4.3. PHASE SHIFT OF THE UNSTEADY COMPONENT

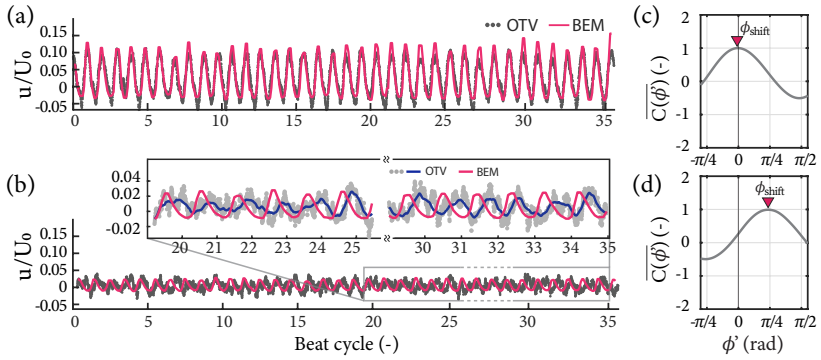


Figure 3.8: The flow velocity is phase-shifted at increasing distance. (a) Close to the cell on the lateral ($y$) side, $y = 23.0\ \mu m \approx 0.16\delta$, experimental and computational results are in phase. (b) At a larger distance, $y = 66.2\ \mu m \approx 0.47\delta$, the measured signal is phase-delayed. Inset: OTV raw data (grey), moving-window-averaged data (blue), and flow computed by BEM (red). (c-d) Using the cross-correlation function $C(\phi') = u(\phi + \phi') \star u_S(\phi)$ to quantify the phase shift between the OTV signal $u(\phi)$ and the BEM computation $u_S(\phi)$. $\overline{C(\phi')}$ is the correlation $C(\phi')$ normalized. (a-b) Reprinted figure with permission from Wei *et al.* [49]. Copyright (2019) by the American Physical Society.

The higher rate of decay is not the only difference between fundamental solutions of the Stokes and the unsteady Stokes equations. A defining feature of solutions to the unsteady Stokes equations is the phase lag between the oscillations of the flow velocity

and the forcing, which develops at increasing distances from the forcing. This phase lag is a characteristics of Stokes second problem as well as of the oscillet. Here we measure this phase lag and present its asymptotic behaviour along different axes.

**Fig. 3.8** demonstrates the phase shift of the axial flow velocity at two locations along the $y$-axis. The OTV measurements, $u$ (grey and blue), are overlaid with the BEM computations, $u_S$ (red), which assume the flow to satisfy Stokes equations, **Fig. 3.8**a-b. Close to the cilia, $r = y = 23.0\ \mu\text{m} \approx 0.16\delta$, the computed flow reproduces the measured flow accurately: they have the same amplitude and reach maximum and minimum simultaneously, **Fig. 3.8**a. Farther away, at $r = y = 66.2\ \mu\text{m} \approx 0.47\delta$, the amplitude of the measured oscillatory flow velocities is lower, and the oscillations are phase-shifted compared to the Stokes computations, **Fig. 3.8**b and inset. The phase shift is approximately $\pi/4$ and the two signals are in quadrature.

We quantify the spatial phase shift of ciliary flow by computing the cross-correlation function between the flow measured by OTV and that computed by BEM. For each recording, we proceed by first determining the ciliary phase $\phi(t)$ as described in the methodology section. This allows us to transform the measured and the computed time series of flow velocity, $u(t)$ and $u_S(t)$, as functions of the ciliary phase $\phi$, or $u(\phi)$ and $u_S(\phi)$. Then, we compute the cross-correlation function $C(\phi') = u(\phi + \phi') \star u_S(\phi)$. The phase shift between the measured velocity and the velocity predicted by Stokes equations corresponds to the phase for which the cross-correlation function reaches a maximum $C_{\max} = C(\phi_{\text{shift}})$. In **Fig. 3.8**c and d we plot the normalized cross-correlation function, $\overline{C(\phi')} = C(\phi')/C_{\max}$, between the signals shown in **Fig. 3.8**a and b, respectively. In the vicinity of the cell, $r \approx 0.16\delta$, $\phi_{\text{shift}} \approx 0$; while at a larger distance, $r \approx 0.47\delta$, $\phi_{\text{shift}} \approx \pi/4$.

We further characterize the phase shift of both the axial ($u'$) and the lateral ($v'$) oscillatory flow, along the $x$-, $y$-, and $z$-axis, and over the $xy$-plane. For consistency and simplicity, we denote the spatial phase shift $\phi_{\text{shift}}$ of $u$ and $v$ as $\theta_u(\mathbf{r})$ and $\theta_v(\mathbf{r})$ respectively in the following parts.

In **Fig. 3.9** we present $\theta_u$ along the $x$, $y$, and $z$-axis, and $\phi_v$ along the $y$-axis, respectively. For each cases, there is a clear phase shift between the measured flow and the forcing, which increases with the distance to the cilia. The increase of this phase-delay is highly dependent on the direction, as can be seen from the different slopes in **Fig. 3.9**. The phase-delay is 2-3 times stronger along directions perpendicular to the oscillating velocity, compared to the direction of the oscillating force. Quantitatively, the slopes for $\theta_u$ along the $x$-axis and $\theta_v$ along the $y$-axis are $0.30\ \pi/\delta$ and $0.52\ \pi/\delta$, respectively, **Fig. 3.9**a and d; while the slopes for $\theta_u$ along the $y$- and the $z$-axis are $1.08\ \pi/\delta$ and $1.16\ \pi/\delta$, respectively, **Fig. 3.9**b and c. The significant difference in the phase-delay along the different directions agrees with the oscillet solution. The dashed line in each panel represents the corresponding phase shift predicted by an oscillet (**Fig. 3.3**b) and is in excellent agreement with the experimental results. Note that the resemblance between $\theta_u$ along $y$- and $z$-axis (**Fig. 3.9**b and c) reflects the axisymmetry of an oscillet Eq. (3.6).

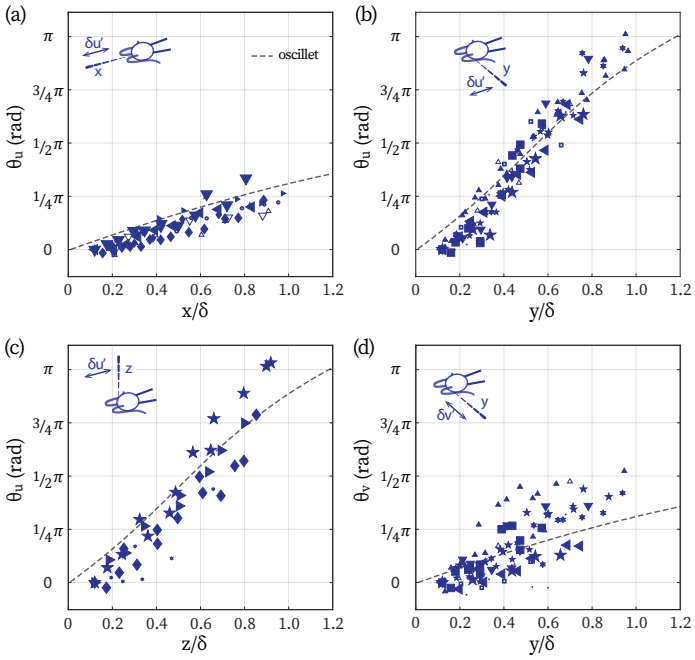


Figure 3.9: (a-c) Phase delay of the axial oscillatory flow ($\theta_u$) along the $x$-, $y$-, and $z$-axis. (d) Phase delay of the lateral oscillatory flow ($\theta_v$) along the $y$-axis. Dashed lines: corresponding phase delay predicted by an oscillet. The set of symbols are consistent with the one used in **Fig.** 3.6 and **Fig.** 3.7.

## 3.5. UNSTEADY VELOCITY FIELDS IN THE BEATING PLANE OF CILIA

In the previous section we have systematically studied the asymptotic behaviours of the flow created by beating cilia and found them to be in qualitative agreement with the oscillet. We further proceed to resolve the spatiotemporal features of the entire flow field around beating cilia and perform time-resolved direct numerical simulations (DNS) to compare with our measurements and the BEM simulations.

### 3.5.1. OTV MEASUREMENTS OF THE ENTIRE FLOW FIELD

The time-resolved flow field over the $xy$-plane is reconstructed from measurements performed at points $\mathbf{r}_i$ on a rectangular grid on one side of a cell. The grid covers the area where $x \in [-30, 30]$ µm and $y \in [0, 160]$ µm with a grid size of 10 µm. In total, there are N=78 sampling points. At each point, OTV measurements were carried out at 10 kHz for 5 s, and high speed videography was performed synchronously at a frame rate of 669 Hz. Each recording is time-stamped in order to construct the ciliary phase $\phi$ for ~40-50 consecutive beats, following the methodology detailed previously (**Sec.** 3.3.2). The time series of velocity measurements are interpolated at N=20 equally spaced phases

$\phi_j$ ($j = 1,2,...,20$) between $\phi = 0$ and $2\pi$, and the velocity measurements over the consecutive beats are binned for each of the phases $\phi_j$. The flow velocity $\mathbf{u}(\mathbf{r}_i,\phi)$ at each measurement location $\mathbf{r}_i$, is calculated as the median of the marked cycles. **Fig. 3.5**e-f display the median flow velocity cycles and the interquartile ranges that are calculated based on the signals shown in **Fig. 3.5**b-c. Snapshots of the flow velocity field on the $xy$-plane for each phase $\phi_j$ is obtained through two dimensional linear interpolation of the velocity between the sampling points $\mathbf{r}_i$

**Fig. 3.10** represents the time-resolved flow field around a single captured cell. The panels show the reconstructed flow field at different instants that correspond to the shown ciliary phase $\phi$ approximately. The vector field represent the velocity field, and the contours represent the magnitude of the velocity.



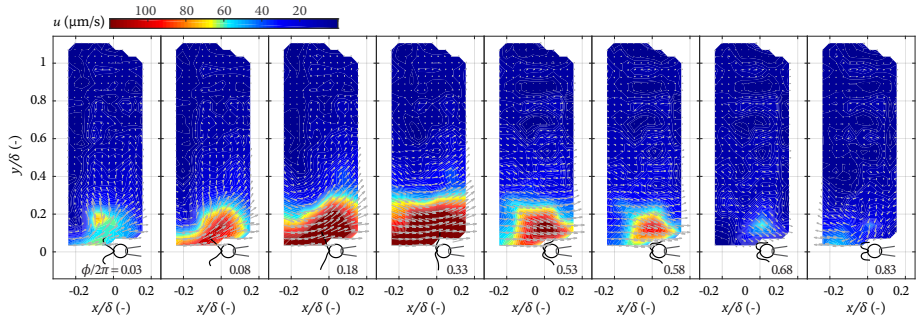


Figure 3.10: Ciliary flow field measured experimentally. Snapshots of flow field are taken at the time when the cilia display shown shapes. Vector field: flow velocity; contour: flow speed. Both axes are scaled by $\delta = \sqrt{\mu/\rho f} \approx 140\,\mu$m.

### 3.5.2. NUMERICAL SIMULATION: DNS-BEM METHOD

We perform direct numerical simulations (DNS), which solves Navier-Stokes equations Eq. (3.1), in order to compare with our measurements of the unsteady velocity field. The DNS solution includes the effect of all terms of Navier-Stokes equations, including the unsteady and the nonlinear ones, see Eq. (3.1). Here, we use a structured Cartesian grid. The implementation of our numerical approach makes use of the BEM solution, described earlier in section **Sec. 3.3.3**, to propagate the no-slip boundary condition to the grid point immediately surrounding the fluid/solid interface.

We do this by dividing the computational domain in an inner and an outer region. The inner region corresponds to the flow domain in the direct vicinity of the cilia, the cell body and the pipette, see region marked pink and grey in **Fig. 3.11**. In this region, Stokes equations remain valid, and the solution on the nodes within this region are computed using the BEM method described in **Sec. 3.3.3**, which appropriately impose the no-slip boundary condition at the surfaces of the cilia, the cell body, and the pipette. This allows to transfer the no-slip boundary condition to the neighboring grid nodes. In practice, the inner region includes the nodes where the cell and the pipette are in, the nodes that

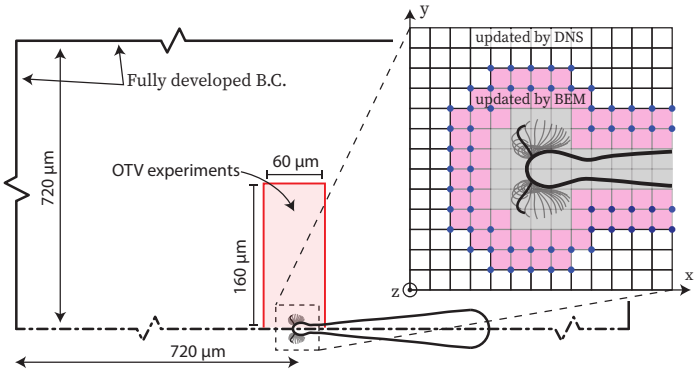


Figure 3.11: Computational domain for the DNS consists of a staggered grid with a grid size of 4 µm. The domain size is 720 µm in $z$ and 1440 µm in $x$ and $y$. The cell is placed in the middle of the domain. Red rectangular region marks where the OTV experiments are performed. Zoom-in: division of the computational domain. Grey and pink region: where the velocity is computed by the BEM, and then used as velocity boundary conditions for the DNS. The rest: where the velocity is computed by the DNS with all boundary conditions shown.

the cilia swipe across during a beat, and nodes within 2 grid cells outwards from the aforementioned (pink region in **Fig. 3.11**).

The outer region corresponds to the rest of the computational domain, which represents the space between $x = 0$ and $x = 1440$ µm, $y = 0$ and $y = 1440$ µm, and $z = 0$ and $z = 720$ µm. In the outer region, the Navier-Stokes equations Eq. (3.1) are solved using finite volume scheme, the operator splitting, and solenoidal projection technique [60], on a staggered grid with discretization size of 4 µm. A second-order Adams-Bashforth is used for explicit time integrations. Lastly, free slip boundary conditions are applied on $z = 0$ and $z = 720$ µm, and fully developed boundary conditions on $x, y = 0$, $x, y = 1440$ µm, as shown in **Fig. 3.11**. We confirm that the size of the computational domain is large enough so that the boundary conditions on the edge of the domain have a negligible effect on the flow velocity within our experimentally measured region (the red rectangle in **Fig. 3.11**).

### 3.5.3. PHASE SHIFT OVER THE CILIARY BEATING PLANE

We have previously highlighted the anisotropy in phase lag along axis parallel and normal to the force direction (**Sec. 3.4.3**). Here, we consider the axial component of the oscillatory flow ($u'$) and present the spatial phase shift ($\theta_u(x, y)$) between the flow velocity measured experimentally and computed by the DNS-BEM approach, see **Fig. 3.12**.

From the experimental results shown in **Fig. 3.12**a, we see that the contours of equal phase shift are not conspherical, i.e., the increase in phase is not isotropic. They have a notch shape or a V-shape in the $y$-direction normal to the force direction. This feature indicates that the phase shift increases the fastest along the lateral ($y$) direction and the slowest along the axial ($x$) direction, as shown in **Fig. 3.9**a-c; and that the phase shift

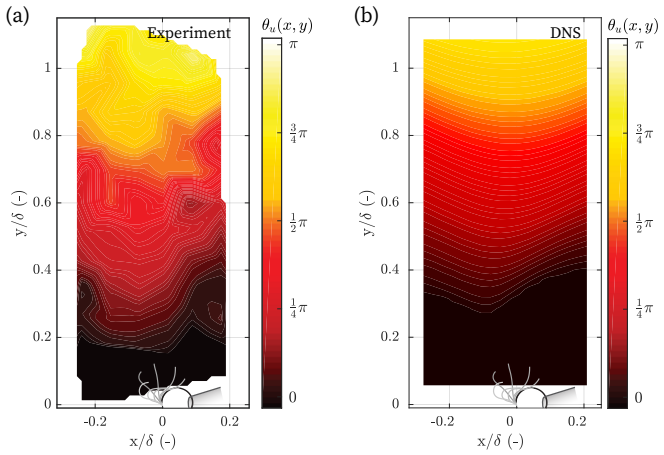


Figure 3.12: (a) Experimentally measured phase shift of the axial oscillatory flow over the ciliary beating plane, or $\theta_u(x,y)$. (b) Same phase shift computed by the DNS-BEM approach.

along $x \approx -0.1\delta$ is the maximum. The phase lag in the velocity field therefore strongly depends on the relative spatial position. Due to the axisymmetry between the $y$ and $z$, the phase shift contour in the $xz$-plane is expected to be the same as our results for the $xy$-plane, while the contours of equal phase over the $yz$-plane is expected to be concentric circles.

The measured phase lag field, **Fig. 3.12**a, is similar to the one predicted by the oscillet solution **Fig. 3.3**a and in quantitative agreement with the phase lag field computed from our simulations **Fig. 3.12**b. For both experiments and simulations, the V-shape equal phase contours have a maximum phase shift along $x \approx -0.1\delta$.

These results have implications in studies of hydrodynamic synchronization between cilia. The oscillatory flow has the strongest contribution to the hydrodyanmics interaction and is 2-5 folds larger in amplitude than the average flow, see **Fig. 3.6** and **Fig. 3.7**. The synchronization of cilia beating is characterized by metachronal rhythm, which originates from a spatially organized phase delay, between thousands of cilia. While the origin of metachrony remains unclear, an accurate representation of the hydrodynamic interactions between the cilia should account for the unsteady effects and the phase lag characterized here. Indeed, the magnitude of the spatial rate of increase of the phase delay is comparable to that observed in the metachronal wave in *Volvox* [61].

### 3.5.4. VORTICITY DIFFUSION

Finally, we characterize spatiotemporal features of the flow field around beating cilia in the $xy$-plane. As discussed in **Sec. 3.2.1**, the fundamental difference between the steady and the unsteady Stokes equations is the quasi-steady assumption, which neglects the time scale for vorticity (momentum) to diffuse. We deduce the vorticity field from the point measurements of the velocity (**Fig. 3.13**). Snapshots of the vorticity field at differ-

ent times during a ciliary beat are presented for the unsteady velocity fields measured experimentally and for the fields computed by the DNS and the BEM approach in **Fig. 3.13**a, b, and c respectively. From left to right, column 1-5 are during the power stroke and 6-8 the recovery stroke.

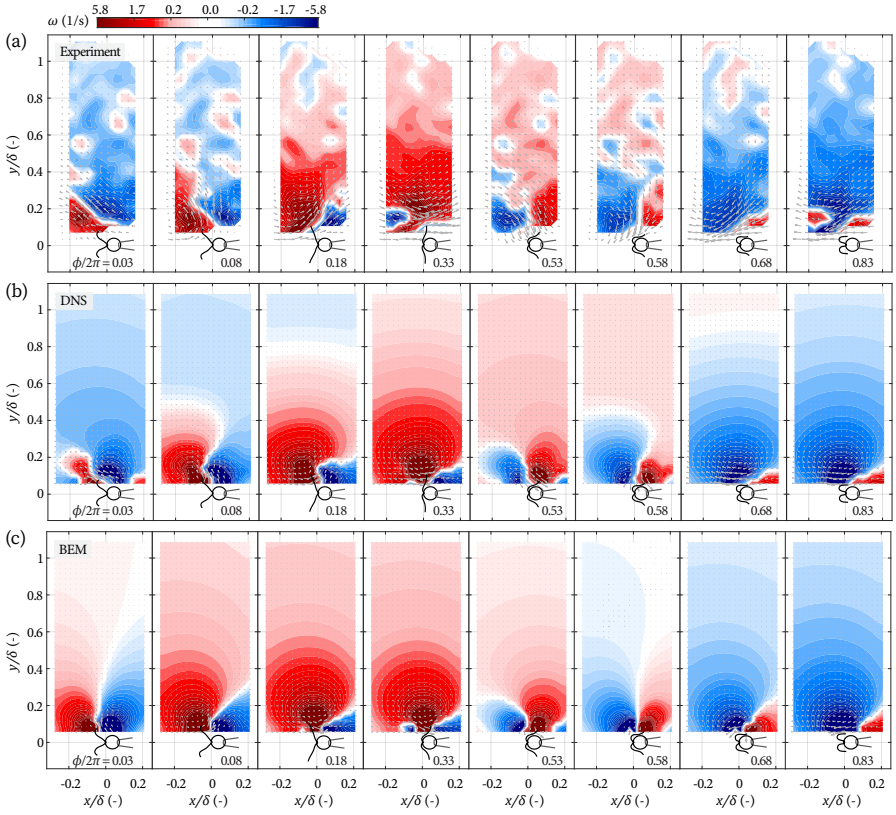


Figure 3.13: Vorticity field measured experimentally (a), and computed with the DNS (b) and the BEM (c). The vorticity $\boldsymbol{\omega} = \nabla \times \mathbf{u}$ at different times during the power stroke and the recovery stroke are displayed. Corresponding ciliary shape and ciliary phase $\phi$ are shown respectively for each panel. Grey arrows: the unsteady velocity component.

The computed vorticity field around a beating cilium (**Fig. 3.13**b-c) can be compared with the those of the stokeslet and the oscillet (**Fig. 3.2**a-b). The no-slip boundary conditions on beating cilia lead to more complex spatiotemporal patterns than the point forces. The vorticity field are not symmetric around the $x = 0$ axis while the fields associated with the point-force are. The sign of vorticity changes in front of the cilia, at $x \approx -0.1\delta$, see **Fig. 3.13** at $\phi/2\pi = 0.08$ at the beginning of the power stroke and $\phi/2\pi = 0.58$ during the recovery stroke.

The BEM solution (**Fig. 3.13**c) presents the same differences compared to the DNS

solution (**Fig. 3.13**b) as the stokeslet compared with the oscillet. These are best seen in the middle of the power stroke $\phi/2\pi = 0.18$ and in the middle of the recovery stroke $\phi/2\pi = 0.68$. In both cases, the vorticity immediately surrounding the cilia has a different sign compared to that far away from the cilia at $y/\delta \geq 0.8$. This is due to the finite time required for the vorticity to diffuse, which is captured by the DNS solution (**Fig. 3.13**b), but not by the BEM solution solving Stokes equations (**Fig. 3.13**c).

The vorticity field reconstructed from the OTV measurements (**Fig. 3.13**a) is most similar to the DNS simulations. The point of sign inversion in the vorticity field can be seen to diffuse away from the cilia, signifying the importance of taking into account the unsteady effect.



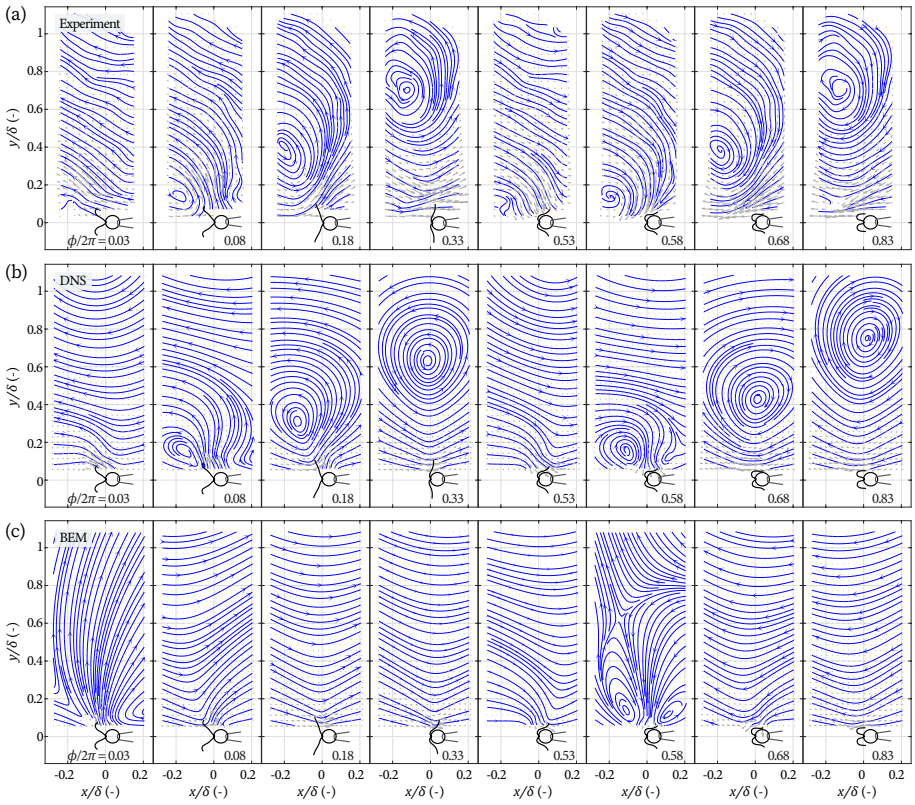


Figure 3.14: Velocity field measured experimentally (a), and computed with the DNS (b) and the BEM (c), visualized by streamlines.

The agreement between the DNS simulations and the experimental measurements can be clearly seen when considering the director field of the flow velocity. To allow a better comparison with the oscillet, we represent the director field of the oscillatory component $u'$, for which the average flow has been subtracted. **Fig. 3.14** represents

the streamlines associated with the $u'$ field for the same snapshots as in **Fig. 3.13**. The pattern of streamlines obtained from the experimental data (**Fig. 3.14**a) is in agreement with the DNS simulations (**Fig. 3.14**b). Both include closed streamlines around a stagnation point, on each side of which the flow direction changes. These closed streamlines are clearly absent in the BEM simulations (**Fig. 3.14**c), which assume Stokes flow. The closed streamlines are created in the vicinity of the cilia at the beginning of both the power and recovery stroke, and propagate away from the cell along the $y$-axis, see **Fig. 3.14**. The streamline pattern has a typical signature, which is also in close agreement with that of the oscillet and very different from that of a stokeslet, see **Fig. 3.1**.

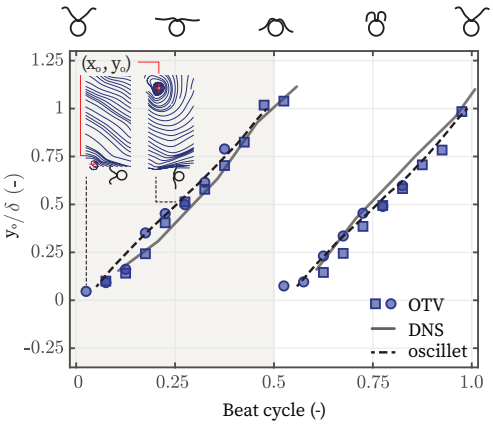


Figure 3.15: The propagation of the stagnation point. Inset: two panels from left to right show the creation of the stagnation point and its propagation after approximately 1/4 cycle respectively. The stagnation point is marked by the red cross: $(x_o, y_o)$. Squares and circles: experiments performed with two different cells, with the squares representing the cell used for **Sec. 3.5**. Shaded area marks the power stroke.

We quantify the time scale for the propagation of the closed streamlines away from the cilia. We do this by tracking the stagnation point at the centre of these closed streamlines $(x_o, y_o)$, which also corresponds to the flow inversion point. The tracking of the inversion point is represented in **Fig. 3.15** for the experimental fields, the DNS solution and the oscillet. The inset demonstrates how we mark the stagnation point, $(x_o, y_o)$ (red crosses). During the propagation, $x_o$ remains approximately unchanged, and we thus focus on $y_o$. We report the results for two typical cells presented with different markers. Our experimental measurements are in excellent agreement with the DNS simulations and the oscillet. In all datasets, the stagnation point propagates to a distance of $r = \delta$ after approximately half a cycle. Thus, for *C. reinhardtii*, the diffusive time scale of vorticity is $\tau \approx 1/2f \approx 10$ ms.

The measured time scale of vorticity diffusion also provides another way to consider the spatial phase shift of the unsteady flow. In **Fig. 3.15**, the linear best-fit to the experimental results gives a speed of vortex propagation of $dy_o/dt = 2.10\delta$ per cycle $(2\pi)$. This is equal to a phase delay of 0.95 $\pi/\delta$, which agrees well with the rate of phase shift $\theta_u$ along the $y$-axis reported previously in **Sec. 3.4.3**, $\partial\theta_u/\partial y \approx 1.08\,\pi/\delta$, see **Fig. 3.9**b.

## 3.6. CONCLUSION

By exploiting the high spatial and temporal resolution of the OTV technique, we are able to systematically characterize the steady and the unsteady component of flow created by beating cilia. We first resolved the flows' asymptotic behaviours along different axes, compared those behaviours with fundamental solutions to Stokes equations (Eq. (3.3)) and the unsteady Stokes equations (Eq. (3.4)) respectively. Finally, we characterize the unsteady velocity field over the entire ciliary beating plane to resolve its spatiotemporal dynamics. Experimental results are compared again with numerical simulations, and are found to be in agreement with the solution to the unsteady Stokes equations and to show significant differences with the solution to Stokes equations.



For the steady component (the average flow) of ciliary flow, our results show the ciliary beating can be well reproduced by the stokeslet flow field, in agreement with previous studies [17, 18]. Moreover, for a captured *C. reinhardtii* cell, the average flow velocity along the $x$ and $y$ axes can be quantitatively reproduced with a single stokeslet (Blake tensor), whose forcing is towards the cell's posterior end. Averaged over cells, the magnitude of the forcing is $F = 23.3$ pN.

For the unsteady component (the oscillatory flow), we measure the rates of decay and the rates of phase shift along different axes. We show that it decays faster than the average flow, which indicates that the governing equations for these two components must be different, and we show that the decay rates are closer to those predicted by the unsteady Stokes equations.

We present the time-resolved ciliary flow field over the beating plane. Our experimental results reveal rich spatiotemporal dynamics of the unsteady velocity field. By comparing the experimental results with the computed flow fields of an oscillet, that from the direct numerical simulations (DNS), and that computed with the boundary element method (BEM), we are able to visualize and characterize the finite scale of vorticity diffusion. We discuss an important consequence of the finite time scale for vorticity diffusion, namely, the phase-lag between the velocity and the forcing. This phase lag becomes significant at distances, which are shorter than the characteristic diffusive length scale. Furthermore, we show that phase increase is highly direction-dependent, and the different rates are all quantitatively predicted by the fundamental solution to the unsteady Stokes equations, or the oscillet Eq. (3.6).

These results confirm the breakdown of the quasi-steady approximation assumed by Stokes equations, and provide insights to the realistic ciliary flow field. Our study highlights the limit of using stokeslets to represent unsteady flows generated by beating cilia and more generally by microswimmers. This is true in particular for studies of synchronization with hydrodynamic interactions.

## 3.7. SUPPLEMENTARY MATERIAL

In this section, we attempt to explore a reduced model to represent the unsteady flow created by captured *C. reinhardtii*. Previously, the two cilia of *C. reinhardtii* has been modelled as two spheres orbiting in the opposite directions [29, 62]. In this case, each cilium can be further simplified as two orthogonal oscillets along the $x$- and $y$-direction respectively. We can infer the oscillets' strengths from the flow measurements at short

distance from and on the lateral side of a captured cell. At such locations, the cell body screens most of the flow generated by the farther cilium's beating, and therefore $\delta u'$ and $\delta v'$ measures the flow created by the closer cilium (see supplementary material of **Ref.** [20]). At $y = 0.1\delta$, $\delta u' \approx \delta v' \approx 0.2U_0$ (**Fig. 3.7**b, d), suggesting that the two orthogonal oscillets representing the beating of one cilium are of the same strength. Quantitatively, we estimate the forcing of each oscillet to be 23 pN. This agrees well with the recently reported oscillatory force generated by captured *C. reinhardtii* [63], which is $26 \pm 5$ pN.



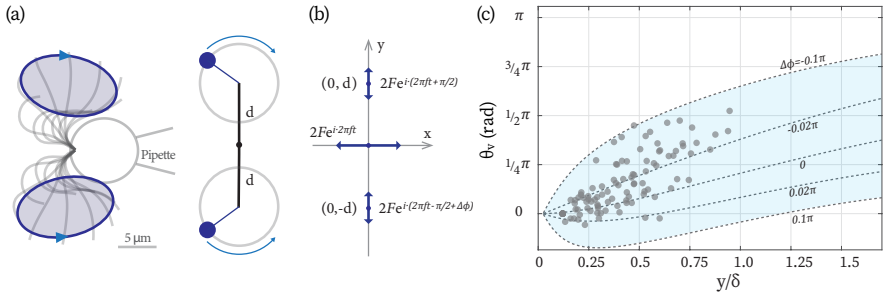


Figure 3.16: (a) A two-sphere model to describe captured *C. reinhardtii*. The mirror-symmetric and synchronous ciliary beating is idealized as two spheres orbiting circularly in the opposite directions, while remaining in sync with each other. The distance between the centres of the orbit is $2d = 16.0\,\mu\text{m} \approx 0.12\delta$. (b) Reduced model of captured *C. reinhardtii*. The two orbiting spheres in (a) are further reduced to three oscillets. The $\pm\pi/2$ in the phases of the lateral forcings represent the clockwise and the counter-clockwise rotation of the two spheres, respectively. An extra phase difference $\Delta\phi$ is used to reflect the fact that the anti-phase synchrony between the two spheres may not be perfect (c) Effect of $\Delta\phi$ on $\theta_v(y)$. Dashed lines from top to bottom represent $\theta_v(y)$ computed by the reduced model with $\Delta\phi = -0.1\pi, -0.02\pi, 0, 0.02\pi, 0.1\pi$. Among them $\Delta\phi = -0.02\pi$ is the best fit in the least-squares sense. The scattered points are the same as the data shown in **Fig. 3.9**d but with unified symbol.

**Fig. 3.16**a illustrates the idealization of the ciliary beating of captured *C. reinhardtii* as two counter-rotating spheres. In total, two cilia beating anti-symmetrically can be represented by 4 oscillets, 2 along the $x$-directions oscillating in-phase, and 2 long the $y$-direction in anti-phase. We denote the strength each oscillet as $F$. **Fig. 3.16**b displays the model further reduced to three oscillating forces (oscillets) by combining the two axial forces in-phase as one single oscillet of strength $2F$. The combined axial ($x$) oscillet is then placed at (0, 0) and the two lateral ($y$) oscillets are placed at $(0, \pm d)$, respectively. In **Fig. 3.16**b, $\pm\pi/2$ in the phase of the lateral ($y$) oscillets represent that their oscillations are in anti-phase. An additional term $\Delta\phi$ is included to represent the fact that one cilium is often slightly lagging in the synchrony [64]. Based on realistic cell geometry, we take $2d = 16.0\,\mu\text{m} \approx 0.12\delta$.

This reduced model helps to elucidate data shown in **Fig. 3.9**. We observe that the slopes for $\theta_u$ along the $x$-axis and $\theta_v$ along the $y$-axis are 0.30 $\pi/\delta$ and 0.52 $\pi/\delta$, respectively, **Fig. 3.9**a and d (**Sec. 3.4.3**). These two measured values differ by 70%, whereas axisymmetry would predict them to be the same. Additionally, $\theta_v$ along the $y$-axis appears to more variable from cell to cell than $\theta_u$ along the $x$-axis. We find both of these phenomena can be explained by representing the cilia with oscillets.

We find that the phase shift of the lateral oscillatory flow, $\theta_v(y)$, is significantly influenced by $\Delta\phi$. Dashed lines represent $\theta_v(y)$ predicted by the reduced model with the

shown $\Delta\phi$. Surprisingly, a slight change of $\Delta\phi = \pm 0.02\pi$ (1/100 of a cycle) will significantly change the curve. On the other hand, $\theta_u(x)$ is not sensitive to $\Delta\phi$[1]. As each cell's breaststroke beating may hae slightly different lag, this explains why $\theta_v(y)$ displays much larger cell-to-cell variability than $\theta_u(x)$, **Fig. 3.9**a and d. Additionally, our experimental data all fall in the region between $\Delta\phi \in [-0.1\pi, 0.1\pi]$. The values $\pm 0.1\pi$ agrees well with the observations from **Ref.** [64], where the *trans* cilium was found to often lagged for approximately 1/20 of a cycle ($0.1\pi$). As our measurements were carried randomly on the side of either the leading or the lagging cilium, $\Delta\phi$ can be of either sign.



## 3.8. AUTHOR CONTRIBUTIONS

D. W. conducted the experiments, analyzed the data, and wrote the manuscript. P. G. D. designed and performed the DNS and the BEM computations. D. T. and M.-E. A.-T. supervised the work and critically revised the manuscript. D. W. and P. G. D. contributed equally to this work.

## 3.9. ACKNOWLEDGMENTS

The authors thank R. Kieffer for technical support. D. W. thanks Shuyue Wang for her help in performing some early OTV measurements.

## REFERENCES

[1] M. L. Ginger, N. Portman, and P. G. McKean, *Swimming with protists: perception, motility and flagellum assembly,* Nature Reviews Microbiology **6**, 838 (2008).

[2] J.-B. Raina, V. Fernandez, B. Lambert, R. Stocker, and J. R. Seymour, *The role of microbial motility and chemotaxis in symbiosis,* Nature Reviews Microbiology **17**, 284 (2019).

[3] P. Satir and S. T. Christensen, *Overview of structure and function of mammalian cilia,* Annual Review of Physiology **69**, 377 (2007).

[4] M. Fliegauf, T. Benzing, and H. Omran, *When cilia go bad: cilia defects and ciliopathies,* Nature Reviews Molecular Cell Biology **8**, 880 EP (2007).

[5] E. Lauga and T. R. Powers, *The hydrodynamics of swimming microorganisms,* Reports on Progress in Physics **72**, 096601 (2009).

[6] J. Elgeti, R. G. Winkler, and G. Gompper, *Physics of microswimmers—single particle motion and collective behavior: a review,* Reports on Progress in Physics **78**, 056601 (2015).

[7] A. E. Tilley, M. S. Walters, R. Shaykhiev, and R. G. Crystal, *Cilia dysfunction in lung disease,* Annual Review of Physiology **77**, 379 (2015).

[1] In fact, the combination of the axial oscillets are carried out after confirming $\theta_u(x)$ being insensitive to $\Delta\phi$.

[8] S. A. Halbert, D. L. Patton, P. W. Zarutskie, and M. R. Soules, *Function and structure of cilia in the fallopian tube of an infertile woman with Kartagener's syndrome.* Human Reproduction **12**, 55 (1997).

[9] D. M. Woolley, R. F. Crockett, W. D. I. Groom, and S. G. Revell, *A study of synchronisation between the flagella of bull spermatozoa, with related observations,* **212**, 2215 (2009).

[10] K. Y. Wan, *Coordination of eukaryotic cilia and flagella,* Essays In Biochemistry **62**, 829 (2018).

[11] K. Y. Wan, *Synchrony and symmetry-breaking in active flagellar coordination,* Philosophical Transactions of the Royal Society B: Biological Sciences **375**, 20190393 (2020).

[12] A. Funfak, C. Fisch, H. T. Abdel Motaal, J. Diener, L. Combettes, C. N. Baroud, and P. Dupuis-Williams, *Paramecium swimming and ciliary beating patterns: a study on four RNA interference mutations,* Integrative Biology **7**, 90 (2014).

[13] K. Drescher, J. Dunkel, L. H. Cisneros, S. Ganguly, and R. E. Goldstein, *Fluid dynamics and noise in bacterial cell–cell and cell–surface scattering,* Proceedings of the National Academy of Sciences **108**, 10940 (2011).

[14] K. Ishimoto, H. Gadêlha, E. A. Gaffney, D. J. Smith, and J. Kirkman-Brown, *Human sperm swimming in a high viscosity mucus analogue,* Journal of Theoretical Biology **446**, 1 (2018).

[15] J. Elgeti, U. B. Kaupp, and G. Gompper, *Hydrodynamics of sperm cells near surfaces,* Biophysical Journal **99**, 1018 (2010).

[16] D. J. Smith, E. A. Gaffney, J. R. Blake, and J. C. Kirkman-Brown, *Human sperm accumulation near surfaces: a simulation study,* Journal of Fluid Mechanics **621**, 289 (2009).

[17] K. Drescher, R. E. Goldstein, N. Michel, M. Polin, and I. Tuval, *Direct measurement of the flow field around swimming microorganisms,* Physical Review Letters **105**, 168101 (2010).

[18] J. S. Guasto, K. A. Johnson, and J. P. Gollub, *Oscillatory flows induced by microorganisms swimming in two dimensions,* Physical Review Letters **105**, 168102 (2010).

[19] D. R. Brumley, K. Y. Wan, M. Polin, and R. E. Goldstein, *Flagellar synchronization through direct hydrodynamic interactions,* eLife **3**, e02750 (2014).

[20] G. Quaranta, M.-E. Aubin-Tam, and D. Tam, *Hydrodynamics versus intracellular coupling in the synchronization of eukaryotic flagella,* Physical Review Letters **115**, 238101 (2015).

[21] G. J. Amador, D. Wei, D. Tam, and M.-E. Aubin-Tam, *Fibrous flagellar hairs of Chlamydomonas reinhardtii do not enhance swimming,* Biophysical Journal **118**, 2914 (2020).

[22] R. E. Pepper, M. Roper, S. Ryu, N. Matsumoto, M. Nagai, and H. A. Stone, *A new angle on microscopic suspension feeders near boundaries,* Biophysical journal **105**, 1796 (2013).

[23] E. Lushi, V. Kantsler, and R. E. Goldstein, *Scattering of biflagellate microswimmers from surfaces,* Physical Review E **96**, 023102 (2017).

[24] A. J. T. M. Mathijssen, D. O. Pushkin, and J. M. Yeomans, *Tracer trajectories and displacement due to a micro-swimmer near a surface,* Journal of Fluid Mechanics **773**, 498 (2015).

[25] A. Vilfan and F. Jülicher, *Hydrodynamic flow patterns and synchronization of beating cilia,* Phys. Rev. Lett. **96**, 058102 (2006).

[26] B. Guirao and J.-F. Joanny, *Spontaneous creation of macroscopic flow and metachronal waves in an array of cilia,* Biophysical Journal **92**, 1900 (2007).

[27] T. Niedermayer, B. Eckhardt, and P. Lenz, *Synchronization, phase locking, and metachronal wave formation in ciliary chains,* Chaos: An Interdisciplinary Journal of Nonlinear Science **18**, 037128 (2008).

[28] N. Uchida and R. Golestanian, *Synchronization and collective dynamics in a carpet of microfluidic rotors,* Phys. Rev. Lett. **104**, 178103 (2010).

[29] B. M. Friedrich and F. Jülicher, *Flagellar synchronization independent of hydrodynamic interactions,* Phys. Rev. Lett. **109**, 138102 (2012).

[30] M. Theers and R. G. Winkler, *Synchronization of rigid microrotors by time-dependent hydrodynamic interactions,* Phys. Rev. E **88**, 023012 (2013).

[31] V. F. Geyer, F. Jülicher, J. Howard, and B. M. Friedrich, 10.1073/pnas.1300895110.

[32] Y. Ding, J. C. Nawroth, M. J. McFall-Ngai, and E. Kanso, *Mixing and transport by ciliary carpets: a numerical study,* Journal of Fluid Mechanics **743**, 124–140 (2014).

[33] H. Guo, L. Fauci, M. Shelley, and E. Kanso, *Bistability in the synchronization of actuated microfilaments,* Journal of Fluid Mechanics **836**, 304–323 (2018).

[34] B. Chakrabarti and D. Saintillan, *Spontaneous oscillations, beating patterns, and hydrodynamics of active microfilaments,* Phys. Rev. Fluids **4**, 043102 (2019).

[35] B. Chakrabarti and D. Saintillan, *Hydrodynamic synchronization of spontaneously beating filaments,* Phys. Rev. Lett. **123**, 208101 (2019).

[36] D. Tam and A. E. Hosoi, *Optimal stroke patterns for purcell's three-link swimmer,* Phys. Rev. Lett. **98**, 068105 (2007).

[37] D. Tam and A. E. Hosoi, *Optimal feeding and swimming gaits of biflagellated organisms,* Proceedings of the National Academy of Sciences **108**, 1001 (2011).

[38] J. B. Keller and S. I. Rubinow, *Slender-body theory for slow viscous flow,* Journal of Fluid Mechanics **75**, 705 (1976).

[39] D. Saintillan, *Rheology of active fluids,* Annual Review of Fluid Mechanics **50**, 563 (2018).

[40] E. Lauga and S. Michelin, *Stresslets induced by active swimmers,* Physical review letters **117**, 148001 (2016).

[41] T. Ishikawa, M. Simmonds, and T. J. Pedley, *Hydrodynamic interaction of two swimming model micro-organisms,* Journal of Fluid Mechanics **568**, 119 (2006).

[42] D. Saintillan and M. J. Shelley, *Orientational order and instabilities in suspensions of self-locomoting rods,* Physical review letters **99**, 058102 (2007).

[43] C. M. Pooley, G. P. Alexander, and J. M. Yeomans, *Hydrodynamic interaction between two swimmers at low reynolds number,* Phys. Rev. Lett. **99**, 228103 (2007).

[44] E. M. Purcell, *Life at low reynolds number,* American Journal of Physics **45**, 3 (1977).

[45] S. Wang and A. M. Ardekani, *Unsteady swimming of small organisms,* Journal of Fluid Mechanics **702**, 286–297 (2012).

[46] K. Ishimoto, *A spherical squirming swimmer in unsteady stokes flow,* Journal of Fluid Mechanics **723**, 163–189 (2013).

[47] D. Takagi and J. R. Strickler, *Active hydrodynamic imaging of a rigid spherical particle,* Scientific Reports **10**, 2665 (2020).

[48] G. Li, A. Ostace, and A. M. Ardekani, *Hydrodynamic interaction of swimming organisms in an inertial regime,* Phys. Rev. E **94**, 053104 (2016).

[49] D. Wei, P. G. Dehnavi, M.-E. Aubin-Tam, and D. Tam, *Is the zero reynolds number approximation valid for ciliary flows?* Physical Review Letters **122**, 124502 (2019).

[50] P. G. Dehnavi, D. Wei, M.-E. Aubin-Tam, and D. Tam, *Optical tweezers-based velocimetry: a method to measure microscale unsteady flows,* to be published (2020).

[51] C. Pozrikidis, *Introduction to theoretical and computational fluid dynamics* (Oxford University Press, New York, 2011).

[52] S. Kim and S. J. Karrila, *Microhydrodynamics: Principles and Selected Applications* (Dover Publications, Mineola, NY, USA, 2013).

[53] G. S. Klindt and B. M. Friedrich, *Flagellar swimmers oscillate between pusher- and puller-type swimming,* Phys. Rev. E **92**, 063019 (2015).

[54] P. Almendarez-Rangel, B. Morales-Cruzado, E. Sarmiento-Gómez, R. Romero-Méndez, and F. G. Pérez-Gutiérrez, *A microflow velocity measurement system based on optical tweezers: A comparison using particle tracking velocimetry,* European Journal of Mechanics - B/Fluids **72**, 561 (2018).

[55] F. Gittes and C. F. Schmidt, *Interference model for back-focal-plane displacement detection in optical tweezers,* Optics Letters **23**, 7 (1998).

[56] A. Farré, F. Marsà, and M. Montes-Usategui, *Optimized back-focal-plane interferometry directly measures forces of optically trapped particles,* Opt. Express **20**, 12270 (2012).

[57] M. J. Lang, C. L. Asbury, J. W. Shaevitz, and S. M. Block, *An automated two-dimensional optical force clamp for single molecule studies,* Biophysical Journal **83**, 491 (2002).

[58] E. E. Keaveny and M. J. Shelley, *Applying a second-kind boundary integral equation for surface tractions in stokes flow,* Journal of Computational Physics **230**, 2141 (2011).

[59] J. R. Blake, *A note on the image system for a stokeslet in a no-slip boundary,* Mathematical Proceedings of the Cambridge Philosophical Society **70**, 303–310 (1971).

[60] C. Pozrikidis, *Fluid dynamics: theory, computation, and numerical simulation* (Springer, 2016).

[61] D. R. Brumley, M. Polin, T. J. Pedley, and R. E. Goldstein, *Hydrodynamic synchronization and metachronal waves on the surface of the colonial alga volvox carteri,* Phys. Rev. Lett. **109**, 268102 (2012).

[62] R. R. Bennett and R. Golestanian, *Emergent run-and-tumble behavior in a simple model of chlamydomonas with intrinsic noise,* Phys. Rev. Lett. **110**, 148102 (2013).

[63] T. J. Böddeker, S. Karpitschka, C. T. Kreis, Q. Magdelaine, and O. Bäumchen, *Dynamic force measurements on swimming Chlamydomonas cells using micropipette force sensors,* Journal of The Royal Society Interface **17**, 20190580 (2020).

[64] K. Y. Wan, K. C. Leptos, and R. E. Goldstein, *Lag, lock, sync, slip: the many phases of coupled flagella,* Journal of The Royal Society Interface **11**, 20131160 (2014).

# 4

# MASTIGONEME OF *C. reinhardtii* DOES NOT ENHANCE SWIMMING

**G. J. Amador*, D. Wei*, D. S. W. Tam, M. -E. Aubin-Tam**

*The flagella of Chlamydomonas reinhardtii possess fibrous ultrastructures of nanometer-scale thickness known as mastigonemes. These structures have been widely hypothesized to enhance flagellar thrust; however, detailed hydrodynamic analysis supporting this claim is lacking. In this study, we present a comprehensive investigation into the hydrodynamic effects of mastigonemes using a genetically modified mutant lacking the fibrous structures. Through high speed observations of freely swimming cells, we found the average and maximum swimming speeds to be unaffected by the presence of mastigonemes. In addition to swimming speeds, no significant difference was found for flagellar gait kinematics. Following our observations of swimming kinematics, we present direct measurements of the hydrodynamic forces generated by flagella with and without mastigonemes. These measurements were conducted using optical tweezers, which enabled high temporal and spatial resolution of hydrodynamic forces. Through our measurements, we found no significant difference in propulsive flows due to the presence of mastigonemes. Direct comparison between measurements and fluid mechanical modelling revealed that swimming hydrodynamics were accurately captured without including mastigonemes on the modelled swimmer's flagella. Therefore, mastigonemes do not appear to increase the flagella's effective area while swimming, as previously thought. Our results refute the longstanding claim that mastigonemes enhance flagellar thrust in C. reinhardtii, and so their function still remains enigmatic.*

This chapter have been published in [1], under a Creative Commons license 4.0.
* Equal contribution

## 4.1. INTRODUCTION

Hair-like, or fibrous, structures are ubiquitous features in biology. They are present in organisms ranging from plants to mammals, birds, and insects. Their functions range from temperature control [2] to sensing [3], cleaning [4], adhering [5], flying [6, 7], and feeding [8, 9]. A number of these functions rely on hydrodynamic interactions between the fibrous structures and the surrounding fluid. The structures provide a resistance to fluid flow, and this resistance has been exploited by various organisms–*e.g.*, to enhance the spatial resolution of chemoreception in moth antennae [10], to minimize fluid evaporation from and dust deposition to mammalian [11] and insect [12] eyes, to capture food particles in aquatic filter feeders [8], to entrain viscous nectar in pollinators [9], and to generate aerodynamic lift in flapping flight of birds [13] and insects [7]. Fluid-structure interactions thus appear to play a crucial role in the specialized function of certain fibrous structures.



In addition to multi-cellular organisms, single-celled eukaryotes have been observed to possess nanometer-scale hair-like fibres, or mastigonemes [14–18]. mastigonemes are present on the flagella, and so are also referred to as flagellar hairs [19]. Since these organisms swim via drag-based interactions between their solid flagella and fluid-filled environments using wavelike stroke patterns [20], their mastigonemes are expected to affect swimming performance through hydrodynamic interactions.

Previous studies have shown significant contributions to drag from rigid mastigonemes on the posterior flagella of the golden algae *Ochromonas* [21–23]. These algae swim using a travelling wave through their anterior flagellum. Using both theoretical [21] and numerical [23] modelling, these studies determined that mastigonemes with a particular stiffness are necessary to capture the swimming speed and direction observed experimentally [22]. If the mastigonemes are too flexible, then the models predict they would bend and their contribution to the overall drag of the flagellum would be negligible; however, above a certain stiffness, they contribute significantly. In fact, in these swimmers the hydrodynamic effect of mastigonemes is so significant that swimming direction is contrary to the expected direction for a flagellum without mastigonemes [20]. A similar thrust reversal was observed in artificial helical microswimmers with rigid mastigoneme-like structures [24].

Microscopic swimmers vary significantly in morphology and swimming gaits. In swimmers where the cell body and undulating filament are one in the same, such as *Caenorhabditis elegans*, an increase in thickness would result in a significant decrease in swimming speed [25]. However, when an undulating flagellum is pushing a cell body, a thicker flagellum can lead to an increase in swimming speed [26]. Besides undulating a posterior flagellum, another common swimming strategy observed in eukaryotic cells is the use of two anterior flagella. These two flagella beat in a synchronous pattern akin to a human swimmer's breast stroke. Such a swimming gait is exhibited by the organism used in this study, *Chlamydomonas reinhardtii* (**Fig. 4.1**a). The flagella of *C. reinhardtii* cells were inherited from the common ancestor of land plants and animals; as such, this organism has long served as the model organism used for studies of the structure, assembly, and function of eukaryotic flagella [27].

The mastigonemes of *C. reinhardtii* are of the fibrous type, as opposed to the tubular mastigonemes found in algae *Ochromonas* [19]. While tubular mastigonemes are thicker

and their hydrodynamics have been studied extensively [21, 22], studies into the hydrodynamics of fibrous mastigonemes are lacking, despite the fact that their bearer, *C. reinhardtii*, has drawn much attention and its swimming kinematics are well characterized [28–34].

Following their initial observation and characterization [16], the mastigonemes of *C. reinhardtii* (shown in **Fig. 4.1**b) were widely hypothesized to enhance hydrodynamic performance of flagella by increasing the flagella's effective area [19, 35] because of their long length and high density. However, experimental evidence supporting their hydrodynamic function has been limited to the observation of a decrease in swimming speed of $20-30\%$ for *C. reinhardtii* cells treated with mAb-MAST1 [36], a monoclonal antibody that was reported to trigger the loss of mastigonemes. Since this is the only experimental observation on the hydrodynamics of fibrous mastigonemes, and other information such as their effects on gait kinematics and drag force are lacking, we were motivated to gather more detailed knowledge in this regard. We thus conducted our research to resolve the function of these ultrastructures at the single cell level.



In the present study, we used a genetically modified mutant that possesses no mastigonemes [37], and therefore avoid using an antibody to remove mastigonemes. This mutant, referred to as *mstg*, is generated via insertional mutagenesis, where the mutation is inserted into the gene predicted to code for a mastigoneme protein (Genbank entry AF508983, MST1) [38]. The parent strain used for mutation is *cw15*, a cell wall-deficient strain of the wildtype *C. reinhardtii*. While *cw15* lacks a cell wall [39], it still possesses mastigonemes on its flagella. For completeness, we also included the extensively characterized wildtype strain cc-125 mt+ as another control group, and denote it as *cc125*. Through a thorough comparative study in the cells' free-swimming dynamics, flagellar kinematics, and flagellar hydrodynamics across the three strains (*mstg*, *cw15*, and *cc125*), we investigate the potential hydrodynamic effects of mastigonemes.

We first assessed the presence of mastigonemes in the flagella of the three strains of *C. reinhardtii* with transmission electron microscopy (TEM). Through these observations, we confirmed the presence of mastigonemes in *cc125* and *cw15*, and their absence in the *mstg* mutant. We then analyzed the trajectories of freely swimming cells. In these observations we compared the swimming speeds, beating frequencies, and turning rates to determine how mastigonemes affect locomotory performance and kinematics. Then, we compared the flagellar gait kinematics with high speed videography of captured single cells, to determine how they are affected by the removal of the cell wall or mastigonemes. Next, we performed velocimetry measurements using optical tweezers-based flow velocimetry (OTV) following the protocol in [34]. The OTV technique measures the displacement of an optically-trapped particle within the laser, from which fluid force and velocity are inferred directly. Our technique provides high temporal resolution to characterize the hydrodynamic effects of the mastigonemes near a captured algal cell. Finally, following our measurements, we compared our experimental results to numerical simulations that solve Stokes equations around a beating cell assuming smooth (hairless) flagella.

## 4.2. MATERIALS AND METHODS

### 4.2.1. CELLS AND CELL CULTURE

Three strains of *Chlamydomonas reinhardtii* were used in experiments: wildtype *cc125* (cc-125 mt+), cell wall-deficient *cw15* (cc-4453 mt-), and cell wall- and mastigoneme-deficient *mstg*. The *mstg* mutant, LMJ.RY0402.136134, was generated by the Chlamydomonas Library Project (CLiP) using *cw15* as the parent strain [37]. The *cw15* and *mstg* strains obtained from the *Chlamydomonas* Resource Center were propagated in the lab conditions over several months for acclimation to temperature and humidity.

All three strains were grown in identical conditions following established protocols, see **Ref.** [40]. Specifically, they were cultured in Tris-minimal medium (pH = 7.0) with sterile air bubbling. The cultures were subjected to light:dark (14 : 10 h) cycles with light intensity of 230 $\mu$E m$^{-2}$ s$^{-1}$. They were harvested on the fourth day after inoculating the liquid culture, when reaching a density of $\sim 2 \times 10^5$ cells ml$^{-1}$, and then diluted in fresh Tris-minimal medium (pH = 7.0).



### 4.2.2. TRANSMISSION ELECTRON MICROSCOPY

Transmission electron microscopy (TEM) observations were done with a JEM-1400 (JEOL USA). Liquid cultures of *cc125*, *cw15*, and *mstg* were simultaneously harvested and washed with fresh Tris-minimal medium. Thereafter, we centrifuged the cells (600 g's for 5 min) twice to increase the cell concentration.

Immediately after the concentrated cell suspensions were obtained, a droplet was placed on a carbon-coated copper TEM grid for a duration of 2 minutes. Afterwards, the excess cell suspension was removed by blotting with a filter paper and the grids were stained by immersion in 2% uranium acetate during 1 minute. We only recorded the cells with clearly attached flagella and with no sign of cell lysis.

### 4.2.3. HIGH SPEED IMAGING AND LIGHT MICROSCOPY

For our observations of freely swimming and captured cells, we used an inverted microscope (Nikon Eclipse Ti-U) with a 60× water immersion objective (Nikon CFI Plan Apo VC 60X NA = 1.20). The high speed videography was conducted using a sCMOS high speed camera (PCO.edge 5.5). We obtained a spatial resolution of 0.1 µm px$^{-1}$, and temporal resolution of 301 Hz and 699 Hz for observations of freely swimming and captured cells, respectively.

All cells were observed in conditions similar to those in [34, 40]. Cells suspended in Tris-minimal medium were placed within a custom flow chamber (20 mm wide by 2 mm high). The chamber was sealed using silicone oil to ensure no background flows were present due to fluid evaporation. Before every experiment, suspended particles or cell debris were observed to confirm the absence of background flows. The flow chamber was fixed onto a piezoelectric stage (Nano-Drive, Mad City Labs) integrated on the inverted microscope. For the free swimming experiments, the cells were then observed directly using high speed videography.

For the flagellar kinematics and optical tweezers-based velocimetry (OTV) experiments, the cells were held by micro-pipettes made of borosilicate glass. The micropipette was mounted onto a micro-manipulator (SYS-HS6, WPI).

### 4.2.4. ANALYSIS OF FREELY SWIMMING CELLS

Frame rates of the videography for free swimming observations were set at 301 Hz, which were sufficient to detect the cells' motion and resolve their flagella beating at $f_0 \approx 50$ Hz. The focal plane was placed at a height of 100 µm above the bottom of the flow chambers (to match our OTV measurements), and swimming tracks within ± ~30 µm of the focal plane with minimal visual variation in the vertical axis were collected.

Our results consisted of $N = 51$, 53, and 52 tracks of the *cc125*, *cw15*, and *mstg* strains, respectively, with a mean track duration of 0.9 s or 45 beat cycles. From the videos, centres of the cell body were tracked, as shown in **Fig. 4.2**a.

We calculated the mean and the maximum advancing speed for each track. Instantaneous velocity for each track (inset **Fig. 4.2**a) was used to find the maximum advancing speed $U_{max}$. $U_{max}$ was the median of the peak velocities, as highlighted by the triangles in the inset of **Fig. 4.2**a.

For the mean speed, we discarded the oscillatory part of the track, which corresponds to the back-and-forth component of motion, by applying a low-pass filter (< 10 Hz), and calculated the mean speed as the arc length of the resulting trajectory divided by the track duration.

To find the beating frequency $f_0$, we used two methods involving the Fast Fourier Transformation (FFT) function in MATLAB. The first method has been used in previous studies to resolve the beating frequency of both single cells and populations of cells [41–44]. This method uses visual vibration of the cell body in the video as input. Practically, sums of pixel value of each frame were first used to construct a time series, which records the bodily vibrations directly resulting from flagellar beating, and $f_0$ was resolved from the FFT of the time series. To highlight the informative part, we applied a tracking mask that blacked out all but a circular region of radius ~8 µm around the cell centre, and kept the spectrum higher than 10 Hz for frequency analysis. The second method used FFT of the tracks of the cell centres (red curve in **Fig. 4.2**a). In the frequency domain, the peaks represented the rate at which the cell body proceeded back and forth along the track. For each track, the sharpest peak between the two methods was reported as $f_0$ (**Fig. 4.2**c). The two methods made use of different input information, namely, the flagellar beating-induced fluctuation in the cell's shading and the flagellar beating-induced locomotion. When an observed cell is slightly out of focus or the net forward motion is not substantial, then the FFT of the image results in a sharper peak of $f_0$. On the other hand, when the cell is in focus and has substantial forward motion, then the FFT of the track results in a sharper peak. However, results of the two methods corroborate each other well.

The turning rate was calculated using the cells' heading direction $\theta$, depicted by the white arrows in **Fig. 4.2**a. $\theta$ was found from the smoothed trajectory used for the mean speed calculations (using the < 10 Hz low-pass filter). The smoothed trajectory did not contain the cells' back and forth motion. The turning rate was then calculated as the average value of the absolute rate of change of the cells' heading direction or $|\overline{\frac{d\theta}{dt}}|$.

### 4.2.5. OPTICAL TWEEZERS-BASED VELOCIMETRY

In order to measure the flow fields around beating cells, we used an optical tweezers-based velocimetry (OTV) method following [34]. This method measures the hydrodynamic force on an optically-trapped bead in the vicinity of a beating cell. The optical

tweezers used in the study are similar to those in [45]. Namely, a high-powered laser (1064 nm wavelength) was focused through a water immersion objective (Nikon CFI Plan Apo VC 60X NA = 1.20) to generate a trapping force $\mathbf{F} = -k\Delta\mathbf{x}$, where $\Delta\mathbf{x}$ is the bead displacement from the centre of the trapping laser and $k$ is the trap stiffness. The bead displacement $\Delta\mathbf{x}$ was measured at a sampling frequency of 10 kHz using back focal plane interferometry. The beads had radii of either $a = 1$ or 2.5 µm, with trap stiffness values of $k = 12 - 50$ pN µm $^{-1}$.

The flow velocity $\mathbf{u}(t) = (u, v)$ at the location of the trapped bead (**Fig. 4.4**a) was determined from the measured bead displacement $\Delta\mathbf{x}$ following the Boussinesq-Basset-Oseen (BBO) equation. Since the particle Reynolds number $\mathrm{Re}_a = \frac{\rho a|\mathbf{u}|}{\mu} \approx 10^{-5} - 10^{-4}$ is low and inertia, added mass, and Basset forces are negligible [46], the BBO equation can be reduced to a first order equation where the trapping force $\mathbf{F}$ and hydrodynamic drag are balanced, or $\Delta\dot{\mathbf{x}} + \frac{k}{\zeta}\Delta\mathbf{x} = \mathbf{u}(t)$, where $\zeta = 6\pi\mu a$. Similar methods have been used in previous studies to measure flows in microfluidic devices [47–50].



### 4.2.6. NUMERICAL SIMULATIONS

In order to model the flow fields around individual beating cells, we solved the 3D Stokes equations using a hybrid boundary element method (BEM) and slender-body approach, similar to [34, 46]. The Stokes equations are $\nabla \cdot \mathbf{u} = 0$ and $-\nabla p + \mu\nabla^2\mathbf{u} = 0$, where $p$ is the pressure field. These equations have been found to accurately depict the flow dynamics close to the cell ($y < 0.2\delta$, where $\delta = \sqrt{\nu/f_0}$ and $\nu$ is the kinematic viscosity of water) [34], and so we conducted our simulations within this range.

To capture the fluid-structure interactions for the cell body and glass micro-pipette, we represented them with a completed double layer boundary integral equation [51, 52]. The singularities of the completion flow were distributed along the centreline of the micro-pipette. The flagella were represented using slender-body theory with 26 discrete points along each of the flagella's centreline [53]. The time dependent motion of each of the 26 discrete points on a beating flagellum were tracked from high speed videos (≈ 700 Hz), as discussed in **Sec. 4.2.3**. We then obtained the simulated flow field $\mathbf{u_s}(t) = (u_s, v_s)$, which we compared with the OTV measurements $\mathbf{u}(t) = (u, v)$.

## 4.3. RESULTS AND DISCUSSION

### 4.3.1. TRANSMISSION ELECTRON MICROSCOPY

The *mstg* mutant used in this study carries a mutation in the MST1 gene coding for a mastigoneme-like flagellar protein. Transmission electron microscope (TEM) was used to confirm the presence of mastigonemes in the *cc125* and *cw15* cells, and their lack in *mstg* cells. **Fig. 4.1**b-d show representative TEM images of flagella from *cc125*, *cw15*, and *mstg* cells, respectively. From these images we measured the flagella length $L = 12.0 \pm 1.7$ µm and flagella radius $r = 0.23 \pm 0.02$ µm. The flagella from *cc125* and *cw15* exhibit two rows of mastigonemes and the *mstg* flagella appear smooth without any mastigonemes. The mastigonemes on the *cc125* and *cw15* cells appear to be $l_m = 850 \pm 97$ nm in length and $d_m = 16 \pm 3$ nm in diameter, in agreement with previous observations [19], and with densities of $10.1 \pm 0.8$ mastigonemes per µm. These measured values may not accurately represent the physical dimensions of the mastigonemes since the delicate structures

may be affected by the staining procedure.

We observed mastigonenemes in 27 out of 28 *cc125* cells and 20 out of 21 *cw15* cells. In contrast, we found mastigonemes for none of the 22 *mstg* cells observed. Moreover, after ~10 times of slant propagation over 18 months, during which the experiments were conducted, we repeated the comparison to confirm whether the genetic mutation was stable. Consistently, all *cc125* ($N = 6$) and *cw15* cells ($N = 6$) showed mastigonemes, while none of the *mstg* cells ($N = 6$) did. Therefore, we conclude that the mutation of the MST1 gene was effective and stable.

Using the TEM measurements, we can estimate the possible contribution of these mastigonemes to swimming performance. Following [21, 23], one can estimate the total drag force on a flagellum, to leading order, as the linear summation of two parts: the drag of the flagellum without mastigonemes and the drag of each mastigoneme. Since the expected drag coefficients depend linearly on length and weakly on radius, hydrodynamic effects of radius are neglected and only those of the total lengths are compared. The mastigonemes are relatively long ($l_m \sim 0.8$ µm) and are present at high densities (~ 10 per µm). Their total combined length is an order of magnitude longer than the flagellum (130 µm compared to 12 µm). Therefore, if they would not deflect, we expect free swimming speed to be significantly affected by their presence [21–23].

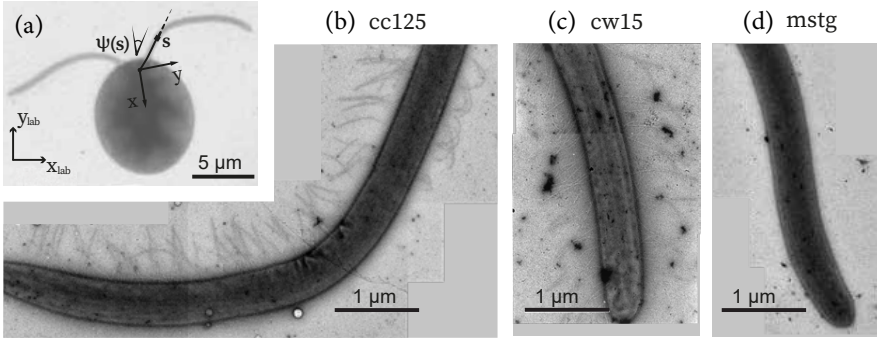


Figure 4.1: **Microscopy of flagella with and without mastigonemes** (a) Transmission electron microscope (TEM) image of wildtype (*cc125*) *Chlamydomonas reinhardtii*. (b-d) Representative TEM images of flagella from (b) *cc125*, (c) cell wall-deficient strain (*cw15*), and (d) cell wall-deficient strain without mastigonemes (*mstg*). The *cc125* and *cw15* cells clearly exhibit mastigonemes, while the *mstg* cells do not.

### 4.3.2. OBSERVATIONS OF FREELY SWIMMING CELLS

After confirmation of the lack of mastigonemes in *mstg* and the presence of mastigonemes in *cc125* and *cw15*, we compared the free swimming speed, beating frequencies, and turning rates of the three strains. The algae were observed in flow chambers 20 mm wide and 2 mm in height. The observed cells swam 100 µm above the closest wall in order to minimize any near-field wall effects.

Our observations were made using high speed videography with spatial resolution of

0.1 µm px$^{-1}$. The videos were taken at a frame rate of 301 Hz, well above the minimum sampling rate required to resolve their flagella beating at frequencies $f_0 \approx 50$ Hz. An image sequence from a typical observation is shown in **Fig. 4.2**a. The average duration of each acquisition was 0.9 s.

The red curve in **Fig. 4.2**a depicts the trajectory of the cell body's centroid and the inset shows a typical plot of the instantaneous swimming speed as a function of time. From the trajectory and instantaneous velocity we extract the mean swimming speed, beating frequency $f_0$, and maximum swimming speed $U_{max}$. The white arrows in **Fig. 4.2**a represent the heading direction $\theta$ of the swimming cell within the imaging plane, which is used to compute the turning rate.



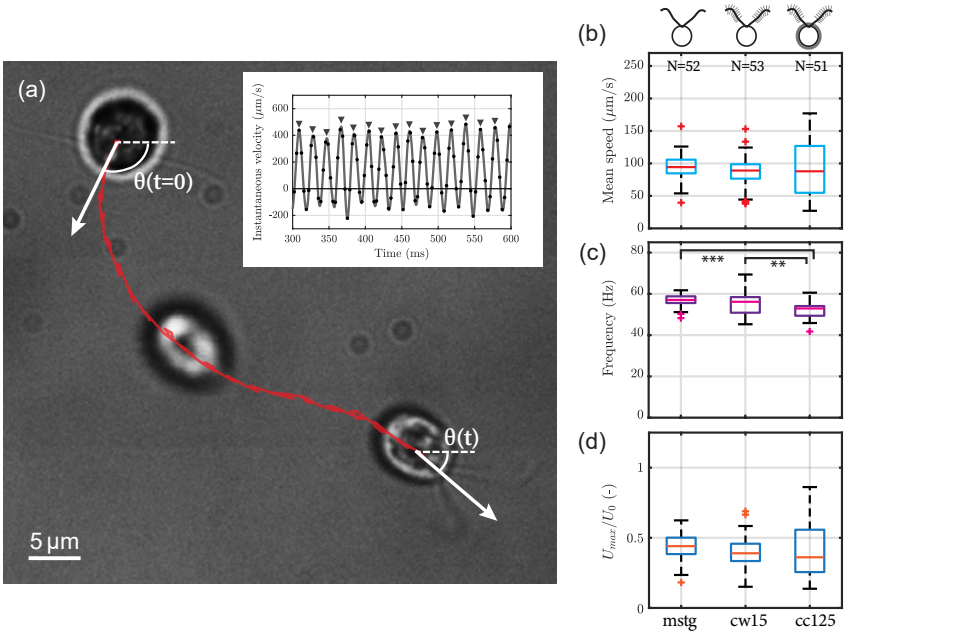


Figure 4.2: **Kinematics of freely swimming cells** (a) Overlaid image sequence from a typical observation. The time interval between the overlaid snapshots is 200 milliseconds. The red line represents the position of the centre of the tracked cell. The white arrows depict the heading angle $\theta$ of the cell. The inset shows the instantaneous velocity for the cell in the image with the maximum velocities highlighted by the triangles. (b-d) Comparison of (b) mean swimming speed, (c) beating frequency $f_0$, and (d) maximum swimming speed $U_{max}$ for *mstg*, *cw15*, and *cc125* cells from left to right, respectively. (d) $U_{max}$ represents the median of the peak velocities depicted in the inset of (a) and is normalized by $U_0 = Lf_0$, where $L$ is flagella length. In (c) $**$ represents $p < 0.01$ and $***$ represents $p < 0.001$. The distributions in (b-d) are compared using the Kruskal-Wallis One-Way ANOVA statistical test. For (b-d), and all distributions in the subsequent figures, the red lines represent the medians and the bottom and top of the boxes the 25th and 75th interquartiles, respectively. The whiskers represent data between $q_1 - 1.5(q_3 - q_1)$ to $q_3 + 1.5(q_3 - q_1)$, where $q_1$ and $q_3$ are the 25th and 75th interquartiles, respectively. Any points outside of this range are marked as red crosses and considered outliers.

The swimming trajectories of the cells were helical, as reported before [54, 55]. Our measurements were 2D projections of this 3D motion, and this is the typical method-

ology for velocity measurements adopted in the literature [56]. This approach and its reliability are detailed in the Supplementary Information.

**Fig. 4.2**b shows the average swimming speed distributions for *mstg*, *cw15*, and *cc125* cells, from left to right, respectively. The distributions in mean speeds are not statistically different between the different cell strains (Kruskal-Wallis One-Way ANOVA, $p > 0.05$). Our observations differ from those reported for cells with mastigonemes removed by an antibody, where a decrease of $20-30\%$ was observed after their removal [36]. The mean swimming speed of the wildtype cells measured by Nakamura *et al.* was $137.3 \pm 16.0$ µm/s [36], while ours was $90.2 \pm 39.0$ µm/s (average ± standard deviation). While our observed swimming speeds are a bit lower, both observations agree with those previously reported for cells swimming in 3D ($110 \pm 12$ µm/s [40], $136 \pm 12$ µm/s [57], and ~130 µm/s [58, 59]).

The beating frequency $f_0$ distributions are represented in **Fig. 4.2**c. We find that the cell wall-deficient strains (both *mstg* and *cw15*) exhibit significantly higher beating frequencies ($f_0 = 57.0 \pm 2.9$ Hz and $55.2 \pm 5.0$ Hz, respectively) when compared to *cc125* cells ($f_0 = 52.2 \pm 4.1$ Hz). The higher frequencies may be a result of the lack of cell wall. The two flagella protrude from the cell wall, and possibly make contact with it while beating. It is possible that either the mechanical confinement or coupling provided by the cell wall influences beating frequency, since mechanical coupling between flagella is known to affect their synchronized beating frequency [40, 60].

In **Fig. 4.2**d, we present the distributions of the maximum speed $U_{max}$, scaled with the characteristic velocity $U_0 = Lf_0$ to account for the variability in beating frequency and flagella length. The maximum speed $U_{max}$ was computed, for each track, as the median value of the peak velocities of each beat cycle (see inset of **Fig. 4.2**a). We did not observe any significant differences in $U_{max}/U_0$ between the strains (Kruskal-Wallis One-Way ANOVA, $p > 0.05$). Therefore, even though the *mstg* and *cw15* strains beat faster than *cc125*, they were still propelling themselves at the same maximum speed during their power stroke relative to their flagella beating speed $U_0$. Previous observations of $U_{max} \sim 320$ µm/s [59] for *cc125* are within the range of our observations of $U_{max} = 254.3 \pm 110.1$ µm/s.

Incidentally, **Fig. 4.8** shows the turning rate distributions for *mstg*, *cw15*, and *cc125* cells and an image sequence of a representative turning event with a large turning rate. The turning rates were determined from the time derivative of the heading direction $\theta$ or $\frac{d\theta}{dt}$. This derivative was computed for every time step, the absolute value of the derivative is taken, and then an average value for the duration of each acquisition was reported as the turning rate, or $|\overline{\frac{d\theta}{dt}}|$. We found that *mstg* had a significantly higher turning rate compared to *cw15* and *cc125*. However, upon close inspection of the recordings, we see the increased turning to be a direct result of a decrease in symmetry between the beating of the two flagella, either because of slipping (Movie S1 online), where the flagella briefly lose their synchrony, or because of an asymmetry in the flagellar kinematics (Movie S2 online), where one flagellum swipes a larger area than the other.

From our observations of freely swimming cells, we find that mastigonemes do not enhance swimming performance. We find no significant differences in either mean or maximum forward swimming speeds between cells with or without mastigonemes. Our results differ from the observations of Nakamura *et al.* [36], which used a monoclonal an-

tibody to remove the mastigonemes and observed a decrease of the swimming velocity for the cells without mastigonemes.

### 4.3.3. COMPARISON OF FLAGELLAR WAVEFORM

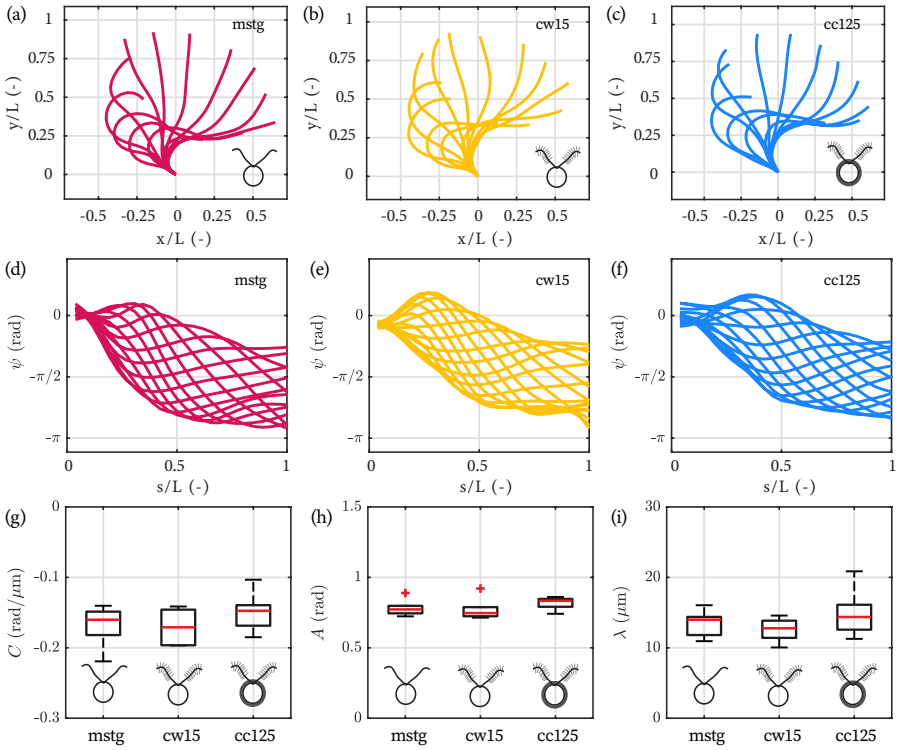


Figure 4.3: **Flagellar gait kinematics.** (a-c) Representative flagellar waveforms with respect to the cell's frame of reference ($x$, $y$), defined in **Fig. 4.1**a, for (a) *mstg*, (b) *cw15*, and (c) *cc125* cells. (d-f) Representative flagellar waveforms with respect to the local frame of reference ($s$, $\psi$), defined in **Fig. 4.1**a, for (d) *mstg*, (e) *cw15*, and (f) *cc125* cells. Here, $\psi$ is the local tangent angle and $s$ the arc length along the centreline of the flagellum. The flagellum length $L$ is used to normalize spatial coordinates $x$, $y$, and $s$. (g-i) Comparison of fitting parameters for flagellar waveforms of *mstg*, *cw15*, and *cc125* cells from left to right, respectively. The parameters are (g) average curvature $C$, (h) traveling wave amplitude $A$, and (i) wavelength $\lambda$. The sample size for (g-i) is $N = 6$ for each strain.

The swimming velocity of flagellated organisms is determined by both the hydrodynamic drag on the flagella and the kinematics of the flagellar deformation. Both need to be fully characterized in order to assess the hydrodynamic effect of mastigonemes.

Therefore, we proceed by analyzing the flagellar gait kinematics to determine whether strain mutations and their subsequent morphological differences affect beating patterns. High speed videos of flagellar beating of cells held by a micro-pipette were recorded at 700 Hz. Typical flagellar waveforms are shown with respect to the cell's frame of reference ($x$, $y$) in **Fig. 4.3**a-c. The cell's frame of reference is defined schematically in the inset of **Fig. 4.1**a. In order to quantify gait kinematics, we parameterized the flagel-

lar waveform of cells from each strain following the method used in [61] and similar to [62, 63].

This parameterization divides the motion of a flagellum into a static and dynamic component, where the flagellar motion is represented as a circular arc (static) and a sinusoidal traveling wave (dynamic). For the analysis, we measured the local angle $\psi$ tangent to the flagellum for 26 discrete points along the flagellar arc length $s$ for each recorded frame at time $t$, which resulted in a relationship for $\psi(s,t)$. The parameters $s$ and $\psi$ are defined in **Fig. 4.1**a. Typical flagellar waveforms are shown with respect to the local frame of reference $(s, \psi)$ in **Fig. 4.3**d-f. The static component of the motion is $\psi_1(s) = Cs$, where $C$ represents the mean curvature of the flagellum. The dynamic component of the motion is $\psi_2(s,t) = A\sin(2\pi(f_0 t + s/\lambda))$, where $A$ is the amplitude of the traveling wave, $f_0$ the beating frequency, and $\lambda$ the wavelength.

Combining the static $\psi_1(s)$ and dynamic $\psi_2(s,t)$ components yields an expression for the tangent angle along the flagellar length, or $\psi(s,t) = Cs + A\sin(2\pi(f_0 t + s/\lambda))$. The parameters $C$, $A$, and $\lambda$ were extracted for each flagellum of $N = 6$ cells per strain. For all three strains, we compared the mean curvature $C$ (**Fig. 4.3**g), traveling wave amplitude $A$ (**Fig. 4.3**h), and wavelength $\lambda$ (**Fig. 4.3**i). In each panel, *mstg*, *cw15*, and *cc125* are displayed respectively from left to right. For all three waveform parameters, we find no statistical differences between the strains (Kruskal-Wallis One-Way ANOVA, $p > 0.05$).

The mean curvature is $C = -0.17 \pm 0.03$, $-0.17 \pm 0.02$, and $-0.15 \pm 0.02$ rad µm $^{-1}$ (average ± standard deviation) for *mstg*, *cw15*, and *cc125* cells, respectively. The values of $C$ for *cc125* cells are in agreement with those of previous studies ($-0.17 \pm 0.005$ rad µm $^{-1}$ [61, 64] and $-0.21 \pm 0.07$ rad µm $^{-1}$ [63]). The traveling wave amplitude is $A = 0.78 \pm 0.05$, $0.77 \pm 0.07$, and $0.82 \pm 0.04$ rad (average ± standard deviation) for *mstg*, *cw15*, and *cc125* cells, respectively. The values of $A$ for *cc125* are also in agreement with those of previous studies ($1.08 \pm 0.09$ rad [61, 64] and ~$0.89 \pm 0.06$ rad [63]). Finally, the wavelength is $\lambda = 13.5 \pm 1.7$, $12.6 \pm 1.5$, and $14.9 \pm 3.1$ µm (average ± standard deviation) for *mstg*, *cw15*, and *cc125* cells, respectively. Values of $\lambda$ for *cc125* cells are again in agreement with previous studies ($15.1 \pm 2.0$ µm [61, 64]).

In conclusion, because there are no significant differences for all three parameters that characterize the flagellar waveform, the flagellar gait kinematics and deformations appear unaffected by the presence of mastigonemes.

### 4.3.4. OPTICAL TWEEZERS-BASED VELOCIMETRY

After having observed no significant differences in the free swimming characteristics or flagellar kinematics of cells with and without mastigonemes, we directly probed the hydrodynamics of captured cells using optical tweezers-based velocimetry (OTV) [34]. This technique allowed us to locally measure the flow field generated by beating flagella with and without mastigonemes.

A schematic depicting our OTV experiments is shown in **Fig. 4.4**a, with a picture from our experiments in the inset at the top right. A polystyrene bead of diameter 2 or 5 µm was trapped in the vicinity of a flagellum. We measured the local 2D flow field $\mathbf{u}(t) = (u, v)$, $u$ (axial) and $v$ (lateral), generated by the cell at the location of the bead. The flow field was recorded at increasing lateral distances from the cell by moving the bead along the $y$-axis. This procedure was previously implemented to study the flow

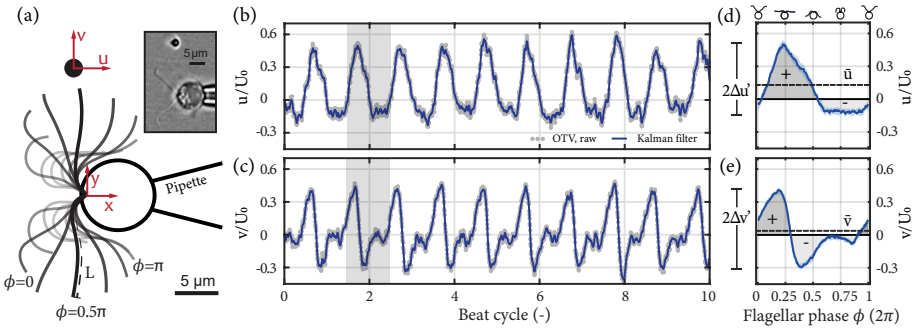


Figure 4.4: **Optical tweezers-based velocimetry (OTV).** (a) Schematic of the OTV measurements with an algal cell captured by a micro-pipette and optically-trapped bead to measure flow velocities $u$ and $v$. Inset shows a light microscope image from a typical experiment. Scale bars represent 5 µm. (b-c) Periodic signals of (b) axial $u$ and (c) lateral $v$ flow velocities as a function of beat cycle. The gray points are raw OTV data and blue solid curve is data filtered with a Kalman filter. A typical beat cycle is shaded; it begins with the most forward-reaching flagellar shapes, defined as flagellar phase $\phi = 0$, shown in the inset of (a).The median cycle is constructed based on ~50 cycles and shown in (d-e). (d-e) Flow velocities (d) $u$ and (e) $v$ over one average beat cycle. In (d), the dark gray "+" represent the power stroke, when propulsive flows are generated. The light gray "−" represent the recovery stroke, when the flagella move opposite to the swimming direction. In (e), the + and −, together with their shadings, mark respectively the propulsion outwards and inwards in the cell's lateral direction. The flow amplitudes $\Delta u'$ and $\Delta v'$ are depicted on the left. The dashed lines represent the average velocities $\overline{u}$ and $\overline{v}$. The data shown in (b-e) is from a *cc125* cell.

around *cc125* cells [34]. We also defined the flagellar phase $\phi$ to represent the flagellar shapes during a beat cycle. The most forward reaching shape, as shown in the inset of **Fig. 4.4**a, was set as the beginning of a cycle ($\phi = 0$). Typically, the power stroke ends at $\phi \approx \pi$, shown in **Fig. 4.4**a.

The periodic signal of axial $u$ and lateral $v$ velocities were recorded over successive flagellar beat cycles with a high temporal resolution of 10 kHz, see **Fig. 4.4**b-c. To compare the hydrodynamics of individual cells across strains, we reconstructed an average beat cycle for each cell and extracted the amplitude of the oscillations and the time-averaged flow velocity generated in the axial ($\Delta u'$ and $\overline{u}$, respectively) and lateral directions ($\Delta v'$ and $\overline{v}$, respectively) for each individual cell.

**Fig. 4.4**d-e represent the flow velocity of a typical beat cycle, constructed as the median over 50 cycles. The asymmetry in the power-recovery stroke is clearly visible in the axial flow $u$, with the power stroke generating a strong positive flow for the first half of the cycle ($\phi < \pi$), and the recovery stroke subsequently generating a weaker negative flow. The flow amplitudes ($\Delta u'$ and $\Delta v'$) and average flows ($\overline{u}$ and $\overline{v}$) are extracted from the typical beat cycle as represented on **Fig. 4.4**d-e. Schematics representing the shapes at each flagellar phase $\phi$ are displayed in the upper horizontal axis of **Fig. 4.4**d.

We use the flow parameters $\overline{u}$, $\overline{v}$, $\Delta u'$, and $\Delta v'$ to investigate the flow field around beating cells and compare between the three strains to determine the hydrodynamic effects of mastigonemes. The distributions of average flows and amplitude of flow oscillations are reported in **Fig. 4.5**. The distance $y$ from the cell is scaled by the diffusive length

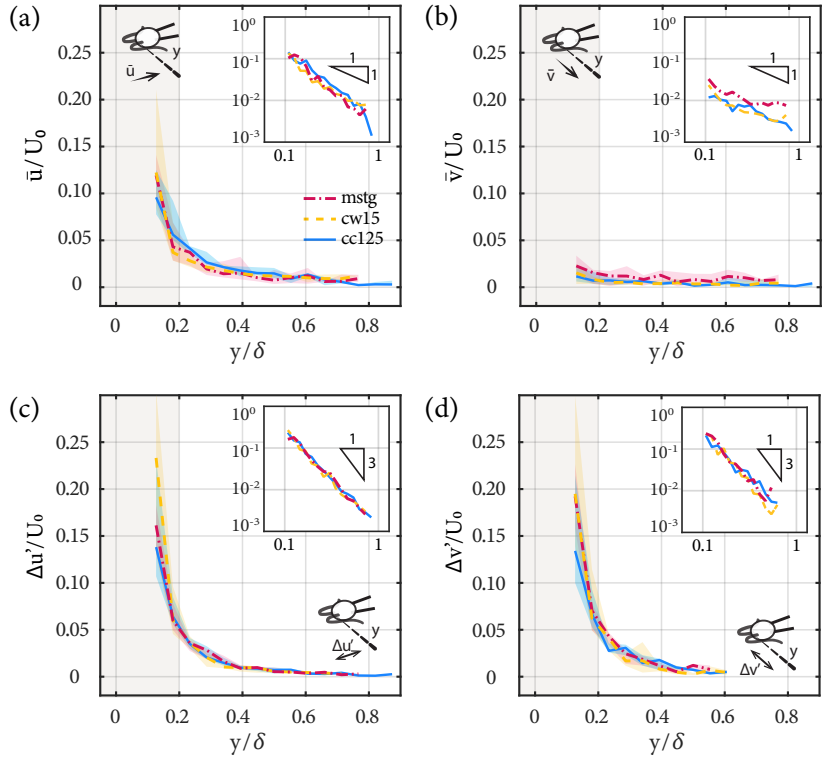


Figure 4.5: **Hydrodynamics of beating flagella from optical tweezers-based velocimetry (OTV).** (a-b) Relationship between average (a) axial $\overline{u}$ and (b) lateral $\overline{v}$ flows and distance $y$ from the mid-plane of the cell. (c-d) Relationship between flow amplitudes in (c) axial $\Delta u'$ and (d) lateral $\Delta v'$ directions and distance $y$. The red dash-dot line is for *mstg* ($N = 9$), the yellow dashed line for *cw15* ($N = 11$), and the solid blue line for *cc125* ($N = 14$) cells. The lines represent the median, while the shaded region the interquartile. The distance $y$ is normalized by $\delta = \sqrt{\nu/f_0}$, where $\nu$ is the kinematic viscosity of water. Insets show data plotted in log-log scale to highlight the rates of spatial decay for the flows.

scale $\delta = \sqrt{\nu/f_0}$, where $\nu$ is the kinematic viscosity of water. The insets present the same data in log-log scale, and highlight the rate of spatial decay of the velocity field. The beating flagella generate a flow, which is significantly stronger in the axial $x$-direction, **Fig. 4.5**a, compared with the lateral $y$-direction, **Fig. 4.5**b. The magnitude of the average flow decays in $\sim 1/y$ as expected from the stokeslet flow (**Fig. 4.5**a-b). The amplitude of the flow oscillations $\Delta u'$ and $\Delta v'$ is large in the vicinity of the flagella but decays in $\sim 1/y^3$, faster than the average flow [34], see **Fig. 4.5**c-d.

The spatial distributions of average velocity and amplitude of oscillation reveal no significant differences in the flow fields generated by the three different strains, see **Fig. 4.5**. The measurements were performed for each strain for different cells with $N = 9-14$. The variability of the measurements for a given strain is represented by the interquartile range in **Fig. 4.5**, and is comparable to the variability observed in swimming velocities,

see **Fig. 4.2**. The differences in the flow fields generated by *mstg*, *cw15*, and *cc125* are within the variability observed within a given strain. Overall, experimental measurements do not evidence an increase in flow generation due to the presence of mastigonemes.

### 4.3.5. COMPARISONS WITH HYDRODYNAMIC MODELLING

To directly quantify the hydrodynamic effect of mastigonemes, we performed computational fluid dynamic simulations to compute the flow field close to the flagella and directly compared them with our time resolved flow measurements. To account for individual cell to cell variations between our experiments, we first tracked the flagellar shapes for each recording, see **Fig. 4.3**, and used the deformations as boundary conditions for the simulation. The flagellar kinematics are tracked using high-speed videography (~700 Hz). The flow is simulated by solving Stokes equations, which have been shown previously to accurately model fluid flows in the near-field, for $y < 0.2\delta$ [34]. Our hydrodynamic model assumes the flagella to be cylindrical, and so without mastigonemes; therefore, agreement with measurements from *mstg* and disagreement with measurements from *cw15* and *cc125* would reveal the hydrodynamic contributions from mastigonemes.

**Fig. 4.6**a-c show the relationship between flow velocity, $u$ (left) and $v$ (right), and beat cycle for (a) *mstg*, (b) *cw15*, and (c) *cc125* cells. The red curves represent our simulations using a hybrid boundary element method (BEM) and slender-body approach to solve Stokes equations around beating cells [34, 46, 52, 53]. Movie S3 shows a representative flagellar stroke from experiments, followed by the flow field predicted from the simulations.

Since our simulations assume that the flagella do not have mastigonemes, we begin by comparing with experiments for *mstg*. From **Fig. 4.6**a, we observe good agreement between measurements and BEM. Quantitatively, we compute the mean absolute error (MAE), which is the average deviation of the instantaneous flow velocity between BEM and experiments, or $\mathrm{MAE}_{\mathbf{u}} = \frac{\sum_{i=1}^{n} |\mathbf{u_{s,i}} - \mathbf{u_i}|}{n}$, where $\mathbf{u_{s,i}}$ is the instantaneous velocity predicted by simulation and $n$ is the total number of instantaneous points measured/simulated. In **Fig. 4.6**d-e, we show the error of our simulations in the axial and lateral direction for *mstg* normalized by the flow amplitude, or (d) $\mathrm{MAE}_u/2\Delta u'$ and (e) $\mathrm{MAE}_v/2\Delta v'$, respectively. The error values are around 0.15. Therefore, our simulations accurately capture the flow field generated by beating flagella.

After validation of our simulations with the mastigoneme-less mutant *mstg*, we proceed by comparing simulations and experiments for *cw15* and *cc125* cells. Similar to *mstg*, we find good agreement between experiments and BEM in **Fig. 4.6**b-c, which are confirmed quantitatively in **Fig. 4.6**d-e. Moreover, we find no statistical differences between errors in simulation predictions across the three strains (Kruskal-Wallis One-Way ANOVA, $p > 0.05$).

If the mastigonemes contributed to the hydrodynamics, we would have expected better agreement between measurements and simulations for the *mstg* cells since our modelled flagella are smooth. Instead, we find no differences between strains, and, in all cases, the observed hydrodynamics around beating cells are well captured by representing the flagella as smooth, *i.e.*, neglecting the mastigonemes.

This is unlike what we expect if mastigonemes are rigid and dense and increase the effective width of a flagellum. By direct computation using BEM, we solve Stokes equations around slender flagella of different cross-sectional geometries and obtain their drag coefficients, see Supplemental Information for details. Assuming the mastigonemes do not deform, we estimate the drag coefficient of a straight flagellum of length $L = 12$ µm, width $w = 2(r + l_m) = 2$ µm, and thickness $h = 2r$. The width $w$ accounts for the two rows of mastigonemes of length $l_m$ observed in **Fig. 4.1**b. The geometry is shown in **Fig. 4.7**. We compare this value with the drag coefficient of a straight and smooth flagellum of length $L = 12$ µm and diameter $2r = 0.5$ µm.

We find the drag increase is 50% for flow in the direction perpendicular to the mastigonemes, and 30% for flow in the direction parallel to them. The 50% increase is comparable with estimates of the drag coefficient around a cylinder of increased diameter from $2r = 0.5$ µm to $2(r + l_m) = 2$ µm [65]. Alternatively, for an undulating swimmer without a separate cell body (*Caenorhabditis elegans*), a 30% reduction in swimming speed is predicted for the same increase in diameter [25]. Therefore, according to both models, the hydrodynamic effect of straight and rigid mastigonemes would be significant and clearly measurable given the accuracy of the OTV technique.



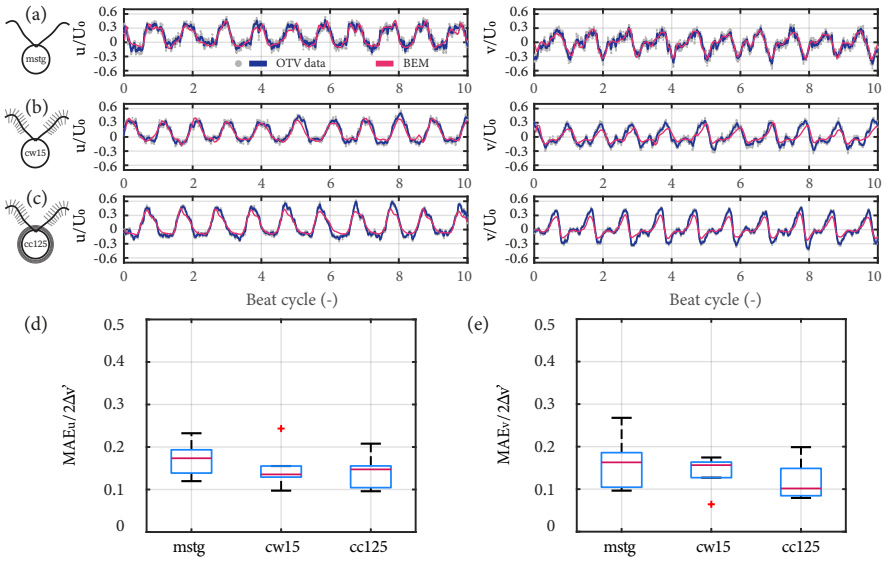


Figure 4.6: **Near-field hydrodynamics of beating flagella.** (a-c) Axial $u$ (left) and lateral $v$ (right) flow as a function of beat cycle for a typical (a) *mstg*, (b) *cw15*, and (c) *cc125* cell. The red solid curve is the prediction from hydrodynamic modelling (BEM). (d-e) Comparison of mean absolute error (MAE) of BEM predictions for (d) axial flows $\mathrm{MAE}_u$ and (e) lateral flows $\mathrm{MAE}_v$, for *mstg*, *cw15*, and *cc125* strains from left to right, respectively. The data represented is from within ~20 µm of a beating cell ($y < 0.2\delta$), or the lightly shaded areas in **Fig. 4.5**. The sample size for (d-e) is $N = 6$ for each strain.

Overall, from our OTV observations and hydrodynamics modelling, we conclude that

the mastigonemes do not contribute to the flows generated by beating flagella and do not have a direct hydrodynamic effect. There are no differences between the axial $u$ or lateral flows $v$ generated per stroke by *mstg*, *cw15*, or *cc125* cells. Additionally, our hydrodynamic model, which assumes smooth flagella without mastigonemes, accurately represents the fluid dynamics around both cells with mastigonemes (*cc125* and *cw15*) and cells without (*mstg*).

Since we do not observe any hydrodynamic differences due to the presence of mastigonemes, we can conclude that the increased turning rate in *mstg* is not due to a direct hydrodynamic effect of the mastigonemes and, more likely, results from either differences in flagella swiping areas or slipping events (see **Sec. 4.3.2**). These behavioural differences would require further studies to determine whether and how they are linked to the presence of mastigonemes.



Our results refute the hypothesis currently accepted in the literature that the fibrous mastigonemes increase the effective area of *C. reinhardtii*'s flagella during their beating strokes [19]. A possible explanation may be the flexibility of the mastigonemes of *C. reinhardtii*. Since they are thin and of the fibrous-type [19], they may bend and deflect when the flagella moves through the fluid. As pointed out by [21, 23], if the flexibility of the mastigonemes is below a critical value, then they would not contribute to the drag of the flagellum, and the drag force would be equivalent to that of a smooth flagellum.

## 4.4. CONCLUSION

Our study thoroughly investigated the possible hydrodynamic contribution of the mastigonemes of *Chlamydomonas reinhardtii* using a mutant lacking these structures. In conclusion, we confirmed through TEM imaging that the *mstg* mutant used in our study lacks mastigonemes, while the *cw15* and *cc125* cells possess them. From observations of freely swimming cells, we find that mastigonemes do not increase swimming velocity. Furthermore, mastigonemes do not affect flagellar gait kinematics. Finally, from our OTV measurements, we find that mastigonemes do not help produce larger hydrodynamic forces or propulsive flows per stroke, as has been previously hypothesized [19, 35, 36]. Future studies into the bending stiffness of *C. reinhardtii* mastigonemes may help confirm whether mastigonemes bend and deflect during swimming, which render them useless for hydrodynamic enhancement. Additionally, future studies into the effects of mastigonemes on swimming behaviour could shed light on functions of mastigonemes other than mere hydrodynamics. Overall, our study found that mastigonemes do not contribute to the swimming propulsion of *C. reinhardtii*. Their function still remains enigmatic. More studies into their contributions to sensing, adhesion, or feeding may reveal their function and evolution.

## 4.5. SUPPLEMENTARY MATERIAL

### 4.5.1. FREE SWIMMING HELICAL TRAJECTORY

For our measurements, we observed the 2D projections of the cells' 3D helical trajectories. As such, we may underestimate the trajectory length.

Here we use the parametric equations for a 3D helix with $x$ the translational direction, to estimate the error in 2D measurements:

$$\begin{aligned} x(t') &= b\cos(t'), \\ y(t') &= ct', \\ z(t') &= b\sin(t'), \end{aligned} \tag{4.1}$$

Here, $t'$ ranges from 0 to $2\pi$ for a single cycle, $b$ is the radius of the helix, and $c$ represents its wavelength. Following previous measurements [54, 55], we assume $b = 5$ µm. The wavelength $c$ is found using the trajectory lengths we measured for the 2D projections assuming a helix frequency of 2 Hz [54, 55]. We calculate the 2D trajectory length $L_{2D}$ as follows:

$$L_{2D} = \int_0^{2\pi} \sqrt{\left(\frac{dx}{dt'}\right)^2 + \left(\frac{dy}{dt'}\right)^2}\, dt', \tag{4.2}$$

which we approximate as the average swimming speed divided by the helix frequency, or $L_{2D} = 45$ µm. Substituting Eq. (4.1) into Eq. (4.2), we can solve for $c = 6.3$ µm. Using this value for $c$, we can find the 3D trajectory length $L_{3D}$ following:

$$L_{3D} = \int_0^{2\pi} \sqrt{\left(\frac{dx}{dt'}\right)^2 + \left(\frac{dy}{dt'}\right)^2 + \left(\frac{dz}{dt'}\right)^2}\, dt'. \tag{4.3}$$

We can then estimate the error as $(L_{3D} - L_{2D})/L_{3D}$. Substituting Eq. (4.1) into Eq. (4.3), we get an error estimate of 10%.

### 4.5.2. COMPUTATION OF HYDRODYNAMIC DRAG

To estimate the potential direct hydrodynamic effect of mastigonemes when fluid does not flow between the fibres, we compute the drag coefficients on slender flagella of different cross-sectional geometry using the boundary element method (BEM). Our numerical approach solves the Stokes equations using the completed double-layer boundary integral equation [51], with a completion flow due to a distribution of singularities along the central axis [52].

We estimate the drag coefficient on a straight flagellum without mastigonemes, which we represent as a straight cylindrical rod of length $L = 12$ µm and radius $r = 0.25$ µm, see **Fig. 4.7**. The value obtained differs less than 1% from that predicted by the analytical solution $4\pi\mu L/(\ln(L/r) - 0.5 + \ln 2)$, derived by Cox [65] for a motion in the direction perpendicular to the centreline, corresponding to a motion in the $Y$ or $Z$ direction on **Fig. 4.7**.

This value is compared with a model flagellum with straight rigid mastigonemes, which we represent as a rigid flagellum with an increased effective area. This flagellum is represented as a flattened flagellum of length $L = 12$ µm, with the same thickness as

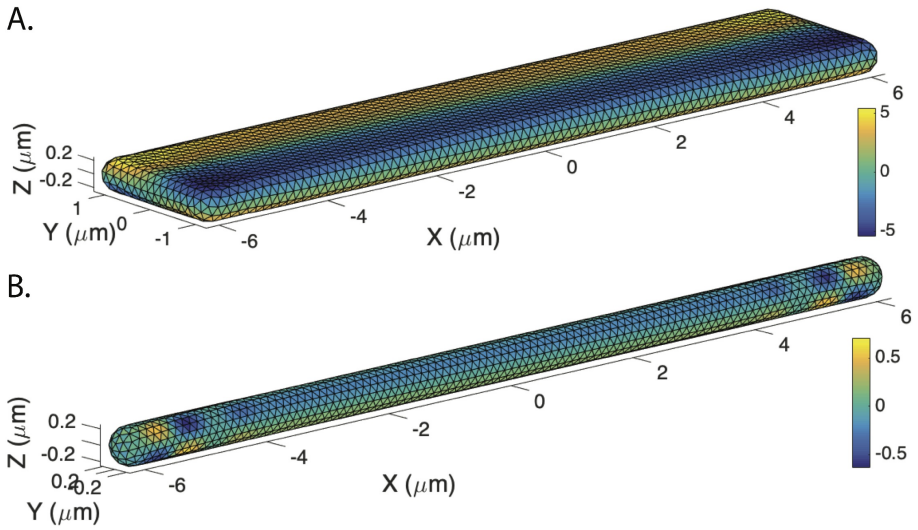


Figure 4.7: **Drag coefficient for different cross-sections.** Computation of drag coefficient using BEM on an unstructured triangular mesh. The colormap represents the intensity of one component of the double layer potential. (a) Model flagellum representing a flagellum with two rows of rigid mastigonemes where fluid does not flow between them. (b) Cylindrical flagellum without mastigonemes.

the cylindrical flagellum $2r = 0.5$ µm but with a width corresponding to that of the axoneme increased by the two rows of mastigonemes $2(r + l_m) = 2$ µm, see **Fig. 4.7**. We find the drag coefficient to be significantly larger than for the cylindrical flagellum, with an increase in drag of 32% for a motion in the $Y$-direction and 50% for a motion in the $Z$-direction.

### 4.5.3. DRASTIC TURNING BY *mstg*

Freely swimming *mstg* cells exhibit a larger turning rates, see **Fig. 4.8**. This can either be due to a slip event, where the two flagella are out of sync and it results in the cell turning dramatically without forward progress. Or the drastic turning can be due to asymmetric motion of the flagella. Specifically, in **Fig. 4.8**, the flagellum on the left swipes a larger area than the one on the right. This results in a larger hydrodynamic thrust generated by the flagellum on the left, which causes the cell to turn to the right.

## 4.6. AUTHOR CONTRIBUTIONS

D. W. and G. J. A. performed research; all authors designed research, analyzed data and wrote the manuscript. D. T. and M.-E. A.-T. supervised the work. D. W. and G. J. A. contributed equally to this work.

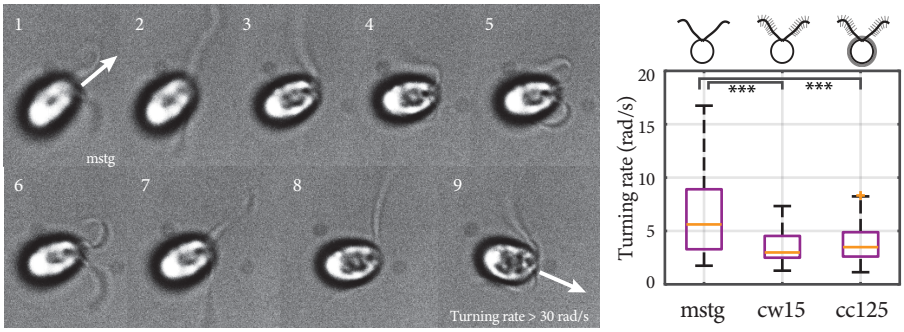


Figure 4.8: **Turning in free swimming observations.** (1-9) Image sequence of *mstg* cell during a turning event with a large turning rate. The white arrows represent the cell's heading direction. The time step between the images is 3.3 ms. Comparison of average turning rate for *mstg*, *cw15*, and *cc125* cells from left to right, respectively. Here, $***$ represents $p < 0.001$ following a Kruskal-Wallis One-Way ANOVA statistical test.



## 4.7. ACKNOWLEDGMENTS

The authors thank B. Beaumont for a useful suggestion and R. Kieffer for technical support.

## REFERENCES

[1] G. J. Amador, D. Wei, D. Tam, and M.-E. Aubin-Tam, *Fibrous flagellar hairs of Chlamydomonas reinhardtii do not enhance swimming,* Biophysical Journal **118**, 2914 (2020).

[2] A. Bejan, *Theory of heat transfer from a surface covered with hair,* Journal of Heat Transfer **112**, 662 (1990).

[3] J. Casas and O. Dangles, *Physical ecology of fluid flow sensing in arthropods,* Annual Review of Entomology **55**, 505 (2010).

[4] G. J. Amador and D. L. Hu, *Cleanliness is next to godliness: Mechanisms for staying clean,* Journal of Experimental Biology **218**, 3164 (2015).

[5] K. Autumn, M. Sitti, Y. A. Liang, A. M. Peattie, W. R. Hansen, S. Sponberg, T. W. Kenny, R. Fearing, J. N. Israelachvili, and R. J. Full, *Evidence for van der Waals adhesion in gecko setae,* Proceedings of the National Academy of Sciences **99**, 12252 (2002).

[6] J. P. Swaddle, M. S. Witter, I. C. Cuthill, A. Budden, and P. McCowen, *Plumage condition affects flight performance in common starlings: Implications for developmental homeostasis, abrasion and moult,* Journal of Avian Biology , 103 (1996).

[7] K. Sato, H. Takahashi, N. Minh-Dung, K. Matsumoto, and I. Shimoyama, *Effectiveness of bristled wing of thrips,* in *2013 IEEE 26th International Conference on Micro Electro Mechanical Systems (MEMS)* (IEEE, 2013) pp. 21–24.

[8] D. I. Rubenstein and M. Koehl, *The mechanisms of filter feeding: Some theoretical considerations,* The American Naturalist **111**, 981 (1977).

[9] A. Nasto, P.-T. Brun, and A. Hosoi, *Viscous entrainment on hairy surfaces,* Physical Review Fluids **3**, 024002 (2018).

[10] S. Vogel, *How much air passes through a silkmoth's antenna?* Journal of Insect Physiology **29**, 597 (1983).

[11] G. J. Amador, W. Mao, P. DeMercurio, C. Montero, J. Clewis, A. Alexeev, and D. L. Hu, *Eyelashes divert airflow to protect the eye,* Journal of the Royal Society Interface **12**, 20141294 (2015).

[12] G. J. Amador, F. Durand, W. Mao, S. Pusulri, H. Takahashi, V.-T. Nguyen, I. Shimoyama, A. Alexeev, and D. Hu, *Insects have hairy eyes that reduce particle deposition,* The European Physical Journal Special Topics **224**, 3361 (2015).

[13] G. Spedding, *The wake of a kestrel (Falco tinnunculus) in flapping flight,* Journal of Experimental Biology **127**, 59 (1987).

[14] D. R. Pitelka, *Electron-Microscopic Structure of Protozoa: International Series of Monographs on Pure and Applied Biology* (Elsevier, Oxford, UK, 2013).

[15] T. L. Jahn, M. D. Lanoman, and J. R. Fonseca, *The mechanism of locomotion of flagellates. II. Function of the mastigonemes of Ochromonas,* The Journal of Protozoology **11**, 291 (1964).

[16] D. L. Ringo, *Flagellar motion and fine structure of the flagellar apparatus in Chlamydomonas,* The Journal of Cell Biology **33**, 543 (1967).

[17] S. Loiseaux and J. A. West, *Brown algal mastigonemes: Comparative ultrastructure,* Transactions of the American Microscopical Society , 524 (1970).

[18] G. B. Bouck, *The structure, origin, isolation, and composition of the tubular mastigonemes of the Ochromonas flagellum,* The Journal of Cell Biology **50**, 362 (1971).

[19] R. A. Bloodgood, *The Chlamydomonas flagellar membrane and its dynamic properties,* in *The Chlamydomonas Sourcebook* (Elsevier, Oxford, UK, 2009) pp. 309–368.

[20] G. I. Taylor, *Analysis of the swimming of microscopic organisms,* Proceedings of the Royal Society of London A **209**, 447 (1951).

[21] C. Brennen, *Locomotion of flagellates with mastigonemes,* Journal of Mechanochemistry and Cell Motility **3**, 207 (1975).

[22] M. Holwill and M. Sleigh, *Propulsion by hispid flagella,* Journal of Experimental Biology **47**, 267 (1967).

[23] S. Namdeo, S. Khaderi, J. den Toonder, and P. Onck, *Swimming direction reversal of flagella through ciliary motion of mastigonemes,* Biomicrofluidics **5**, 034108 (2011).

[24] S. Tottori and B. J. Nelson, *Artificial helical microswimmers with mastigoneme-inspired appendages,* Biomicrofluidics **7**, 061101 (2013).

[25] R. Berman, O. Kenneth, J. Sznitman, and A. Leshansky, *Undulatory locomotion of finite filaments: lessons from Caenorhabditis elegans,* New Journal of Physics **15**, 075022 (2013).

[26] S. Childress, *Mechanics of Swimming and Flying* (Cambridge University Press, New York, NY, USA, 1981).

[27] S. S. Merchant, S. E. Prochnik, O. Vallon, E. H. Harris, S. J. Karpowicz, G. B. Witman, A. Terry, A. Salamov, L. K. Fritz-Laylin, L. Maréchal-Drouard, W. F. Marshall, L.-H. Qu, D. R. Nelson, A. A. Sanderfoot, M. H. Spalding, V. V. Kapitonov, Q. Ren, P. Ferris, E. Lindquist, ..., and A. R. Grossman, *The Chlamydomonas genome reveals the evolution of key animal and plant functions,* Science **318**, 245 (2007).

[28] M. Polin, I. Tuval, K. Drescher, J. P. Gollub, and R. E. Goldstein, *Chlamydomonas swims with two "gears" in a eukaryotic version of run-and-tumble locomotion,* Science **325**, 487 (2009).

[29] K. Drescher, R. E. Goldstein, N. Michel, M. Polin, and I. Tuval, *Direct measurement of the flow field around swimming microorganisms,* Physical Review Letters **105**, 168101 (2010).

[30] D. Tam and A. Hosoi, *Optimal feeding and swimming gaits of biflagellated organisms,* Proceedings of the National Academy of Sciences **108**, 1001 (2011).

[31] H. Kurtuldu, D. Tam, A. Hosoi, K. A. Johnson, and J. Gollub, *Flagellar waveform dynamics of freely swimming algal cells,* Physical Review E **88**, 013015 (2013).

[32] D. R. Brumley, K. Y. Wan, M. Polin, and R. E. Goldstein, *Flagellar synchronization through direct hydrodynamic interactions,* eLife **3**, e02750 (2014).

[33] P. Sartori, V. F. Geyer, A. Scholich, F. Jülicher, and J. Howard, *Dynamic curvature regulation accounts for the symmetric and asymmetric beats of Chlamydomonas flagella,* eLife **5**, e13258 (2016).

[34] D. Wei, P. G. Dehnavi, M.-E. Aubin-Tam, and D. Tam, *Is the zero Reynolds number approximation valid for ciliary flows?* Physical Review Letters **122**, 124502 (2019).

[35] G. Bouck, *Architecture and assembly of mastigonemes,* in *Advances in Cell and Molecular Biology*, Vol. 2 (Academic Press, Cambridge, MA, USA, 1972) pp. 237–271.

[36] S. Nakamura, G. Tanaka, T. Maeda, R. Kamiya, T. Matsunaga, and O. Nikaido, *Assembly and function of Chlamydomonas flagellar mastigonemes as probed with a monoclonal antibody,* Journal of Cell Science **109**, 57 (1996).

[37] X. Li, W. Patena, F. Fauser, R. E. Jinkerson, S. Saroussi, M. T. Meyer, N. Ivanova, J. M. Robertson, R. Yue, R. Zhang, J. Vilarrasa-Blasi, T. M. Wittkopp, S. Ramundo, S. R. Blum, A. Goh, M. Laudon, T. Srikumar, P. A. Lefebvre, A. R. Grossman, and M. C.

Jonikas, *A genome-wide algal mutant library and functional screen identifies genes required for eukaryotic photosynthesis,* Nature Genetics **51**, 627 (2019).

[38] X. Li, R. Zhang, W. Patena, S. S. Gang, S. R. Blum, N. Ivanova, R. Yue, J. M. Robertson, P. A. Lefebvre, S. T. Fitz-Gibbon, *et al.*, *An indexed, mapped mutant library enables reverse genetics studies of biological processes in Chlamydomonas reinhardtii,* The Plant Cell **28**, 367 (2016).

[39] R. Zhang, W. Patena, U. Armbruster, S. S. Gang, S. R. Blum, and M. C. Jonikas, *High-throughput genotyping of green algal mutants reveals random distribution of mutagenic insertion sites and endonucleolytic cleavage of transforming DNA,* The Plant Cell **26**, 1398 (2014).

[40] G. Quaranta, M.-E. Aubin-Tam, and D. Tam, *Hydrodynamics versus intracellular coupling in the synchronization of eukaryotic flagella,* Physical Review Letters **115**, 238101 (2015).

[41] H. Sakakibara and R. Kamiya, *Functional recombination of outer dynein arms with outer arm-missing flagellar axonemes of a Chlamydomonas mutant,* Journal of Cell Science **92**, 77 (1989).

[42] S. Takada and R. Kamiya, *Beat frequency difference between the two flagella of Chlamydomonas depends on the attachment site of outer dynein arms on the outer-doublet microtubules,* Cell Motility and the Cytoskeleton **36**, 68 (1997).

[43] R. Kamiya, *Analysis of cell vibration for assessing axonemal motility in Chlamydomonas,* Methods **22**, 383 (2000).

[44] N. Okita, N. Isogai, M. Hirono, R. Kamiya, and K. Yoshimura, *Phototactic activity in Chlamydomonas 'non-phototactic' mutants deficient in $Ca^{2+}$-dependent control of flagellar dominance or in inner-arm dynein,* Journal of Cell Science **118**, 529 (2005).

[45] M. J. Lang, C. L. Asbury, J. W. Shaevitz, and S. M. Block, *An automated two-dimensional optical force clamp for single molecule studies,* Biophysical Journal **83**, 491 (2002).

[46] S. Kim and S. J. Karrila, *Microhydrodynamics: Principles and Selected Applications* (Dover Publications, Mineola, NY, USA, 2013).

[47] B. A. Nemet and M. Cronin-Golomb, *Microscopic flow measurements with optically trapped microprobes,* Optics Letters **27**, 1357 (2002).

[48] G. Knöner, S. Parkin, N. R. Heckenberg, and H. Rubinsztein-Dunlop, *Characterization of optically driven fluid stress fields with optical tweezers,* Physical Review E **72**, 031507 (2005).

[49] A. M. R. Kabir, D. Inoue, Y. Kishimoto, J.-i. Hotta, K. Sasaki, N. Kitamura, J. P. Gong, H. Mayama, and A. Kakugo, *Drag force on micron-sized objects with different surface morphologies in a flow with a small Reynolds number,* Polymer Journal **47**, 564 (2015).

[50] P. Almendarez-Rangel, B. Morales-Cruzado, E. Sarmiento-Gómez, R. Romero-Méndez, and F. G. Pérez-Gutiérrez, *A microflow velocity measurement system based on optical tweezers: A comparison using particle tracking velocimetry,* European Journal of Mechanics B **72**, 561 (2018).

[51] H. Power and G. Miranda, *Second kind integral equation formulation of Stokes' flows past a particle of arbitrary shape,* SIAM Journal on Applied Mathematics **47**, 689 (1987).

[52] E. E. Keaveny and M. J. Shelley, *Applying a second-kind boundary integral equation for surface tractions in stokes flow,* Journal of Computational Physics **230**, 2141 (2011).

[53] J. B. Keller and S. I. Rubinow, *Slender-body theory for slow viscous flow,* Journal of Fluid Mechanics **75**, 705 (1976).

[54] N. Isogai, R. Kamiya, and K. Yoshimura, *Dominance between the two flagella during phototactic turning in Chlamydomonas,* Zoological Science **17**, 1261 (2000).

[55] H. C. Crenshaw, *A new look at locomotion in microorganisms: Rotating and translating,* American Zoologist **36**, 608 (2015).

[56] K. C. Leptos, J. S. Guasto, J. P. Gollub, A. I. Pesci, and R. E. Goldstein, *Dynamics of enhanced tracer diffusion in suspensions of swimming eukaryotic microorganisms,* Phys. Rev. Lett. **103**, 198103 (2009).

[57] T. Yagi, I. Minoura, A. Fujiwara, R. Saito, T. Yasunaga, M. Hirono, and R. Kamiya, *An axonemal dynein particularly important for flagellar movement at high viscosity: Implications from a new Chlamydomonas mutant deficient in the dynein heavy chain gene DHC9,* Journal of Biological Chemistry **280**, 41412 (2005).

[58] K.-i. Wakabayashi, T. Ide, and R. Kamiya, *Calcium-dependent flagellar motility activation in Chlamydomonas reinhardtii in response to mechanical agitation,* Cell Motility and the Cytoskeleton **66**, 736 (2009).

[59] B. Qin, A. Gopinath, J. Yang, J. P. Gollub, and P. E. Arratia, *Flagellar kinematics and swimming of algal cells in viscoelastic fluids,* Scientific Reports **5**, 9190 (2015).

[60] K. Y. Wan and R. E. Goldstein, *Coordinated beating of algal flagella is mediated by basal coupling,* Proceedings of the National Academy of Sciences **113**, E2784 (2016).

[61] V. Geyer, P. Sartori, B. Friedrich, F. Jülicher, and J. Howard, *Independent control of the static and dynamic components of the Chlamydomonas flagellar beat,* Current Biology **26**, 1098 (2016).

[62] K. E. VanderWaal, R. Yamamoto, K.-i. Wakabayashi, L. Fox, R. Kamiya, S. K. Dutcher, P. V. Bayly, W. S. Sale, and M. E. Porter, *bop5 mutations reveal new roles for the IC138 phosphoprotein in the regulation of flagellar motility and asymmetric waveforms,* Molecular Biology of the Cell **22**, 2862 (2011).

[63] M. Bottier, K. A. Thomas, S. K. Dutcher, and P. V. Bayly, *How does cilium length affect beating?* Biophysical Journal **116**, 1292 (2019).

[64] C. Brokaw and D. Luck, *Bending patterns of Chlamydomonas flagella I. Wild-type bending patterns,* Cell Motility **3**, 131 (1983).

[65] R. Cox, *The motion of long slender bodies in a viscous fluid Part 1. General theory,* Journal of Fluid Mechanics **44**, 791 (1970).

# 5

# *C. reinhardtii* USES ITS *cis* FLAGELLUM TO COUPLE TO EXTERNAL FLOWS

**D. Wei, G. Quaranta, D. S. W. Tam, M. -E. Aubin-Tam**

*Microorganisms like bacteria and microalgae often use flagella for locomotion, adopting different steering mechanisms. In the case of the biflagellate microalgae Chlamydomonas reinhardtii (CR), steering is achieved through different amplitudes of motion of its two flagella. Although seemingly identical, dissimilarities have been reported between the two flagella of CR. In this study, we report a novel difference between the two CR flagella, which has important consequence on the cell's response to external flow and on its beating frequency. Our experimental approach consists of selectively loading one of the two flagella with an oscillating external flow. We find that the load on the cis flagellum, which is the one closer to the cell's eyespot, determines the cell's coupling strength to the external flow, whereas the load on the other flagellum has a negligible effect. As CR's two flagella are known to respond to calcium concentration differently, we test if calcium depletion affects this novel flagellar difference, and show that it does not. Lastly, with ptx1, a mutant which does not display any known flagellar difference, we show that the novel flagellar difference is also lost.*

## 5.1. INTRODUCTION

Motile micro-organisms swim towards more desirable environments for their survival. For example, bacteria are found to accumulate around nutrients [1, 2], and microalgae swim towards suitable light conditions [3, 4]. These behaviours in general are known as tactic behaviours, and investigation into their mechanisms will help us understand the dynamic microbial ecology [5].

To achieve tactic behaviour, the organism's sensory system translates environmental cues into physiological signals inside the organism, which then leads to adjusted motility. Eukaryotic micro-swimmers swim by beating flagella (cilia) [6], which is an active organelle driven by dynein motors [7, 8], and motility control is mostly achieved by the modulation of flagellar beating. In particular, uniflagellates such as sea urchin sperm tend to change the degree of symmetry of their flagellar waveform [9]. Biflagellates such as *Chlamydomonas reinhardtii* (CR) alter the propulsive force of its two flagella [10, 11]. And ciliates such as *Paramecium* and *Volvox rousseletii* reverse the direction of the effective ciliary stroke, the beating frequency, and the beating waveform [4, 12].



A model organism for the study of the biflagellates' motility is *Chlamydomonas reinhardtii* (CR). It possesses two representative flagella inherited from the common ancestors of land plants and animals [13], and is capable of phototaxis [10, 14, 15], chemotaxis [16, 17], and gravitaxis [18, 19]. Its two flagella are termed based on their distance to the light-sensing organelle, the eyespot. The flagellum closer to the eyespot is termed the *cis* flagellum, and the other one the *trans*. During swimming, the two flagella beat in a gait akin to the breaststroke of a human swimmer. To understand the steering mechanism, and ultimately the tactic behaviours of this model organism, ones needs to investigate the modulation of flagellar beating, which hinges on the difference between its two flagella.

To the current knowledge, there are two major differences between the *cis* and the *trans* flagellum of a CR cell [11]. The first difference is that the *trans* flagellum beats faster. When one flagellum is removed or when the cell is demembrananted and reactivated, the *trans* flagellum beats at 65-75 Hz, which is on average 30%-40% faster than the *cis* flagellum (40-50 Hz) [20–23]. The well-defined frequencies of beating emerge from a concerted effort of thousands of flagellar dyneins; and such difference in intrinsic frequency is currently hypothesized to result from certain subunits of the outer dynein arm in the two flagella being different [24–26].

The second difference between the *cis* and the *trans* flagellum is that their beating amplitudes are modulated differently by calcium [22, 27], and this is key to steering [10, 27]. At low free calcium concentration ($[Ca^{2+}]_{free} < 10^{-8}$ M), the *trans* flagellum beats with smaller amplitude than the *cis*; while at high free calcium concentration ($[Ca^{2+}]_{free} > 10^{-7}$ M), the *cis* amplitude is smaller. Currently, the molecular mechanism responsible for this flagellar difference is still unknown, whereas it is known to be independent from the flagellar difference in beating frequency [28].

Despite much effort in illuminating the *cis-trans* difference, the whole picture remains largely incomplete. One reason for that is that the known differences are mostly observed on cells with impaired motility or on reactivated detergent-treated cell models, and therefore have limited implication for efficiently swimming wildtype cells whose flagella beat synchronously with a similar amplitude. However, observing *cis-trans* dif-

ference directly on such cells is challenging, as it is difficult to stimulate the two flagella differently. Till now, observation in this regard is limited to the different flagellar response to light stimuli [10]. In this study, we devise a novel way to impose different hydrodynamic forces on the flagella, and we study the cells' responses to resolve the *cis-trans* difference during synchronous beating.

The two flagella are able to beat in sync because they are mechanically coupled by the fibrous structures at their anchor sites [29, 30]. After being coupled, both flagella beat at the same frequency of ~55 Hz, which is closer to the intrinsic frequency of the *cis* flagellum (40-50 Hz), than to that of the *trans* flagellum (65-75 Hz) [30, 31]. This leads to an assumption that the coupling between the two flagella is asymmetric, so that the *cis* flagellum has a larger weight in determining the collective frequency.

We attempt to break the synchrony at different frequencies by employing external oscillatory flow. However, we find that the synchrony can hardly be broken, and thus the two flagella beating in sync shall be seen as one entity, a collective oscillator.

To proceed, we study the response of the synchronous beating towards external flows along different directions. Given the cell's symmetry around its long axis, when it is subjected to forces symmetric around the same axis, the *cis-trans* difference during synchrony is likely to result in different responses. As a result, we find that a cell is entrained more effectively when the flow is applied perpendicularly to the *cis* flagellum in its most forward-reaching shape. Through hydrodynamic computation, we find that the cell's coupling strength to external flows is determined by the hydrodynamic load on the *cis* flagellum. Additionally, as the two flagella are known to be modulated differently by calcium concentration, we test if calcium depletion from the external media affects the cell's asymmetric flow entrainability, and show that it does not. Lastly, we confirm that this newly observed flagellar difference is lost in the mutant *ptx1*, which also fails to display any known flagellar differences.



## 5.2. METHODS AND TECHNIQUES

### 5.2.1. PREPARATION OF CELLS

CR wildtype (*wt*) strain cc125 (mt+) and flagellar dominance mutant *ptx1* cc2894 (mt+) are cultured in TRIS-minimal medium (pH=7.0) with sterile air bubbling, in a 14h/10h day-night cycle. Experiments are always performed on the 4th day after inoculating the liquid culture. The culture then is still in exponential growth, and has a concentration of $\sim 2\times10^5$ cells per mL. Cells are collected from the liquid culture and resuspended in fresh TRIS-minimal medium (pH=7.0) before experiments. In the assay with the medium depleted of free calcium, TRIS-minimal medium + 0.5 mM EGTA (pH=7.0) is used instead for resuspension.

### 5.2.2. SINGLE CELL EXPERIMENTS

Single cells of CR are studied following a protocol similar to the one described in [29]. A custom-made flow chamber of height h ≈ 1.5 mm, with a 15 × 1.5 mm rectangular opening on one side, is filled with the cell suspension until the air-water interface is pinned on all edges of the opening. A glass micro-pipette held by a micro-manipulator (SYS-HS6, WPI) enters the flow chamber to capture single cells by aspiration.

To subject a captured cell to external oscillatory flow, the flow chamber is connected to a piezoelectric stage (Nano-Drive, Mad City Labs), which moves the chamber and the fluid therein altogether. Meanwhile, the cell remains stationary in the laboratory frame of reference, as the cell, the pipette, and the manipulator are isolated from the flow chamber and the piezoelectric stage. From this relative motion, the cell experiences an imposed flow.

For observation, the flow chamber is mounted on an inverted microscope (Nikon Eclipse Ti-U) with a 60× water immersion objective. Bright field microscopy is performed with a sCMOS camera (PCO.edge) at 600-1000 Hz. Video recordings of the flagellar beating are taken before, during and after the application of external flows.

For each cell, we measure its average beating frequency $f_0$ from 2 s recording of the cell over 100 beats. For *ptx1* cells, $f_0$ is reported for in-phase (IP) synchronous beats. Thereafter, as shown in **Fig. 5.1**a, the cell is exposed to external flows along 3 different directions with the same amplitude = 780±50 µm/s (mean±std.). Along each direction, flows are applied at 12 equidistant frequencies covering the range $[f_0-7,\ f_0+7]$ Hz. The flow amplitude is chosen to give an entraining frequency range of approximately 6 Hz, which can be fully captured within our measurement scope (~14 Hz) with sufficient resolution (5-8 data points). The recording for a flow along a particular direction at a given frequency has a duration of 12 s. The waveform and the amplitudes of the applied flows are individually calibrated by tracking micro-beads in the flow chamber.

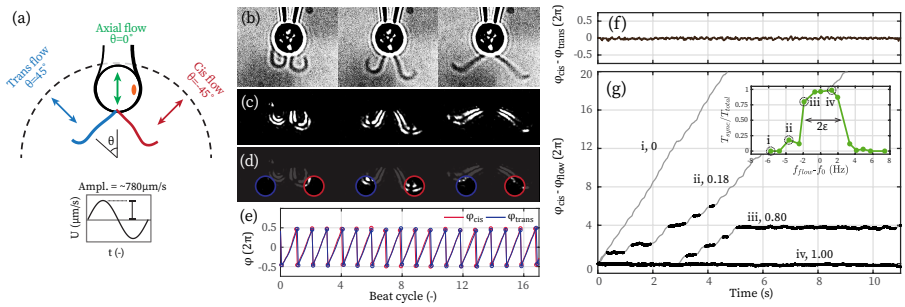


Figure 5.1: **Experimental setup to selectively load one flagellum and to study flagellar phase dynamics.** (a) Schematic drawing of a *Chlamydomonas reinhardtii* cell held by a glass micropipette. Captured cells are subjected to sinusoidal flows along different directions ($\theta$) in the $xy$-plane. Flows along $\theta = 45°, 0°, -45°$ are termed as trans, axial, and cis flow, respectively. Flows have the same amplitude, 780±50 µm/s (mean ± std., inset). (b-e) Image analysis to extract flagellar phase $\varphi_{\text{cis}}$ and $\varphi_{\text{trans}}$. Raw images (b) are thresholded and contrast-adjusted to highlight the flagella (c). Two user-defined interrogation windows then sample the flagellar beating by the mean pixel value within them over time (d). Hilbert transformation is performed to generate the flagellar phase (e). (f) Difference between the unwrapped phase of the two flagella, $\varphi_{\text{cis}} - \varphi_{\text{trans}}$, over a representative recording. (g) Phase difference between the flagella and the external flow, $\Delta\varphi(t) = \varphi_{\text{cis}}(t) - \varphi_{\text{flow}}(t)$, at different frequencies of the external flow $f_{\text{flow}}$. $\varphi_{\text{flow}}=2\pi f_{\text{flow}} t$. Flow entrainment manifests as plateaus (thick black lines) in $\Delta\varphi(t)$. The time fraction of flow entrainment, $\xi=T_{\text{sync}}/T_{\text{total}}$, decreases with increasing absolute value of detuning $|\nu|=|f_{\text{flow}} - f_0|$. Inset: the entrainment profile, $\xi(\nu)$, measures the coupling between the beating and the external flow, $2\varepsilon$, as its width in $\nu$ where $\xi(\nu) > 0.5$.

### 5.2.3. DERIVATION OF FLAGELLAR PHASE BY IMAGE ANALYSIS

Phase dynamics of the flagella are obtained by video analysis in a similar fashion as in [23, 29, 32]. The pipette and the cell body are masked out, and the rest of the image thresholded so that the flagella are highlighted, **Fig. 5.1**b-c. Thereafter, two sampling windows within the swept area of the flagella are defined, **Fig. 5.1**d. The mean pixel value of each window corresponds to a pseudo-periodic signal which can be used to characterize the flagellar phase dynamics. This is done by performing Hilbert transformation on the signal, **Fig. 5.1**e.

### 5.2.4. CHARACTERIZING ENTRAINMENT OF FLAGELLAR BEATING

Entrainment of the flagellar beating by the applied flows is used to characterize the cell's response. The cell beating synchronously is modeled as a self-sustained oscillator at $f_0$, with its entrainment by an external periodic forcing at frequency $f_{\text{flow}}$ described by the Adler equation [29, 32–34]:

$$\frac{d\Delta\varphi}{dt} = -2\pi\nu - 2\pi\varepsilon\sin(\Delta\varphi) + \zeta(t) \tag{5.1}$$

Here $\varphi$ is the flagellar phase, and can be the phase of either the *cis* ($\varphi_{\text{cis}}$) or the *trans* flagellum ($\varphi_{\text{trans}}$), as the two flagella beat in sync, **Fig. 5.1**f. $\Delta\varphi = \varphi - 2\pi f_{\text{flow}} t$ is the phase difference between the cell and the external flow. $\nu = f_{\text{flow}} - f_0$ is termed detuning. $\zeta$(t) is the white noise that satisfies $\langle\zeta(t+\tau)\zeta(t)\rangle = 2T_{\text{eff}}\delta(\tau)$, with $T_{\text{eff}}$ the effective temperature, describing how strong the noise is, and $\delta(\tau)$ the Kronecker delta.

The key parameter for the flow entrainment is the coupling strength $\varepsilon$. It characterizes the effectiveness of a given forcing (external flow) in enslaving an oscillator (the cell), by quantifying how much detuning it is able to counteract [33]. In *wt* cells, as the noise is weak ($T_{\text{eff}} \ll \varepsilon$) [29, 32], the frequency range in detuning $\nu$ where the flow is able to entrain the cell is:

$$-\varepsilon < \nu < \varepsilon \tag{5.2}$$

Entrainment is marked by a plateau in $\Delta\varphi$, shown in **Fig. 5.1**g as thick black lines. The ratio $\xi$ between the total entrained time $T_{\text{sync}}$, and the duration of applied flow $T_{\text{total}}$, $\xi = T_{\text{sync}}/T_{\text{total}}$, quantitatively tells whether there is entrainment, and how stable the entrainment is.

Practically, time fractions longer than 0.2 s wherein the signal maintains a slope $|\frac{d\Delta\varphi}{dt}| < 0.3\cdot 2\pi/s$, are marked as entrained. **Fig. 5.1**g demonstrates how $\xi$ is used to measure the coupling strength $\varepsilon$. $\xi$ increases at decreasing $|\nu|$ (i to vi). $\xi$ as a function of $\nu$ is displayed in the inset of **Fig. 5.1**g. With this entrainment profile $\xi(\nu)$, $\varepsilon$ is measured by the half width in $\nu$ where $\xi$ >0.5.

At low noise level, $T_{\text{eff}} \ll \varepsilon$, this method of extracting $\varepsilon$ from $\xi(\nu)$ is equivalent to the method used in [23, 29], which extracts $\varepsilon$, $T_{\text{eff}}$, and $\nu$ simultaneously by fitting phase dynamics. The fitting method is also employed in this study for the *ptx1* mutant, where the noise appears to be much stronger. See **Sec. 5.6.3** in the supplementary material for the noise in *ptx1*.

### 5.2.5. BOUNDARY ELEMENT METHOD (BEM)

Flow entrainment ultimately derives from mechanical interaction between the flagella and the flow, and therefore it is critical to calculate the hydrodynamic load on the flagella. In this study, a boundary element method (BEM) is used to compute the drag forces and the viscous powers exerted on the flagella.

To describe the cell body and the micro-pipette, a mesh grid is used. Stokeslets and rotlets are distributed along its centreline, and stresslets on its surface. Altogether, a no-slip boundary condition is met on the surface.

For flagella, we track their shapes from videos where the cells are entrained, and represent them using slender body theory by 26 discrete points along each of the flagellum's centreline [35]. Based on the tracking, the time-dependent velocity of each of the 26 points are calculated by its displacement across frames. Furthermore, stokeslets are distributed along the centrelines of the flagella, so that no-slip boundary conditions are met on their surfaces.

The distribution of stokeslets $\mathbf{f}(s)$ along a flagellum allows us to compute the total drag force $\mathbf{F}$ on it by integrating $\mathbf{f}(s)$ over the flagellar shape $\mathbf{F} = \int_0^{l_F} \mathbf{f}(s)ds$, with $l_F$ the flagellar length. Similarly, the viscous power can be computed as $P = \int_0^{l_F} \mathbf{f}(s) \cdot \mathbf{U}(s)ds$, where $\mathbf{U}(s)$ is the flagellar velocity.

## 5.3. RESULTS

### 5.3.1. ONLY IN-PHASE SYNCHRONOUS BEATING CAN BE ENTRAINED

Separately, the *cis* and the *trans* flagellum beat at different intrinsic frequencies [20, 21, 25, 27]. When coupled together, they beat synchronously at frequency $f_0$, which is much closer to the intrinsic frequency of the *cis* flagellum [23]. This hints at a more dominant role of the *cis* flagellum in frequency coordination. To test this further, we try to entrain the flagellar beating with external flows around the *cis* and the *trans* intrinsic frequencies. If they can be entrained, we may thereafter compare their coupling strengths to external flows.

Previously, Quaranta et al. [29] demonstrated the entrainment of *wt* cells by external oscillatory flows around $f_0$. Here we apply external flows along the cell-pipette axis over larger ranges of frequency and amplitude to entrain *wt* cells. **Fig. 5.2**a shows the result for a representative *wt* cell. The flow frequency $f_{\text{flow}}$ ranges from 40 to 75 Hz (N=22 equidistant frequencies) and the flow amplitude $U$ from 390 µm/s to 2340 µm/s (N=6 equidistant amplitudes). Here $f_0$ is around 50 Hz and fluctuates by up to 2 Hz during the experiment. Flow amplitude is scaled by $U_0$=110 µm/s. The diagram is color coded by the time fraction of flow entrainment $\xi = T_{\text{sync}}/T_{\text{total}}$, which reflects whether the flagellar beating is entrained and how stable the entrainment is.

The coupling strength $\varepsilon$ under flows of different amplitudes is described by the frequency range where $\xi > 0.5$, displayed as the red and yellow region in **Fig. 5.2**a. $\varepsilon$ increases with flow amplitude, giving a broadening range of flow entrainment around $f_0$. Such a feature is known as an Arnold tongue [33, 36]. The absence of other Arnold tongues in both the *cis* frequency range (40-50 Hz) [22, 27] and the *trans* frequency range (65-75 Hz) [22, 27] indicates that it is impossible to entrain the flagellar beating at such frequencies. Even up to the highest flow amplitude of 2340 µm/s, when the flows are

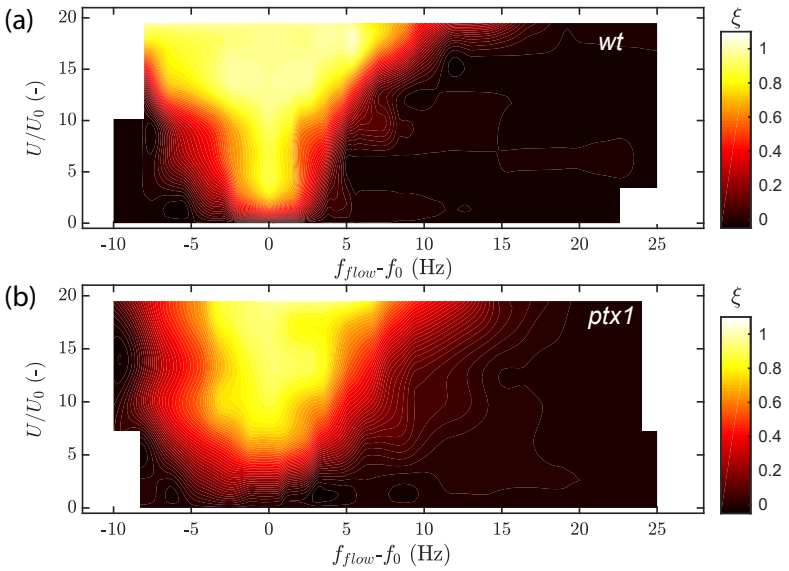


Figure 5.2: **Flow entrainment of flagellar beating for *wt* and *ptx1* cells** (a) Flows of frequencies $f_{\text{flow}}$ ranging from 40-75 Hz, and of amplitude $U$ ranging from 390µm/s to 2340 µm/s are applied to entrain a representative *wt* cell. The contour is interpolated from 132 measurements (6 equidistant amplitudes × 22 equidistant frequencies), and color-coded by $\xi = T_{\text{sync}}/T_{\text{total}}$. Here $T_{\text{sync}}$ is the duration of entrainment, and $T_{\text{total}}$ the duration of the applied flow. (b) Same as (a) but obtained with a representative *ptx1* cell. $\xi = T_{\text{sync}}/T_{\text{IP}}$ in this case, where $T_{\text{IP}}$ is the total duration of in-phase synchronous beating under the applied flow.

strong enough to occasionally disrupt the synchronous beating, there is still no entrainment.

We further perform the same test with the flagellar dominance mutant *ptx1* [28]. Both flagella of *ptx1* have similar intrinsic frequency as the *wt trans* flagellum [22, 28, 37]. They can beat synchronously either in-phase (IP) and in anti-phase (AP) [37, 38]. While the IP mode is similar to the beating of *wt*, which is at ~50 Hz, the AP mode is at 65-75 Hz, coinciding again with the intrinsic frequency range of the *wt trans* flagellum.

We cannot entrain the flagellar beating of *ptx1* except for its IP mode around 50 Hz - as is the case for *wt*. The Arnold tongue is also very similar, **Fig. 5.2**b. Scanned range in frequency and flow amplitude are the same as **Fig. 5.2**a, while $\xi$ is calculated as $\xi = T_{\text{sync}}/T_{\text{IP}}$, with $T_{\text{IP}}$ the total duration of IP mode during the application of flows.

To summarize, as it is essentially impossible to entrain flagella separately or collectively at the *cis* or *trans* intrinsic frequencies by external flows, flagellar beating in sync shall be seen as one oscillator in the context of external flow entrainment.

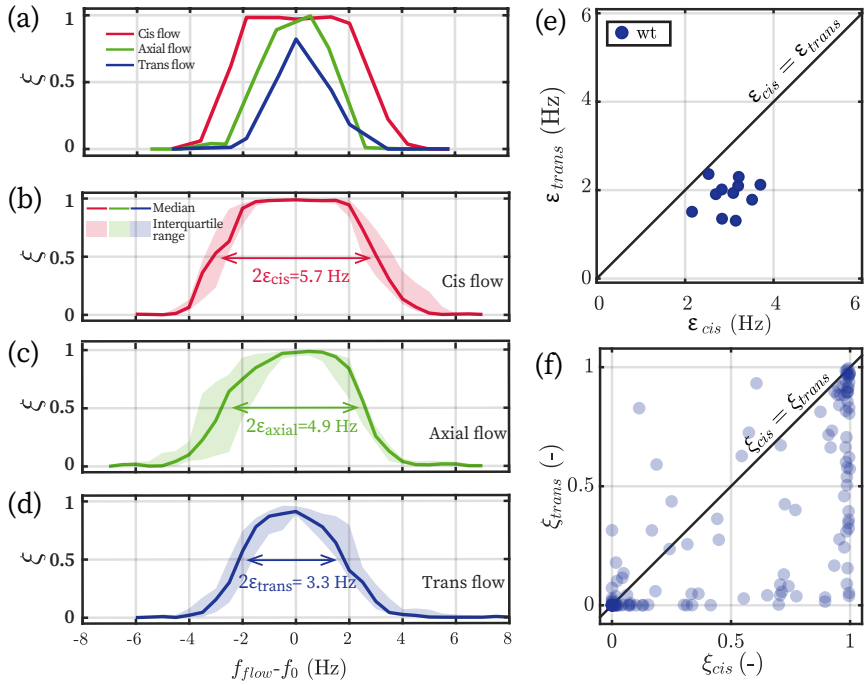


Figure 5.3: **Asymmetric flow entrainability of *wt* cells.** (a) A typical set of entrainment profiles $\xi(\nu)$ ($\nu = f_{\text{flow}} - f_0$) of a representative *wt* cell with the cis ($\theta$=-45°), the axial ($\theta$=0°) and the trans flow ($\theta$=45°). (b-d) Entrainment profiles $\xi(\nu)$ of N=11 *wt* cells. Solid lines and shaded areas represent the median and the interquartile range, respectively. (e) Comparing *wt* cells' (N=11) coupling with the cis flow $\varepsilon_{\text{cis}}$ to that with the trans flow $\varepsilon_{\text{trans}}$. Each point represents one cell. Below the identity line $\varepsilon_{\text{cis}} = \varepsilon_{\text{trans}}$ indicates $\varepsilon_{\text{cis}} > \varepsilon_{\text{trans}}$. (f) Asymmetric flow entrainability represented with the entrained time fraction $\xi$. For each cell and at each applied frequency $f_{\text{flow}}$, the entrained time fraction of the cell under the cis flow $\xi_{\text{cis}}$ and under the trans flow $\xi_{\text{trans}}$ are paired up, and plotted as a blue circle in the $\xi_{\text{cis}} - \xi_{\text{trans}}$ plane. Below the identity line $\xi_{\text{cis}} = \xi_{\text{trans}}$ indicates $\xi_{\text{cis}} > \xi_{\text{trans}}$. 132 pairs of entrainment experiments (12 pairs per cell, N=11 cells) are plotted, more than 90% of the points are under the identity line.

### 5.3.2. ASYMMETRIC SUSCEPTIBILITY TO EXTERNAL FLOW ENTRAINMENT IN *wt*

We proceed with testing the response of synchronous flagellar beating towards directional hydrodynamic forces. The rationale is that, given the cell's symmetry within the ciliary beating plane, if symmetrically-applied external forces can trigger different cell responses, such difference must derive from and reflect the inherent flagellar difference. For this purpose, flows symmetric around the cell-pipette axis along $\theta = \pm 45°$ are employed. As a reference, flow along the cell-pipette axis ($\theta = 0°$) is also applied. For simplicity, we term these three directional flows respectively as follows: when a cell's eyespot is pointing to the right, we refer to flows along $\theta = 0°$ as axial flows, $\theta = -45°$ as cis flows, and $\theta = 45°$ as trans flows (**Fig.** 5.1a). Since we can only entrain the flagellar beating

around $f_0$, we focus on the cell's response near this frequency. For each cell tested, we apply cis, axial, and trans flows, of the same amplitude 780±50 µm/s, at a same set of 12 frequencies around $f_0$, as described in **Sec. 5.2.2**. The time fraction during which the flagellar beating is entrained, $\xi$, is calculated for flows at each frequency; then further used to measure the coupling strengths to the flows ( $\varepsilon_{\text{cis}}$, $\varepsilon_{\text{axial}}$, $\varepsilon_{\text{trans}}$).

When comparing $\xi$ for the cis, the axial or the trans flows, a consistent trend is found: the cis flow has the broadest entrainment profile $\xi(\nu)$, and therefore the largest $\varepsilon$. A typical set of entrainment profiles is shown in **Fig. 5.3**a, and it indicates $\varepsilon_{\text{cis}} > \varepsilon_{\text{axial}} > \varepsilon_{\text{trans}}$. We see that at very small detuning ($|\nu|$ <0.5Hz), both the cis and the trans flow entrain the cell. However, the cis flow maintains the entrainment for the whole time ($\xi_{\text{cis}}$=1), while the trans flow for a slightly smaller time fraction. This is due to phase-slips in $\Delta\varphi$, and means that the entrainment with the trans flow is less stable. For intermediate detuning (0.5Hz< $|\nu|$ <4Hz), $\xi_{\text{cis}}$ is always larger than $\xi_{\text{trans}}$. In some cases, the cis flow entrains the cell fully whereas the trans flow fails completely (*e.g.*, at $\nu = -2$ Hz in **Fig. 5.3**a). In all, **Fig. 5.3**a shows that: a flow of a given amplitude entrains the cell for a larger fraction of time if it is applied at $\theta = -45°$ (cis flow) as opposed to $\theta = 45°$ (trans flow).

To rule out the possibility that this is due to either the micro-pipette, specific cell culture, or possible directional light source in the environment, the experiments are repeated with cells from multiple cultures, captured on different pipettes, and with different eyespot orientations (~50% heading rightward in the imaging plane). The entrainment profiles of N=11 *wt* cells in TRIS-minimal medium (pH=7.0) are displayed in **Fig. 5.3**b-d. On average, $\varepsilon_{\text{cis}}$ = 2.9 Hz and is 70% larger than $\varepsilon_{\text{trans}}$ = 1.7 Hz.

Furthermore, in **Fig. 5.3**e we show that $\varepsilon_{\text{cis}} > \varepsilon_{\text{trans}}$ holds true for all the cells tested (11/11). Each cell is represented by a scatter point in the $\varepsilon_{\text{cis}}$- $\varepsilon_{\text{trans}}$ plane. Being below the identity line ( $\varepsilon_{\text{cis}} = \varepsilon_{\text{trans}}$) indicates that $\varepsilon_{\text{cis}} > \varepsilon_{\text{trans}}$ for this cell, and all cells clearly cluster below the line.

This asymmetric flow entrainability that predominantly favors the cis flow can also be visualized differently by the time fraction of entrainment $\xi$. In **Fig. 5.3**f, experiments conducted with the cis and the trans flow at the same frequency are paired up. A pair of experiments is then plotted as a point in the $\xi_{\text{cis}}$-$\xi_{\text{trans}}$ plane, with $\xi_{\text{cis}}$ and $\xi_{\text{trans}}$ the entrained time fraction of the same cell under the cis and the trans flow respectively. The location of each point on the plane with respect to the identity line $\xi_{\text{cis}}$=$\xi_{\text{trans}}$ marks the relative entrainment effectiveness of the two flows at a particular frequency. 132 experiment pairs for *wt* cells (12 pairs per cell, N=11 cells) are plotted. Most (>90%) of them appear below the identity line, meaning $\xi_{\text{cis}} > \xi_{\text{trans}}$. Within these points, many dwell near the right and the bottom edge of the plot. The right edge corresponds to situations where the cis flow entrains the cell fully ($\xi_{\text{cis}} \approx 1$) while the trans flow is less effective. The bottom edge corresponds to situations where the trans flow completely fails to entrain the cell ($\xi_{\text{trans}} \approx 0$) while cis flow still can.

Altogether, we show unequivocally that, when the two flagella beat in sync and are regarded as a collective oscillator, their difference persists and manifests in the cell's asymmetric entrainability by directional flows.

### 5.3.3. COMPUTATION OF THE HYDRODYNAMIC LOAD ON THE FLAGELLA

After finding that the cis flow is more effective at entraining cells, we then seek to quantitatively relate the entrainment efficiency to the mechanical loads on the *cis* or the *trans* flagellum. To achieve this we use hydrodynamic computations.

We obtain the total drag force **F** and the total viscous power $P$ exerted on a flagellum using the boundary element method described in **Sec. 5.2.5**. With the presence of an external flow, **F** has three distinct origins: first the motion of the flagellum itself, second the motion of the other flagellum, and third the applied flow. From the linearity of the Stokes equations, the flow velocity field can be computed as the superposition of these three components. Additionally, in the previous study [29], the contribution from the other flagellum is confirmed to be negligible when compared to the other two. As a consequence, the total force **F** can be written as $\mathbf{F} = \mathbf{F}_{\text{Self}} + \mathbf{F}_{\text{Flow}}$, and the total viscous power $P$ as $P = P_{\text{Self}} + P_{\text{Flow}}$.

To isolate the contribution of the applied flow, $\mathbf{F}_{\text{Flow}}$ and $P_{\text{Flow}}$, we run the numerical computation twice: once with external flow and once without. Results from the one without the external flow give us $\mathbf{F}_{\text{Self}}$ and $P_{\text{Self}}$. Therefore, we can obtain $\mathbf{F}_{\text{Flow}}$ and $P_{\text{Flow}}$ by subtraction: $\mathbf{F}_{\text{Flow}} = \mathbf{F} - \mathbf{F}_{\text{Self}}$ and $P_{\text{Flow}} = P - P_{\text{Self}}$. Please note that the sign of $P_{\text{Flow}}$ is set to positive when the flagella beat along with the flow, *i.e.* energy is transferred from the flow to the cell.

Computations are based on videos of a representative cell which originally beats at ~50 Hz, and is fully entrained by the axial, the cis and the trans flow at 49.2 Hz. Flow amplitudes are set to 780 µm/s, as is the case for the experiments. Computations begin with the onset of background flows, and each covers a period of 30 beats (500 frames, 801 fps) during which the cell is gradually entrained. The magnitude of the drag force $F_{\text{Flow}} = |\mathbf{F}_{\text{Flow}}|$, and the viscous power of the applied flow $P_{\text{Flow}}$ are computed for each frame. Results for the axial, the cis, and the trans flow, are shown in **Fig. 5.4**a-d, **Fig. 5.4**e-h, and **Fig. 5.4**i-l, respectively. Onsets of the background flows are marked by the dashed lines at t=0. After several cycles shaded in blue, the cell becomes entrained. **Fig. 5.4**c,g,k and **Fig. 5.4**d,h,l show the median $F_{\text{Flow}}$ and $P_{\text{Flow}}$ over the entrained cycles, respectively. Force magnitudes are scaled by $F_0 = 6\pi\mu RU_0 = 9.9$ pN, which is the Stokes drag on a sphere of a radius R = 5 µm, moving at the cells' average free swimming speed $U_0 = 110$ µm/s; while the viscous powers are scaled by $P_0 = F_0U_0 = 6\pi\mu RU_0^2 = 1.1$ fW. Here $\mu = 0.95$ mPa·s is the dynamic viscosity of water at 22 $^o$C.

Under the axial flow, $F_{\text{Flow}}$ and $P_{\text{Flow}}$ are the same for the two flagella, both before and after entrainment, **Fig. 5.4**a-d. For both flagella, the mean drag over an entrained cycle, $\overline{F}_{\text{Flow}} = (\int_0^{2\pi} |\mathbf{F}_{\text{Flow}}| d\varphi)/2\pi$, is 3.4 pN, and the mean power, $\overline{P}_{\text{Flow}} = (\int_0^{2\pi} P_{\text{Flow}} d\varphi)/2\pi$, is 3.1 fW, **Fig. 5.4**c-d. Here $\varphi$ is the flagellar phase, where $\varphi = 0$ marks the most forward reaching flagellar shapes. Corresponding flagellar shapes are shown as the upper x-axes of **Fig. 5.4**c,g,k.

The cis (trans) flow exerts a larger drag on the *cis* (*trans*) flagellum. Under the cis flow, the maximum drag on the *cis* flagellum is 10.0 pN, twice as that on the *trans* flagellum. During entrainment, $\overline{F}_{\text{Flow}} = 4.8$ pN for the *cis* flagellum, but is only 2.5 pN for the *trans*, **Fig. 5.4**g. Under the trans flow, this selectivity is reversed, with $\overline{F}_{\text{Flow}} = 2.5$ pN and 4.9 pN for the *cis* and the *trans* flagellum respectively, **Fig. 5.4**k.

For the viscous power $P_{\text{Flow}}$, the selectivity is less straightforward. Under the cis flow,

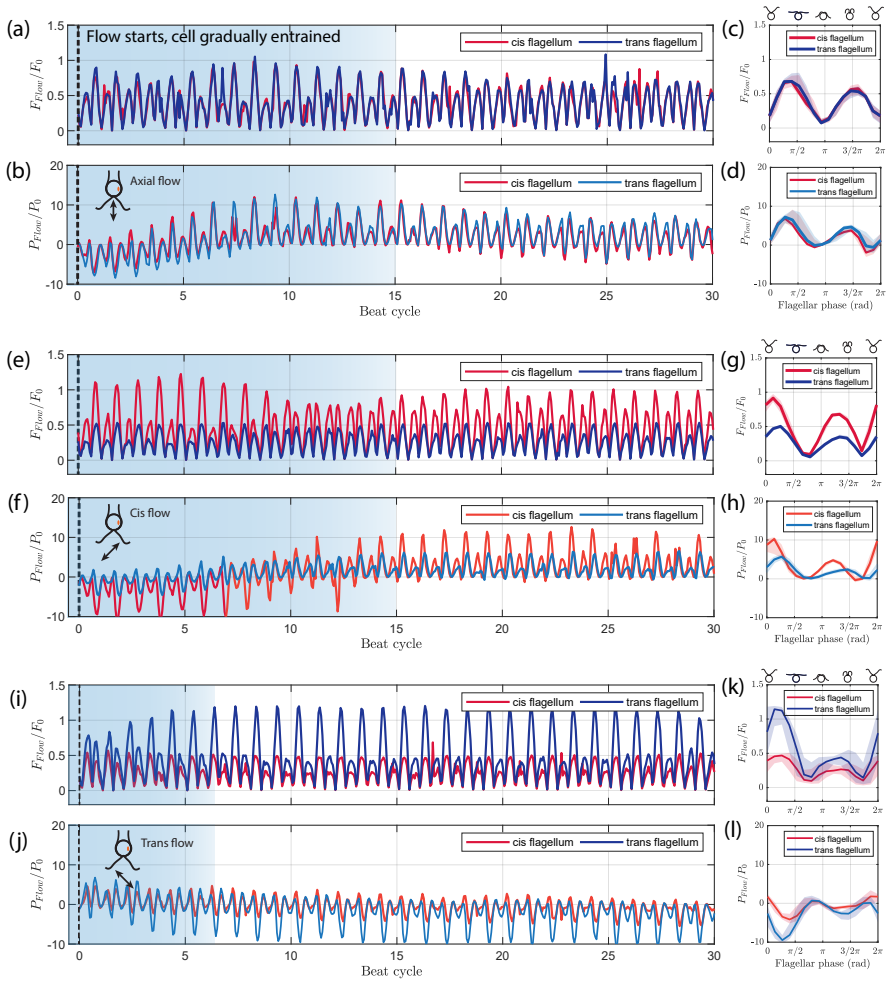


Figure 5.4: **Analyzing the hydrodynamic load on the flagella by a boundary element method (BEM)** BEM computations are based on recordings of different directional flows (49.2 Hz) entraining the same cell ($f_0 \approx 50$ Hz). (a-b) Computed drag force and viscous power exerted by the axial flow ($\theta = 0°$) on the *cis* (red) and the *trans* (blue) flagellum for 30 cycles. Black dashed lines mark the onset of the applied flow. Blue shading in the background represents the beating cycles before the cell is entrained. (c-d) Magnitude of the drag forces $F_{\text{Flow}}$ and viscous power of the flow $P_{\text{Flow}}$ averaged over the entrained cycles. The solid lines and the shaded areas represent the median and the interquartile range respectively. (e-h) Same as (a-d) but for the cis flow ($\theta$=-45°). (i-l) Results for the trans flow ($\theta$=45°). Scaling factors $F_0$=9.9 pN and $P_0$=1.1 fW.

mean viscous power over an entrained cycle is $\overline{P}_{\text{Flow}}$ = 4.0 fW and 2.2 fW, for the *cis* and the *trans* flagellum respectively, **Fig.** 5.4h. Under the trans flow, $\overline{P}_{\text{Flow}}$ = -0.7 fW and -2.9 fW, for the *cis* and the *trans* flagellum respectively, **Fig.** 5.4i. These negative values suggest that the flagella are effectively working against the applied flow.

Surprisingly, in spite of beating against the trans flow ($P_{\text{Flow}} < 0$) for most of the time,

a cell can still be entrained. We therefore investigate how the cell is phase-locked to the flows. **Fig.** 5.5 shows the Poincaré sections at the moments of the peak external flow speed. **Fig.** 5.5a-c (**Fig.** 5.5d-f) display the snapshots when the external flow velocity maximizes upward (downward) in y direction. Flagellar shapes from 15-25 entrained cycles are collapsed into the point clouds, with the solid lines showing the median shape. Mean flagellar velocity are plotted as vectors along the *cis* (red, right) and the *trans* (blue, left) flagellum.

Under the axial (**Fig.** 5.5a-b) and the cis flow (**Fig.** 5.5d-e), the phase-locking of the cell is similar, and is such that when the external flow velocity peaks upward, the cell is approximately in the middle of its power stroke (**Fig.** 5.5a-b), where its flagellar velocity also maximizes and points upward. Similarly, when the external flow velocity peaks downward, the flagellar velocity peaks downward too, approximately. In other words, under both the axial and the cis flow, the cell's flagellar beating works along with the external flows.



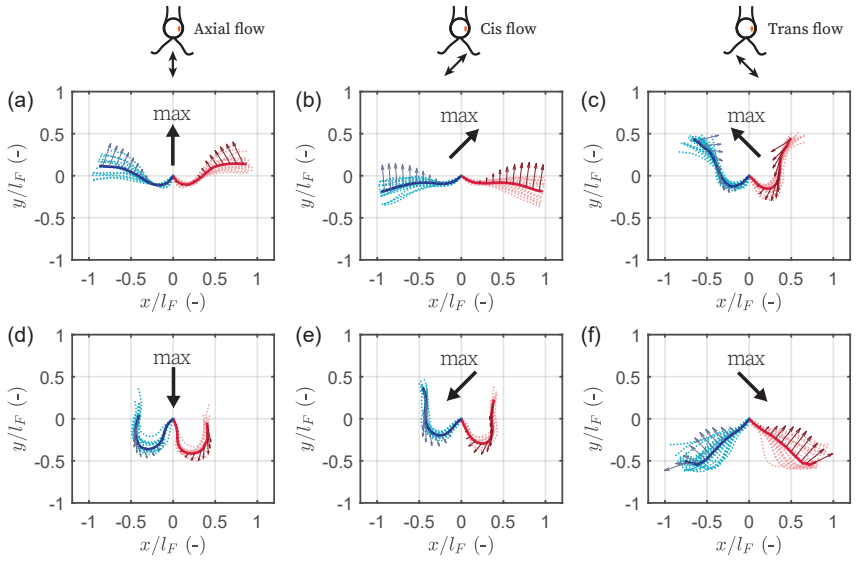


Figure 5.5: **Poincaré section of the flow entrainment.** The shapes and velocities of the *cis* (red) and the *trans* flagellum (blue) at the peak velocities of the axial (a,d), the cis (b,e), and the trans flow (c,f). Point clouds represent shapes collapsed from 15-25 entrained cycles. Solid line represents the median shape. Vectors: mean flagellar velocity. (a)-(c) correspond to when the flow speed maximizes upwards in y direction. (d)-(f) correspond to when it maximizes downwards. x and y axes are scaled by the flagellar length $l_F$.

On the other hand, for the trans flow (**Fig.** 5.5c,f), the phase-locking is such that both flagella work against the external flow in y direction constantly. Meanwhile, in the x direction, the *trans* flagellum also works against the flow, but the *cis* now works along. Therefore, this last factor must help at establishing the entrainment; and it points to an even more important role of the *cis* flagellum in flow entrainment.

Lastly, in **Fig.** 5.6, we plot the cell's coupling strengths as a function of the loads on

its flagella. $\overline{F}_{\text{Flow}}$ and $\overline{P}_{\text{Flow}}$ are employed to characterize such loads. In **Fig.** 5.6a-b and **Fig.** 5.6c-d, $\varepsilon$ is plotted as a function of $\overline{F}_{\text{Flow}}$ and $\overline{P}_{\text{Flow}}$ on the two flagella, respectively. Comparing **Fig.** 5.6a with **Fig.** 5.6b, and **Fig.** 5.6c with **Fig.** 5.6d, we see that $\varepsilon$ correlates well with both the force and the power on the *cis* flagellum but not with those on the *trans* flagellum[1]. This is the same message conveyed by **Fig.** 5.5.

In all, by consulting hydrodynamic computations, we find the determinant of $\varepsilon$ to be the load on the *cis* flagellum, while the load on the *trans* appears to play a negligible role.

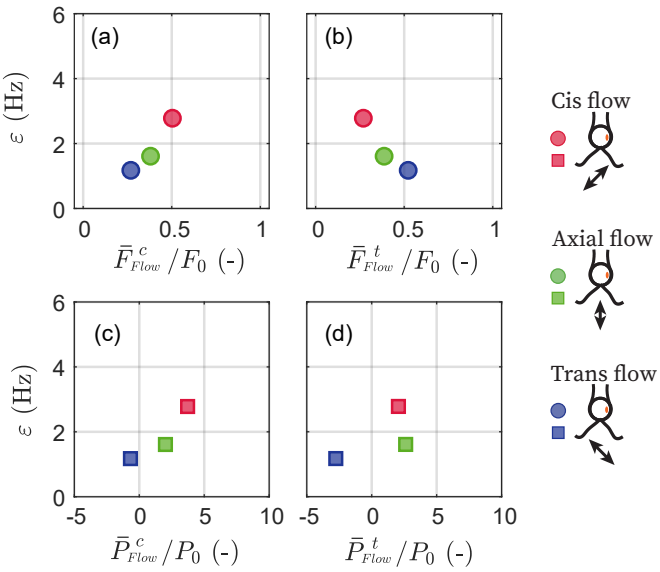


Figure 5.6: **Resolving the determinant of $\varepsilon$.** Relation between $\varepsilon$ and the flagellar loads. (a-b) $\varepsilon$ as a function of the mean magnitude of the drag force on the *cis* (a) and on the *trans* (b) flagellum. (c-d) $\varepsilon$ as a function of the mean viscous power on the *cis* (c) and on the *trans* (d) flagellum. Color coding reflects the flow direction; circles represent forces, squares represent powers.

### 5.3.4. ASYMMETRIC FLOW ENTRAINABILITY IS NOT AFFECTED BY CALCIUM DEPLETION

CR cells actively exchange calcium with the environment through calcium channels in the flagellar and cell membranes [39–43], and this leads to various behaviours such as phototaxis, photoshock response, mechano-perception, mechanical agitation, deflagellation, and basal body contraction [43–47].

[1] Admittedly, there is obvious anti-correlation between $\varepsilon$ and the load on the *trans* flagellum. However, we argue that it is not logical that weaker forcing on the *trans* would lead to stronger flow entrainment. Instead, the anti-correlation is most likely due to the total force on the two flagella being a constant $\sim 0.7F_0$ (**Fig.** 5.12a), so that less force on the *trans* simply means more force on the *cis*.

Particularly, calcium concentration is known to modulate the beating of the *cis* and the *trans* flagellum differently. In live cells, as well as in reactivated cell models, calcium depletion is found to inactivate the *trans* flagellum but not the *cis*, *i.e.* it leads to a reduced beating amplitude or a completely stopped beating of the *trans* flagellum but not of the *cis* flagellum [27].

To test whether this also affects the cell's asymmetric coupling strength to external flows, we apply the directional flows to cells subjected to calcium depletion. Calcium depletion is induced following the protocol described in [46]. Cells examined here are washed and resuspended with TRIS-minimal medium + 0.5 mM EGTA (pH=7.0). Free calcium concentration is estimated to drop from 0.33 mM in the TRIS-minimal medium, to 0.01 $\mu$M in the altered medium [46]. Experiments start at least one hour after the resuspension in order to acclimate the cells.



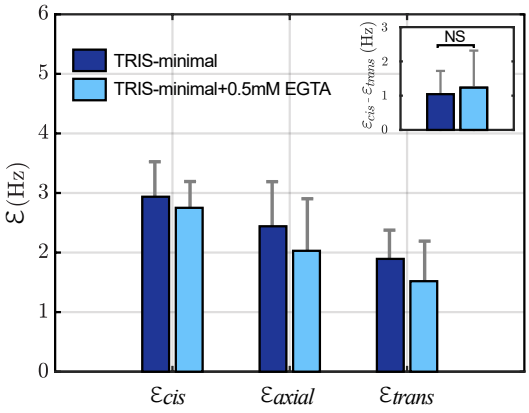


Figure 5.7: **Asymmetric flow entrainability is not affected by calcium depletion.** The mean coupling strength $\varepsilon$ of *wt* cells with different flows are displayed as bar graphs. Dark blue: N=11 *wt* cells in TRIS-minimal medium (pH=7.0); light blue: N=6 *wt* cells in TRIS-minimal medium + 0.5 mM EGTA (pH=7.0). Error bars: one standard deviation. $\varepsilon_{\text{cis}} > \varepsilon_{\text{trans}}$ holds true for every single cell tested. Inset: statistics of $\varepsilon_{\text{cis}}$- $\varepsilon_{\text{trans}}$ in the two media. NS: not significant, p>0.05, Kruskal-Wallis test, One-Way ANOVA.

The signs of calcium depletion align with previous reports. Similar to [27], the number of freely swimming cells drops significantly in EGTA-containing medium, however, the cells remaining freely swimming are found to be able to beat synchronously for hours after capture. Meanwhile, mechanical deflagellation fails for almost all of the captured cells that beat in sync (18/19), as opposed to cells observed in TRIS-minimal medium, where pipette suction on the flagellum consistently induces flagella shedding [23, 48].

After confirming the calcium depletion, we perform flow entrainment experiments on those cells. **Fig. 5.7** shows the coupling strength $\varepsilon$ of cells with the cis, the axial, and the trans flow. Cells in TRIS-minimal + 0.5 mM EGTA (light blue, N=6) display the same trend as the cells in TRIS-minimal (dark blue, N=11), with $\varepsilon_{\text{cis}} > \varepsilon_{\text{axial}} > \varepsilon_{\text{trans}}$. Mean values of $\varepsilon$ appear to vary slightly, but do not differ with statistical significance (p>0.05,

Kruskal-Wallis test, One-Way ANOVA). $\varepsilon_{\text{cis}} > \varepsilon_{\text{trans}}$ again applies for every single cell under calcium depletion. Moreover, the difference between the coupling strengths, $\varepsilon_{\text{cis}}$-$\varepsilon_{\text{trans}}$, shown in the inset of **Fig. 5.7**, is also not affected by calcium depletion (p>0.05, Kruskal-Wallis test, One-Way ANOVA).

Therefore, we conclude that calcium depletion does not affect the cell's asymmetric flow entrainability.

### 5.3.5. ASYMMETRIC FLOW ENTRAINABILITY IS LOST IN *ptx1*

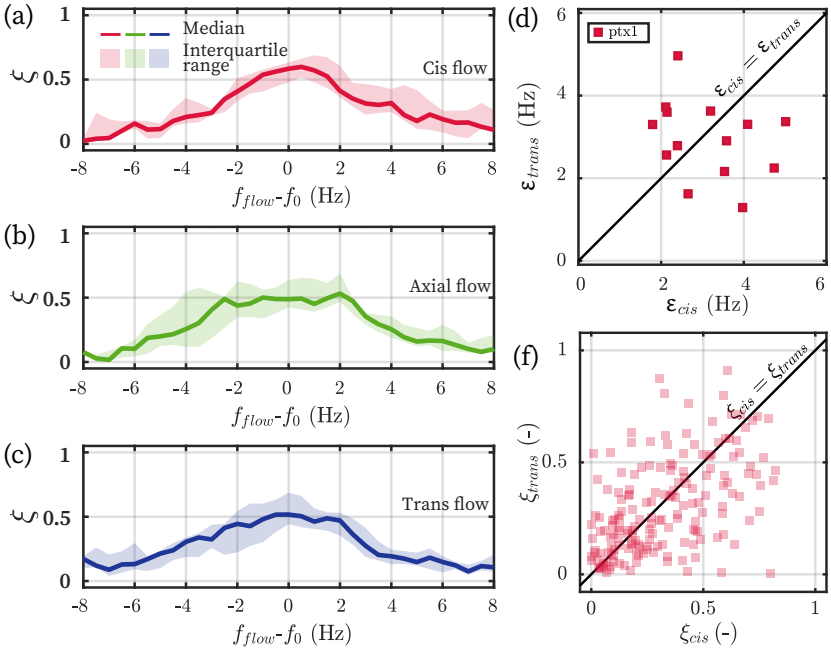


Figure 5.8: **Asymmetric flow entrainability is lost in the flagellar dominance mutant *ptx1*.** (a-c) Flow entrainment profiles $\xi(\nu)$ of the cis (red), the axial (green), and the trans flow (blue) of the *ptx1* mutant. Solid lines and shaded areas represent the mean and the interquartile range over N=14 cells, respectively. (d) Comparing the coupling strengths $\varepsilon_{\text{cis}}$ and $\varepsilon_{\text{trans}}$. Each point represents one cell. Below the identity line $\varepsilon_{\text{cis}} = \varepsilon_{\text{trans}}$ indicates $\varepsilon_{\text{cis}} > \varepsilon_{\text{trans}}$. Half (7/14) of the *ptx1* cells are under the line. (f) Comparing the entrained time fraction under the cis $\xi_{\text{cis}}$ and the trans flow $\xi_{\text{trans}}$ for *ptx1* cells. Each point represents two flow entrainment experiments at the same frequency $f_{\text{flow}}$ in the same cell. $\xi_{\text{cis}}$ and $\xi_{\text{trans}}$ are paired up and represented by a red square in the $\xi_{\text{cis}} - \xi_{\text{trans}}$ plane. Below the identity line $\xi_{\text{cis}} = \xi_{\text{trans}}$ indicates $\xi_{\text{cis}} > \xi_{\text{trans}}$. 154 points are present (12 pairs per cell, N=14 cells), ~50% of which are under the identity line ($\xi_{\text{cis}} > \xi_{\text{trans}}$).

We then test whether the asymmetric flow entrainability exists in *ptx1* cells. In this mutant, both flagella respond similarly to calcium modulation [28] and have similar intrinsic frequencies [22]. As the IP mode is the only mode that can be entrained by external flow (**Sec. 5.3.1**), we report $\xi$ as $\xi = T_{\text{sync}} / T_{\text{IP}}$ for the *ptx1* mutant.

The flow entrainment profiles $\xi(\nu)$ of *ptx1* submitted to the cis, the axial, and the

trans flows are shown in **Fig.** 5.8a-c. The median entrainment profiles under different flows are of similar width and height, and therefore indistinguishable from each other. Nevertheless, at single cell level, we confirm that the asymmetric entrainability does exist: either the entrainment profile $\xi(v)$ under cis flow or that under trans flow can be obviously broader and higher than the other. Additionally, we notice that the shapes of *ptx1* entrainment profiles $\xi(v)$ are less regular, *i.e.* they are often not symmetric around $f_0$ and fluctuate much. As these phenomena signify a stronger noise, we extract coupling strength from fitting flagellar phase dynamics [29, 32, 33]. Details of the fitting method can be found in the **Sec.** 5.6.1 of the supplementary material.

**Fig.** 5.8d displays the $\varepsilon_{\text{cis}}$ and $\varepsilon_{\text{trans}}$ of the *ptx1* cells obtained by fitting. The cells dwell evenly on the two sides of the identity line (7 above and 7 below the line). Therefore, the robust asymmetric entrainability $\varepsilon_{\text{cis}} > \varepsilon_{\text{trans}}$ in *wt* is lost in *ptx1*. **Fig.** 5.8e displays the same message: 154 experiment pairs for *ptx1* cells (12 pairs per cell, N=14 cells) again dwell almost evenly (~50%) around $\xi_{\text{cis}} = \xi_{\text{trans}}$.

Altogether, we confirm that the asymmetric susceptibility to external flow entrainment is lost in the mutant *ptx1*.

5

## 5.4. DISCUSSION

### 5.4.1. *wt* CELLS USES THE *cis* FLAGELLUM TO COUPLE TO EXTERNAL FLOWS

Motivated by the fact that the synchronous beating frequency $f_0$ of *wt* is much closer to the intrinsic frequency of the *cis* flagellum, we start investigating the *cis-trans* flagellar difference during synchronous beating by testing whether the two flagella can be entrained by an external source (flow) at their intrinsic beating frequencies, **Sec.** 5.3.1. However, we find it impossible to entrain them at frequencies other than $f_0$. In addition, it is also impossible to entrain the anti-phase (AP) synchronous beating of *ptx1* around the AP beating frequency. Therefore, the two flagella beating synchronously in-phase is considered as one collective oscillator, and we only focus on the in-phase beating in this study.

As the collective oscillator - the cell and its flagella beating in phase - is symmetric around the cell-pipette axis, we apply flows of the same symmetry, and investigate the cell's response, so as to reveal the *cis-trans* flagellar difference.

Among the three directional flows: the cis, the axial, and the trans flow, a trend in the coupling strength is repetitively observed, which is $\varepsilon_{\text{cis}} > \varepsilon_{\text{axial}} > \varepsilon_{\text{trans}}$, **Fig.** 5.3a-d. Especially, $\varepsilon_{\text{cis}} > \varepsilon_{\text{trans}}$ applies for all the *wt* cells tested. This significant asymmetry in the cell's entrainability reveals that the *cis* and the *trans* flagellum do play different roles in external flow entrainment.

Therefore, we use hydrodynamic computations to resolve what determines the coupling strength between a cell and a directional flow. With a boundary element method, we compute the drag forces and the viscous powers exerted on the two flagella, **Fig.** 5.4. Intriguingly, the cell is entrained by the trans flow such that it works against the flow most of the time ($P_{\text{flow}} < 0$ in **Fig.** 5.4l). We visualize the phase-locking between the flagella and the flows by the Poincaré sections at the moments of the maximized external flow speed, **Fig.** 5.5.

**Fig.** 5.5c,f highlight the determinant role of the *cis* flagellum in the external flow

entrainment. The sole drive of the trans flow entrainment turns out to be the alignment between the lateral velocity of the *cis* flagellum and the external flow, in spite of the *trans* flagellum working against the flow constantly.

Furthermore, we quantitatively study the relation between the coupling strength and the hydrodynamic loads on each flagellum. Plotting $\epsilon$ as a function of those computed metrics ($\overline{F}_{\text{flow}}$, $\overline{P}_{\text{flow}}$), we confirm that the determinant of $\epsilon$ is the load on the *cis* flagellum, **Fig. 5.6**.

Lastly, as calcium concentration is known to modulate the beating of the *cis* and the *trans* flagellum differently, we test whether calcium depletion affects the asymmetric flow entrainability in the *wt* cells. In the experiments, we apply 0.5 mM of calcium chelator EGTA to deplete the free environmental calcium [46]. We confirm by the much reduced fraction of freely swimming cells, and by the disabled deflagellation of the ones remaining freely swimming, that the cells are under calcium depletion. However, the asymmetric flow entrainability persists, **Fig. 5.7**. The only change is a slight decrease in the coupling strength, which can possibly be explained by the model proposed by [49]. In the model, a cell's coupling strength with external flow depends on the ratio of the rate of mechanical power of flagellar beating, to the rate of the cell's total chemical energy consumption. As a cell under osmotic stress is likely to consume more chemical energy to maintain homeostasis, and we do not find the mechanical power of flagellar beating (frequency and swept area) to change under calcium depletion, the ratio will decrease and hence the coupling strength decreases. Therefore, we conclude that calcium depletion does not affect the asymmetric flow entrainability in the *wt* cells.

To summarize, our investigation in the *cis-trans* flagellar difference illuminates that the load on the *cis* flagellum determines a cell's coupling strength to external flows, whereas the load on the *trans* appears irrelevant. In other words, the *trans* flagellum follows the *cis* primarily, disregard the external loads applied on it. In this light, the *cis* flagellum can be seen as the regulator of beating, which could explain why the cell's synchronous beating frequency is closer to the *cis* intrinsic frequency. More investigation is needed to gain a mechanistic understanding of this coordinating role of the *cis*. As mechanical interaction through fibrous structures is known to be the dominant flagellar coupling mechanism in *C. reinhardtii* [29], it may again play an important role in this newly found flagellar difference. A possibility is that the rootlets and the basal body-associated fibres [50] together create a mechanical mesh that facilitates unilateral influence between the two flagella.

### 5.4.2. ASYMMETRIC FLOW ENTRAINABILITY IS LOST IN *ptx1*

We also investigate whether the asymmetric flow entrainability exists in the *ptx1* mutant. The mutant does not show flagellar difference in response to calcium [22, 28], nor flagellar difference in intrinsic frequency [22]. By testing *ptx1*, we want to know whether the newly observed flagellar difference can be displayed independently from the previously studied difference in calcium-response and intrinsic frequency.

We confirm that the asymmetric flow entrainability in *ptx1* is lost by two observations. First, over cells, the median entrainment profiles of *ptx1* under different flows appear indistinguishable from each other (**Fig. 5.8**a,c), whereas the entrainment profile of *wt* under the cis flow appears clearly broader than that under the trans flow (**Fig.**

5.3b,d).

Second, whether the asymmetric flow entrainability favors the cis or the trans flow is random in *ptx1*. Only in ~50% of the cases, the cis flow entrains a given *ptx1* cell more effectively. This is shown in both **Fig. 5.8**d and **Fig. 5.8**e, as the cells/experiment pairs distribute evenly around the identity line. Both of these results are in clear contrast to those of *wt*: all the *wt* cells (11/11) cluster below the identity line in **Fig. 5.3**e, and more than 90% points appear below the identity line in **Fig. 5.3**f, indicating that $\varepsilon_{\text{cis}} > \varepsilon_{\text{trans}}$ and $\xi_{\text{cis}} > \xi_{\text{trans}}$ hold true consistently.

Altogether, the asymmetric flow entrainability is lost in the *ptx1* mutant. Therefore, the mechanism at the origin of this newly found flagellar difference that we observe, could have a relation with the mechanisms that give rise to the flagellar difference in intrinsic frequencies and/or calcium response.

Last but not least, throughout our experiments with the *ptx1* mutant, we find its IP beating to be not exactly the same as the synchronous beating of *wt*, as it is much noisier, *i.e.* the interflagellar phase-locking is less stable and the beating frequency fluctuates much more. It leads to the Arnold tongue shown in **Fig. 5.2**b being less symmetric in shape, and having a broader transition zone between entraining frequencies and non-entraining frequencies. It also leads to the entrainment profiles being broader, lower, and less regular than those of *wt* (**Fig. 5.3**a-d and **Fig. 5.8**a-c). For more details regarding the noise we point the readers to **Sec. 5.6.3** in the supplementary material.

## 5.5. CONCLUSION

This study is motivated by the fact that the *cis-trans* flagellar difference during synchronous beating, while largely unstudied, is highly relevant to steering and hence to understanding the tactic behaviours of *C. reinhardtii*.

After confirming that it is not possible to entrain the synchronous flagellar beating at the intrinsic frequencies of either flagellum, we proceed with comparing the different responses of the beating with flows along different directions.

We focus on comparing the entrainability of flagellar beating by the cis and the trans flow, which are along the directions that are about perpendicular to the *cis* and the *trans* flagellum, respectively, at the start of the power stroke. For all cells tested, the cis flow entrains the cell more effectively, and its coupling strength ( $\varepsilon_{\text{cis}}$) is on average 70% larger than that of the trans flow ( $\varepsilon_{\text{trans}}$). We resolve the differentiating factor between the flows to be the load on the *cis* flagellum by using hydrodynamic computations. We further subject the cells to calcium depletion, which is a condition known to affect the beating of the *cis* and *trans* flagellum differently, but the asymmetric flow entrainability turns out to be unaffected. Lastly, we test if this newly found flagellar difference is displayed by the mutant *ptx1*, which displays no known flagellar difference. As a result, the asymmetric flow entrainability is confirmed to be lost in *ptx1*.

To better understand the underlying mechanism of this newly found flagellar difference reported here, more research is needed. One possible direction to investigate is to characterize the mechanical property of the intra-cellular connecting and anchoring structures of the two flagella.

## 5.6. SUPPLEMENTARY MATERIAL

### 5.6.1. COMPARING THE COUPLING STRENGTH EXTRACTED BY TWO DIFFERENT METHODS

In this study, the coupling strength $\varepsilon$ in *wt* cells are mainly measured by the half of the width in $\nu$ where $\xi(\nu)$ >0.5, as noise is proven to be weak ($T_{\text{eff}} \ll \varepsilon$) in *wt* [29, 32]. However, this is not applicable for the *ptx1* dataset. Therefore, in this case, we obtain $\varepsilon$ from the dynamics of the phase difference between the cell and the external flows.

The method has been described in [33] and employed previously [29, 32]. The principle of working is that, when a cell is entrained, phase-locking between the cell and the flow results in a peaked probability distribution of $\Delta\varphi$ in [0,2$\pi$], whereas the distribution will be uniform if the cell beats independently from the flow. The distribution, $P(\Delta\varphi)$, can be mathematically derived from the Adler equation (**Eq. (1)** in the main text):

$$P(\Delta\varphi) = \int_{\Delta\varphi}^{\Delta\varphi+2\pi} exp(\frac{V(\Delta\varphi') - V(\Delta\varphi)}{T_{\text{eff}}}) d\Delta\varphi' \tag{5.3}$$

Here $V(\Delta\varphi) = \nu\Delta\varphi - \varepsilon cos(\Delta\varphi)$ is a wash-board potential. Therefore, by fitting the experimental probability distribution with Eq. (5.3), we obtain $\varepsilon$, $T_{\text{eff}}$, and $f_0$ altogether. For more details the readers are referred to **Appendix.** C.

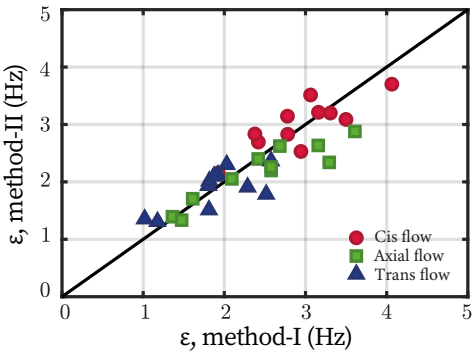


Figure 5.9: **Equivalence of extracting coupling strength $\varepsilon$ by two methods** Each point represents one cell under either the axial (green square), the cis (red circle), or the trans flow (blue triangle). The x coordinate of the point is the coupling strength $\varepsilon$ measured by the half width of entrainment profile $\xi(\nu) > 0.5$ (method-I); and the y coordinate is obtained by fitting the flagellar phase dynamics (method-II).

For all *wt* cells tested in the TRIS-minimal medium (N=11), we measure the coupling strength $\varepsilon$ both by the half width of the entrainment profile $\xi(\nu)$ (method-I) and by fitting the flagellar phase dynamics (method-II) [29, 32]. Values obtained by the two methods are plotted against each other, as shown in **Fig. 5.9**. Each point represents one cell under either the axial (green square), the cis (red circle), or the trans flow (blue triangle). All points centre around the identity line, showing excellent agreement between $\varepsilon$ obtained by both methods.

### 5.6.2. DEPENDENCY OF THE COUPLING STRENGTH ON THE FLAGELLAR LOAD

To further substantiate the dependency of $\varepsilon$ on the force and power on the *cis* flagellum, we include an extra flow direction in the experiment and computation. The same cell shown in **Fig. 4** is further entrained the flow along $\theta = 90°$, termed the cross flow. **Fig. 5.10** shows the computed load during entrainment; and **Fig. 5.11** shows the phase-locking of the entrainment. Figure settings are similar to **Fig. 5.4** and **Fig. 5.5** in the main text, respectively.

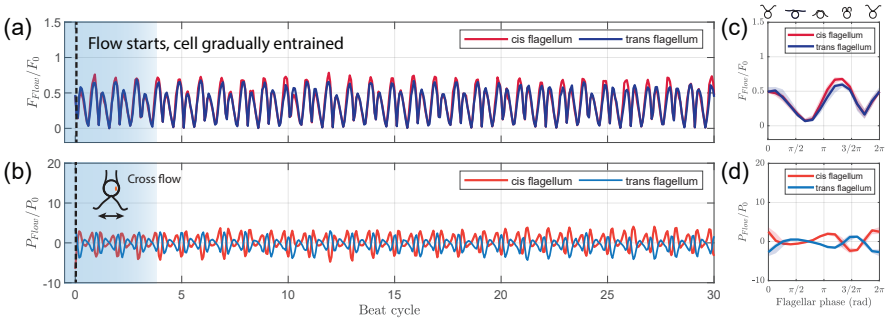


Figure 5.10: **Computation results for the cross flow.** (a-b) Drag forces (a) and viscous powers (b) of the cross flow. Black dashed lines: the onset of the background flow. Blue shading: cycles before the cell is entrained. (c-d) Magnitudes of the drag forces $F_{\text{flow}}$ (c) and viscous powers $P_{\text{flow}}$ (d) of the flow averaged over the entrained cycles. Solid lines and shaded areas in (c-d): the median and the interquartile range.

Under the cross flow, the mean drag force magnitudes on the *cis* and the *trans* flagellum over an entrained cycle, $\overline{F}_{\text{flow}}$, are 3.7 pN and 3.4 pN, respectively. The flow's mean viscous powers over an entrained cycle $\overline{P}_{\text{flow}}$ are -0.16 fW and -0.46 fW, for the *cis* and the *trans* flagellum, respectively.

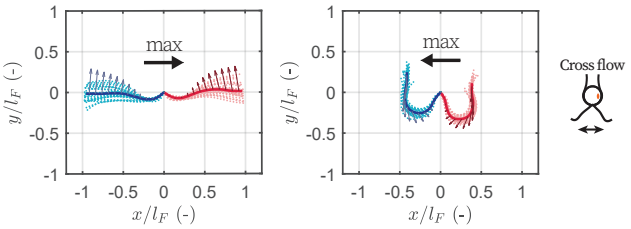


Figure 5.11: **Poincaré section of the flow entrainment.** The shapes and velocities of the *cis* (red) and the *trans* flagellum (blue) at the moments of the peak velocities of the cross flow. Point clouds represent shapes collapsed from 25 entrained cycles. Solid lines: median shapes. Vectors: mean flagellar velocity. Thick arrows: peak velocity directions. x and y axes are scaled by the flagellar length $l_F$.

Adding the computed loads under the cross flow to **Fig. 5.6** in the main text, we obtain **Fig. 5.12**. Highlighted in **Fig. 5.12**b and **Fig. 5.12**e, the extra data points (black symbols) agree well with the trend obtained previously.

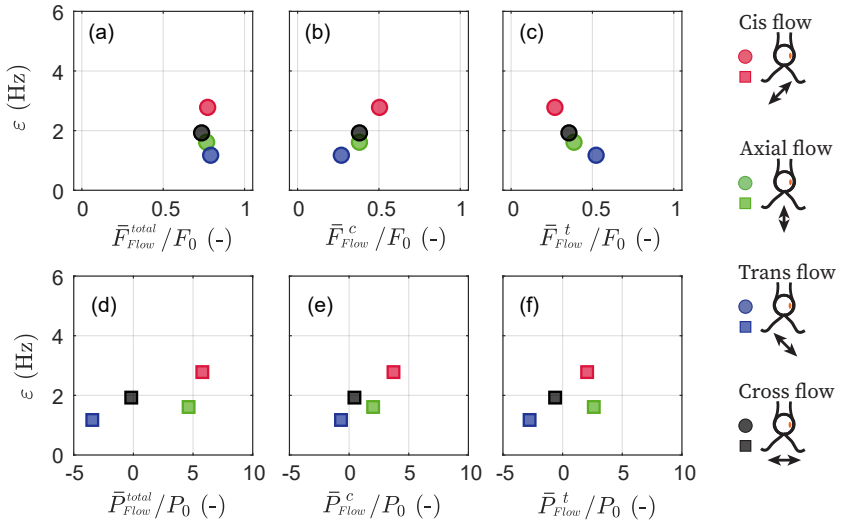


Figure 5.12: **Resolving the determinant of $\varepsilon$.** Relation between $\varepsilon$ and the load on the flagella by the flows. (a-c) $\varepsilon$ against the mean magnitudes of drag force on: both flagella in total (a), on the *cis* flagellum (b), and on the *trans* flagellum (c). (d-f) $\varepsilon$ against the mean viscous powers on: both flagella in total (d), on the *cis* flagellum (e), and on the *trans* flagellum (f).

### 5.6.3. FREQUENCY FLUCTUATION OF THE IN-PHASE (IP) MODE OF THE *ptx1* MUTANT

In the main text, we show that the entrainment profile of *ptx1* is lower, broader, and less regular than that of *wt*, and we argue that it does not weaken the conclusion that the asymmetric entrainment susceptibility is lost in *ptx1*. Here we show more details about the stronger noise in beating frequency of *ptx1*, how it has led to the lower, broader, and less regular entrainment profile $\xi(\nu)$, and why it does not weaken our conclusion.

The IP mode of synchronous beating in *ptx1* mutant has a similar waveform and frequencies to the breaststroke beating of *wt* cells [28, 37]. However, after close inspection, we find that the frequency of the IP mode fluctuates much more than its counterpart in *wt* cells.

**Fig. 5.13** displays how the frequency of captured *ptx1* cells beating under no external flow fluctuates over time. Over 30 seconds (~1500 beating), compared to a typical frequency distribution of *wt* (**Fig. 5.13**a) which appears as a narrow peak centred at $f_0$, both the IP and the AP mode of *ptx1* cells fluctuate much more, shown as the much broader peaks in **Fig. 5.13**b-e. Such difference is quantified in **Fig. 5.13**f. We display the mean beating frequency, $\langle f_0 \rangle$, and the standard frequency deviation, $\sigma(f_0)$, over 30 seconds of recording for each cell. The breaststroke beating of *wt*, the IP, and the AP mode of *ptx1* each forms a cluster. While *wt* clusters tightly around $\big(\langle f_0 \rangle, \sigma(f_0)\big) = (50.5 \pm 2.6, 0.8 \pm 0.3)$ Hz (mean±std.), the IP and the AP mode of *ptx1* cluster loosely around $(47.4 \pm 3.1, 3.4 \pm 0.9)$ Hz and $(67.6 \pm 2.1, 1.9 \pm 0.7)$ Hz, respectively. Particularly,

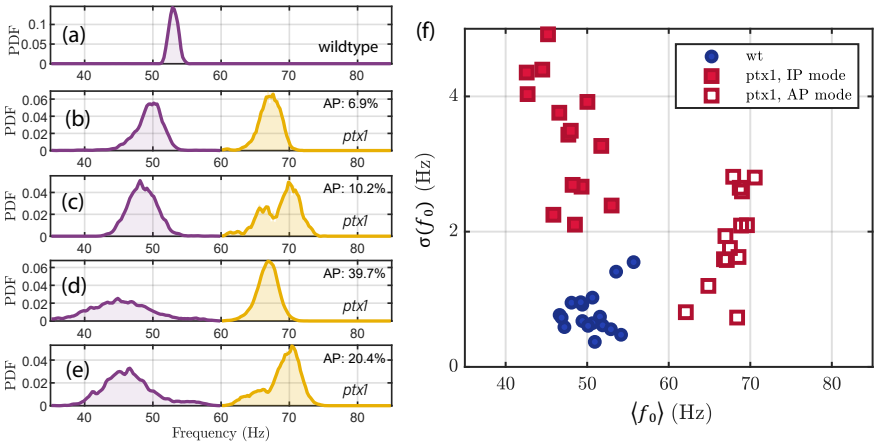


Figure 5.13: **Stronger frequency fluctuation of the IP mode of *ptx1* cells.** (a-e) Representative probability distributions of the beating frequency of 1 *wt* (a) and 4 *ptx1* cells (b-e) over 30 seconds. Probability distributions of the IP (purple) and AP mode (yellow) are respectively normalized for better visualization. The time fractions of the AP mode are noted in each panel. (f) Each *wt* and *ptx1* cell is represented by its mean beating frequency, $\langle f_0 \rangle$, and the standard deviation of beating frequency over time $\sigma(f_0)$. IP and AP mode of each *ptx1* cell are displayed separately in solid and empty red squares.

$\sigma(f_0)$ of *ptx1*'s IP mode can be 10 folds larger than that of *wt*'s breaststroke gait.

Observation from the video recordings further illuminates this fluctuation. **Fig. 5.14** shows how such large variation in frequency happens. The duration of 20 consecutive beats is shown in **Fig. 5.13**d. From beat No.3 to No.8, which is ~0.1 s, cycle duration increases dramatically, and the corresponding beating frequency plummets from 50 Hz to 35 Hz. After this, the beating switches back to 50 Hz over one cycle (No.9).

From multiple observations, we conclude that the fluctuation results from a randomly postponed start of the recovery stroke. During this postponement, flagella stagnate along the sides of the cell body, shown as the upper row of snapshots in **Fig. 5.14**

Such large and sudden variation in $f_0$ of *ptx1*'s IP mode, will destabilize any entrainment by the flow, making its entrainment profile lower, broader, and less regular than *wt*'s. Under a flow of given frequency $f_{\text{flow}}$, $f_0$ fluctuations equal to the fluctuations in detuning $\nu = f_{\text{flow}} - f_0$. When $\nu$ suddenly varies to a value outside the range $[-\varepsilon, \varepsilon]$, entrainment fails. Meanwhile, the strongly varying $\nu$ also means that, at each $f_{\text{flow}}$, there can be a fraction of time when $\nu$ varies into the range $[-\varepsilon, \varepsilon]$, so that the cell gets entrained.

However, the presence of stronger fluctuations cannot explain the loss of the consistent asymmetry in flow entrainability. Although the stronger fluctuations in $f_0$ render the entrainment profiles of each cell less regular and more flat than those of a *wt* cell, it applies equally for entrainment experiments with the cis and the trans flows. Therefore, given that there is a consistent difference between the entrainment profiles of the cis and the trans flow, it will still be present in the median profile. In fact, notwithstanding the strong noise, we still observe clearly that either the profile $\xi(\nu)$ of the cis or the trans flow

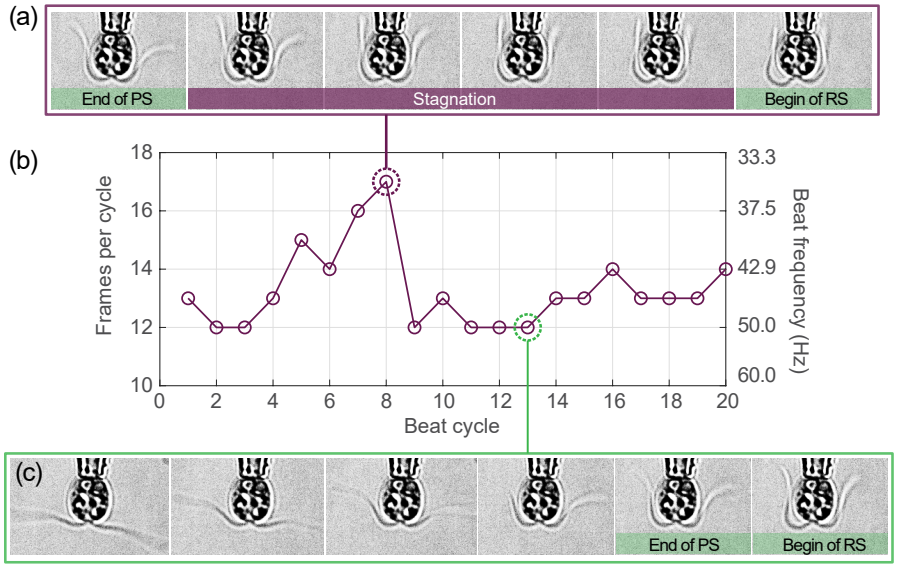


Figure 5.14: **Beating frequency fluctuates greatly and abruptly in the IP mode of *ptx1* cells** (a) Start of the recovery stroke (RS) in an extremely slow IP cycle of *ptx1*. Frame rate: 600 fps. (b) Duration of 20 consecutive cycles of the *ptx1* cell shown in **Fig. 5.13**d. Purple circle: the slow cycle (No.8) shown in (a). Green circle: an cycle with no obvious difference from a synchronous cycle of *wt* cells, whose detail is shown in (c)

to be higher and broader at single cell level. Therefore, median entrainment profiles become identical not because the strong noise has rendered them identical, but because neither $\xi_{\text{cis}}(v)$ nor $\xi_{\text{trans}}(v)$ is consistently higher and broader than the other.

## 5.7. AUTHOR CONTRIBUTIONS

D.T. conceived the study. D.W. and G.Q. carried out the experiments, analyzed the data. D.W. drafted the manuscript. M.A. and D.T. supervised the project and critically revised the manuscript.

## 5.8. ACKNOWLEDGMENTS

The authors thank R. Kieffer for technical support.

## REFERENCES

[1] D. R. Brumley, F. Carrara, A. M. Hein, Y. Yawata, S. A. Levin, and R. Stocker, *Bacteria push the limits of chemotactic precision to navigate dynamic chemical gradients*, Proceedings of the National Academy of Sciences **116**, 10792 (2019).

[2] S. Smriga, V. I. Fernandez, J. G. Mitchell, and R. Stocker, *Chemotaxis toward phyto-*

*plankton drives organic matter partitioning among marine bacteria,* Proceedings of the National Academy of Sciences **113**, 1576 (2016).

[3] P. Hegemann and P. Berthold, *Chapter 13 - sensory photoreceptors and light control of flagellar activity,* in *The Chlamydomonas Sourcebook (Second Edition)*, Vol. 3, edited by E. H. Harris, D. B. Stern, and G. B. Witman (Academic Press, London, 2009) pp. 395–429.

[4] N. Ueki, S. Matsunaga, I. Inouye, and A. Hallmann, *How 5000 independent rowers coordinate their strokes in order to row into the sunlight: Phototaxis in the multicellular green alga volvox,* BMC Biology **8**, 103 (2010).

[5] J.-B. Raina, V. Fernandez, B. Lambert, R. Stocker, and J. R. Seymour, *The role of microbial motility and chemotaxis in symbiosis,* Nature Reviews Microbiology **17**, 284 (2019).

[6] K. Son, D. R. Brumley, and R. Stocker, *Live from under the lens: exploring microbial motility with dynamic imaging and microfluidics,* Nature Reviews Microbiology **13**, 761 (2015).

[7] M. L. Ginger, N. Portman, and P. G. McKean, *Swimming with protists: perception, motility and flagellum assembly,* Nature Reviews Microbiology **6**, 838 (2008).

[8] S. M. King and R. Kamiya, *Chapter 6 - axonemal dyneins: Assembly, structure, and force generation,* in *The Chlamydomonas Sourcebook (Second Edition)*, edited by E. H. Harris, D. B. Stern, and G. B. Witman (Academic Press, London, 2009) pp. 131–208.

[9] C. Brokaw, R. Josslin, and L. Bobrow, *Calcium ion regulation of flagellar beat symmetry in reactivated sea urchin spermatozoa,* Biochemical and Biophysical Research Communications **58**, 795 (1974).

[10] U. Rüffer and W. Nultsch, *Flagellar photoresponses of Chlamydomonas cells held on micropipettes: II. Change in Flagellar Beat Pattern,* Cell Motility and the Cytoskeleton **18**, 269 (1991).

[11] N. Ueki and K. ichi Wakabayashi, *12 - dynein-mediated photobehavioral responses in chlamydomonas,* in *Dyneins (Second Edition)*, edited by S. M. King (Academic Press, 2018) second edition ed., pp. 368 – 385.

[12] Y. Naitoh and H. Kaneko, *Reactivated triton-extracted models of paramecium: Modification of ciliary movement by calcium ions,* Science **176**, 523 (1972).

[13] S. S. Merchant, S. E. Prochnik, O. Vallon, E. H. Harris, S. J. Karpowicz, G. B. Witman, A. Terry, A. Salamov, L. K. Fritz-Laylin, L. Maréchal-Drouard, W. F. Marshall, L.-H. Qu, D. R. Nelson, A. A. Sanderfoot, M. H. Spalding, V. V. Kapitonov, Q. Ren, P. Ferris, E. Lindquist, ..., and A. R. Grossman, *The Chlamydomonas genome reveals the evolution of key animal and plant functions,* Science **318**, 245 (2007).

[14] T. Takahashi and M. Watanabe, *Photosynthesis modulates the sign of phototaxis of wild-type Chlamydomonas reinhardtii,* FEBS Letters **336**, 516 (1993).

[15] N. Ueki, T. Ide, S. Mochiji, Y. Kobayashi, R. Tokutsu, N. Ohnishi, K. Yamaguchi, S. Shigenobu, K. Tanaka, J. Minagawa, T. Hisabori, M. Hirono, and K.-i. Wakabayashi, *Eyespot-dependent determination of the phototactic sign in Chlamydomonas reinhardtii,* Proceedings of the National Academy of Sciences **113**, 5299 (2016).

[16] R. D. Sjoblad and P. H. Frederikse, *Chemotactic responses of Chlamydomonas reinhardtii,* Molecular and Cellular Biology **1**, 1057 (1981).

[17] H. I. Choi, J. Y. H. Kim, H. S. Kwak, Y. J. Sung, and S. J. Sim, *Quantitative analysis of the chemotaxis of a green alga, Chlamydomonas reinhardtii, to bicarbonate using diffusion-based microfluidic device,* Biomicrofluidics **10**, 014121 (2016).

[18] V. Kam, N. Moseyko, J. Nemson, and L. J. Feldman, *Gravitaxis in Chlamydomonas reinhardtii: Characterization using video microscopy and computer analysis,* International Journal of Plant Sciences **160**, 1093 (1999).

[19] K. Yoshimura, Y. Matsuo, and R. Kamiya, *Gravitaxis in Chlamydomonas reinhardtii Studied with Novel Mutants,* Plant and Cell Physiology **44**, 1112 (2003).

[20] R. Kamiya and E. Hasegawa, *Intrinsic difference in beat frequency between the two flagella of Chlamydomonas reinhardtii,* Experimental Cell Research **173**, 299 (1987).

[21] U. Rüffer and W. Nultsch, *Comparison of the beating of cis- and trans-flagella of Chlamydomonas cells held on micropipettes,* Cell Motility and the Cytoskeleton **7**, 87 (1987).

[22] N. Okita, N. Isogai, M. Hirono, R. Kamiya, and K. Yoshimura, *Phototactic activity in Chlamydomonas 'non-phototactic' mutants deficient in $Ca^{2+}$-dependent control of flagellar dominance or in inner-arm dynein,* Journal of Cell Science **118**, 529 (2005).

[23] K. Y. Wan, K. C. Leptos, and R. E. Goldstein, *Lag, lock, sync, slip: the many phases of coupled flagella,* Journal of The Royal Society Interface **11**, 20131160 (2014).

[24] H. Sakakibara and R. Kamiya, *Functional recombination of outer dynein arms with outer arm-missing flagellar axonemes of a Chlamydomonas mutant,* Journal of Cell Science **92**, 77 (1989).

[25] S. Takada and R. Kamiya, *Beat frequency difference between the two flagella of Chlamydomonas depends on the attachment site of outer dynein arms on the outer-doublet microtubules,* Cell Motility and the Cytoskeleton **36**, 68 (1997).

[26] H. Sakakibara, D. R. Mitchell, and R. Kamiya, *A Chlamydomonas outer arm dynein mutant missing the alpha heavy chain,* The Journal of cell biology **113**, 615 (1991).

[27] R. Kamiya and G. B. Witman, *Submicromolar levels of calcium control the balance of beating between the two flagella in demembranated models of Chlamydomonas,* Journal of Cell Biology **98**, 97 (1984).

[28] J. Horst and G. B. Witman, *Ptx1, a nonphototactic mutant of Chlamydomonas, lacks control of flagellar dominance,* The Journal of Cell Biology **120**, 733 (1993).

[29] G. Quaranta, M.-E. Aubin-Tam, and D. Tam, *Hydrodynamics versus intracellular coupling in the synchronization of eukaryotic flagella,* Physical Review Letters **115**, 238101 (2015).

[30] K. Y. Wan and R. E. Goldstein, *Coordinated beating of algal flagella is mediated by basal coupling,* Proceedings of the National Academy of Sciences **113**, E2784 (2016).

[31] U. Rüffer and W. Nultsch, *High-speed cinematographic analysis of the movement of Chlamydomonas,* Cell Motility **5**, 251 (1985).

[32] M. Polin, I. Tuval, K. Drescher, J. P. Gollub, and R. E. Goldstein, *Chlamydomonas swims with two "gears" in a eukaryotic version of run-and-tumble locomotion,* Science **325**, 487 (2009).

[33] A. Pikovsky, M. Rosenblum, and J. Kurths, *Synchronization: A Universal Concept in Nonlinear Sciences*, Cambridge Nonlinear Science Series (Cambridge University Press, 2001).

[34] B. Friedrich, *Hydrodynamic synchronization of flagellar oscillators,* The European Physical Journal Special Topics **225**, 2353 (2016).

[35] J. B. Keller and S. I. Rubinow, *Slender-body theory for slow viscous flow,* Journal of Fluid Mechanics **75**, 705 (1976).

[36] L. Fredrickson-Hemsing, S. Ji, R. Bruinsma, and D. Bozovic, *Mode-locking dynamics of hair cells of the inner ear,* Physical review. E, **86**, 021915 (2012).

[37] K. C. Leptos, K. Y. Wan, M. Polin, I. Tuval, A. I. Pesci, and R. E. Goldstein, *Antiphase synchronization in a flagellar-dominance mutant of Chlamydomonas,* Physical Review Letters **111**, 1 (2013).

[38] U. Rüffer and W. Nultsch, *Flagellar coordination in Chlamydomonas cells held on micropipettes,* Cell Motility and the Cytoskeleton **41**, 297 (1998).

[39] J. S. Hyams and G. G. Borisy, *Isolated flagellar apparatus of Chlamydomonas: characterization of forward swimming and alteration of waveform and reversal of motion by calcium ions in vitro.* Journal of Cell Science **33**, 235 (1978).

[40] H. Harz and P. Hegemann, *Rhodopsin-regulated calcium currents in Chlamydomonas, Nature,* Nature **351**, 489 (1991).

[41] K. Yoshimura, *Mechanosensitive channels in the cell body of Chlamydomonas,* Journal of Membrane Biology **166**, 149 (1998).

[42] P. Collingridge, C. Brownlee, and G. L. Wheeler, *Compartmentalized calcium signaling in cilia regulates intraflagellar transport,* Current Biology **23**, 2311 (2013).

[43] P. Bickerton, S. Sello, C. Brownlee, J. K. Pittman, and G. L. Wheeler, *Spatial and temporal specificity of $Ca^{2+}$ signalling in Chlamydomonas reinhardtii in response to osmotic stress,* New Phytologist **212**, 920 (2016).

[44] M. Hayashi, T. Yagi, K. Yoshimura, and R. Kamiya, *Real-time observation of $Ca^{2+}$-induced basal body reorientation in Chlamydomonas,* Cell Motility and the Cytoskeleton **41**, 49 (1998).

[45] G. L. Wheeler, I. Joint, C. Brownlee, P. Place, and C. Hill, *Rapid spatiotemporal patterning of cytosolic $Ca^{2+}$ underlies flagellar excision in Chlamydomonas reinhardtii,* The Plant Journal , 401 (2008).

[46] K.-i. Wakabayashi, T. Ide, and R. Kamiya, *Calcium-dependent flagellar motility activation in Chlamydomonas reinhardtii in response to mechanical agitation,* Cell Motility and the Cytoskeleton **66**, 736 (2009).

[47] K. Yoshimura, *Stimulus perception and membrane excitation in unicellular alga chlamydomonas,* in *Coding and Decoding of Calcium Signals in Plants*, edited by S. Luan (Springer Berlin Heidelberg, Berlin, Heidelberg, 2011) pp. 79–91.

[48] L. Quarmby and H. Hartzell, *Two distinct, calcium-mediated, signal transduction pathways can trigger deflagellation in Chlamydomonas reinhardtii,* The Journal of Cell Biology **124**, 807 (1994).

[49] G. S. Klindt, C. Ruloff, C. Wagner, and B. M. Friedrich, *Load response of the flagellar beat,* Physical Review Letters **258101**, 1 (2016).

[50] S. K. Dutcher and E. T. O'Toole, *The basal bodies of Chlamydomonas reinhardtii,* Cilia **5**, 1 (2016).

# 6

# Outlook

*To live, to err, to fall, to triumph, to recreate life out of life.*

James Joyce

## 6.1. STUDYING THE DYNAMICS OF FLAGELLAR FREQUENCY WITH OTV

In **Chap. 2**, **Chap. 3**, and **Chap. 4**, we have demonstrated the spatiotemporal resolution of the OTV technique. Another merit of this technique is that, compared to the image-based flow velocimetry techniques, the OTV read-out takes negligible disk space, and is computationally much lighter. For example, monitoring flow velocity at a given point for 1 min at 1 kHz by OTV takes ~ 1 MB, while the corresponding video would take at least 1 GB disk space. To further calculate the flow velocity from the raw OTV recording, only one step of linear conversion is needed, whereas to extract the flow field from image sequences requires multiple processes that are computationally more intensive, *e.g.*, particle tracking and convolution. This feature makes the OTV technique ideal for projects that require monitoring of flow dynamics for a long time with high temporal resolution.

This is especially valuable in studying the evolution of the flagellar beating frequency during regrowth, a process that lasts about an hour [1]. During this process, a cell synthesizes different proteins and assembles a new flagellum or two new flagella with the proteins [1, 2]. The new flagellum(a) starts beating after approximately 15 min, and interflagellar synchrony emerges after approximately 30 min [3].

We are particularly interested in the frequency dynamics of the remaining flagellum after partial deflagellation. The current models based on two coupled oscillators (**Sec. 5.2.4**) would predict, along with the conventional assumption [4], that each of the two oscillators (flagellum) bears an ingrained frequency, so that as soon as the other oscillator is removed, the remaining one will manifest its intrinsic frequency.

We are curious about whether this model is accurate, and how the assembly process and the different states of a new flagellum affect the beating frequency of the remaining one. Although similar experiments have been performed in **Ref.** [3, 5], frequency evolution was not their focus. Now, with the OTV technique, we can track the beating frequency accurately for every second during the whole ~ 1 hour period of regrowth.

A typical experiment goes as follows. We partially deflagellate the captured cell by micro-pipette suction. Right after deflagellation, the cell is reoriented so that its flagellum beats in the focal plane. Then OTV flow measurements start with a flow probe placed near the cell, as shown in **Fig. 6.1**a. The recordings are taken at 1-2 kHz for ~1 h. A window of 1-5 s is used to scan the whole recording, and fast Fourier transformation (FFT) is performed to resolve the frequency composition of the signal within the window span. In each frequency spectrum, each of the cell's frequency modes displays as a peak, whose width shows how stable the beating frequency is. FFT spectra during consecutive time windows are gathered and plotted as a heat map, which is known as a spectrogram, **Fig. 6.1**b. In the diagram, the brighter colors correspond to higher magnitudes and thus indicate the major frequency component at the corresponding times.

In the experiment shown in **Fig. 6.1**b, the *cis* flagellum was deflagellated, and recording started within 60 s after deflagellation. The data suggests that the whole regrowth consists of three stages. The first stage is from the deflagellation to the new flagellum starts beating, shown as the 0-15 min period in **Fig. 6.1**b. There is only one major frequency component in the signal, and it indicates the beating frequency of the remaining

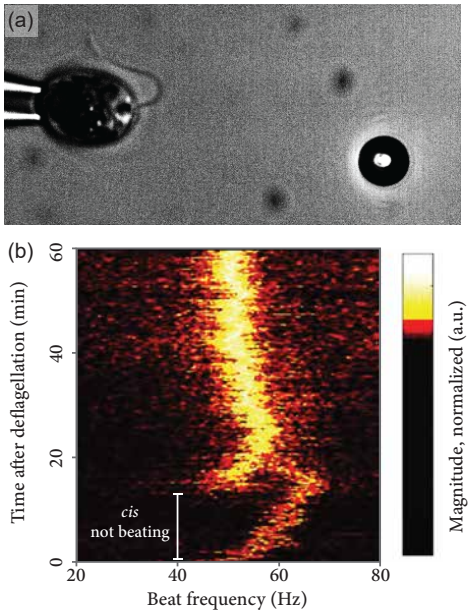


Figure 6.1: **Monitoring flagellar beating frequency with OTV during flagellar regrowth.** (a) Experimental setting: a cell is partially deflagellated and its remaining flagellum beats mostly in the focal plane. An optically trapped bead is placed in the vicinity of the cell. Flow at the position of the bead is recorded by the OTV during the whole regrowth period. (b) Spectrogram of the OTV data. Each horizontal transect of the spectrogram is a frequency spectrum of the signal within a sampling window of 5 s, at the time indicated by the *y* axis.



(*trans*) flagellum. At the end of this stage, the new flagellum has burgeoned but is less than 1 µm long. The second stage is from the new flagellum starting to beat to the two flagella mostly beat in sync, shown as the 15-25 min period in **Fig. 6.1**b. At the end of this stage, the new flagellum reaches approximately 5 µm. The rest is the third stage, where two flagella beat synchronously, and their frequency decreases slightly over time as the new flagellum grows into its full length. The frequency evolution during the last stage is similar to that observed in **Ref.** [3].

When the *cis* is the remaining flagellum, the regrowth consists of three similar stages. In the first stage, 0-15 min, beating frequency of the remaining *cis* flagellum goes lower gradually to ~45 Hz. In the second stage, after ~15 min, the new *trans* begins to beat at a frequency that can be as low as 10 Hz. Then the frequencies of both flagella gradually increase together, with the new *trans* increasing faster, and eventually converge to the same frequency. This process takes ~10 min. In the last stage, the synchronous beating frequency also drops slightly as the new flagellum grows into its full length. Among the cells studied (N=12), where either the *cis* or the *trans* was the remaining flagellum, similar patterns were observed in approximately 70% of them.

Strikingly, data of the first two stages reveal two unreported features: first, the remaining flagellum will not instantaneously shift to its presumed intrinsic frequency but

changes gradually towards it. Second, when the regrown flagellum starts to beat, the "intrinsic frequencies" of both flagella evolve with time also gradually, and finally converges to the synchronous beating frequency. These two features are both in sharp contrast to the model of coupled oscillators.

Our results lead to many intriguing questions regarding the currently assumed "intrinsic frequency" of the two flagella. For example, what modulates the beating frequency of the remaining flagellum during the first 10-15 min, when it is beating "alone"? Does the gradual convergence of the beating frequencies during the second stage mean that the *cis-trans* intrinsic frequency difference could be overestimated? Could the coupling mechanism between the two flagella be dependent on pre-existing biochemical conditions of the two flagella? Lastly, can we resolve the molecular origin of the flagellar frequency difference by investigating the protein synthesis right after partial deflagellation?

Regarding the last question, one promising approach is the single-cell proteomic analysis [6]. This technique is able to amplify the trace amount of different proteins of single cells and reconstruct a spectrum of the abundance of these proteins. The technique has been undertaking rapid progress in the recent decade [7–10]. Very recently, it has been further improved to reveal proteome heterogeneity of embryonic cells during differentiation [9], and macrophage cells [10]. Implementing this technique to resolve the proteome difference between partially deflagellated cells and the intact cells seems to be an attainable goal. Especially, such difference during the first 15 min after partial deflagellation will be crucial to shed light on the molecular basis of flagellar frequency modulation.



Lastly, it needs to be noted that the data we have gathered so far is not conclusive, and this is because several datasets acquired during the early stage of the development of the OTV technique are noisy. To obtain more high-quality data similar to that shown in **Fig. 6.1**, and hence to better support our finding, I would like to list some practical advice about further using OTV in monitoring the flagellar beating frequency:

1. Keep the cell concentration at minimum ($\sim 2\times10^4$ cells/mL). In hindsight, surprisingly, the key factor that determines the success of an OTV experiment, especially the experiments that last long, is the cell concentration. The reason is that cells swimming across the trap almost certainly result in bead loss, and it is almost impossible to recover the measurement settings within 10 min. Missing this critical portion of recording very often leads to the failure of an experiment. Therefore, the more cells there are in the environment, the larger chance an OTV recording fails.

2. Use beads of ~5 μm diameter. Previously, beads of 1-2 μm diameter were often used. However, a bead is lost easily by the entering of small particles (0.5-1 μm, possibly cell debris) into the trap. Even when the bead is not lost, the signal-to-noise ratio would be deteriorated afterwards. In general, beads much larger than the particle size are much less affected, and better suits the purpose of monitoring the flow for a long time. However, on the other hand, one should also avoid using too large beads (*e.g.*, 10 μm diameter), as trapping larger beads with the same stiffness requires higher laser power, and the stronger laser occasionally disrupts the

flagellar synchrony. 5 µm bead trapped with a stiffness of 10 pN/µm is empirically an optimal choice.

3. Get rid of dead or immobile cells from the suspension as much as possible. An OTV experiment usually lasts for hours. I find the number of floating particles to increase considerably after several hours of experiment, and many of them appear to be cell debris. The use of early cell culture is one solution to this problem. Furthermore, another solution is to centrifuge cell suspension and discard the pellet that does not recover to swimming after 10 min.

## 6.2. SLIPPAGE AND TURNING RATE OF *mstg* MUTANTS

In **Chap. 4** we refute the hypothesis that the fibrous mastigoneme of *C. reinhardtii* enhances the swimming speed, and reopen the question to the function of this ultrastructure. When investigating the free-swimming cells' trajectories, we find that the turning rate of the mastigoneme-less cells, or the *mstg* mutants, are much larger, and varied a lot from cell to cell when compared to the other two strains *cw15* and *cc125*, **Fig. 6.2**a.

The increased turning rate has a significant effect on the nature of cell motion. **Fig. 6.2**b displays the mean square displacement $\langle \Delta r^2 \rangle$ of the trajectories of each strain versus time $\Delta t$. For purely diffusive trajectories, $\langle \Delta r^2 \rangle \sim \Delta t$, while for ballistic trajectories, $\langle \Delta r^2 \rangle \sim \Delta t^2$. It has been shown that with similar measurement settings to ours, trajectories of *cc125* cells are ballistic up to several seconds [11]; and our results obtained with *cw15* and *cc125* agree well with the previous finding. However, for *mstg* mutants, approximately 50% of the trajectories begin to deviate from being ballistic within 1 s, see the first panel of **Fig. 6.2**b.

By observing the recordings closely, we found two key factors resulting in the *mstg*'s higher rate of turning. First, the *mstg* cells seem to slip more often during swimming than the other two strains, and the slips often result in drastic turning events whose 2D-projected turning angle can be as large as $\pi$ rad. Second, the two flagella seem to undergo more often asymmetric but still synchronized beating, which also results in drastic turnings. In short, the flagellar balance in the *mstg* cells is more often disrupted than the other strains.

Is it possible that the role of mastigonemes is more linked to swimming behaviour, *e.g.*, sensory, rather than swimming hydrodynamics?

This speculation is not groundless. The fact that the mastigonemes appear in two arrays instead of being randomly distributed have led researchers to believe that they have anchor points on the axoneme (see [12] Vol.3, Chap.11).Mastigonemes have been observed to connect directly to the axonemal microtubule in *C. reinhardtii* [13], *Euglena* [14], and *Ochromonas* [15]. Moreover, in an axonemal proteomic study of *C. reinhardtii*, the mastigoneme-related proteins are found in purified axonemes [2] that do not contain flagellar membrane or membrane appendages. If fibrous mastigonemes of *C. reinhardtii* are indeed anchored on axonemal microtubule, then direct mechanical interaction between mastigonemes and the inner- and outer-dynein arms would not be impossible, and this could bring up a completely new perspective to view the dynein regulation.

However, our current observation of the behavioural changes are still preliminary. To explore this intriguing possibility, we first need to substantiate the observations of

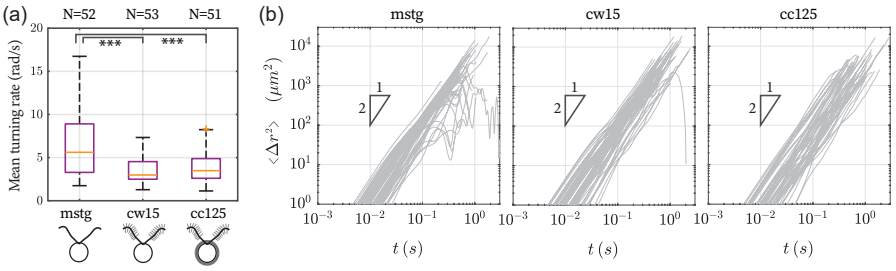


Figure 6.2: **Cell displacement over time and the turning rates of *mstg*, *cw15*, and *cc125*** (a) The turning rates are computed from the heading direction of the swimming cell, $\theta$. For every time step, the derivative $|d\theta/dt|$ is computed, and then the average value for the duration of the trajectory, $\overline{|d\theta/dt|}$, is reported as the turning rate for this trajectory. The distribution is compared using the Kruskal-Wallis One-Way ANOVA statistical test, $***$ represents $p < 0.001$. (b) Mean square displacement $\langle \Delta r^2 \rangle$ from $t = 0$ of each trajectory, plotted as a function of the time interval $t$.

slips and asymmetric beatings. In our current experimental setup, the flow chamber is essentially 3D and thus cannot confine the cells within our focal plane. As a result, the cells only swim within the focal plane briefly (~1 s ≈ 50 beats), and their two flagella are rarely visible simultaneously, making it difficult to identify slips and asymmetric beats. Therefore, I propose to study the free swimming of *mstg*, *cw15*, and *cc125* cells in a flow chamber that is confined in the $z$ axis, similar to the ~15 µm-thick flow chamber used in **Ref.** [16]. By experimenting in an essentially 2D environment, we will be able to track the cells for longer time, quantify the rate the slip and the asymmetric but synchronized flagellar beats, and correlate the two behaviours with turnings quantitatively. With a new round of experiments performed, we will see if this direction is worthy of further exploration.

## 6.3. FURTHER INVESTIGATION OF THE EXTERNAL FLOW ENTRAINMENT

In **Chap. 5**, we have systematically studied the external flow entrainment of the flagellar beating of *C. reinhardtii*. In those experiments, external oscillatory flows are applied within the flagellar beating plane from 4 different directions in total (3 in the main text and 1 in the supplementary material). We show by the asymmetry in the entrainability, that a *C. reinhardtii* cell couples to external flows predominantly through its *cis* flagellum.

A serendipitous finding that helped us confirm this conclusion is that during the trans flow entrainment, both flagella work effectively against the flow. It turned out that the alignment between the lateral velocity of the *cis* flagellum and the external flow was able to establish a stable entrainment in this case. This finding leads to an interesting question: does the external load on the *cis* flagellum along the lateral direction have a more significant influence than the load along the axial direction?

Examining this question will help us gather detailed information about how cells per-

ceive external hydrodynamic load. To explore this question, one needs to test the external flow entrainment of captured cells along more flow directions. Probably, expanding the current set of flow directions $\theta = 0°, \pm 45°, 90°$, to $\theta = 0°, \pm 23°, \pm 45°, \pm 67°, 90°$ would be enough. In this case, 8 directions will be experimentally tested for a captured cell, and numerical computations need to be performed based on the realistic entrainment videos. Along the intermediate directions ($\theta = \pm 23°, \pm 67°$), one possibility is that we will observe entrainment with phase-locking that is also intermediate between the phase-locking observed during the cis and the trans flow entrainment. Another possibility is that we will observe entrainment with bi-stable configurations, which would suggest that the two configurations are equally favorable for the cell energetically. In either case, by comparing the loads exerted by the axial and the lateral flow drag on the *cis* flagellum, we will be able to quantify their different weight, or different role, in determining the entrainment configuration.

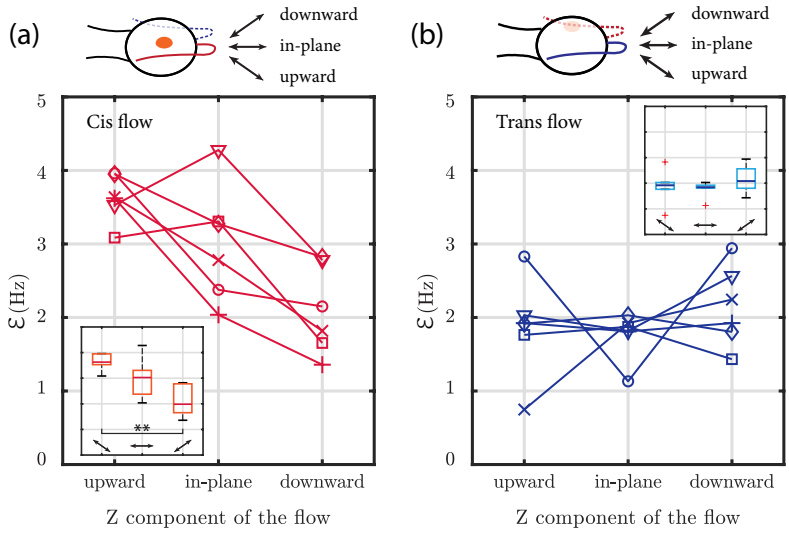


Figure 6.3: **External flow entrainment experiments with flow component in *z*.** (a-b) Coupling strength $\varepsilon$ of wild-type cells with downward, in-plane, and upward cis flows (a) and trans flows (b). Different symbols represent different cells (N=6). Insets: boxplots of the cells' coupling strength with the flows ($** : p < 0.01$, Kruskal-Wallis One-Way ANOVA statistical test).

Furthermore, we find that the asymmetry of entrainability in *C. reinhardtii* is not limited to 2D, *i.e.*, within the flagellar beating plane. Perpendicular to the plane, in the $z$ axis, there exists another asymmetry that predominantly favors entrainment with upward flows.

In addition to the cis and the trans flows within the ciliary beating plane, we apply flows from upward and downward to the cells. The downward and upward flows are both of the same amplitude as the in-plane flows employed previously,which is $780 \pm 50\mu m/s$. In the laboratory frame of reference, the $x$, $y$, and $z$ component of the upward

and downward flows are of the same amplitude. Thus, within the beating plane ($xy$-plane), they approach the cell from $\theta = \pm 45°$, the same as the cis and the trans flow. However, in $z$, the downward and upward flows approach the cell from $\theta_z = 35°$ and $\theta_z = -35°$, respectively. The directions are displayed in the upper row of drawings in **Fig. 6.3**.

In **Fig. 6.3** we show the results obtained from N = 6 wild-type cells tested in TRIS-minimal medium. Evidently, upward cis flow entrains a cell more effectively than the downward cis flow, and this holds true for every single cell tested, **Fig. 6.3**a. Statistically, the cells' coupling with upward cis flow is significantly larger than that with the downward cis flow ($**: p < 0.01$, Kruskal-Wallis One-Way ANOVA statistical test), **Fig. 6.3**a inset. Meanwhile, we see from **Fig. 6.3**b that $\theta_z$ of the trans flows does not significantly affect the coupling strength ($p > 0.05$). This is in line with our conclusion in **Chap. 5**: as trans flow loads mostly the *trans* flagellum, the variation of the load on the *cis* flagellum due to the change in $\theta_z$ is probably too small to change $\varepsilon$ observably.

What does this extra asymmetry in entrainability imply? There are several possibilities. The first one is related to the eyespot position of the cell, which breaks a cell's geometric symmetry. In **Chap. 1**, we see in **Fig. 1.8**a and k that the location of the eyespot is 45° from the ciliary beating plane. In the side view of a cell with its *cis* flagellum pointing outward the paper (as shown by the drawing in **Fig. 6.3**a), the eyespot is in the upper half of the cell. Is this possibly the reason behind the asymmetric entrainability in $z$? The answer is unlikely. For the N=6 cells tested, 3 of them have their *cis* flagellum as the right flagellum in the focal plane (top view). This means that only half of them have their eyespot at a higher height ($z$) than the flagellar beating plane. So if the asymmetry of flow entrainability in $z$ is due to the eyespot position and thus ultimately the arrangement of the anchoring rootlets, half of the cells will show larger coupling strength with the downward cis flow.

The second possibility is that it is an artefact due to the cells being held tilted by the pipette, and hence the $z$-symmetry breaks. However, this is also unlikely to be the case. First, the pipette is tilted downward only by approximately 6°; second, the cells' orientation is adjusted according to the focal plane and is thus irrelevant to the pipette tilting angle.

The third possibility is related to the out-of-plane beating of the two flagella. *C. reinhardtii* cells swim in helical paths, meaning that their flagellar beating are not completely 2D. It is possible that the flagellar beating of the *cis* has an out-of-plane component, which results in that the upward cis flow exerts a larger load than the downward cis flow does. Intriguingly, in early literature, it was mentioned that the *trans* flagellum beats more out of plane [17], rather than the *cis*[1]. To resolve this, we need to better visualize the flagellar beating in 3D, possibly by recording the beating at different $z$, and reconstructing an average beat.

[1] With our experiments with captured cells, we find neither flagellum to beat more out-of-plane consistently. The discrepancy might be due to that **Ref.** [17] used an light-insensitive mutant that can endure very strong light intensity.

## 6.4. EFFECT OF OSMOTIC CALCIUM STRESS ON FLAGELLAR BEATING

In **Chap. 5** we have attempted to alter the asymmetric flow entrainability of *C. reinhardtii* cells by subjecting them to calcium depletion, but our results suggest that calcium depletion does not affect the asymmetry. In addition to examining cells under calcium depletion, we have also examined cells in media that have much higher free calcium concentration ($[Ca^{2+}_{free}]$) than the original TRIS-minimal medium. Originally, our intention was to alter the intra-cellular free calcium concentration level, possibly slightly, to see whether the $Ca^{2+}$-modulated flagellar activity is related to the cells' coupling strength to external flows of different directions. Practically, we consider it possible to alter the cell's calcium homeostasis based on two pieces of evidence. First, cells under high external calcium concentration undergoes intermittent calcium influx [18, 19], which can trigger deflagellation [20]. Second, higher external calcium concentration affects the photosynthesis of *C. reinhardtii* cells through an intra-cellular calcium-sensing protein [21]. However, admittedly, there is no direct evidence showing how much the intra-cellular calcium level can be altered by the external calcium concentration, except for that it can be completely depleted with EGTA.

**Fig. 6.4** together with **Fig. 5.7** show our results obtained from N=46 cells subjected to various external calcium concentrations. Higher external free calcium concentration in the media is obtained by adding $CaCl_2$ to the original TRIS-minimal medium while maintaining a pH of 7.0. In total, the calcium concentrations tested are $[Ca^{2+}_{free}] = \sim 10^{-5}$ mM (N=6, TRIS-minimal+0.5 mM EGTA), 0.3 mM (N=11, TRIS-minimal), 1.2 mM (N=5), 3.5 mM (N=5), 5.0 mM (N=5), 20.0 mM (N=5), 30.0 mM (N=5), and 60.0 mM (N=4). To better visualize the trend, we group the cells according to the order of magnitude of free calcium concentration, and therefore, the three groups, $O$(0.1mM), $O$(1mM), and $O$(10mM) include 11, 15, and 14 cells, respectively. In all these cells together with the N=6 cells tested under calcium depletion (**Fig. 5.7**), $\varepsilon_{cis} > \varepsilon_{trans}$ applies for almost all of them (45/46). Statistically, by Kruskal-Wallis One-Way ANOVA test, $\varepsilon_{cis}$ is significantly larger than $\varepsilon_{trans}$ with $p < 0.005$ for all cells shown in **Fig. 6.4**a. When grouped by the type of flow used to entrain the cell, $\varepsilon_{trans}$ under $[Ca^{2+}_{free}] = O$(10mM) is significantly ($p < 0.05$) lower than $\varepsilon_{trans}$ under other calcium concentrations, see **Fig. 6.4**b. On the other hand, $\varepsilon_{cis}$ is less affected by the external calcium concentration than $\varepsilon_{trans}$ does. Possibly, the fact that $\varepsilon_{trans}$ under hyper-osmotic stress becomes lower can also be explained by the model introduced in **Ref.** [22] (see **Sec. 5.4.1** for detail), however, why $\varepsilon_{cis}$ is less affected is unknown.

Meanwhile, the data from captured cells beating under different external calcium concentration allows us to examine the effect of osmotic stress on the flagellar beating too. In the following parts I study the flagellar beating of the cells subjected to extremely low and high external calcium concentrations. More specifically, the tested cells are put into 3 groups labeled by "EGTA", "TRIS", and "HighCa". These three groups refer to cells tested in TRIS-minimal+0.5mM EGTA medium (calcium depletion), in TRIS-minimal medium, and in TRIS-minimal+$CaCl_2$ medium, respectively. The external calcium concentrations are $\sim 10^{-5}$ mM, 0.33 mM, and 20-60 mM, respectively. The number of cells examined are N=22, 58, and 17, respectively. The dataset is larger than that shown in **Fig.**

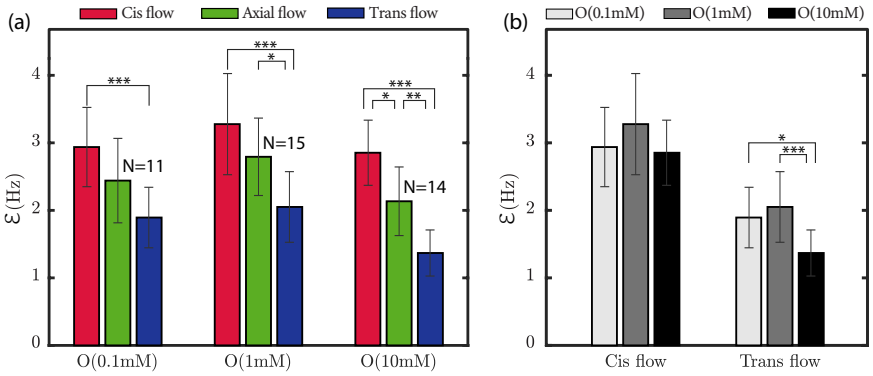


Figure 6.4: **Effect of external $Ca^{2+}$ on the asymmetric entrainability.** Tested cells are grouped by the free calcium concentration of the media (a), and by the direction of the applied flows (b). Comparison is performed by Kruskal-Wallis One-Way ANOVA statistical test, $*$, $**$, and $***$ stand for $p < 0.05$, $p < 0.01$, and $p < 0.005$, respectively.

6.4a because many cells were examined without external flow applied.

The rate of phase slips in captured cells is first examined. Recording of each cell lasts ~30 s, which is approximately 1500 beats. Slips are identified from the step-like features in the flagellar phase difference $\varphi_{cis} - \varphi_{trans}$, which is computed by the method described in **Fig.** 5.1. Each slip is then checked by the user in the video to avoid misrecognition. The rate of slip is then calculated as the total number of slips during the recording divided by the duration of the recording.

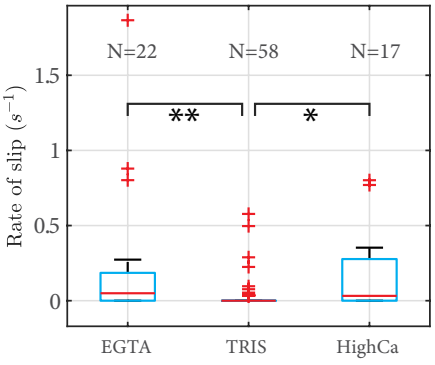


Figure 6.5: **Effect of external $Ca^{2+}$ on the rate of phase slips.** Rate of phase slips for cells under different external calcium concentrations. EGTA: TRIS-minimal+0.5mM EGTA, corresponding to $[Ca^{2+}_{free}] \approx 10^{-5}$ mM in the medium. TRIS: TRIS-minimal, $[Ca^{2+}_{free}] = 0.33$ mM. HighCa: $[Ca^{2+}_{free}] = O(10$ mM). $*$ and $**$ stand for $p < 0.05$ and $p < 0.01$ respectively, Kruskal-Wallis test. pH = 7.0 for all media.

The cells' slip rates are displayed in **Fig.** 6.5. The slip rate is higher under $O$(10mM)

calcium concentration. This agrees with the finding that under high external calcium concentration, intermittent single shots of calcium influx will be taking place [19] and will result in transient loss of flagellar synchrony [23]. On the other hand, we also find calcium depletion (TRIS-minimal+0.5mM EGTA) to increase the slip rate. Since there is no intermittent free calcium influx in this case, the higher slip rate indicates other mechanisms that can disrupt flagellar synchrony.

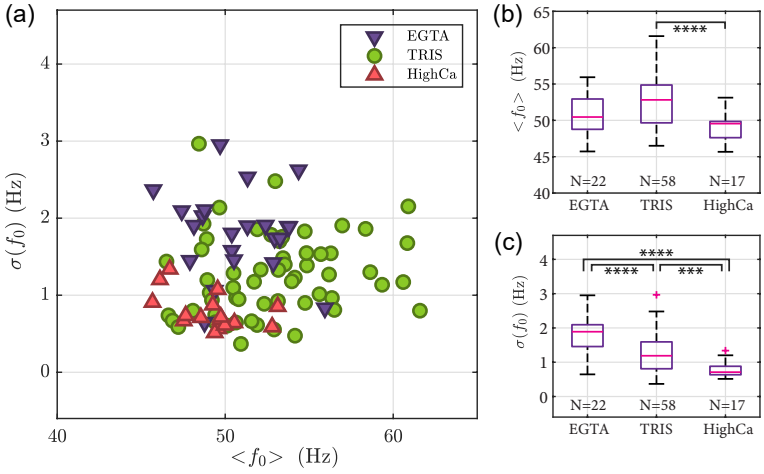


Figure 6.6: **Effect of external $Ca^{2+}$ on beating frequency.** (a) Each cell is registered with its average beating frequency $\langle f_0 \rangle$ and the standard deviation of $f_0$, or $\sigma(f_0)$, during a recording of ~30 s. (b-c) Comparing $\langle f_0 \rangle$ (b) and $\sigma(f_0)$ (c) between the three groups with Kruskal-Wallis test. $***$ and $****$ stand for : $p < 0.005$ and $p < 0.001$ respectively.

We proceed with examining the cells' beating frequencies. **Fig. 6.6**a shows the average beating frequency $\langle f_0 \rangle$, versus the fluctuation of beating frequency $\sigma(f_0)$ for each cell. $f_0(t)$ is extracted from the reconstructed flagellar phase $\varphi_{\text{cis,trans}}$ [24] during the synchronous beats, as $f_0(t) = d\varphi_{\text{cis,trans}}/dt$. $\sigma(f_0)$ is calculated as the standard deviation of $f_0(t)$ during the recording. In **Fig. 6.6**a, each point represents one cell. The three groups of cells form 3 clusters, with the ones examined in TRIS-minimal medium having the largest variation. Strikingly, the N=17 cells tested under 20-60 mM external calcium concentration clusters much more closely than the other two groups. **Fig. 6.6**b-c further quantify the differences between the three groups (Kruskal-Wallis test). The HighCa group has significantly lower $\langle f_0 \rangle$ than the TRIS group, and $\sigma(f_0)$ decreases with increasing external calcium concentration ($*** : p < 0.005$, $**** : p < 0.001$).

As $f_0(t)$ is computed as the time derivative of $\varphi(t)_{\text{cis,trans}}$ during the cells' synchronous beating, $\sigma(f_0)$ is then linked to the temporal fluctuation of and hence the noise in $\varphi(t)_{\text{cis,trans}}$. More specifically, the much reduced $\sigma(f_0)$ in the HighCa group implies a much reduced noise. Intrigued by this finding, we now quantify this noise level.

The math and methodology are described in **Ref.** [25–27]. In short, the strength of a white noise $\zeta(t)$ is quantified by the effective temperature $T_{\text{eff}}$, as $\langle \zeta(t)\zeta(t') \rangle = 2T_{\text{eff}}\delta(t -$

$t'$), where $\delta(t)$ is the Kronecker delta function. Therefore, $\zeta(t)$ during synchronous beating can be extracted from the auto-correlation of the flagellar phase difference, which is $\delta\varphi = \varphi_{cis} - \varphi_{trans}$. The auto-correlation of $\delta\varphi(t)$, $C(t)$, decreases as $C(t) = C_0 e^{-t/\tau}$. $C_0$ describes the amplitude of temporal phase fluctuation. $\tau$ depends on the intrinsic flagellar frequency difference $\delta f$ and the inter-flagellar coupling strength $\varepsilon_{flag}$, as $\tau \sim 1/\sqrt{\varepsilon_{flag}^2 - \delta f^2}$ [27]. By fitting the decay exponentially, $C_0$ and $\tau$ can be obtained simultaneously, and $T_{eff}$ is then calculated as $T_{eff} = C_0/\tau$.

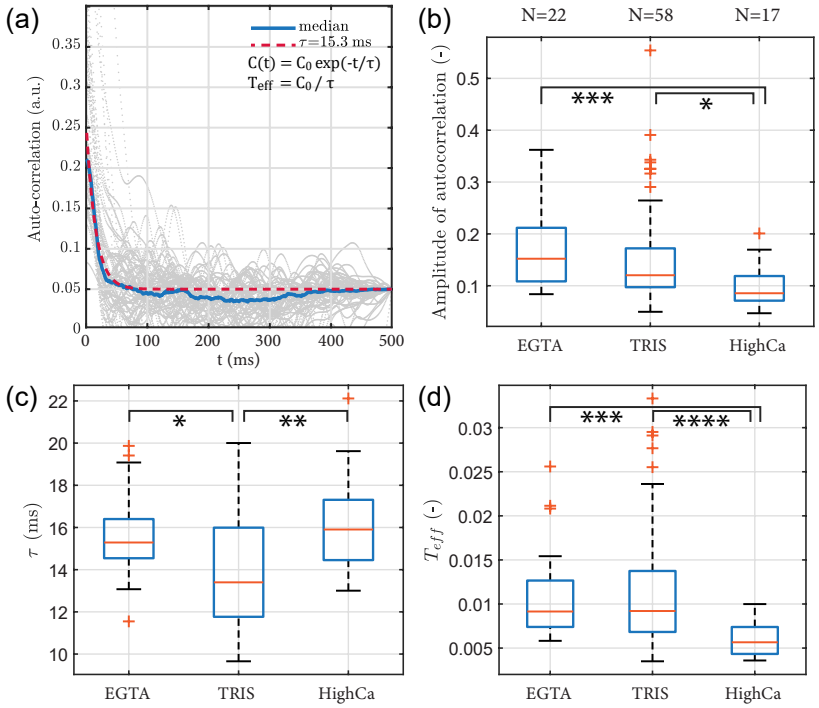


Figure 6.7: **Effect of external $Ca^{2+}$ on the flagellar phase dynamics** (a) $C_0$ and $\tau$ are obtained by fitting the median auto-correlation (blue) with $C(t) = C_0 e^{-t/\tau}$ (red). Auto-correlation of the 0.5 s-long segments of the signal is plotted as grey lines in the background. (b-d) Statistical comparison of $C_0$ (b), $\tau$ (c), and $T_{eff} = C_0/\tau$ (d), respectively. Comparison is performed by Kruskal-Wallis One-Way ANOVA statistical test, $*$, $**$, $***$, and $****$ stand for $p < 0.05$, $p < 0.01$, $p < 0.005$, and $p < 0.001$, respectively.

**Fig.** 6.7a demonstrates how $C_0$ and $\tau$ are obtained. A typical ~30 s time series of $\delta\varphi(t)$ is segmented into shorter ones of 0.5 s duration. Auto-correlations of those segments (grey thin lines in the background) and the median of them (blue line) are computed. The median auto-correlation is fitted by an exponential decay (red dashed line), and gives $C_0$ and $\tau$. **Fig.** 6.7b and c compare $C_0$ and $\tau$ between the three test groups respectively. In line with the decreasing trend of $\sigma(f_0)$ as a function calcium concentration (**Fig.** 6.6c), the amplitude $C_0$ displays a similar trend. Interestingly, **Fig.** 6.7c shows that

under both high and depleted external free calcium concentration, $\tau$ are both higher. As $\tau \sim 1/\sqrt{\varepsilon_{\text{flag}}^2 - \delta f^2}$, this could mean either a decrease of $\varepsilon_{\text{flag}}$ or an increase in $\delta f$. **Fig. 6.7**d shows that the effective temperature that characterizes the noise level, $T_{\text{eff}}$. As a result, the cells subjected to 20-60 mM external calcium concentration display a drastically ($\sim 50\%$) reduced $T_{\text{eff}}$.

As the noise in flagellar phase fluctuation is shown to be of an active origin [28] and is linked to the collective motion of flagellar dyneins, our finding suggests that an osmotic stress induced by high external calcium concentration could have an effect on the dynein motors. It would be interesting to see how the reduced level of noise affects the flagellar kinematics in the future. Moreover, it is intriguing to study how this calcium-dependent noise manifests in the free-swimming cells. It is a tempting thought that by changing external calcium concentration one can alter the swimming pattern of cells (speed, pitch and radius of the helical path *etc.*). This would await future experiments of 2D or 3D tracking of the free-swimming cells in different media.

## REFERENCES


[1] J. L. Rosenbaum, J. E. Moulder, and D. L. Ringo, *Flagellar elongation and shortening in Chlamydomonas. the use of cycloheximide and colchicine to study the synthesis and assembly of flagellar proteins,* The Journal of cell biology **41**, 600 (1969).

[2] G. J. Pazour, N. Agrin, J. Leszyk, and G. B. Witman, *Proteomic analysis of a eukaryotic cilium,* The Journal of Cell Biology **170**, 103 (2005).

[3] R. E. Goldstein, M. Polin, and I. Tuval, *Emergence of synchronized beating during the regrowth of eukaryotic flagella,* Physical Review Letters **107**, 1 (2011).

[4] R. Kamiya and E. Hasegawa, *Intrinsic difference in beat frequency between the two flagella of Chlamydomonas reinhardtii,* Experimental Cell Research **173**, 299 (1987).

[5] K. Y. Wan, K. C. Leptos, and R. E. Goldstein, *Lag, lock, sync, slip: the many phases of coupled flagella,* Journal of The Royal Society Interface **11**, 20131160 (2014).

[6] B. Orsburn, *The single cell proteomics revolution,* https://www.bioanalysis-zone.com/2020/02/11/single-cell-proteomics-revolution_bo/ (2019), [Online; accessed 21-March-2020].

[7] J. R. S. Newman, S. Ghaemmaghami, J. Ihmels, D. K. Breslow, M. Noble, J. L. DeRisi, and J. S. Weissman, *Single-cell proteomic analysis of s. cerevisiae reveals the architecture of biological noise,* Nature **441**, 840 (2006).

[8] D. B. Bekker-Jensen, C. D. Kelstrup, T. S. Batth, S. C. Larsen, C. Haldrup, J. B. Bramsen, K. D. Sørensen, S. Høyer, T. F. Ørntoft, C. L. Andersen, M. L. Nielsen, and J. V. Olsen, *An optimized shotgun strategy for the rapid generation of comprehensive human proteomes,* Cell Systems **4**, 587 (2017).

[9] B. Budnik, E. Levy, G. Harmange, and N. Slavov, *Scope-ms: mass spectrometry of single mammalian cells quantifies proteome heterogeneity during cell differentiation,* Genome Biology **19**, 161 (2018).

[10] H. Specht, E. Emmott, A. A. Petelski, R. Gray Huffman, D. H. Perlman, M. Serra, P. Kharchenko, A. Koller, and N. Slavov, *Single-cell mass-spectrometry quantifies the emergence of macrophage heterogeneity,* (2019), 10.1101/665307.

[11] K. C. Leptos, J. S. Guasto, J. P. Gollub, A. I. Pesci, and R. E. Goldstein, *Dynamics of enhanced tracer diffusion in suspensions of swimming eukaryotic microorganisms,* Phys. Rev. Lett. **103**, 198103 (2009).

[12] E. H. Harris, *The Chlamydomonas Sourcebook, 2nd Edition* (Elsevier, Oxford, UK, 2009).

[13] R. A. Bloodgood, *Advances in molecular and cell biology,* (Elsevier, 1987) Chap. Glycoprotein Dynamics in the Chlamydomonas Flagellar Membrane, pp. 97–130.

[14] G. Bouck, A. Rogalski, and A. Valaitis, *Surface organization and composition of Euglena. II. Flagellar mastigonemes,* The Journal of Cell Biology **77**, 805 (1978).

[15] D. R. Markey and G. B. Bouck, *Mastigoneme attachment in ochromonas,* Journal of Ultrastructure Research **59**, 173 (1977).

[16] J. S. Guasto, K. A. Johnson, and J. P. Gollub, *Oscillatory flows induced by microorganisms swimming in two dimensions,* Physical Review Letters **105**, 168102 (2010).

[17] U. Rüffer and W. Nultsch, *Comparison of the beating of cis- and trans-flagella of Chlamydomonas cells held on micropipettes,* Cell Motility and the Cytoskeleton **7**, 87 (1987).

[18] G. L. Wheeler, I. Joint, C. Brownlee, P. Place, and C. Hill, *Rapid spatiotemporal patterning of cytosolic $Ca^{2+}$ underlies flagellar excision in Chlamydomonas reinhardtii,* The Plant Journal , 401 (2008).

[19] P. Bickerton, S. Sello, C. Brownlee, J. K. Pittman, and G. L. Wheeler, *Spatial and temporal specificity of $Ca^{2+}$ signalling in Chlamydomonas reinhardtii in response to osmotic stress,* New Phytologist **212**, 920 (2016).

[20] L. Quarmby and H. Hartzell, *Two distinct, calcium-mediated, signal transduction pathways can trigger deflagellation in Chlamydomonas reinhardtii,* The Journal of Cell Biology **124**, 807 (1994).

[21] D. Petroutsos, A. Busch, I. Janßen, K. Trompelt, S. V. Bergner, S. Weinl, M. Holtkamp, U. Karst, J. Kudla, and M. Hippler, *The Chloroplast Calcium Sensor CAS Is Required for Photoacclimation in Chlamydomonas reinhardtii,* The Plant Cell **23**, 2950 (2011).

[22] G. S. Klindt, C. Ruloff, C. Wagner, and B. M. Friedrich, *Load response of the flagellar beat,* Physical Review Letters **258101**, 1 (2016).

[23] K. Yoshimura, C. Shingyoji, and K. Takahashi, *Conversion of beating mode in Chlamydomonas flagella induced by electric stimulation,* Cell Motility **36**, 236 (1997).

[24] B. Kralemann, L. Cimponeriu, M. Rosenblum, A. Pikovsky, and R. Mrowka, *Phase dynamics of coupled oscillators reconstructed from data,* Phys. Rev. E **77**, 066205 (2008).

[25] A. Pikovsky, M. Rosenblum, and J. Kurths, *Synchronization: A Universal Concept in Nonlinear Sciences*, Cambridge Nonlinear Science Series (Cambridge University Press, 2001).

[26] R. E. Goldstein, M. Polin, and I. Tuval, *Noise and synchronization in pairs of beating eukaryotic flagella,* Phys. Rev. Lett. **103**, 168103 (2009).

[27] M. Polin, I. Tuval, K. Drescher, J. P. Gollub, and R. E. Goldstein, *Chlamydomonas swims with two "gears" in a eukaryotic version of run-and-tumble locomotion,* Science **325**, 487 (2009).

[28] R. Ma, G. S. Klindt, I. H. Riedel-Kruse, F. Jülicher, and B. M. Friedrich, 10.1103/PhysRevLett.113.048101.

# ACKNOWLEDGEMENTS

I have been planning to write the acknowledgements even before writing this thesis. However, till this point, I am still not sure how to put it properly. The four years of PhD in TU Delft, which I tried to wrap up with this thesis, have been an invaluable experience for me. Thanks to this period, I started to understand (but is still learning) how to balance between passion and pragmatism; and I have made sure I love doing research. I am a very very slow learner in these regards, and I am thus especially grateful for those who have advised me, guided me, bolstered me, and accompanied me through this process.

First and foremost, I want to thank my supervisors Dr. Marie-Eve Aubin-Tam and Dr. Daniel Tam. Without your advice and guidance during these years, I would be basically chasing my tail all the time. In retrospect, I feel lucky and grateful that I have both of you as my supervisors. You two have distinct coaching styles, different specialties, and often different focuses on one subject. From these I learned to see things from more than one angles. On the other hand, you both have the same high standard for the quality of research. As a PhD student, I was often blinded by the urge to publish with whatever I had and by the fear to admit useless effort, so that I often forgot how crucial it is to keep one's standard high. I only came to appreciate this when I started seeing research as my career - something that I want to spend decades doing. And now I learned a trick to spot if I was subconsciously trying to just get by with whatever I had - I ask myself: dare I send this to you guys directly?

I want to also express my gratitude to the rest of the committee members (in alphabetical order): Dr. G. Amador, Prof. dr. G. H. Koenderink, Dr. ir. L. Laan, Prof. dr. ir. J. M. J. den Toonder, and Prof. dr. ir. J. Westerweel for accepting to review my work.

I would like to thank Prof. dr. Marileen Dogterom for being my promotor in the first place; Prof. dr. Andreas Engel for his insightful comments and bolstering my morale during the job-search when we are both in Basel; Dr. Timon Idema for being my mentor; Dr. Bertus Bermont for the crucially helpful discussion that made **Chap. 4** possible. Also, I want to thank the our faculty staff Susanne Hage for always being there to help, and Sacha Khaiboulov for both his help and his great recommendation of novels.

I would also like to thank Prof. dr. Jiang Hong-Wen at UCLA. Prof. dr. Klaus Ensslin at ETHZ, and Dr. Tu Tao at USTC, for willing to be my referees when I wanted to switch research field from nano-electronics to biophysics. Without your help I would never be able to start this new chapter, and hence this thesis would be non-existent. I am as grateful as five years ago for your endorsement. A special thanks goes to Prof. dr. Ritsu Kamiya at Gakushuin University, who encouraged me during the writing of this thesis and shared with me his valuable insights into the ciliary difference in *C. reinhardtii*.

Among my dear colleagues and friends, I would like to first thank Victor Marin and Greta Quaranta, who built the foundation for the research in this thesis. Back in mid-August 2015, I arrived at Delft from Schiphol in a rainy night. Victor was there near the

Aula to pick me up and walked me to the apartment. Although there was quite some detour and the walk was almost Brownian, I felt very warmly welcomed. Victor built the optical tweezers setup with which I started to imagine what could be done to study the locomotion of *C. reinhardtii*. In parallel, I learned everything about culturing and experimenting with *C. reinhardtii* cells from Greta, who had spent great efforts in making the protocols work. Without their help, it would be impossible for me to have so much fun in exploring the interface between these two topics. For that I would always be in your debt.

Next I want to thank Dr. Roland Kieffer - the name that appeared in every single acknowledgement of my research work and the one who came to my rescue every time when I was helpless, both in research and in personal life. I want to thank you for "cleaning up" the noise spectrum of the optical tweezers, for the useful programs and surprising gadgets that made many experiments possible, and for helping me to handle the 712 kg demolition waste (an odd example, pardon me).

Meanwhile, I owe thanks to the other early members of Marie's group, Dr. Simon Lindhoud, Dr. Jacqueline Enzlin, Dominik (now Dr. Schmieden), and Vanessa (now Dr. Carvalho) who included me warmly into the group.

I am lucky to have shared the office with Victor, Dominik, and Vanessa during this time. I deeply cherish those days seeing Victor wearing T-shirt with two wet armpits, hearing him talking about lipid bilayer capacitance and the moon being hollow at the same time. Next to a sweating Victor, Vanessa would be in her jacket and her wool scarf, wearing her headset singing at a low volume, and clicking FtsH from TEM images. Only by observing Dominik could I be sure that my sense of temperature was just normal. In a typical day, he would always keep a gentle smile, talk calmly, but suddenly throw some great jokes. And even before I stopped laughing, he could recover the gentile smile as if he was in his LinkedIn photo. Time spent with them was never boring and I want to thank them for those valuable memories. Also, a special thanks goes to Jacqueline Enzlin, who tutored me in Dutch. I practiced speaking and writing with her for a year and half. With her help, I can finally say proudly that Dutch is the second foreign language that I can get by.

Starting from the second half of my PhD, Dr. Guillermo Amador, Dr. John Buchner, and Parviz Ghoddoosi Dehnavi joined Daniel's lab. I am so happy to have you guys on board and want to take the chance to thank each of you here.

I collaborated closely with Guillermo in the project studying the fibrous flagellar hairs of *C. reinhardtii*, and have been learning a lot from him, both professionally and personally. Thank you for being present when I need consultation, for being so open-minded and willing to try new ideas during the project, and for your constant feedback on my writing (including this thesis). John, talking with you was always a thrill. We both have the same tendency of using talking as a way of organizing thoughts, and therefore, our conversation easily became bombardment of ideas on each other. I could always use a conversation with you to know what was actually going on in my mind - it worked better than any meditation. Parviz, thank you for your excellent modelling and theoretical insights. Without your contribution, half of this thesis would have been incomplete. Also, I hope I was not a too bad teacher in getting you acquainted with the setup and the OTV measurement scheme. I would never forget the hilarious typo in your slide: "Fitting

of Da's excremental results". It's been a lot of fun to collaborate with you. For all these I am genuinely grateful.

A special thanks goes again to John and to Dr. Marianne Hoogmoed for helping translating and proofreading the summary and the propositions. Naturally, all remaining errors are my own.

I also had the privilege to work with other members of Marie's group: Lisa Dreesens, Dr. Liang Kuang, Chaline van Aartrijk, Yu Kui, Dr. Ewa Spiesz, Dr. Ramon van der Valk, Dr. Aurora Dols Perez, Dr. Irfan Prabudiansyah, Dr. Martin Caldarola, Dr. Srikkanth Balasubramanian; and members of Daniel's group: Koen Muller, Ankur Kislaya, Junaid Mehmood. I am sorry that I can only list your names here instead going into details of how great you guys were, please pardon me.

Thanks to the system here in the Netherlands, I had the chance to supervise several Bachelor/Master Ending Projects. I want to thank my students for teaching me how to become a better teacher. They are (in chronological order): Vinesh Badloe, Maarteen den Hollander, Saffira Tjon, Lois van der Drift, Enzo Nio, Maarten Joosten, Kabir Razack, and Mats van Tongeren.

Apart from research, our department is a dynamic place full of all sorts of talent. I could never imagined concerts and rehearsals being a part of my PhD, but they indeed were. For that I am grateful for Federico Fanalista for including me into this vibrant community when I had just arrived. And I want to say thank you to my dear friends in the band, Hirad Daneshpour, Maurits Kok, Vladimir Volkov, and Louis Reese. I will never forget the rehearsal in the snowy night and in the warm practice room, where you guys filled the air with chords of piano, saxophone, guitar, and double bass. It's such a shame that I screwed up the last rehearsal, for that I am extremely sorry. A special thanks goes to Dr. Carsten Blom and Dr. Benjamin Lehner. I shared office with Carsten for half a year and had much fun in discussing quantum transport in biology. I wish one day my research could actually embrace this topic. Ben is possibly the most surprising guy I know. When we first knew each other, he was practicing Kung-Fu and was (by impression) trying to be an astronaut. Then suddenly he was 3D printing bacteria and asking if I was interested in joining his start-up. Ben, I feel lucky to be your friend and I look forward to being surprised again by the next news you bring.

Finally, it comes to the reserved place for family members. I want to first thank my wife. Shuyue, I cannot imagine what it would be like if you were not here to support me all the time. You were there to make all kinds of tasty but highly irreproducible dishes, you were there to help with countless labor-intensive measurements, you were there to walk me in the Swiss mountains and along the rivers when I burnt out and broke down, and you have brought us our baby daughter. I don't know what life will bring us next, but I know that we can make a lot fun out of whatever that comes. A very reluctant thanks goes to my daughter, Wei Yang, without whom this thesis would have been finished sooner. But who knows, you could make things much worse, so I guess I still owe you one. Lastly, I want to thank my mother, Wang Qiao-Ling, and my father, Wei An-Cai. I realized that I dared to dream not because I was brave, but because you always quietly got my back. I love you both.

# A

# ANALYTICAL FORM OF THE VELOCITY FIELD OF A BLAKE TENSOR

In a seminal paper in 1971 entitled *A note on the image system for a stokeslet in a no-slip boundary*, J.R.Blake gave the analytical form for a stokeslet at a height $h$ above an infinite no-slip wall at $x_3 = 0$, shown in **Fig. A.1**. The distances to the stokeslet and to its image are denoted as **r** and **R**, respectively. The velocity field reads as follows:

$$\begin{aligned} u_j = \frac{F_k}{8\pi\mu}\Bigg\{&(\frac{1}{r}-\frac{1}{R})\delta_{jk}+\frac{r_j r_k}{r^3}-\frac{R_j R_k}{R^3} \\ &+2h(\delta_{k\alpha}\delta_{\alpha l}-\delta_{k3}\delta_{3l})\frac{\partial}{\partial R_l}\left[\frac{hR_j}{R^3}-(\frac{\delta_{j3}}{R}+\frac{R_j R_3}{R^3})\right]\Bigg\} \end{aligned} \tag{A.1}$$

The subscript $k$ denotes the forcing of the stokeslet, $\mathbf{F} = (F_1, F_2, F_3)$; and the subscript $\alpha$ is either 1 or 2. When considering a point force along $x_1$ axis, the forcing is then simplified to $\mathbf{F} = (F, 0, 0)$. Also, note that $\alpha$ and hence $l$ must be 1, Eq. (A.1) reduces to:

$$\begin{aligned} u_j = \frac{F}{8\pi\mu}\Bigg\{&(\frac{1}{r}-\frac{1}{R})\delta_{j1}+\frac{r_j r_1}{r^3}-\frac{R_j R_1}{R^3} \\ &+2h\frac{\partial}{\partial R_1}\left[\frac{hR_j}{R^3}-(\frac{\delta_{j3}}{R}+\frac{R_j R_3}{R^3})\right]\Bigg\} \end{aligned} \tag{A.2}$$

In this thesis, the stokeslet is placed at $(0, 0, h)$. Therefore, the vectors $\mathbf{r} = (x_1, x_2, x3 - h)$ and $\mathbf{R} = (x_1, x_2, x_3 + h)$, and the distances can be written as $r = \sqrt{x_1^2 + x_2^2 + (x_3 - h)^2}$ and $R = \sqrt{x_1^2 + x_2^2 + (x_3 + h)^2}$, respectively. Also, as we mostly focus on the axial velocity component $u_1$ along different axes, we further specify Eq. (A.2) with $j = 1$:

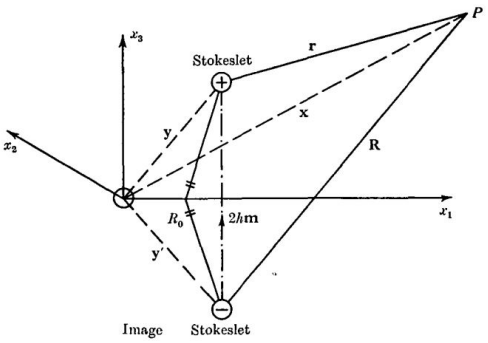


Figure A.1: The position of stokeslet and its image, and relevant vectors **x**, **r**, and **R**. Plane boundary (no-slip wall) **S**: $x_3 = 0$, and with normal vector is $\mathbf{m} = \mathbf{I}_3$

. Reprinted with permission from Cambridge University Press.

$$
\begin{aligned}
u_1 &= \frac{F}{8\pi\mu}\left\{(\frac{1}{r}-\frac{1}{R})+\frac{x_1^2}{r^3}-\frac{x_1^2}{R^3}+2h\frac{\partial}{\partial x_1}\left[\frac{hx_1}{R^3}-\frac{x_1(x3+h)}{R^3})\right]\right\} \\
&= \frac{F}{8\pi\mu}\left\{(\frac{1}{r}-\frac{1}{R})+\frac{x_1^2}{r^3}-\frac{x_1^2}{R^3}-2hx_3\frac{\partial}{\partial x_1}\left(\frac{x_1}{R^3}\right)\right\} \\
&= \frac{F}{8\pi\mu}\left\{(\frac{1}{r}-\frac{1}{R})+\frac{x_1^2}{r^3}-\frac{x_1^2}{R^3}-2hx_3(\frac{1}{R^3}-\frac{3x_1^2}{R^5})\right\}
\end{aligned}
\tag{A.3}
$$

From Eq. (A.3) we can study the behaviour of $u_1$ along different axes analytically. Here we write $u_1$ along $(x_1, 0, h)$ as $u_1(x_1)$, $u_1$ along $(0, x_2, h)$ as $u_1(x_2)$, and $u_1$ along $(0, 0, x_3)$ as $u_1(x_3)$, respectively. They read:

$$
\begin{aligned}
u_1(x_1) &= \frac{F}{8\pi\mu}\left\{(\frac{1}{r}-\frac{1}{R})+\frac{x_1^2}{r^3}-\frac{x_1^2}{R^3}-2h^2(\frac{1}{R^3}-\frac{3x_1^2}{R^5})\right\} \\
u_1(x_2) &= \frac{F}{8\pi\mu}\left\{(\frac{1}{r}-\frac{1}{R})-\frac{2h^2}{R^3}\right\} \\
u_1(x_3) &= \frac{F}{8\pi\mu}\left\{(\frac{1}{r}-\frac{1}{R})-\frac{2hx_3}{R^3}\right\}
\end{aligned}
\tag{A.4}
$$

Note that the distances can be further written as:

$$
\begin{cases}
r = |x_1|, R = \sqrt{x_1^2 + (2h)^2} & \text{for along } (x_1, 0, h) \\
r = |x_2|, R = \sqrt{x_2^2 + (2h)^2} & \text{for along } (0, x_2, h) \\
r = |x_3 - h|, R = |x_3 + h| & \text{for along } (0, 0, x_3),\ x_3 > 0
\end{cases}
\tag{A.5}
$$

In close proximity of the stokeslet ($x_{1,2} \ll h$, $x_3 - h \ll h$, $r \ll h$ and $R \approx h$), the solution reduces to a stokeslet in free space.

Now to analyze the behaviour of the flow in the far field, where $r \gg 2h$. Without loss of generality, we analyze $u_1(x_1)$ with $x_1 \gg 2h$. Starting from Eq. (A.4), and substituting with distance $r$ and $R$ with Eq. (A.5), $u_1(x_1)$ reads:

$$\begin{aligned} u_1(x_1) &= \frac{F}{8\pi\mu x_1}\left\{2 - \mathscr{A}(x_1) - \mathscr{A}(x_1)^3 - \frac{1}{2}\mathscr{A}(x_1)\mathscr{B}(x_1)^2 \right. \\ &\quad \left. + \frac{3}{2}\mathscr{A}(x_1)^3\mathscr{B}(x_1)^2\right\} \\ \mathscr{A}(x_1) &= 1/\sqrt{1+\frac{4h^2}{x_1^2}}, \quad \mathscr{B}(x_1) = 1/\sqrt{1+\frac{x_1^2}{4h^2}} \end{aligned} \tag{A.6}$$

In the far field where $x_1 \gg 2h$, $\frac{4h^2}{x_1^2} \to 0$. Therefore, $\mathscr{A}(x_1) \to 1$ and $\mathscr{B}(x_1) \to 0$. Denoting $\frac{4h^2}{x_1^2}$ as $\varepsilon$, the first-order Taylor expansion of $\mathscr{A}(\varepsilon)$ around $\varepsilon = 0$ is $\mathscr{A}(\varepsilon) = 1 - \varepsilon/2$. Substituting into Eq. (A.6), omitting the $\mathscr{B}(\varepsilon)$ terms, and keeping the leading order term we obtain:

$$u_1(x_1) = \frac{F}{8\pi\mu x_1} \cdot 2\varepsilon = \frac{h^2}{\pi\mu} \cdot \frac{1}{x_1^3} \tag{A.7}$$

Therefore, we see that in the far field, the flow amplitude will decay as $1/r^3$, and this increased rate of spatial decay within the $x_1x_2$-plane is the effect of the presented wall at $x_3 = 0$.

Lastly, to better see how the rate of decay changes from $1/r$ in the near field to $1/r^3$ in the far field, we perform similar analysis of $u_1(x_1)$ at an intermediate distance, where $x_1 \approx 2h$.

This time, we perform first-order Taylor expansion on both $\mathscr{A}(x_1)$ and $\mathscr{B}(x_1)$ around $\varepsilon = 1$, and obtain:

$$\begin{aligned} \mathscr{A}(\varepsilon) &= \frac{1}{\sqrt{2}} - \frac{1}{4\sqrt{2}}(\varepsilon - 1) \\ \mathscr{B}(\varepsilon) &= \frac{1}{\sqrt{2}} + \frac{1}{4\sqrt{2}}(\varepsilon - 1) \end{aligned} \tag{A.8}$$

Substituting Eq. (A.8) into Eq. (A.6), we obtain:

$$\begin{aligned} u_1(x_1) &= \frac{F}{8\pi\mu x_1}\left(2 - \frac{11\sqrt{2}}{16} + \frac{15\sqrt{2}}{64}(\varepsilon - 1)\right) \\ &\approx \frac{F}{8\pi\mu x_1}\left(0.67 + 0.33 \cdot \frac{4h^2}{x_1^2}\right) \end{aligned} \tag{A.9}$$

We see that at this distance within the $x_1x_2$-plane, the $1/r$ decay term is about twice the $1/r^3$ decay term.

As an end note, $u_1(x_2)$ in the near field, intermediate field, and far field can be similarly calculated, respectively. The rate of spatial decay of $u_1$ along $x_2$ is the same as $u_1$ along $x_1$, and the their amplitudes satisfy: $u_1(x_1 \to 0) = 2u_1(x_2 \to 0)$, and $u_1(x_1 \to \infty) = 4u_1(x_2 \to \infty)$.

# B

# ANALYTICAL FORM OF THE VELOCITY FIELD OF AN OSCILLET

Similar to the stokeslet being the flow field generated by a constant point force $\mathbf{F}$, an oscillet describes the flow field generated by a point oscillating force $\mathbf{F}e^{\mathrm{i}\cdot 2\pi f t}$.

A stokeslet can be written as:

$$\begin{aligned} \mathbf{u}_{\text{stokeslet}}(\mathbf{r}) &= \mathbf{F}_S \cdot \frac{\mathbf{G}(\mathbf{r})}{8\pi\mu}, \\ \mathbf{G}_{ij}(\mathbf{r}) &= \frac{\boldsymbol{\delta}_{ij}}{r} + \frac{\mathbf{x}_i \mathbf{x}_j}{r^3} \end{aligned} \tag{B.1}$$

Here $\mathbf{x}_i$ is the $i$th component of the position vector $\mathbf{r} = \mathbf{x}_1 + \mathbf{x}_2 + \mathbf{x}_3$, while $r$ denote the distance. $\mu$ is the dynamic viscosity of the surrounding fluid. Following the same form, an oscillet reads (Chap.6 pp.504 in **Ref.**Pozrikidis2011:

$$\begin{aligned} \mathbf{u}_{\text{oscillet}}(\mathbf{r}) &= \mathbf{F}e^{\mathrm{i}\cdot 2\pi f t} \cdot \frac{\mathbf{S}(\mathbf{r})}{8\pi\mu}, \\ \mathbf{S}_{ij}(\mathbf{r}) &= \frac{\boldsymbol{\delta}_{ij}}{r}\mathscr{A}(R) + \frac{\mathbf{x}_i \mathbf{x}_j}{r^3}\mathscr{C}(R), \\ \mathscr{A}(R) &= 2\left(1 + \frac{1}{R} + \frac{1}{R^2}\right)e^{-R} - \frac{2}{R^2}, \\ \mathscr{C}(R) &= -2\left(1 + \frac{3}{R} + \frac{3}{R^2}\right)e^{-R} + \frac{6}{R^2} \\ R &\equiv \frac{r}{l}e^{-\mathrm{i}\frac{\pi}{4}}, l \equiv \sqrt{\frac{\nu}{2\pi f}} \end{aligned} \tag{B.2}$$

With $R$ is the scaled complex distance, with $|R| = r/l$. The characteristic length $l$ here differs slightly from the characteristic length for vorticity diffusion, $\delta = \sqrt{\nu/f}$, which we used extensively in **Chap.** 2 and **Chap.** 3.

Very close to the oscillating point force, one may confirm $\lim_{R\to 0}\mathscr{A}(R) = 1$ and $\lim_{R\to 0}\mathscr{C}(R) = 1$ as follows. First expand $e^{-R}$ around $R = 0$, $e^{-R} \approx 1 - R + \frac{R^2}{2}$. Substituting this into $\mathscr{A}(R)$ and $\mathscr{C}(R)$ we get:

$$\begin{aligned}\mathscr{A}(R) &\approx 2\left(1+\frac{1}{R}+\frac{1}{R^2}\right)\left(1-R+\frac{R^2}{2}\right)-\frac{2}{R^2} = (1-R+R^2)\\ \mathscr{C}(R) &\approx -2\left(1+\frac{3}{R}+\frac{3}{R^2}\right)\left(1-R+\frac{R^2}{2}\right)+\frac{6}{R^2} = (1+R-R^2)\end{aligned} \tag{B.3}$$

Clearly when $R \to 0$, $\mathscr{A}(R) \to 1$ and $\mathscr{C}(R) \to 1$, and $\mathbf{S}_{ij}(\mathbf{r}) \to \mathbf{G}_{ij}(\mathbf{r})$. And we have $\mathbf{u}_{\text{oscillet}}(\mathbf{r}) \to e^{\mathrm{i}\cdot 2\pi f t}\cdot\mathbf{u}_{\text{stokeslet}}(\mathbf{r})$ in the very close field of the oscillating point force. This indicates that, in the close field, the asymptotic behaviour of $\mathbf{u}_{\text{oscillet}}(\mathbf{r})$ is the same as the stokeslet, which is $u_{\text{oscillet}} \sim r^{-1}$.

$$\begin{aligned}u_1(x_1) &= \frac{Fe^{\mathrm{i}\cdot 2\pi f t}}{8\pi\mu x_1}\cdot 2\\ u_1(x_2) &= \frac{Fe^{\mathrm{i}\cdot 2\pi f t}}{8\pi\mu x_1}(1-R)\end{aligned} \tag{B.4}$$

In the far field, when $R \to \infty$, to study the asymptotic behaviour of $\mathscr{A}(R)$ and $\mathscr{C}(R)$, it is then convenient to rewrite them as:

$$\begin{aligned}\mathscr{A}(R) &= -\frac{2}{R^2}\cdot(1-R^2e^{-R}-Re^{-R}-e^{-R})\\ \mathscr{C}(R) &= \frac{6}{R^2}\cdot(1-\frac{R^2}{3}e^{-R}-Re^{-R}-e^{-R})\end{aligned} \tag{B.5}$$

As $\lim_{R\to\infty} R^n e^{-R} = 0$ ($n$=0,1,2,...), the leading order of $\mathscr{A}(R)$ and $\mathscr{C}(R)$ is then $\frac{1}{R^2}$. Therefore, in the far field, $u_{\text{oscillet}} \sim r^{-3}$. In **Chap. 3**, we observe this transition in the rate of spatial decay in the experimental results.

Consider a point force oscillating at the origin, with $\mathbf{F} = (F,0,0)$, and denote $u_1$ along $(x_1,0,0)$ as $u_1(x_1)$, $u_1$ along $(0,x_2,0)$ as $u_1(x_2)$. $u_1(x_1)$ and $u_1(x_2)$ read:

$$\begin{aligned}u_1(x_1) &= \frac{Fe^{\mathrm{i}\cdot 2\pi f t}}{8\pi\mu x_1}\Big(\mathscr{A}(R)+\mathscr{C}(R)\Big)\\ u_1(x_2) &= \frac{Fe^{\mathrm{i}\cdot 2\pi f t}}{8\pi\mu x_2}\mathscr{A}(R)\end{aligned} \tag{B.6}$$

# C

# IMPLEMENTATION OF THE LANGEVIN DYNAMICS

**SPECIAL NOTE:** The phase difference $\Delta\varphi(t)$ between two oscillators follows the Langevin dynamics. In **Chap.** 5, $\Delta\varphi(t)$ was defined as $\Delta\varphi(t) = \varphi_{\text{cell}} - \varphi_{\text{flow}}$, while the detuning $\nu$ was defined as $\nu = f_{\text{flow}} - f_{\text{cell}}$. Hence, in the phase dynamics, $\frac{d\Delta}{dt} = -2\pi\nu - ....$ This was convenient when dealing with experiment, as we scanned $f_{\text{flow}}$ to map the Arnold tongue and to obtain the entrainment profile $\xi(\nu)$. For discussing the mathematics between two interacting oscillators represented by $\varphi_1(t)$ and $\varphi_2(t)$ respectively, it is more natural to define $\Delta\varphi(t)$ as $\Delta\varphi(t) = \varphi_1(t) - \varphi_2(t)$ and detuning $\nu = f_1 - f_2$. Also, for simplicity, we denote $\Delta\varphi(t)$ as $\Delta$. These applies only to this appendix.

The Langevin dynamics reads:

$$\frac{d\Delta}{dt} = -\frac{dV(\Delta)}{d\Delta} + \zeta(t) \tag{C.1}$$

with $\frac{d\Delta}{dt}$ the rate of change in phase, $-\frac{dV(\Delta)}{d\Delta}$ as a potential field with adjusted unit, and $\zeta(t)$ the white noise.

Originally, the Langevin dynamics constructs a simplified picture of the dynamics of a particle in viscous media:

$$m\frac{d^2x}{dt^2} = -\nabla U(x) - \gamma\frac{dx}{dt} + \sqrt{2\gamma k_B T}R(t) \tag{C.2}$$

The form follows essentially Newton's second law of motion $F = ma$. The left hand side is the mass $m$ times the acceleration $\frac{d^2x}{dt^2}$. The right hand side terms account for the force in a potential field $U(x)$, the viscous force, and the Brownian force, respectively. The Brownian force $\sqrt{2\gamma k_B T}R(t)$ satisfies $\langle R(t)\rangle = 0$ and $\langle R(t+\tau)R(t)\rangle = \delta(\tau)$, with $\delta$ the Kronecker delta function.

The phase dynamics of oscillators Eq. (C.1) omits the acceleration term and adjusted the units of each terms respectively. All terms have the unit of rad/s, and thus the unit of the potential $V(\Delta)$ is $\mathrm{rad}^2/\mathrm{s}$.

Physically, $V(\Delta)$ and $V(\Delta+2n\pi)(n=0,\pm1,\pm2,...)$ should be the equal. Therefore, the low-order implementation is to use a circular function. Meanwhile, to account for the intrinsic frequency difference, a linear term of detuning is $\nu$ included. Altogether, the potential force is chosen as:

$$\frac{dV(\Delta)}{d\Delta} = -2\pi\nu + 2\pi\varepsilon\sin(\Delta) \tag{C.3}$$

and thus the "washboard" potential $V(\Delta)$ is:

$$V(\Delta) = -2\pi\nu\Delta - 2\pi\varepsilon\cos(\Delta). \tag{C.4}$$

The unit of $\nu$ and $\varepsilon$ are both Hz.

Substituting Eq. (C.3) into Eq. (C.1), we obtain the Adler equation:

$$\frac{d\Delta}{dt} = 2\pi\nu - 2\pi\varepsilon\sin(\Delta) + \zeta(t) \tag{C.5}$$

The white noise $\zeta(t)$ satisfies $\langle\zeta(t)\rangle = 0$ and $\langle\zeta(\tau+t)\zeta(\tau)\rangle = 2T_{\mathrm{eff}}\delta(t)$. The effective temperature $T_{\mathrm{eff}}$ characterizes the level of the noise. $T_{\mathrm{eff}}$ has the same unit of $V(\Delta)$, $\mathrm{rad}^2/\mathrm{s}$.

The probability distribution of $\Delta$, $P(\Delta,t)$ satisfies the Fokker-Planck equation:

$$\frac{\partial P}{\partial t} = \frac{\partial V(\Delta)}{\partial\Delta} + T_{\mathrm{eff}}\frac{\partial^2 P}{\partial\Delta^2} \tag{C.6}$$

$P(\Delta)$ of the equilibrium state can be obtained by solving Eq. (C.6) with $\frac{\partial P}{\partial t} = 0$. The time-independent solution is:

$$\tilde{P}(\Delta) = \frac{1}{C}\int_{\Delta}^{\Delta+2\pi} \exp\frac{V(\Delta') - V(\Delta)}{T_{\mathrm{eff}}} d\Delta', \tag{C.7}$$

with $C$ the normalization factor.

Substituting Eq. (C.4) into Eq. (C.7), one obtains:

$$\tilde{P}(\Delta) = \frac{1}{C}\int_{\Delta-2\pi}^{\Delta} \exp\Big\{-\frac{2\pi\nu(\Delta'-\Delta)}{T_{\mathrm{eff}}}\Big\}\cdot\exp\Big\{-\frac{2\pi\varepsilon}{T_{\mathrm{eff}}}\big(\cos(\Delta')-\cos(\Delta)\big)\Big\}d\Delta'. \tag{C.8}$$

We further change the form of the integral, in order to apply Gaussian-Laguerre quadrature to compute $\tilde{P}(\Delta)$. We substitute $2\pi\nu(\Delta'-\Delta)/T_{\mathrm{eff}}$ as $k$. The lower bound $\Delta$ and the upper bound $\Delta+2\pi$ of the integral then become 0 and $4\pi^2\nu/T_{\mathrm{eff}}$ respectively; and $d\Delta'$ becomes $\frac{T_{\mathrm{eff}}}{2\pi\nu}dk$. Altogether, $\tilde{P}(\Delta)$ can be written as:

$$\begin{aligned}\tilde{P}(\Delta) &= \frac{1}{C}\int_0^{\frac{4\pi^2\nu}{T_{\mathrm{eff}}}} \exp\{-k\}F(k)dk \\ F(k) &= \frac{T_{\mathrm{eff}}}{2\pi\nu}\exp\Big\{-\frac{2\pi\varepsilon}{T_{\mathrm{eff}}}\big[\cos(\Delta+\frac{T_{\mathrm{eff}}}{2\pi\nu}k)-\cos(\Delta)\big]\Big\}.\end{aligned} \tag{C.9}$$

Empirically, the upper bound $4\pi^2\nu/T_{\text{eff}}$ can be approximated as $+\infty$, so that the integral can be estimated by the Gauss-Laguerre quadrature method.

The method approximates the integral of the following form as:

$$\int_0^{+\infty} \exp\{-x\}F(x)dx \approx \sum_{i=1}^{n} w_i F(x_i), \tag{C.10}$$

with $x_i$ the $i$-th root of Laguerre polynomial $L_n(x)$ and the weight $w_i = \frac{x_i}{(n+1)^2[L_{n+1}(x_i)]^2}$.

In the code, MATLAB function `GaussLaguerre_2.m`[1] is used to generated $x_i$ and $w_i$. The upper bound of the summation is set to $n = 40$.

To calculate $\tilde{P}(\Delta)$, a customized MATLAB function `P_delta.m` is written and stored in the repository. To fit an experimentally obtained distribution $\tilde{P}(\Delta) \in [-\pi, \pi]$, customized functions named as `lsqFitPhaseLockPDF_*.m` are used. There are three different approaches. One used to fit the distribution where $\Delta$ means the inter-flagellar phase difference. The other two are for fitting the $\tilde{P}(\Delta)$ where $\Delta$ means the phase difference between the external flow and a cell's flagellar beating.

As an end note, $T_{\text{eff}}$ in the output of the fitting functions might need to be divided by $4\pi^2$ to get the value consistent with previous literature.

[1] ©Geert Van Damme, *https://github.com/MNXANL/GRAU-CN/blob/master/Lab12/GaussLaguerre_2.m*.

# CURRICULUM VITÆ

## Da WEI

| | |
|---|---|
| 05-07-1990 | Born in Hefei, China. |

## EDUCATION

| | |
|---|---|
| 2007–2011 | Undergraduate in Physics<br>University of Science and Technology of China, Hefei, China |
| 2011–2014 | Master in Physics<br>University of Science and Technology of China, Hefei, China |
| 2020 | PhD. in Biophysics<br>Technische Universiteit Delft, Delft, Nederland |
| *Thesis:* | Experimental investigation of ciliary flow with *C. reinhardtii*: hydrodynamics, ultrastructure, and ciliary difference |
| *Promotor:* | Dr. M. -E. Aubin-Tam |
| *Copromotor:* | Dr. D. S. W. Tam |

# LIST OF PUBLICATIONS

5. **D. Wei**, P. G., Dehnavi, M. -E., Aubin-Tam, D. S. W., Tam, *Is the Zero Reynolds Number Approximation Valid for Ciliary Flows?*, Physical Review Letters **122**, 124502 (2019).

4. G. J, Amador*, **D. Wei***, D. S. W., Tam, M. -E., Aubin-Tam, *Fibrous Flagellar Hairs of Chlamydomonas reinhardtii Do Not Enhance Swimming*, Biophysical Journal, Vol. **118**, Issue 12 (2020).

3. P. G., Dehnavi, **D. Wei**, M. -E., Aubin-Tam, D. S. W., Tam, *Optical Tweezers-based Velocimetry: a method to measure microscale unsteady flows*, Experiments in Fluids, accepted.

2. **D. Wei***, P. G., Dehnavi*, M. -E., Aubin-Tam, D. S. W., Tam, *Measurements of the unsteady flow field around beating cilia*, in submission.

1. **D. Wei**, G. Quaranta, D. S. W., Tam, M. -E., Aubin-Tam, *C. reinhardtii uses its cis flagellum to couple to external flows*, in submission.